Study of Noise-Induced Dynamics in Model Gas Turbine Combustors

Thesis

by

Neha Vishnoi

(2018MEZ0019)

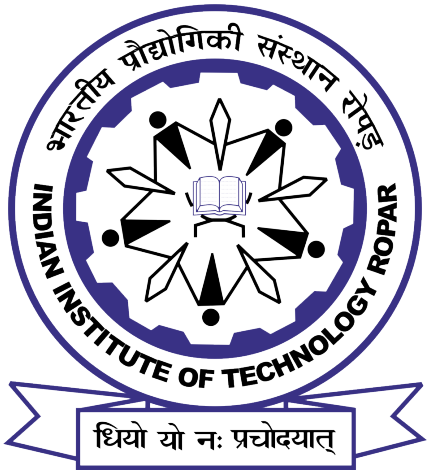

DEPARTMENT OF MECHANICAL ENGINEERING

INDIAN INSTITUTE OF TECHNOLOGY ROPAR

OCTOBER, 2024

Study of Noise-Induced Dynamics in Model Gas Turbine Combustors

A Thesis Submitted

in Partial Fulfilment of the Requirements

for the Degree of

DOCTOR OF PHILOSOPHY

by

Neha Vishnoi

(2018MEZ0019)

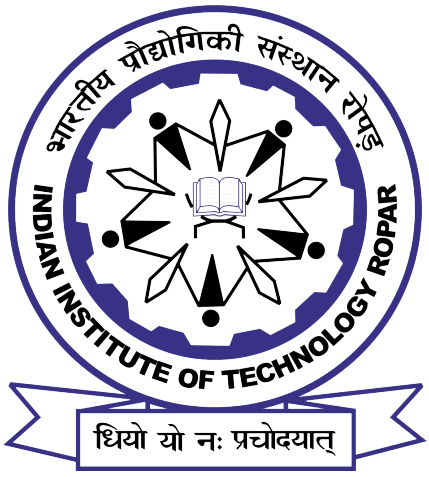

DEPARTMENT OF MECHANICAL ENGINEERING

INDIAN INSTITUTE OF TECHNOLOGY ROPAR

October, 2024

DEDICATED TO FAMILY AND FRIENDS

Declaration of Originality

I hereby declare that the work which is being presented in the thesis entitled **"Study of Noise-Induced Dynamics in Model Gas Turbine Combustors"** has been solely authored by me. It presents the result of my own independent investigation/research conducted during the time period from January 2019 of joining the Ph.D. program to July 2024 of Ph.D. Thesis submission under the supervision of **Dr. Lipika Kabiraj, Assistant Professor, Indian Institute of Technology Ropar, Punjab, India**. To the best of my knowledge, it is an original work, both in terms of research content and narrative, and has not been submitted or accepted elsewhere, in part or in full, for the award of any degree, diploma, fellowship, associateship, or similar title of any university or institution. Further, due credit has been attributed to the relevant state-of-the-art and collaborations (if any) with appropriate citations and acknowledgments, in line with established ethical norms and practices. I also declare that any idea/data/fact/source stated in my thesis has not been fabricated/ falsified/ misrepresented. All the principles of academic honesty and integrity have been followed. I fully understand that if the thesis is found to be unoriginal, fabricated, or plagiarized, the Institute reserves the right to withdraw the thesis from its archive and revoke the associated Degree conferred. Additionally, the Institute also reserves the right to appraise all concerned sections of society of the matter for their information and necessary action (if any). If accepted, I hereby consent for my thesis to be available online in the Institute's Open Access repository, inter-library loan, and the title & abstract to be made available to outside organizations.

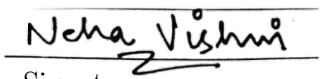

Signature

Name: Neha Vishnoi
Entry Number: 2018MEZ0019
Program: PhD
Department: Mechanical Engineering
Indian Institute of Technology Ropar
Rupnagar, Punjab 140001

Date: 18th October 2024

Acknowledgement

First and foremost, I would like to express my deepest gratitude to my PhD supervisor, Dr. Lipika Kabiraj, for her unwavering support, invaluable guidance, and constant encouragement throughout my doctoral journey. Her expertise, patience, and insightful feedback have been crucial in the successful completion of this thesis.

I am immensely thankful to my faculty collaborators and mentors, Dr. Aditya Saurabh (IIT Kanpur), Dr. Pankaj Wahi (IIT Kanpur), Dr. Vikrant Gupta (GTIIT, China), Dr. Agustin Valera Medina (Cardiff University) and Dr. Syed Mashruk (Cardiff University), for their significant contributions, insightful discussions, and collaborative efforts that greatly enriched my research work. I extend my heartfelt thanks to the members of my doctoral committee, Dr. Partha S. Dutta, Dr. Srikant S. Padhee, Dr. Chander S. Sharma, and Dr. Ekta Singla, for their valuable advice, constructive criticism, and continuous support throughout the course of my research.

To my friends Vivek, Anand, Neeraj, Gopal, Rakesh, Mainak, Raushan, Ajay, Shashikant, Kalyani, Akanksha, Nancy, Pragya, Surbhi, Suraj, Shailja, Kamala and Haydee, thank you for your camaraderie, encouragement, and the cherished memories we have shared. Your support has been a constant source of motivation and joy. A special note of appreciation goes to my family. To my parents, Mrs. Veena Vishnoi and Dr. Anil K. Vishnoi, my brother, Mr. Nikhil Vishnoi, my sister-in-law, Mrs. Monisha Vishnoi, my dearest niece and nephew, Janki and Reyansh, your encouragement, love, patience, understanding, and unwavering support have been the cornerstone of my journey. Thank you for being my rock.

I would also like to acknowledge the IIT Ropar fraternity, including academics and RND staff - Mr Ravinder, Mr Harprit, Mr Karanvir, Mrs Prashi, Mrs Sarabjit, Mrs Kamaljit, Mrs Rubal, Mr Akshpreet and Ms Amrit) and Mechanical Engineering department (HoD - Dr Prabhat Agnihotri and office staff - Mr Kaushal, Mr Jagmail, Mr Vinay and Mr Gurvinder) for providing an inspiring academic environment and the necessary resources to carry out my research. I would like to express my gratitude to the Ministry of Human Resource Development (MHRD) for providing the fellowship that supported my research work. I would also like to acknowledge SPARC-MHRD project for providing me the grant to visit Cardiff University for performing the experiments. Also, I would like to acknowledge the International Travel Grant (ITS) awarded by SERB, DST to attend SoTiC conference (2023) held at ETH Zurich for presenting my work.

This thesis would not have been possible without the support, guidance, and love from all the individuals mentioned above. Thank you all from the bottom of my heart. Lastly, I would like to thank God for His guidance, strength, and blessings that have supported me throughout this journey.

Certificate

This is to certify that the thesis entitled **"Study of Noise-Induced Dynamics in Model Gas Turbine Combustors"**, submitted by **Neha Vishnoi (2018MEZ0019)** for the award of the degree of **Doctor of Philosophy** of Indian Institute of Technology Ropar, is a record of bonafide research work carried out under my guidance and supervision. To the best of my knowledge and belief, the work presented in this thesis is original and has not been submitted, either in part or full, for the award of any other degree, diploma, fellowship, associateship or similar title of any university or institution.

In my opinion, the thesis has reached the standard fulfilling the requirements of the regulations relating to the Degree.

Signature of the Supervisor(s)

Name(s): Dr Lipika Kabiraj

Department(s): Mechanical Engineering

Indian Institute of Technology Ropar

Rupnagar, Punjab 140001

Date: 18th October 2024

Lay Summary

Gas turbine engines, commonly used in power generation and aircraft, can suffer from a serious problem known as thermoacoustic instability. This issue arises from a constructive interaction between the flame and acoustics of the combustion chamber, leading to loud and large amplitude pressure oscillations. These oscillations can cause severe wear and tear on engine components, risking both safety and efficiency.

Noise is an inherent feature of such combustion systems, stemming from fuel-air supply systems, unsteady combustion, turbulence, and aerodynamics. In these systems, noise characteristics are expected to vary with changes in operating conditions (temperature, Reynolds number, equivalence ratio, etc.). Consequently, pressure oscillations in such combustors always contain noise-induced features, regardless of the presence of thermoacoustic instability. These noise-induced features can be utilized to develop control or mitigation strategies for suppressing the instability. Control measures can be either passive, such as employing physical acoustic dampers in the combustors to absorb acoustic energy, or active, such as identifying measures that can help in early prediction of instability before it occurs. In both cases, it is crucial to investigate how changes in inherent noise dynamics, alongside changes in operating conditions and combustor designs, affect thermoacoustic coupling and control measures. This work focuses on investigating how different types of noise affect these dangerous oscillations and seeks to improve prediction and management strategies. For this investigation, the thesis is divided into two main parts:

- Active control of thermoacoustic instability (early warning prediction): This part examines the effect of noise properties on the reliability of early warning indicators that can detect impending instability. The study tests how these indicators perform under different noise conditions to determine which ones work best. It turns out that some indicators, such as those measuring the consistency of the engine's performance, are more reliable than others. In contrast, some indicators are too sensitive to noise and provide misleading signals. This finding helps in selecting the most effective tools for monitoring and maintaining engine safety.

- Noise and turbulent flow: The second part of the research focuses on how noise interacts with the features of turbulent flows inside the engine. Such engines involve complex swirling (or recirculating) flows inside the combustion chamber, which are crucial for efficiently mixing fuel and air. These recirculating flow features have inherent helical instability that can interact with noise and further drive thermoacoustic instability. Therefore, this part focuses on understanding how these interactions occur and how different noise patterns affect the swirling flow and flames. This work identifies which noise features can either suppress or excite unstable oscillations in the system. This insight helps in designing better engine systems that can minimize instability by carefully controlling noise and flame behavior.

In summary, the findings provide valuable guidance for engineers to better design and operate engines, ultimately contributing to more reliable and safer gas turbine technology.

Abstract

This thesis presents a comprehensive analysis of the stochastic dynamics in confined combustion systems, particularly gas turbine combustors, where thermoacoustic instability poses a significant challenge. Thermoacoustic instability refers to self-induced, large-amplitude pressure oscillations resulting from a constructive feedback loop between acoustic waves and unsteady heat release within the combustion system. These oscillations can lead to severe mechanical and thermal stresses that can compromise the structural integrity of the combustor. Noise, an inherent feature in such combustion systems, complicates the phenomenon by affecting the amplitude and behavior of these oscillations. Recent studies have highlighted that noise can lead to complex dynamics in such systems, which vary with changes in operating conditions and combustor designs. Hence, it is crucial to investigate the effect of noise properties on thermoacoustic coupling. Given the challenges posed by thermoacoustic instability, the study emphasizes on the necessity of considering noise properties—correlation time (or color) and intensity—in developing effective prediction, suppression, and control strategies. The work investigates how noise properties interact with thermoacoustic coupling, with a particular focus on early warning prediction of thermoacoustic instability and helical instabilities associated with swirling flows in practical gas turbine configurations.

The thesis is divided into two main parts. The first part examines how noise characteristics influence the reliability of various early warning indicators (EWIs) for predicting thermoacoustic instability in gas turbine combustors. A combination of experimental and numerical approaches is employed, including an electroacoustic Rijke tube simulator, stochastic Van der Pol oscillators, and a lean premixed flat flame combustion system. The study explores how different types of noise, both additive and multiplicative, affect EWIs based on signal amplitude distribution, frequency spectra, fractal, and complexity measures, as the system approaches bifurcation, considering noise color and intensity. These systems exhibit instability through both supercritical and subcritical Hopf bifurcations. The analysis is conducted in the subthreshold regime, where the stable focus remains the only possible asymptotic state. The findings reveal that variations in noise color can lead to non-monotonic trends in EWIs, reducing their reliability. Our results indicate that the coherence factor is a reliable indicator for the entire range of investigated noise color, while variance and decay rates of the autocorrelation function (ACF) are reliable when noise correlation times are either much smaller or larger than the system time scale. Kurtosis, permutation entropy and Jensen-Shannon complexity can be effectively employed in systems where noise exhibits minimal correlation time (resembling white noise). While the Hurst exponent proves a reliable indicator in systems where noise has correlation times much larger than the time scale of the system, multi-fractal spectrum width and skewness are deemed unsuitable as EWIs. These insights enhance the understanding of the effectiveness and limitations of various EWIs in predicting or monitoring impending instability.

The second part of the thesis focuses on how inherent noise interacts with turbulent swirling flows in combustors. Swirling flows, used in gas turbine combustors for flame stabilization, are

prone to precessing vortex core (PVC), a self-excited global hydrodynamic instability associated with vortex breakdown. This instability leads to large-scale coherent structures and significant flame fluctuations, potentially triggering thermoacoustic instability. It is, therefore, crucial to study the interaction between these coherent structures and inherent combustor noise. The aim is to understand how PVC responds to broadband noise excitation, aiding the development of strategies to mitigate thermoacoustic instability. To this end, a novel multiple swirl burner is developed, capable of operating with various hydrogen-enriched fuel blends using RANS simulations. A dual swirl burner configuration showed promise due to its enhanced mixing capabilities. The effects of acoustic excitation on the swirling flow field are examined using Schlieren image velocimetry (SIV), with Proper Orthogonal Decomposition (POD) and Spectral Proper Orthogonal Decomposition (SPOD) analyses employed to identify dominant coherent structures and their interactions with acoustic excitation. The study confirms the presence of single and double helical PVC, marginally stable modes excited by turbulent fluctuations. Acoustic excitation at frequencies lower than the PVC mode is found to suppress the PVC, while broadband forcing excited both single and double helical instabilities, increasing the likelihood of thermoacoustic instability.

Summarizing, this thesis emphasizes the crucial role of noise characteristics in predicting and managing thermoacoustic instability in gas turbine combustors. The findings offer valuable insights for enhancing the design and calibration of monitoring systems, contributing to more reliable and effective control strategies in modern gas turbine systems.

Keywords: Early warning indicators; Hopf bifurcation; Noise-induced dynamics; Precessing vortex core; RANS simulations; Swirling flows; Thermoacoustic instability

List of Publications

Journal: published

1. N. Vishnoi and L. Kabiraj, "Effect of Background Noise on Early Warning Indicators of Thermoacoustic Instability", Combustion and Flame, 269 (2024): 113687. https://doi.org/10.1016/j.combustflame.2024.113687

2. N. Vishnoi, V. Gupta, A. Saurabh, and L. Kabiraj, "Reliability of Early Warning Indicators of Critical Transition in Stochastic Van der Pol Oscillators with Additive Correlated Noise", Nonlinear Dynamics, 112 (2024):15193–15217. https:/doi.org/10.1007/s11071-024-09831-1

3. N. Vishnoi, V. Gupta, A. Saurabh, and L. Kabiraj, "Effect of Colored Noise on Precursors of Thermoacoustic Instability in Model Gas Turbine Combustors", International Journal of Spray and Combustion Dynamics, 16(3) (2024): 80-92. https://doi.org/10.1177/17568277241262168

4. N. Vishnoi, A. Saurabh, and L. Kabiraj, "Schlieren Image Velocimetry and Modal Decomposition Study of Preheated Isothermal Flow from a Generic Multi-Swirl Burner", Journal of Engineering for Gas Turbines and Power, 147(1) (2024): 011012. https://doi.org/10.1115/1.4066243

5. N. Vishnoi, V. Gupta, A. Saurabh, and L. Kabiraj, "Effect of Correlation Time of Combustion Noise on Early Warning Indicators of Thermoacoustic Instability". Chaos: An Interdisciplinary Journal of Nonlinear Science, 34(3) (2024): 033129. https://doi.org/10.1063/5.0174468

6. N. Vishnoi, V. Gupta, A. Saurabh, and L. Kabiraj, "System Parameter Identification of a Colored-Noise-Driven Rijke Tube Simulator", Journal of Engineering for Gas Turbines and Power, 144(9) (2022): 091017. https://doi.org/10.1115/1.4055212

Journal: revisions-submitted/ready for submission

1. N. Vishnoi, R. Steinert, A. Saurabh, C.O. Paschereit and L. Kabiraj, "Effects of Noise Intensity on Early Warning Indicators of Thermoacoustic Instability: An Experimental Investigation on a Lean-Premixed Combustion System", Combustion and Flame, 2024 **(revisions submitted)**.

2. N. Vishnoi, S. Verma, Syed Mashruk, A. Valera-Medina, A. Saurabh, and L. Kabiraj, "Effect of Swirler Configuration on Combustion of Steam Diluted Methane-Hydrogen Mixtures in Dual Swirl Burners", Combustion Science and Technology, 2024 **(ready for submission)**.

Book chapter

1. L. Kabiraj, N. Vishnoi and A. Saurabh, "A Review on Noise-induced Dynamics of Thermoacoustic Systems", Dynamics and Control of Energy Systems (2020), pp.265-281. https://doi.org/10.1007/978-981-15-0536-2_12

Conference Proceedings: peer-reviewed

1. N. Vishnoi, A. Valera-Medina, A. Saurabh, and L. Kabiraj, "Combustion of Hydrogen-Methane-Air-Mixtures in a Generic Triple Swirl Burner: Numerical Studies", Proceedings of Turbo Expo: Power for Land, Sea, and Air, ASME (2021), Vol. 84959, p. V03BT04A016. https://doi.org/10.1115/GT2021-59744

2. N. Vishnoi, P. Wahi, A. Saurabh, and L. Kabiraj, "On the Effect of Noise Induced Dynamics on Linear Growth Rates of Oscillations in an Electroacoustic Rijke Tube Simulator", Proceedings of Turbo Expo: Power for Land, Sea, and Air, ASME (2021), Vol. 84942, p. V03AT04A013. https://doi.org/10.1115/GT2021-58691

3. N. Vishnoi, A. Valera-Medina, A. Saurabh, and L. Kabiraj, "Flow Dynamics in a Triple Swirl Burner", Proceedings of the National Aerospace Propulsion Conference, Lecture Notes in Mechanical Engineering. Springer, Singapore (2020), pp. 583-599. https://doi.org/10.1007/978-981-19-2378-4_34

Conference Proceedings: non peer-reviewed

1. N. Vishnoi, S. Verma, Syed Mashruk, A. Valera-Medina, A. Saurabh, and L. Kabiraj, "Effect of Swirler Configurations on Combustion of Humidified Lean Premixed Methane-Hydrogen Mixtures", AIAA SCITECH (2023) Forum (p. 1060). https://doi.org/10.2514/6.2023-1060

Conference presentations

1. N. Vishnoi and L. Kabiraj, "Ammonia-Methane-Air Combustion in Dual Swirl Burners: A Numerical Investigation", Turbomachinery Technical Conference and Exposition (ASME Turbo Expo), Memphis, Tennessee, USA (2025).

2. N. Vishnoi, A. Saurabh, and L. Kabiraj, "Experimental Investigation of Coherent Structures in a Generic Dual Swirl Burner Under Broadband Noise Excitation", APS Division of Fluid Dynamics (DFD), Salt Lake city, Utah, USA (2024).

3. N. Vishnoi, A. Saurabh, and L. Kabiraj, "Schlieren Image Velocimetry and Modal Decomposition Study of Preheated Isothermal Flow from a Generic Multi-Swirl Burner", Turbomachinery Technical Conference and Exposition (ASME Turbo Expo), London, England, UK (2024).

4. N. Vishnoi, V. Gupta, A. Saurabh, and L. Kabiraj, "Effect of Colored noise on Precursors of Thermoacoustic Instability in Model Gas Turbine Combustor", Symposium on Thermoacoustics in Combustion: Industry meets Academia, ETH Zurich, Switzerland (2023).

5. N. Vishnoi, V. Gupta, A. Saurabh, and L. Kabiraj, "Effect of Noise Color on Fractal Signature and Related Precursors of Thermoacoustic Instability", The 29th International Congress on Sound and Vibration (ICSV29-2023), Prague, Czech Republic (2023).

6. N. Vishnoi, S. Verma, Syed Mashruk, A. Valera-Medina, A. Saurabh, and L. Kabiraj, "Effect of Swirler Configurations on Combustion of Humidified Lean Premixed Methane-Hydrogen Mixtures", AIAA SCITECH Forum, Virtual (2023).

7. N. Vishnoi, S. Verma, A. Valera-Medina, A. Saurabh, and L. Kabiraj, "Flow and Flame Visualization in a Generic Dual Swirl Burner", The 9th International and 49th National conference of Fluid Mechanics and Fluid Power (FMFP-2022), IIT Roorkee, UK (2022).

8. N. Vishnoi, S. Verma, A. Valera-Medina, A. Saurabh, and L. Kabiraj, "Flashback Characteristics of Steam-Diluted Hydrogen-Methane-Air Combustion in a Dual Swirl Burner", 12th Annual meeting of Saudi Arabian Section of the Combustion Institute, Abha, Saudi Arabia (2022).

9. N. Vishnoi, V. Gupta, A. Saurabh, and L. Kabiraj, "System Parameter Identification of a Colored-Noise-Driven Rijke Tube Simulator", Turbomachinery Technical Conference and Exposition (ASME Turbo Expo), Virtual (2022).

10. N. Vishnoi, A. Saurabh, and L. Kabiraj, "Colored and White Noise Effects on a Rijke Tube Simulator", Symposium on Thermoacoustics in Combustion: Industry meets Academia, TUM, Germany (2021).

11. N. Vishnoi, A. Valera-Medina, A. Saurabh, and L. Kabiraj, "Combustion of Hydrogen-Methane-Air-Mixtures in a Generic Triple Swirl Burner: Numerical Studies", Turbomachinery Technical Conference and Exposition (ASME Turbo Expo), Virtual (2021).

12. N. Vishnoi, P. Wahi, A. Saurabh, and L. Kabiraj, "On the Effect of Noise Induced Dynamics on Linear Growth Rates of Oscillations in an Electroacoustic Rijke Tube Simulator", Turbomachinery Technical Conference and Exposition (ASME Turbo Expo), Virtual (2021).

13. N. Vishnoi, S. Mashruk, A. Valera-Medina, A. Saurabh, and L. Kabiraj, "Numerical Study of Lean Premixed Humidified Hydrogen-Methane-Air Combustion in a Generic Triple Swirl Burner", 11th Annual meeting of Saudi Arabian Section of the Combustion Institute, KAUST, Saudi Arabia (2021).

14. N. Vishnoi, A. Valera-Medina, A. Saurabh, and L. Kabiraj, "Flow Dynamics in a Triple Swirl Burner", National Aerospace Propulsion Conference (NAPC), Virtual (2020).

15. N. Vishnoi, P. Wahi, A. Saurabh, and L. Kabiraj, "Influence of Stochastic Forcing on Limit Cycle Dynamics on a Modelled Thermoacoustic System", Conference on Nonlinear Systems and Dynamics, IIT Kanpur (2019).

Poster presentations

1. N. Vishnoi, A. Saurabh, C.O. Paschereit and L. Kabiraj, "Experimental Investigation of Noise-Induced Dynamics in a Thermoacoustic System", Turbomachinery Technical Conference and Exposition (ASME Turbo Expo), London, England, UK, (2024).

2. N. Vishnoi, L. Kabiraj, "Study of Limit Cycle Dynamics on a Modelled Thermoacoustic System", Research Conclave, IIT Ropar (2019).

Awards

1. Selected as a participant from IIT Ropar in Global Young Scientists Summit (GYSS) to be held from 6th - 10th January 2025 at National University of Singapore (NUS).

2. Awarded Enabling Travel Grant by American Physical Society to attend 77th Annual meeting of APS DFD to be held from 24th - 28th November 2024 at Salt Palace Convention Center, Salt Lake City, Utah, USA.

3. Awarded DST International Travel Grant to attend Symposium on Thermoacoustics in Combustion: Industry meets Academia, held from 11th - 14th September 2023 at ETH Zurich, Switzerland.

4. Awarded DST AWSAR (Augmenting writing skills for articulating research) award for PhD research story, 2020.

5. Awarded Best Paper award in National Aerospace Propulsion Conference (NAPC), held from 17th – 19th December 2020 at BMS College of Engineering, Bengaluru.

Courses taken during PhD – CGPA 10

1. Semester I: Convective Heat Transfer, Nonlinear Dynamics and Fluid Machinery

2. Semester II: Advanced Fluid Mechanics

Contents

List of Figures

List of Tables

List of Symbols

$()_0$	Mean quantity
α	ACF decay rates in Part I and Under-relaxation factor in chapter 6
β	Coherence factor
χ	Normalized EWIs
Δf	Spectral width at half maximum
δ	Dirac delta function
δ_l	Flame thickness
$\dot{Q}'$	Heat release rate fluctuations
$\dot{m}_t$	Mass flow rate of air and steam (kg/h)
$\dot{m}_{air}$	Mass flow of air (g/s)
$\dot{m}_{CH_4}$	Mass flow of methane (g/s)
$\dot{m}_{H_2}$	Mass flow of hydrogen (g/s)
ϵ	Deviation of growth rates from true values
$\epsilon(t)$	Gaussian white noise
η	Modal amplitude
Γ	White noise intensity
γ	Ratio of specific heats at constant pressure and volume
CRZ	Central recirculation zone
FPS	Frame per second
ORZ	Outer recirculation zone
POD	Proper orthogonal decomposition
PVC	Precessing vortex core
px	Pixel
RANS	Reynolds averaged Navier-Stokes equation
ROI	Region of interest
RTC	Real-time controller

SIV Schlieren image velocimetry

SNR Signal to noise ratio

SPOD Spectral proper orthogonal decomposition

SVD Singular value decomposition

ν Decay rates of acoustic pressure

ν_r Turbulent viscosity ratio

Ω Mean vorticity (1/s)

ω_0 Eigenfrequency

$\overline{p}$ Mean of data points

ϕ Equivalence ratio

$\phi(t)$ Phase

ϕ_H Hopf point

ϕ_i Spatial modes

ϕ_{SN} Saddle-node point

ρ Density of air

σ RMS of noise intensity (Pa)

$\sum$ Diagonal matrix of mode eigenvalues

τ_c Noise correlation time

τ_d Time delay

θ Angles at which LED and knife edge are placed

$\xi(t)$ Additive colored noise

ζ_j Acoustic damping

A Matrix of spatial modes

a Amplitude of oscillations

a_j Amplitude of jth mode

C Normalizing constant

c Counter clockwise direction

c_0 Speed of sound

C_1, C_2 Damping coefficients

c_1, c_2, c_3 Constants

c_p Specific heat at constant pressure

c_v Specific heat at constant volume

CP Jensen-Shannon complexity

D Colored noise intensity in Part I and Burner exit diameter (mm) in Part II

d_E Embedding dimension

Da Damköhler number

f_p Peak frequency

$F_q(w)$ Fluctuation function

$f_{()}$ Focal length of the parabolic mirrors

$g(\eta)$ Function of η

H Hurst exponent at $q = 2$

H_p Spectral height

H_q q-order Hurst exponent

I_t Turbulent intensity

K Normalized heater power

k Kurtosis

K_H Hopf point

K_{SN} Saddle point

Ka Karlovitz number

KL Kullback-Leibler divergence

L Burner length (mm)

L_a Length of Rijke tube

M Number of partition in Part I and Spatial locations in Part II

M_a Mach number

N Number of acoustic modes in chapter 2, Total number of data points in chapters 3-5 and Number of snapshots in chapter 7

n Number of modes

OU Ornstein-Uhlenbeck process

p Normalized acoustic pressure

P, Q Probability distribution

p' Acoustic pressure oscillations (Pa)

$P_c(a_j)$ PDF of OU process

p_i Pressure time series data points

$P_w(a_j)$ PDF of white noise

PDF Probability distribution function

PE Normalized permutation entropy

PE' Permutation entropy

PSD Power spectral density

q' Heat release rate fluctuations

Re_t Turbulent Reynolds number

S Skewness in Part I and Swirl number in Part II

s^2 Variance of OU process

$S_{\epsilon\epsilon}(\omega)$ Power spectral density of white noise

$S_{\xi\xi}(\omega)$ Power spectral density of OU noise

SDE Stochastic differential equation

St Strouhal number

T_0 Acoustic time period

T_f Flame temperature

T_{in} Inlet temperature (K)

U Instantaneous snapshot matrix

u Normalized acoustic velocity

u_f Acoustic velocity at x_f

u_n Reconstructed field variable

V Variance

V_r Mean radial velocity (m/s)

V_z Mean axial velocity (m/s)

V_0 Burner exit velocity (m/s)

v_e Estimated values of growth rates

v_t True values of growth rates

w Window scale

W^T Matrix of temporal mode coefficients

w_{ri} Temporal coefficients

X Coordinate X

x state variable in chapters 3-4 and Normalized axial direction in chapter 6

$x(\pi)$ Occurrence of each pattern

x, y Coordinates (mm)

x_f Axial location of heater wire mesh

Y Coordinate Y

Z Coordinate Z

ACF Autocorrelation function

CECP Complexity entropy causality plane

CECS Complexity entropy causality space

EWIs Early warning indicators

f Frequency

JSD Jensen-Shannon divergence

LCO Limit cycle oscillations

MFDFA Multi-fractal detrended fluctuation analysis

PDF Probablity distribution function

PMT Photo-multiplier tube

SDEs Stochastic differential equations

t Normalized time

Chapter 1

Introduction

1.1 Thermoacoustic instability

Confined combustion systems, such as those employed in gas turbines, and rocket motors, are susceptible to self-induced, large amplitude acoustic pressure oscillations, known as thermoacoustic instability. These oscillations arise spontaneously from constructive feedback between acoustic pressure oscillations in the combustor (p') and unsteady heat release rate fluctuations ($\dot{q}'$) from the combustion source (e.g., single or multiple turbulent flames) [1], as illustrated in Fig.1.1(A). The occurrence of thermoacoustic instability is explained by the famous Rayleigh criterion [9, 10], which is given as:

$$\int_V \int_T p'_{x,t}\ \dot{q}'_{x,t}\ \mathrm{d}t\ \mathrm{d}V > 0 \tag{1.1}$$

where, $p'_{x,t}$ and $\dot{q}'_{x,t}$ denoting pressure and heat release rate fluctuations respectively. According to this criterion, the combustion process adds (or removes) energy to the acoustic oscillations locally if the above integral is positive (or negative). The sign of this integral depends on the phase difference between p' and q': it is positive (or negative) when this phase difference is smaller (or larger) than 90° [1]. Instability occurs spontaneously only if the energy supplied to the acoustic mode by the combustion process exceeds the mode's energy losses due to, for example, viscous dissipation. Thus, as long as the driving force's magnitude exceeds that of the damping process, the mode's energy will increase over time. Initially, the oscillation amplitude increases exponentially until it saturates at a limit-cycle amplitude, as shown in Fig. 1.1(B). At this point, the time-averaged driving and damping processes are equal, and no net energy is added to the oscillating mode. These instabilities occur at frequencies associated with the combustor's natural acoustic modes—both planar and non-planar. The flame response is typically low-pass in nature [11] and is delayed in time, implying that an accurate description of thermoacoustic instability necessarily involves delayed-differential equations. When combustion and flames are involved, additional complexities, characteristic to the configuration under consideration such as equivalence ratio fluctuations [12] and swirl flow and flame dynamics [13, 14] must be incorporated.

Modern gas turbine technology relies on lean premixed (partially or fully) combustion to minimize NOx emissions. However, this approach, in addition to causing thermoacoustic instability, also introduces challenges such as flame blowout and flashback. The mechanisms identified in the literature that drive instability in such combustion systems are as follows: (also marked in Fig. 1.2(A)).

- *Equivalence ratio fluctuations [1, 15]:* In partially premixed systems, acoustic pressure

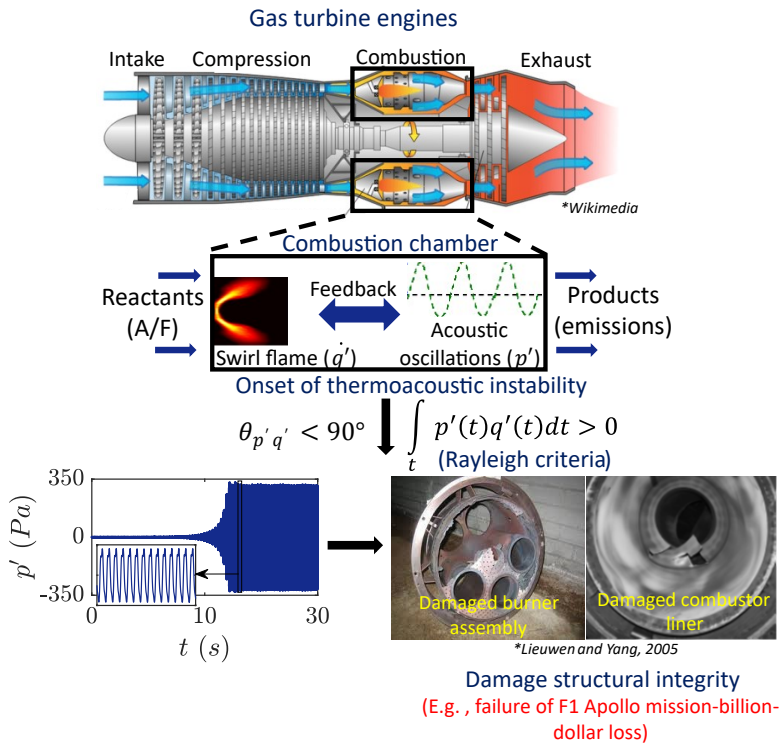

Figure 1.1: (A) An illustration of the occurrence of thermoacoustic instability (TAI) in gas turbine engine. The onset of TAI occurs due to a constructive feedback between unsteady heat release rate from flame and acoustics of the combustion chamber. (B) TAI manifests as the self-induced finite amplitude pressure oscillations, (C) An illustration of the damage caused by TAI: left - damaged burner assembly and right - damaged combustor liner (adapted from Yang and Lieuwen [1]).

oscillations tend to propagate upstream into the plenum/premixing section. Here, the oscillations modulate the mixing processes and fuel/air supply rates, creating a reactive mixture with a periodically varying equivalence ratio. This modulated mixture is convected into the flame, generating heat-release oscillations that drive the instability.

- *Flame area and reaction rate oscillations [16]:* An interaction between acoustic velocity fluctuations and the flame causes modulation of the flame front area, which periodically adds heat to the acoustic field, driving the instability.

- *Coherent structures (vortex-flame interaction):* These combustion systems often utilize either bluff-body or swirling flows for flame stabilization within combustors. Both of these methods, induces a vortex breakdown phenomenon, leading to the creation of a central recirculation zone (CRZ) that sustains the flame by supplying heat and active species [17], as illustrated in Fig. 1.2(A). This promotes efficient mixing of air-fuel mixtures and temperature control, reducing NOx emissions and enhancing safety against auto-ignition and flashback [18, 19]. Nonetheless, intense swirling flows ($S > 0.8$) are susceptible to a self-excited global hydrodynamic instability known as the precessing vortex core (PVC), associated with the vortex breakdown process–large scale coherent structure, shown in Fig. 1.2(B)–resulting in significant flame fluctuations [20–23]. These structures interact

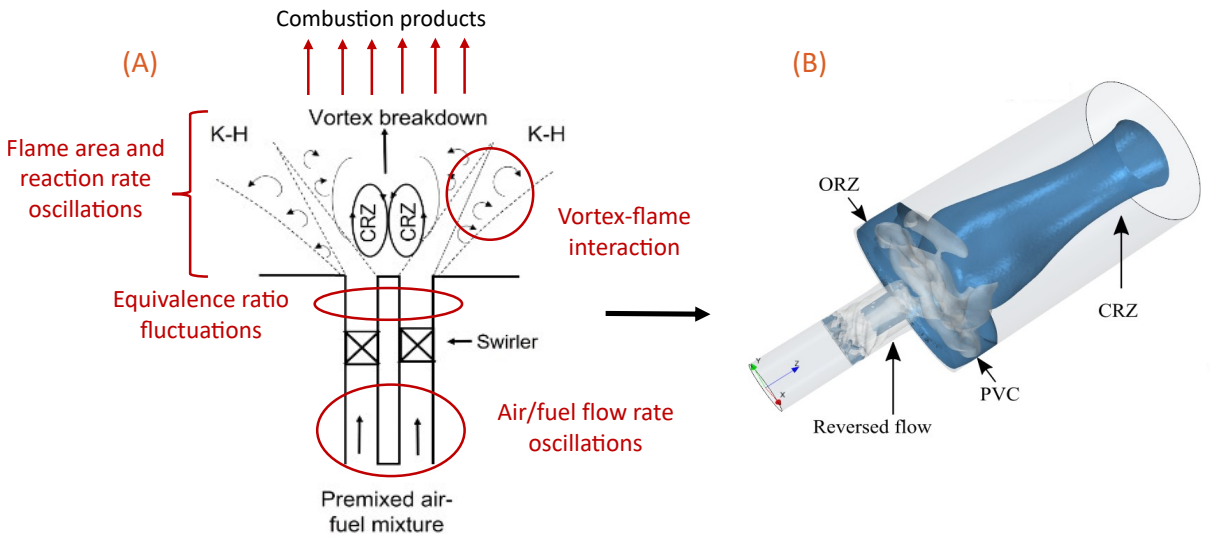

Figure 1.2: (A) Flow and flame processes that can cause thermoacoustic instabilities in premixed combustion systems. (B) Coherent structures associated with swirling flows driving the instability.

with fluctuations from turbulent flow or random changes in operational parameters (such as equivalence ratio, temperature, swirl intensity, and vorticity), further driving the thermoacoustic instability.

To be able to predict and suppress instability is a practical necessity and research in the field has primarily focused on understanding the instability phenomenon and developing methods for prediction and control. The Rayleigh criterion is not of much help in this regard, but the latter—the flame response—allows for the determination of whether a given combustor-flame configuration may become unstable for a given set of operating conditions: the flame response in the form of the flame transfer function and the flame describing function [24, 25] together with input-output representations for acoustics within the combustor provides sufficient information to establish stability boundaries. The method depends on the accurate measurement of the flame response—a task which becomes increasingly difficult if the flame configuration, operating conditions, and the acoustic field expected during the instability in modern combustors are to be exactly represented for the flame response measurements.

One of the interesting recent developments in the field was to note that, characteristic features aside, the combustion system is yet another dynamical system governed by a set of critical parameters. When fluctuations in system variables are small, the evolution is well represented by linear operators; but as the amplitude of fluctuations increases, system dynamics feature nonlinear behaviour such as amplitude saturation, bifurcations, and chaotic scenarios. Such systems features remarkable similarities in its dynamics with a wide spectrum of nonlinear systems implying that fundamental features of thermoacoustic instability may be studied based on a class of governing equations that have been developed for generic nonlinear systems with which thermoacoustic instability shares its dynamic features. As will be discussed, this perspective has also aided in developments in our understanding of noise-induced dynamics in such systems.

Thermoacoustic instability is highly undesirable in practical systems because of the large amplitude pressure oscillations that result in thrust oscillations, severe vibrations that interfere with control-system operation, enhanced heat transfer and thermal stresses to the combustor walls, oscillatory mechanical loads that result in fatigue of system components, and flame blow-off or flashback. These phenomena may result in premature wear of the components of the gas turbine that leads to costly shutdown or catastrophic component and/or mission failure (e.g.: the failure of America's first manned moon mission occurred due to these instabilities in F1 engine [26]. An example of the burner assembly and combustor liner damage due to the occurrence of the instability is shown in Fig. 1.1(C). It becomes necessary either to avoid the operational regime under which these instabilities occurs or to suppress the resulting oscillations. This requires the knowledge of stability margins of a system and the understanding of the dynamics of these instabilities, which are found to be influenced by the interactions between the thermoacoustic instabilities and other processes in a combustor [27]. Emerging trends in practical combustion systems tend to make them more susceptible to this feedback phenomenon. Consequently, determination of the stability boundaries is essential and here a noisy system may lead to problems associated with noise-induced oscillations/transitions. A basic understanding of the primary (Hopf) bifurcation would help understand this effect of noise.
In a stable combustor, large amplitude coherent oscillations (consisting of one or more distinct

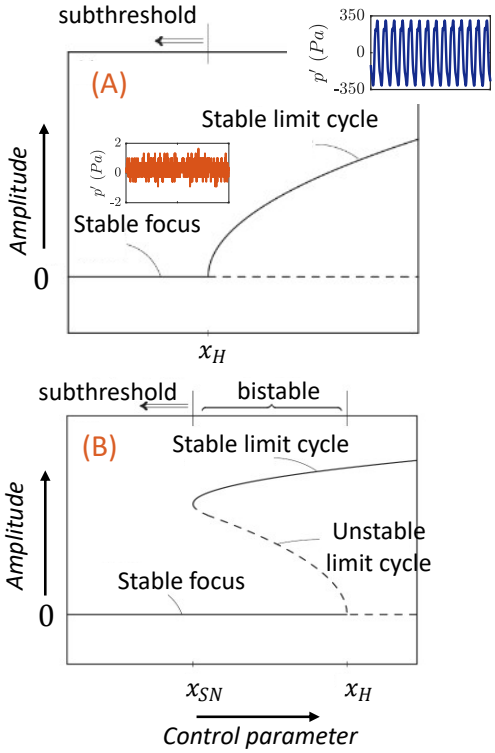

Figure 1.3: (A) Supercritical and (B) Subcritical Hopf bifurcation diagrams. The bifurcation parameter values at the Hopf point and saddle-node point are denoted as x_H and x_{SN}, respectively. The regime preceding x_H in (a) and x_{SN} in (b) features only one stable non-oscillating solution (stable focus) and is referred to as the subthreshold regime (reproduced from Gupta et al. [2]).

peaks in the frequency spectra of acoustic pressure/velocity or heat release rate fluctuations from the flame) will be absent. Fluctuations may still be present due to inherent noise and these might contain small amplitude intermittent coherent oscillations (see inset plot corresponding to stable focus in Fig. 1.3(A)). As a critical/control parameter ($\sim$ operating condition) is varied, large amplitude coherent oscillations will appear in one of the two possible ways: oscillations with gradually increasing amplitude as the control parameter is varied, or oscillations with a sudden jump in the amplitude. These two pathways are associated with the two forms of the Hopf bifurcation. Figure 1.3 presents schematics of the two forms: the supercritical (top) and the subcritical (bottom) Hopf bifurcation. The X-axis is the parameter and the Y-axis the amplitude of oscillations. Solid lines are 'stable' asymptotic states: once the system assumes such a state it will continue to stay at that state in the absence of any large disturbance and further parameter variations. These are also known as 'attractors' because of the property that if the system is disturbed from this state via small perturbations, it will be attracted back to this state. The dashed lines are also states that the system can settle on for a short time, but will eventually be repelled from this state to the closest attractor available. These are therefore 'unstable' states or 'repellers'.

Depending on the nature of the nonlinearity within a system, transition to the oscillatory state may happen via a supercritical or subcritical bifurcation [2, 28]. For a supercritical Hopf bifurcation, the transition to the oscillatory state occurs such that beyond the critical point (also the Hopf point), x_H, the amplitude changes gradually. The role of noise for this case can be expected to be limited to excursions of the system away from the stable states induced by noise, followed by return towards the closest'attractors'.

The subcritical Hopf bifurcation (Fig. 1.3(B)) is more interesting—and also more dangerous than supercritical bifurcation to practical systems. In the most fundamental case of a subcritical Hopf bifurcation, a stable (oscillator) state exists together with the stable steady state (referred to as focus) prior to the Hopf point; and the two are separated by a repeller—an unstable limit cycle. The point at which these two meet is referred to as a 'saddle-node'. The region of coexisting attractors is called 'bistable' region because of the existence of two attractors. The system will evolve on one or the other depending on the initial condition: a large enough perturbation can cause the system to switch from one to the other attractor. Such a condition is dangerous for a practical system because although the system is far away from the Hopf point—which is what may typically be obtained from linear stability analysis of the system—perturbations, including noise may 'trigger' instability (the oscillatory stable attractor).

1.2 Noise-induced dynamics

Such combustion systems are inherently noisy. The noise originates from factors such as aerodynamics [29, 30], unsteadiness in combustion process [31], fluctuations in air/fuel supply ahead of flame caused by mixture coupling [32, 33], fluctuations in the flow (or vorticity) caused by velocity coupling [13, 33–35], turbulence and flow separation [29, 36] within the combustion chambers. Therefore, pressure inside the combustor always consists of fluctuations induced

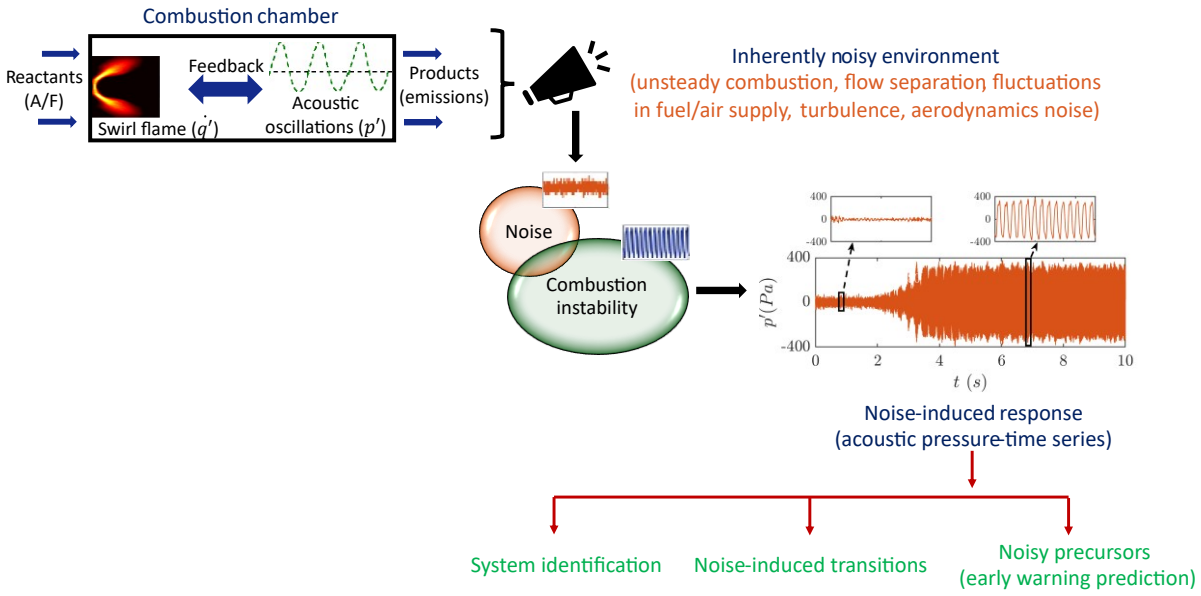

Figure 1.4: An illustration of noise-induced features in gas turbine combustors

by noise irrespective of the occurrence of thermoacoustic oscillations. These fluctuations in acoustic pressure, shown in Fig. 1.4, known as noise-induced response of a system, has been used extensively in literature to investigate the interaction between noise and thermoacoustic coupling.

Noise in combustion systems (Fig. 1.1) has on the one hand delayed the identification of bifurcations and dynamical attractors (cf. [37, 38]) and on the other hand enabled the identification of measures of system stability. The latter has been possible because noise leads to frequent excursions of the system away from its asymptotic dynamics; and characteristics of its evolution back to the asymptotic behaviour (steady state or oscillatory states) is indicative of the system stability. Both the aspects are discussed in further detail later. Transition due to noise is not only limited to the transition from steady to oscillatory states; it is possible for a system to have multiple coexisting oscillatory states; for instance in an annular combustor both standing and rotating acoustic modes are possible during thermoacoustic instability and it has been reported that the transitions between the two, commonly observed in experiments, are likely due to noise in the system [39].

Noise in general has also been identified to result in other more subtle effects in nonlinear systems such as stochastic resonance (SR), where a feeble external periodic forcing to the system is enhanced in the presence of noise [40–43]; coherence resonance, which similar to SR except that it does not require an external signal and internal frequencies are enhanced leading to intermittent burst of periodic behaviour [44–48]. The term 'resonance' in both cases refers to the observation that the amplification of the external periodic signal (SR) and the coherence in noise-induced oscillations (CR) first increases with increasing noise intensity, attains a peak, and subsequently decreases monotonically—similar to a resonance curve. The particularly interesting feature of such noise-induced behaviour is the regime (control parameter range) within which it occurs: for subcritical Hopf bifurcation it occurs before the bistable region (before the saddle

node point), and for supercritical bifurcation it occurs before the Hopf point. Thus, in the presence of inherent noise, such behaviour can be used as precursors, or for advance detection of the proximity of the system to the (practically dangerous) bistable (subcritical Hopf) and linearly unstable (supercritical Hopf) regimes. Only recently has coherence resonance and associated P-bifurcations been demonstrated in experiments [6, 49] and prototypical models of thermoacoustic systems [2].

Another important aspect concerning noise-induced dynamics is that the effects are also dependent on the nature of noise: the composition in terms of the distribution of power over frequency and whether noise appears in the parameters governing the system (parametric noise), whether noise is dependent on the state of the system (multiplicative noise), or if it is unrelated to either the state or parameters (additive noise). These are however mathematical constructs and one may find one or the other form reported in literature. The important point to note is that the different classes of noise have different effects on the system.

Briefly summarizing, noise has been identified as a major contributing factor to the complexity of thermoacoustic instabilities since the 1970s. Combustors are typically noisy environments (Fig. 1.4). Considerable noise sources in practical combustion systems include flow separation, turbulence, and combustion processes. It is expected that the presence of noise will affect in some way the amplitudes and possibly the qualitative behaviour of organized oscillations [50]. The noise-induced dynamics in a system can be used to acquire deterministic system parameters (section 1.2.1), can trigger thermoacoustic instability in the bistable regime and modify the stability margins of the system (section 1.2.2), and can act as a noisy precursor to instability (section 1.2.3). We will now discuss the critical effects identified in recent studies.

1.2.1 System identification

It is reported that in the 1960's or even the 50's, several Russian groups were employing system identification using the statistical features of pressure fluctuations [36]. It was however the reports published in the 80s and 90s—primarily by Culick, Zinn, and their respective groups at Caltech and Georgia tech—that made the major contributions to the theoretical investigation of nonlinear and stochastic dynamics of thermoacoustic instability. The formulations and results developed back then for liquid and solid rocket motors still have relevance for gas turbine combustors and are being employed, extended, and improved for modelling and control strategies.

This early work in particular is based on the approximate analysis for nonlinear instability in combustors developed in [51, 52]. Identifying the cause of triggering in combustors, which was observed frequently in experiments, was the major driving force behind developing a nonlinear framework involving either nonlinear gas dynamics, or nonlinear combustion, or both simultaneously; and it was realized that nonlinear combustion was important to obtain subcritical Hopf bifurcation and the associated triggering phenomenon [53].

Researchers were particularly interested in two questions: firstly, for noise with certain statistical features introduced into the system as multiplicative or additive noise, what are the statistical features of pressure fluctuations; and secondly, given experimental measurements of pressure

fluctuations from a combustor, can the stability margins/measures of the system be inferred. Among the first detailed studies on the effects of noise is the work by [30] where the authors, building on the approximate analysis [51, 52], include parametric (noisy) excitation of the acoustic modes and an additive noise source in the acoustic forcing term of the form:

$$\frac{\mathrm{d}^2\eta_n}{\mathrm{d}t^2} + \omega_n^2\eta_n = F_n^a + \sum_{i=1}^{\infty}\left[\xi_i\eta_i + \xi_i^v\dot{\eta}_i\right] + \Xi_n \tag{1.2}$$

ξ_i, ξ_i^v are parametric noise amplitudes, while Ξ_n is the additive noise amplitude. Acoustic pressure and velocity are expanded as a linear summation of (classical) acoustic modes and η_n is the time-varying amplitude of the n^{th} mode. Accordingly, the governing equations for fluctuations in the combustor appear as set of stochastic differential equations of the form of oscillators with the forcing terms containing contribution from noise. Subsequently, with the use of a two-mode approximation followed by stochastic averaging provides a simplified set of equations for the fluctuations in the modal amplitudes in the presence of noise.

The corresponding Fokker-Planck equations [54] for pressure fluctuations will provide the probability density. To obtain the Fokker-Planck equation, the state variable, η_n and $\dot{\eta}_n$ can be transformed into amplitude and phase equations using the following relation,

$$\begin{aligned}\eta_n &= a_n\cos\left(\omega_n t + \varphi_n\right)\\ \dot{\eta}_n &= -a_n\omega_n\sin\left(\omega_n t + \varphi_n\right)\end{aligned} \tag{1.3}$$

where a_n and φ_n are the instantaneous amplitude and phase of η_n. This substitution is reasonable as, in practical cases, the thermoacoustic systems are categorized as "weakly" amplified/damped systems [55]. Then stochastic differential equations (SDEs) for amplitude and phase coordinates can be obtained by performing stochastic averaging [56]. The corresponding Fokker-Planck equation associated with SDEs is given as,

$$\frac{\partial}{\partial t}P\left(a_n, t\right) = -\frac{\partial}{\partial a_n}\left[m\left(a_n\right)P\left(a_n, t\right)\right] + \frac{\partial^2}{\partial a_n^2}\left[\frac{\sigma\left(a_n\right)}{2}P\left(a_n, t\right)\right] \tag{1.4}$$

where, $m\left(a_n\right)$ and $\sigma\left(a_n\right)$ are drift and diffusion coefficients. Considering that when $a_n \to \infty$, the probability density vanishes, one can obtain the stationary probability density of the acoustic envelope by integrating the above equation. The authors reported a uni-modal, log-normal distribution for pressure fluctuations as the result of this formulation and the description was shown to match well with numerical simulations (Monte-Carlo) of the stochastic equations obtained earlier.

The log-normal distribution of pressure fluctuations were also reported by [57] for the special case when the combustor is close to the stability boundaries. The analysis was based on the Stuart-Landau equation with the effect of noise (specifically due to turbulence) appearing as a fluctuation of the growth rate (multiplicative noise). Furthermore, this was probably the first work to approach transitions between the stable steady and oscillatory states within the bistable region of the subcritical bifurcation due to noise. Further discussion on these transitions is postponed for the section on noise-induced transitions. The authors also pointed out that to

capture noise-induced behaviour correctly, it was important to include nonlinear terms. While qualitatively the results appear to correspond to experimental observations, no further validation of the multiplicative nature of noise or a characterization of changes in the transfer function or the growth rate of the system has been attempted. Concerning multiplicative noise, additional work was more recently undertaken in Ref. [58] where the authors show that in the presence of fluctuations in the system damping and frequency, the stability regime shrinks (in comparison to the boundaries identified from deterministic equations).

The definitive response to the long-standing question of whether the statistical features of pressure fluctuations can give an idea about the stability margins of the system was finally given by Seywert and Culick [36]. Like the previous investigations [30, 50], the authors simplify the governing equations to the form of an oscillator with multiplicative noise affecting the frequency and growth rates of the system; with the system itself represented by four modes. Following 'Burg's method' to curve-fit the power spectrum of the pressure fluctuations from simulations of the stochastic differential equations, they identify the frequencies and growth rates of the system and compare these to known values for the case of a linearly stable system. A very good agreement is found and the method is reported to be robust against the amplitude of noise for the case of additive noise and breaks down for large noise amplitudes for the case of multiplicative noise. More insights on the latter have been obtained in very recent experiments [6, 49].

The authors [36] also applied the method to linearly unstable system but the results are not as promising. The method works only if a single mode is active during instability as it is unable to distinguish between linear and nonlinear effects in the presence of multiple modes. The formulation may also not be accurate as the authors consider nonlinear gas dynamics but a linear flame response.

The idea that noise-induced dynamics could be used for system identification was recently revisited by [59]. Unlike previous studies discussed in the last paragraphs where the authors attempted to arrive at a set of governing stochastic differential equations, [59] and follow up works [60, 61] start with the assumption that only a single acoustic mode is active and the dynamics may be well represented by Van der Pol equations and their stochastic extensions. Noise is considered additive in nature. In [59] the authors propose four different approaches for the determination of the linear growth rate and non-linearity coefficient—the nonlinearity being an assumed form involving a single, constant coefficient. The first of these neglects the nonlinear term and the determination of the growth rate is based on fitting the power spectrum of pressure fluctuations with a function derived for the stochastic Van der Pol equation (with additive noise). The second approach considers a weakly perturbed limit cycle oscillation of the oscillator. It involves linearization about the limit cycle oscillation for which the amplitude depends on nonlinearity coefficient and fitting of the power spectrum with the correspondingly modified functional form. The next approach is based on the Fokker-Plank equation corresponding to the amplitude and phase equations of the stochastic Van der Pol equation. An expression is obtained for the amplitude distribution (Eq. 22 in [59]) and based on fitting experimentally obtained data (Hilbert transform of the pressure oscillations given that Hilbert transform is

applicable[1]) with the function. This approach relaxes the assumption of a weakly perturbed limit cycle. Finally the authors propose another approach based on the Fokker-Plank equations governing the evolution of the transient probability density. The coefficients associated with the convection and diffusion of the probability density with time can be obtained from experimental data and deterministic quantities estimated subsequently. This approach is most general and relaxes the presumption of a stochastic Van der Pol; the result may be cross-checked to identify whether the stochastic Van der Pol is a valid form for the governing equation. In the application of the method on data obtained from the combustor the authors show that for the particular case, the Van der Pol-based description largely holds. Except the first approach, the proposed strategy is applicable for the linearly unstable regime as well.

Further development of the Fokker-Plank based method was presented recently in Boujo and Noiray [62] where the authors provide a more robust estimation methodology based on adjoint Fokker-Plank equations which does not suffer from problems associated with the fact that previous methods relied on band-pass filtered data.

Among the studies mentioned only [36] has investigated the role of noise amplitude; and although the amplitude appears as a parameter in methods studied in [39] and subsequent works, it is implicitly assumed that for all cases the amplitude does not lead to variations in the general form of the power spectrum or the amplitude distribution function. As discussed below, recent experiments and associated analyses however indicate otherwise.

Kabiraj et al. [6] experimentally investigated the response of a model thermoacoustic system to varying amplitudes of acoustic white noise signals for a range of operating conditions prior to the bistable region. As mentioned earlier, in this region the system is linearly stable and the steady non-oscillatory state is the sole attractor of system dynamics.

It was shown by the authors that the response to noise consists of intermittent episodes of oscillatory behaviour at the frequency which would appear if the parameter were to be changed to a value beyond the Hopf point. The episodes occurred more frequently and for a longer mean duration as the system was brought closer to the edge of the bistable region. The most important aspect concerning noise-induced dynamics was the observation that this 'coherent' behaviour was also dependent on the noise intensity; and that this dependence was not monotonous. With increasing noise amplitude the coherent response would increase and then—beyond an optimum induced coherence—decrease. The optimum also depends on the proximity of the system to the bistable region in a way that if the system is close to the bistable region, the optimum is obtained at a lower noise intensity. Such behaviour has known in the nonlinear dynamics community (cf. [47, 48]) and is referred to as 'coherence resonance' due to the resonance-like dependence of the induced coherence on the noise intensity. Such response was identified in pressure as well as heat release rate fluctuations. In the presence of non-linearity, both the peak height and the width are affected by noise [56]. The combined effect of noise on the spectral peak is such that the coherence factors, β, obtained from the power spectra passes through a maximum for intermediate noise levels [45].

The investigation was further expanded in [49] to show the presence of 'P-bifurcations':

[1] With the assumption of a single dominant frequency in the system, this is true.

qualitative changes in the statistical characteristics of pressure fluctuations as the noise intensity is increased. The amplitude distribution functions changes from a uni-modal, log-normal distribution to a bi-modal distribution. From the characteristics of the distribution it could be inferred that the oscillatory attractor that exists in the bistable region and beyond influences the noise-induced behaviour of the system already in the 'subthreshold' region. That such 'P-bifurcations' appear with the phenomenon of 'coherence-resonance' has also been observed in nonlinear systems [48].

In addition to giving insights on the stochastic features of thermoacoustic instability the observations are also practically relevant: such noise-induced behaviour and corresponding trends can be used as precursors for *advance detection of instability*. We will discuss this later in section 1.2.3.

Lately, a similar work analogous to Kabiraj et al. [6] was presented by [63]. They also investigated coherence resonance and stochastic bifurcation behaviours in two modelled standing wave thermoacoustic systems (open-open and closed-open boundary conditions). They reported from the smooth transitions of the stationary probability density function (PDF) that the thermoacoustic system is destabilized via stochastic P bifurcation, as the external noise intensity was continuously increased. This was in good agreement to [6]. In addition, they also reported that the increased noise intensity could shift the hysteresis region, making the system more prone to quasi-periodic oscillations, but also reducing the hysteresis area possibly suggesting the presence of a multiplicative noise component [58].

The phenomenon of coherence resonance was later analysed through numerical simulations in [2]. The authors conducted numerical analysis of noise-induced (additive noise) dynamics in subthreshold regime for models of thermoacoustic instability—Rijke tube as well as the Van der Pol oscillator. The results reported correspond qualitatively to the observations of the experiments [6]. The findings confirmed that the observed phenomenon of coherence resonance in combustion systems is intrinsic to thermoacoustic coupling. Furthermore, investigations on the Van der Pol model, which underwent bifurcation to instability via supercritical bifurcation indicated that coherence resonance is not limited to subcritical bifurcations. The trends in noise-induced coherence as the system approaches Hopf bifurcation for subcritical and supercritical Hopf bifurcations were found to be qualitatively different and indicative of the type of bifurcation. This particular result even has the potential to be used as a basis of system identification prior to the instability. The restriction of additive white Gaussian noise employed by the authors may not be accurate but the qualitative results impress the importance of considering nonlinearity and noise amplitude effects in the modelling (and use in system identification approaches) of thermoacoustic systems.

In order to summarize, the aforementioned discussions made by various researchers provided a strong theoretical modelling of the stochastic forcing in thermoacoustic systems and how the extended study of the model could be used to extract or determine the linear growth rate and non-linearity in the system. It can also be concluded that the knowledge of noise-induced linear growth/decay rates and non-linearity coefficient could help in designing of proper damping device for dissipation of acoustic energy for a thermoacoustic system. But recent results also advocate

the need for further developments in theoretical modelling and system identification approaches.

1.2.2 Noise-induced transitions

Among various practically-relevant aspects of thermoacoustic systems is the possibility of switching between or undergoing transition to different dynamical states. There are two such possibilities:

- Transitions involving thermoacoustically-stable (non-oscillatory) and oscillatory states.
- Transitions involving two oscillatory states.

In both the cases, the switch/transition may be 'triggered' by finite-amplitude disturbances, including inherent noise within the system.
Transition from the stable, non-oscillatory state to an oscillatory state (not limited to limit cycle oscillations [64]) is possible only for the case of a subcritical Hopf bifurcation (see Fig. 1.3). Within the bistable zone, the simultaneous existence of two attractors leads to the possibility of forcing the system to be attracted to one of them by providing an appropriate disturbance: if a disturbance causes the system to fall within the 'basin of attraction' [65] of the oscillatory state or the thermoacoustically-stable state, the system would be attracted to the corresponding state. An illustration for such transition is shown in Fig. 1.5. Such behaviour in thermoacoustic systems was first investigated in the context of rocket engines

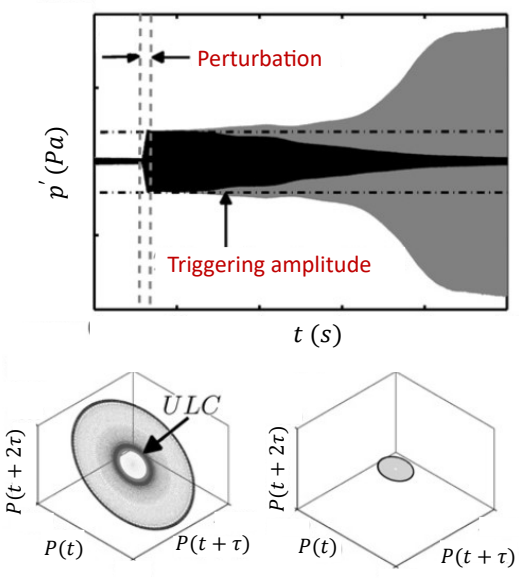

Figure 1.5: Noise-induced transition to instability when the system is in the bistable region (reproduced from Jegadeesan et al. [3]): The pressure-time trace shown in gray corresponds to the system evolving towards limit cycle oscillations, while the pressure-time trace shown in black corresponds to the system evolving towards a stable focus. For the system to reach the limit cycle, a threshold triggering amplitude is required, as indicated by the dashed lines. Bottom - Phase portrait of the system asymptotically reaching a stable state. The term ULC denotes an unstable limit cycle.

where the triggering of thermoacoustic instability via a large amplitude pulse was referred to as hard excitation or triggering instability [66]. Beyond a certain 'threshold' amplitude for the disturbance, which was typically obtained through a small explosions within the combustor, instability could be triggered. Experimentally it is possible to obtain the threshold corresponding to the unstable limit cycle [67], but only for laboratory systems.

In the context of this study, it is important to discuss the fact that triggering is also possible through noise [27]. Thermoacoustic systems can be triggered by low amplitude perturbations of the order of background noise level. Noise in the system may be associated to several sources—noise in operating conditions, noise in the base flow, fluctuations leading to combustion noise, or external sources [68, 69]. It is difficult to accurately model noise solely as additive, multiplicative, or parametric noise; but this difficulty is a limitation of modelling methods. Regardless of the source or classification, it has been known for a long time that noise can induce triggering (cf. [70]) and the theory of dynamical systems, in particular the subcritical Hopf bifurcation, provides us with the required framework to interpret and understand such triggering. Because noise is involved, the analysis, description, and modelling of a thermoacoustic system in the presence of noise must necessarily be probabilistic in nature.

Culick et al. [30] and Clavin et al. [57] were among the first to capture the effects of noise in inducing repeated transitions between the stable oscillatory and stable steady states within the bistable regions. [57], in particular obtained the transformation of the amplitude distribution function from unimodal to bimodal nature—indicating the presence of transitions between the steady and oscillatory states—through the Fokker-Planck formulation of the noisy (multiplicative noise) Stuart-Landau equations that the authors argued is a simplified representation of the thermoacoustic system in the presence of turbulent fluctuations.

Of recent, there have been several reports on noisy thermoacoustic systems, specifically transitions within the bistable region, based on experiments involving prototypical setups; and numerical/analytical analysis on either the Rijke tube formulation [71] with subcritical bifurcation or the Van der Pol oscillator, where transition to instability takes place via a supercritical bifurcation. The latter, due to the lack of a bistable region in the bifurcation, can not be employed to understand transition within the bistable regime; and studies have focussed mostly on the stochastic nature of pressure fluctuations within the system—without transitions between stable attractors.

Waugh and Juniper [72] explored the mechanism of triggering a thermoacoustic system (Rijke tube) with additive noise of different spectral composition—white, blue, and pink—and different amplitudes, within the bistable region. Pink noise was identified to be the most effective in triggering instabilities. Triggering required a certain threshold amplitude of noise depending on the type of noise. If the strength of noise was increased to the point where the intensity was just enough to trigger thermoacoustic oscillations, the system would spend some time at the unstable periodic solution and eventually be attracted to the stable oscillatory solution (limit cycle) and continue oscillating. At higher noise intensities, the system would directly be attracted to the stable limit cycle. Such observation and the presence of the unstable limit cycle was also obtained in experiments involving a periodic signal input for a prototypical system within the bistable

region [67].

In a follow-up numerical study with additive noise [73], again within the bistable region, the authors investigated the effect of noise intensity and the proximity of the system to the Hopf point on the transition dynamics. If the system is close to the Hopf point, the basin boundary for the stable oscillatory solution is closer to the steady state; and it is expected that a low amplitude disturbance will be sufficient to cause transition. This is exactly what the authors found in their study. Correspondingly, as the system is taken further away from the Hopf point, transition would require a larger noise amplitude. Alternatively, for a constant noise amplitude, transition would occur in advance (of the Hopf point); with the distance to the Hopf point for such noise-induced transition increasing for increasing noise intensities (i.e. transition would occur much in advance for a higher noise intensity). The authors investigated noise included as an additional term to the system of equations as well as being included as a perturbation of the acoustic velocity at the heater (driving the electrically-heated Rijke tube) and reported that the results are qualitatively identical. These results explain several experimental observations such as reported by [70], and recently repeated by [74] where the transition of combustors to instability is advanced in the presence of increased noise (flow turbulence in the cited references) intensity.

In experiments, a similar study was reported by [3], where the authors investigated the influence of perturbations in fuel flow in a diffusion flame driven combustor. The configuration is closer to being classified as a parametric noise case than an additive or multiplicative noise scenario. Within the bistable region triggering would occur and the system evolution would pass through the unstable periodic state before ending up at the stable oscillatory state as previously discussed by [73] and [67]. When the system was perturbed by noise (Gaussian white noise), it underwent noise induced transition (NIT) which was observed when the noise intensity was just 1/8th of the triggering amplitude of the system. The evolution along the unstable periodic orbit was found to be intermittent, with pronounced bursts of oscillatory behaviour. The authors reported that with increased fluctuation intensity, the amplitude of triggered oscillations was lower than the amplitude of the limit cycle oscillations for the configuration without noise. The authors provide an explanation for the lowered amplitude based on a previous report of the drifting of the phase between heat release rate and pressure fluctuations (thus, a constantly changed value of the Rayleigh integral) in the presence of additive noise [75]; although if that was the case, the numerical investigations should have identified the effect as well. The mean amplitude in the simulations with additive noise [72, 73] was the same as the limit cycle amplitude obtained without noise.

In experiments on the horizontal configuration of an electrically-heated Rijke tube, [76] identified that the reduction in the hysteresis zone as a result of noise-induced transitions discussed above follows a linear trend with respect to the normalized noise intensity. Such reduction in the bistable/hysteresis zone for systems undergoing subcritical Hopf bifurcation, in the presence of noise has been observed in various other dynamical systems as well [77]. For a sufficiently high noise intensity, the system was shown to undergo repeated transitions between the stable steady and oscillatory states; because of which the bifurcation diagram for the case of subcritical

bifurcation with noise-induced transitions, obtained from noisy data with a representative amplitude (in the cited work, the median of local maxima in acoustic pressure) would resemble a supercritical bifurcation.

The authors recognize that the observed qualitative change in the bifurcation is due to repeated transitions or 'flickering' as such behaviour and later in [78] identify the observation as a stochastic P-bifurcation [48]. The authors compare the experimental observations in terms of the transformation of the unimodal amplitude distribution function to a bimodal structure (P-bifurcations) with increased noise to the analysis (Fokker-Planck formulation) of an idealized single mode oscillator forced to undergo a subcritical Hopf bifurcation via an artificial nonlinearity, and valid as a representation of the Rijke tube for small under several assumptions including small heat release rate fluctuations and a small (in comparison to the oscillation time period) time-delay in the heat release rate response. On account of the assumptions, the oscillator does not feature a saddle-node bifurcation and is valid in a small vicinity of the steady state solution. For the model, the corresponding Fokker-Planck formulation gives bifurcations in the stationary probability distribution functions with variation in the bifurcation parameter and the noise intensity.

Concerning the second possibility for transitions within a thermoacoustic system, noise has also been reported to cause transition between coexisting modes of the system. Noiray et al. [79] studied the transition between azimuthal standing and rotating modes in an annular combustor. The modal dynamics were characterized and transitions between the two modes were noted. To seek an explanation, the authors investigated the phase dynamics of a coupled stochastic oscillator system with the flame nonlinearity modelled as a cubic nonlinearity. The switch between rotating and standing modes was a long-standing aspect frequency observed in industrial combustors and the influence of noise was found to provide the most consistent explanation for such behaviour in modern annular systems.

1.2.3 Noisy precursors (or early warning prediction)

More recently, noise-induced dynamics have been used to identify parameters known as early warning indicators (EWIs) or noisy precursors that change prior to the onset of instability when the system is stable. These indicators exhibit a consistent trend, either increasing or decreasing, as the system approaches instability. Monitoring these changes helps detect a system's proximity to thermoacoustic oscillations. EWIs can be broadly classified into two categories [80, 81]: (i) model-based indicators and (ii) metric-based indicators. These indicators are based on the fact that the pressure signal inside a combustor undergoes a quantitative change before instability. Examples of model-based indicators include the threshold of time-variant auto-regressive models [82], non-parametric drift-diffusion-jump models [83], and potential well estimators [84].

The metric based indicators include an increase in variance of time series as the system approaches the instability [85–90]. The increase in variance is attributed to two factors: under small perturbation, the system can exhibit sliding around the stable state; and under large perturbation the system can flicker (can be excited to another stable attractor). An increase in skewness [80, 89, 91, 92]–a measure of the symmetry of probability distribution about its mean–

and kurtosis [80,89,91]–a measure of the distribution tails– are the critical indicators associated with the statistics. Conditional heteroskedasticity which is a measure of variations in the time series pattern is another critical indicator [87, 93]. Conditional heteroskedasticity is indicated by the persistence in the conditional variance of the statistical residuals.

The indicators based on the spectral content of time series are coherence factor (height-width ratio of the spectral peak in a noisy signal) and the autocorrelation function [2, 6, 44, 45, 94, 95]. An increase in the coherence factor as the system approaches the bifurcation (Hopf) point acts as the precursor to instability. Autocorrelation function (ACF) is an another time series based early warning indicator, related to the phenomenon of CR [44]. The time series obtained from a combustor in general has an ACF with decaying amplitudes [6,95] which implies the presence of coherence in the data. Both the coherence factor and the ACF are proportional to the quality factor ($f_p/\Delta f$; where f denotes frequency and f_p is the peak frequency) and increases as the system approach the instability.

Multi-fractality, which indicates the degree of self-similarity in a time series by measuring its short and long time memory is another critical early warning indicator [89, 96–99]. As the system approaches the bifurcation point, loss in multi-fractality is observed. This loss in multi-fractality indicates impending instability and is quantified by the gradual decrease of the Hurst exponent and singularity spectrum width, which serve as EWIs [96]. Increased duration of intermittent bursts of periodic oscillations as the system approaches the Hopf bifurcation has also been proposed to predict the instability [98–102]. The associated EWIs are a decrease in the recurrence rate, time that a system spends in the intermittent state and Shannon entropy of the time series. Recently, Baba et al. [90] and Fu et al. [99] reported that the construction of a 2d space using joint symbolic and ordinal transition pattern-based recurrence plots can also effectively capture the transition to thermoacoustic instability.

A decrease in permutation entropy [108–110,114] and an increase in Jensen-Shannon complexity [108] of the system well prior to the instability are also proposed to be effective EWIs in

Table 1.1: Types of metric based early warning indicators employed commonly to predict the onset of thermoacoustic instability.

Early warning indicator	Phenomenon		Reference
	Increase	Decrease	
ACF decay rates	✓		[101, 103]
Coherence factor	✓		[2, 6, 94, 104, 105]
Conditional heteroskedasticity	✓		[87]
Intermittency	✓		[90, 98–102]
Jensen-Shannon complexity	✓		[106–108]
Kurtosis	✓		[89]
Lag-1 autocorrelation	✓		[87–89]
Multi-fractality		✓	[89, 96, 98, 99]
Permutation entropy		✓	[108–110]
Skewness	✓		[89]
System identification	✓		[111–113]
Variance	✓		[87–89]

literature. A more accurate EWI based on the combination of permutation entropy and Jensen-Shannon complexity known as complexity entropy causality plane (CECP) is further proposed [106, 110, 115]. In the CECP plane, three zones corresponding to combustion noise, transition, and thermoacoustic instability are defined which are used to predict the instability [106, 107]. Lee et al. [108] further extended this approach to a three-dimensional CECS space (complexity-entropy causality space), which considers the entropy and complexity of both the pressure and heat release rate. The author [108] proposed CECS to be more accurate EWI than CECP. Lee et al. [111,113] in their studies on the noise-induced dynamics in the unconditionally stable region of a low-density jet [111] and swirl-stabilized lean premixed combustor [113] reported that the measures of system identification (decay rates of acoustic oscillations and non-linearity coefficients) can also be used to predict the instability. A summary of the various metric based EWIs employed commonly in thermoacoustic systems along with their monotonic trend is tabulated in Table 1.1.

1.3 Motivation (or research gap)

Most studies on noise-induced dynamics, including the early works by Culick et al. [30], Burnley [50] and Clavin et al. [57] as well as recent reports [36, 59, 116–118] have modelled noise in the system by additive Gaussian white noise. Such an assumption has helped in understanding various aspects of noise-induced dynamics to a great extent. However, various numerical [5, 36] and experimental studies [4, 5] have shown that the background noise actually features a non-constant power spectrum (Fig. 1.6): the power spectrum of combustion noise increases at low frequencies up to a cutoff frequency following $P \propto f^2$, attains a maximum and then decays following $P \propto f^{-r}$ (left plot in Fig. 1.6) whereas the power spectrum for flow noise remains constant (or flat) up to a cutoff frequency and then decays following the power law ($P \propto f^{-r}$) – right plot in Fig. 1.6. Here, r represents the decay rate of power spectrum and is proportional to the noise color (or correlation time), P is the power spectral density and f is the frequency. A

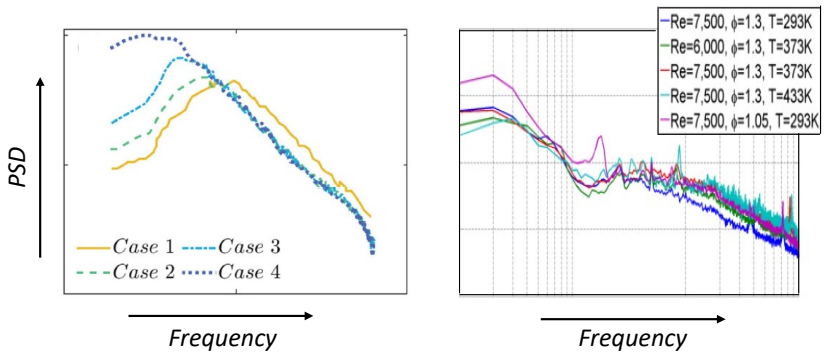

Figure 1.6: Left: Typical power spectra of combustion noise of turbulent premixed flames adapted from Rajaram and Lieuwen [4]: case 1 and 2 → fuel-acetylene at $\phi = 0.71$ and 0.64 respectively, case 3 → fuel-propane at $\phi = 1.03$ and case 4 → fuel-natural gas at $\phi = 0.95$. Right: Power spectrum of several cases of reacting flows adapted from Nawroth et al. [5].

change in the combustor operating conditions (via parameters such as temperature (T), Reynolds number, (Re), or equivalence ratio (ϕ)) causes a change in the amplitude, peak frequency, and decay rate r, which causes significant changes in system dynamics. Hence, background noise in a combustion system is not purely white Gaussian in nature.

The correlation time (also called as noise color) of background noise has been reported to affect the phenomenon of coherence resonance: induces peak coherence at higher noise intensity [105, 119–121] and reduces the quality of induced coherence [122]. Bonciolini et al. [61] have shown the importance of noise correlation time in system identification and have conclusively reported that the noise correlation time and its intensity significantly affects the estimation of growth rates of thermoacoustic oscillations in model gas turbine combustors. Noise correlation time also affects the rate-dependent tipping-delay phenomena and it is reported that any variations in noise color are beneficial to dodging bifurcation [123–125]. Colored noise has also been reported to be more effective in causing noise-induced triggering than white noise [116].

The background noise features contributions not only from additive sources arising from aerodynamics and combustion but also from multiplicative sources arising from coupling mechanisms such as velocity, pressure and mixture coupling [1, 33, 36]. Lieuwen and Banaszuk [58] have reported that the multiplicative noise alters the stability margins of the combustor and purely additive noise is not sufficient enough to predict the pressure amplitude. Following this, recently, Li et al. [126, 127] investigated the effect of noise correlation time of both multiplicative and additive noise on the stability margins of a thermoacoustic system (open-end Rijke tube) exhibiting subcritical Hopf bifurcation. The authors reported decreasing the noise correlation time of multiplicative noise can lead to a decrease in both bistable and linearly stable regions. Hence noise correlation time of multiplicative noise has been reported to changes the qualitative dynamics of a system.

In practical systems, inherent noise typically exhibits finite correlation time and intensity, which vary with operating conditions (equivalence ratio, flame configuration, fuel split, Reynolds number, etc.) [5]. Both these effects must be considered when estimating system stability to detect the system's proximity to thermoacoustically-unstable conditions. Information on how noise correlation time of background noise (including both additive and multiplicative sources) affects the reliability of early warning indicators for accurately predicting thermoacoustic instability in practical systems is limited. In the thermoacoustic community, only Zhang et al. [125] have investigated the effect of noise color on variance, autocorrelation, skewness, kurtosis, and entropy, finding that among these EWIs, autocorrelation, skewness, and entropy can serve as reliable indicators. The lack of investigations on the effect of background noise characteristics, including both additive and multiplicative sources, on the efficacy of various EWIs motivates the first part of the present work.

Another aspect of flame-acoustic interaction crucial to the thermoacoustic instability is the helical instability (PVC) associated with the swirling flows. Numerous experimental and numerical investigations in the literature have focused on understanding the excitation and suppression mechanisms of the Precessing Vortex Core (PVC) phenomenon [17, 128–131]. Paschereit et al. [20] demonstrated the excitation of axisymmetrical and helical modes in a

model premixed burner by modifying the boundary conditions of the combustion chamber. Iudiciani and Duwig [132] reported that acoustic excitation at frequencies lower than the PVC mode effectively suppresses PVC, while excitation at twice the PVC frequency amplifies the helical instability. The damping efficiency of low-frequency forcing has been corroborated by Khalil et al. [133], and Lacarelle et al. [129]. In a recent reactive experimental study, Moeck et al. [134] successfully suppressed the natural helical instability through acoustic forcing at a lower frequency than the natural frequency. Besides suppression, attention has also been directed towards understanding the interaction between the PVC and the structures induced by external forcing. It has been reported that flame and flow field oscillates at linear combinations of PVC and external forcing frequency [134]. A dramatic increase in turbulent kinetic energy, as a result of changes in the structure of a turbulent jet with a high swirl number forced at the PVC frequency, was reported by Alekseenko et al. [135]. Wang et al. [136] instead used a numerical approach to study a swirl injector. They found that the excitation did not relevantly affect the central recirculation zone while it excited the outer shear layer in a case where the excitation frequency matched the intrinsic frequency of vortex shedding.
So far in literature, the mechanisms for suppressing/exciting PVC are discussed based on single frequency acoustic excitation. Information on how the coherent structures associated with global instability interact with inherent noise inside the combustor is not explored. Part 2 of the thesis focuses on this aspect. The hypothesis is that introducing a broad range of frequencies may suppress or excite the coherent structures associated with instability. This information is significant for developing mitigation and control strategies for thermoacoustic instability in practical combustion systems.

1.4 Objectives of the present work

The main objective of this thesis is to advance the understanding of the interaction between thermoacoustic coupling and noise in gas turbine combustors, with a focus on practical applications. We specifically focus on two aspects: (i) how reliably can noise-induced dynamics be used for early warning prediction of impending thermoacoustic oscillations whilst the system is stable (or is in subthreshold region – Fig. 1.3) and (ii) how noise interact with the coherent structures associated with swirling flow that leads to the onset of thermoacoustic instability in gas turbine combustors. This information on how noise interact with the instability can help develop strategic mitigating and control measures. We achieve these objectives through analytical, numerical and experimental modelling of inherent (background) noise and thermoacoustic coupling.

1.5 Structure of the thesis

The thesis is structured into two main parts, which aggregate the single studies that are contained in each chapter.
The first part of the thesis is dedicated to model and time series based parameter identification

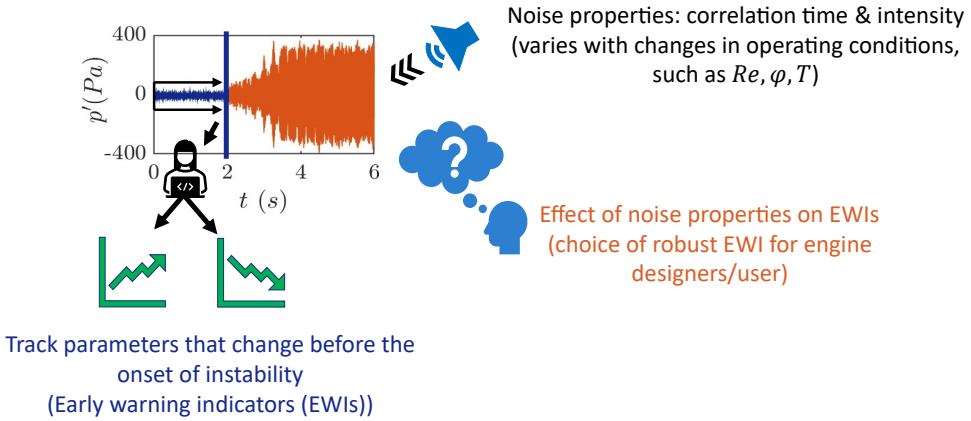

Figure 1.7: An illustration of the objectives for PART I of the thesis.

(growth rates of thermoacoustic oscillations and early warning indicators) for control and early prediction of thermoacoustic instability, schematically shown in Fig. 1.7. This investigation is conducted in following systems:

- A well controlled experiment allowing to mimic thermoacoustic coupling in gas turbine combustion chambers is setup. More specifically, the electroacoustic feedback which is used allows to reproduce the non-linear flame response to acoustic perturbations.
- Numerical simulations are performed employing a reduced-order combustion dynamics model which can effectively capture the occurrence of thermoacoustic instability within the combustion chambers.
- The practical implementation of noise-induced dynamics is shown on a practical combustion system operating on lean premixed natural gas-air mixtures.

The second part of the thesis is dedicated to investigate the interaction between noise/acoustic excitation and swirling flow, schematically shown in Fig. 1.8. The following studies are conducted for this investigation:

- A novel multi-swirl burner is designed and developed through RANS numerical simulations.

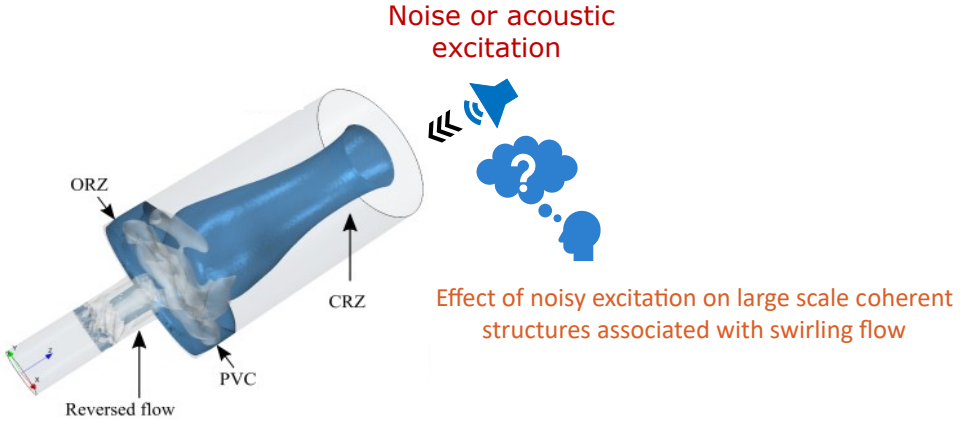

Figure 1.8: An illustration of the objectives for PART II of the thesis.

- Experimental investigation employing time-resolved Schlieren imaging to obtain mean flow characteristics of the burner and subsequently, proper orthogonal decomposition (POD) analysis is employed to identify and extract the dominant coherent structures in the flow.

PART I: Noise Effects on Prediction of Thermoacoustic Instability

Part contents

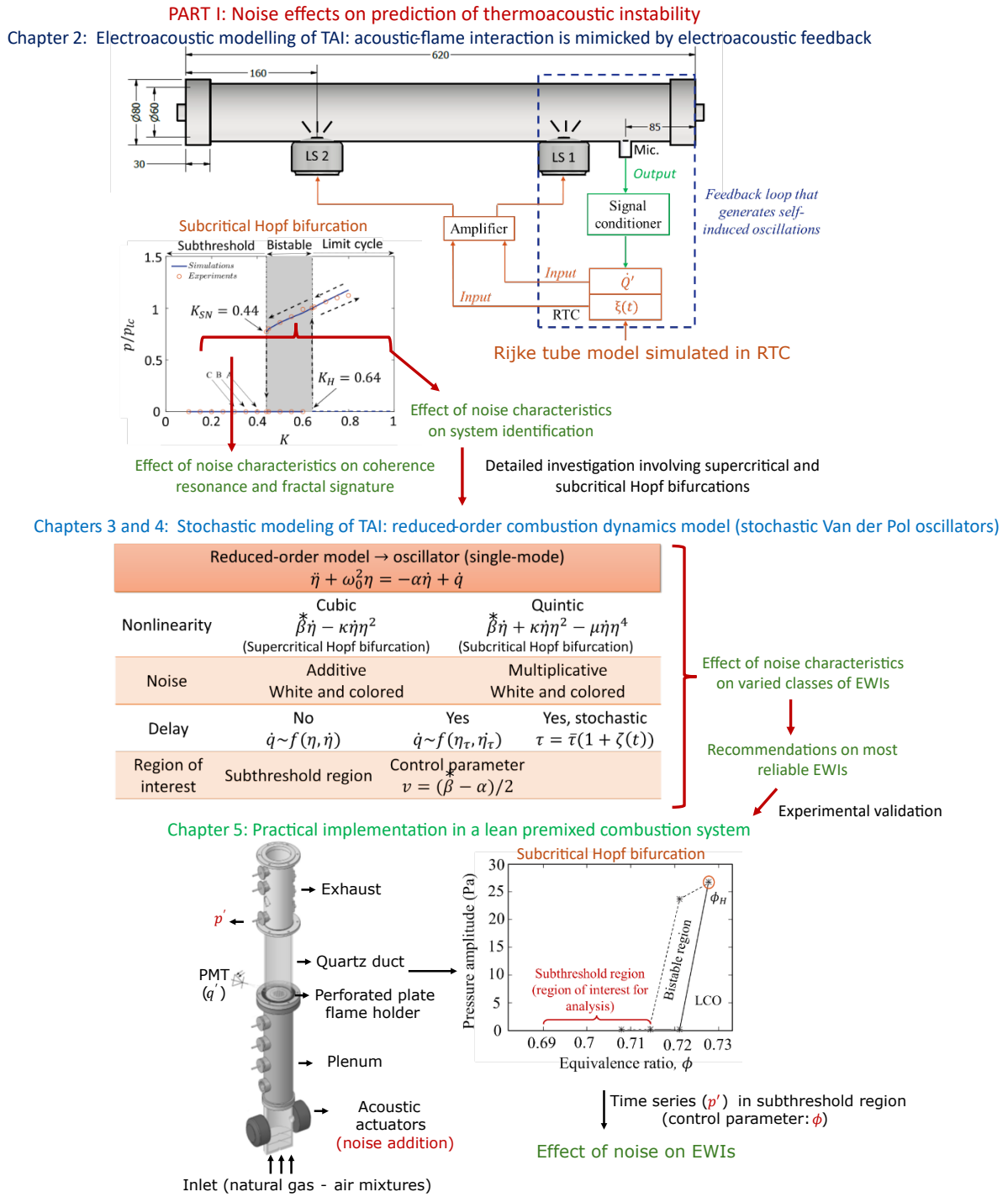

Overview of the chapter contents of PART I: this part is divided into four chapters, (i) Top (chapter 2): electroacoustic modelling of thermoacoustic instability; (ii) Middle (chapters 3 and 4): stochastic modelling of thermoacoustic instability and (iii) Bottom (chapter 5): practical implementation to a lean premixed combustion system.

Summary

This part of the thesis systematically assesses the application and limitations of different classes of EWIs as a function of noise color and intensity through detailed numerical simulations and experiments. Specifically, we address how variations in background noise characteristics influence the effectiveness of different classes of EWIs and which EWIs are most reliable considering that noise characteristics depend on the system and may change with control parameters. We investigate indicators based on statistical measures (variance, skewness, and kurtosis), autocorrelation and spectral properties (coherence factor), system identification (growth/decay rates of pressure oscillations), multi-fractality (Hurst exponent and multi-fractal spectrum width), and time series complexity (permutation entropy and Jensen Shannon complexity), as tabulated in Table 1.1. The entire investigation is carried out in the subthreshold region where the system is asymptotically stable. The investigation uses three types of systems: (i) an electrically driven Rijke tube simulator (a prototypical thermoacoustic system) exhibiting subcritical Hopf bifurcation, (ii) reduced-order combustion dynamics model (stochastic Van der Pol oscillators – supercritical and subcritical Hopf bifurcation), and (iii) a lean premixed flat flame combustion system operating on natural gas-air mixtures exhibiting subcritical Hopf bifurcation. In all cases, we subjected the systems to two types of noise: (i) white noise and (ii) colored noise at varied noise correlation times and intensity.

This part includes four chapters. In Chapter 2, we investigate the effects of noise characteristics on system identification, coherence resonance and fractal signature using an electroacoustic simulator, which serves as a prototypical thermoacoustic system. In Chapters 3 and 4, we perform detailed numerical simulations using a reduced-order combustion dynamics model and investigate the effects of both additive (Chapter 3) and multiplicative (Chapter 4) noise characteristics on a broad spectrum of EWIs, as tabulated in Table 1.1. We provide recommendations on the most reliable EWIs for implementation in practical systems. In Chapter 5, we implement the recommendations from numerical simulations in a lean premixed combustion system where noise is systematically varied and identify the most robust EWI. The results from this part of the thesis provide valuable insights for selecting appropriate EWIs for engine monitoring in the absence of information on noise properties and their variation with operating conditions. This practical information is of direct relevance and interest to any gas turbine manufacturer or user.

Chapter 2

Electroacoustic Modelling of Thermoacoustic Instability

2.1 Overview

In this chapter, we present an experimental and numerical investigation into the noise-induced dynamics of thermoacoustic coupling using an electroacoustic Rijke tube simulator (Fig. 2.4), a prototypical thermoacoustic system, which exhibits instabilities via subcritical Hopf bifurcation with variation in heater power. The electroacoustic simulator is designed to mimic the classical Rijke tube, wherein an electroacoustic feedback allows to reproduce the non-linear flame response to acoustic perturbations. Our focus is on the effects of noise characteristics (such as correlation time and intensity) on system parameter identification (growth/decay rates of acoustic oscillations) and the early warning prediction of thermoacoustic instabilities. We model the inherent (background/combustion) noise as an additive Ornstein-Uhlenbeck (OU) process.

We employ the Fokker-Planck formulation, associated with the stochastic differential equations of amplitude and phase coordinates derived from the Rijke tube model subjected to both white and OU noise for system identification. We discuss the limitations of the white noise approximation in the stable, bistable, and linearly unstable regions to better understand the thermoacoustic system driven by colored noise. This understanding is crucial for designing acoustic damping devices for passive control and for developing decay-rate-based early warning indicators for the active control of thermoacoustic instabilities.

Subsequently, we focus our investigation on the stable region (prior to the occurrence of instability) and study the effects of noise characteristics on the estimation of two types of noise-induced dynamics: (i) the coherence factor and (ii) the Hurst exponent and multi-fractal spectrum (multi-fractality). As coherence resonance and multi-fractal measures are related to trends observed in various precursors—such as variance, autocorrelation function, permutation entropy, duration of intermittent bursts, conditional heteroskedasticity, skewness, and kurtosis of the amplitude distribution—this investigation covers the effects of noise color one might expect to observe in a spectrum of early warning indicators for detecting the system's proximity to thermoacoustically unstable conditions.

This chapter is further divided into four sections. Section 2.2 describes the numerical model of a representative thermoacoustic system, the electrically-driven Rijke tube exhibiting subcritical Hopf bifurcation with variations in heater power; the colored noise model; the derivation of the Fokker-Planck formulation; and the experimental setup used in this chapter. Section 2.3 experimentally investigates the influence of noise characteristics on system identification.

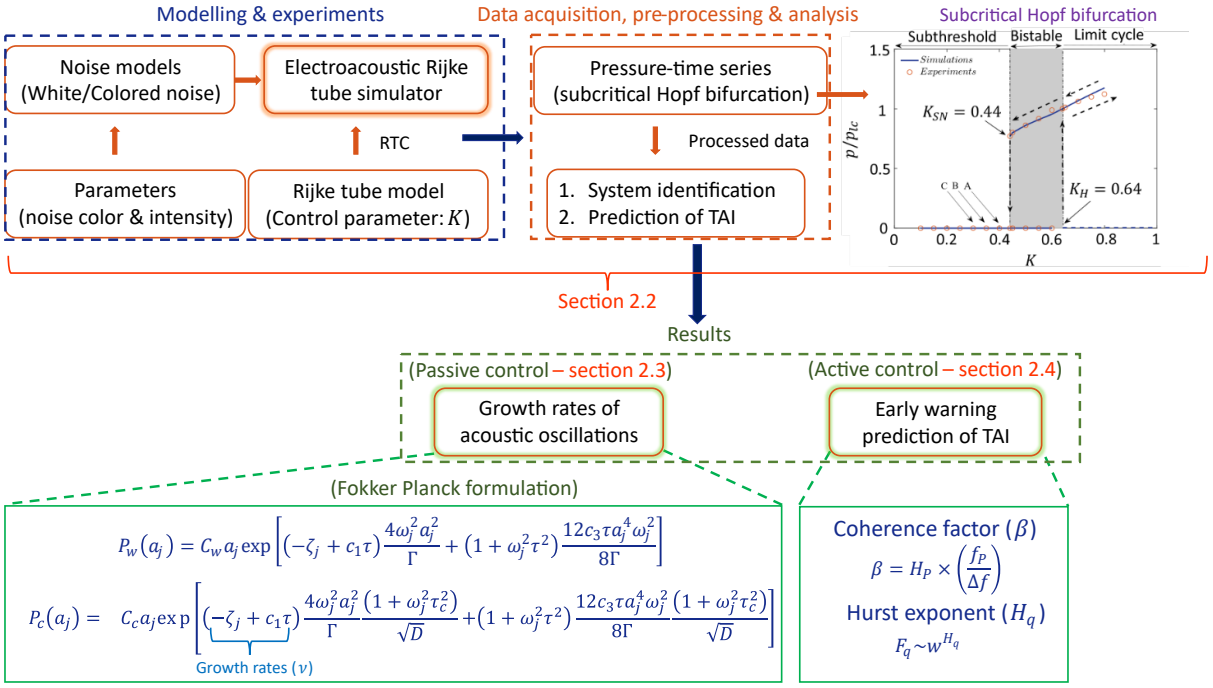

Figure 2.1: Visual summary of the contents of Chapter 2. TAI stands for thermoacoustic instability.

Section 2.4 presents both numerical and experimental investigations on the influence of noise characteristics on the coherence factor and measures of multi-fractality. A brief overview of the summary for the contents of the chapter is shown in Fig. 2.1.

2.2 Model and experimental setup description

2.2.1 The Rijke tube model

Rijke tube [137–139] is a simple thermoacoustic system consisting of a hot wire gauze placed inside a tube with open ends. Thermoacoustic instability arises in this system due to feedback coupling between acoustic oscillations associated with duct acoustic modes and heat release rate fluctuations from the hot wire gauze. The momentum and energy equations for an electrically-heated Rijke tube with the mean flow and temperature gradients neglected in the dimensionless form are given as [140]:

$$\begin{aligned} \frac{\partial u}{\partial t} &= -\frac{1}{\gamma M_a}\frac{\partial p}{\partial x} \\ \frac{\partial p}{\partial t} &= -\gamma M_a \frac{\partial u}{\partial x} - \zeta p + \dot{Q}'\delta\left(x - x_f\right) \end{aligned} \tag{2.1}$$

here, x represents the duct's longitudinal coordinate normalized by its length, L_a; t represents time normalized by L_a/c_0 (c_0 is the speed of sound); u and p represents the velocity and pressure fluctuations normalized by the mean velocity, u_0, and the mean pressure, p_0, respectively. $\dot{Q}'$ represents the dimensionless heat release rate fluctuations, normalized by $\frac{\rho c_0^3}{\gamma(\gamma-1)}$, where γ is the ratio of specific heat at constant pressure and volume ($\gamma = c_p/c_v$). ζ represents the acoustic

damping in the system. M_a is the Mach number (u_0/c_0) of the mean flow and δ is the standard Dirac distribution employed to indicate that the heat release occurs at the heater location, x_f. A model for the heat release rate fluctuations, $\dot{Q}'$, is given by the modified form of King's law [138]:

$$\dot{Q}' = K\left[\sqrt{\left|\frac{1}{3} + u_f(t-\tau)\right|} - \frac{1}{\sqrt{3}}\right] \tag{2.2}$$

where τ is the time-delay representing thermal inertia of heat transfer from the hot wire gauze to the duct acoustics, normalized by L_a/c_0; K is the normalized heater power which is a function of physical and thermodynamic properties of the hot wire gauze and the fluid; and u_f is the non-dimensional acoustic velocity at x_f.

Acoustic velocity, u, and pressure, p are projected onto N Galerkin base modes resulting in a set of $2N$ ordinary differential equations [141]. The Galerkin modes satisfy the closed-closed boundary condition and therefore, the decomposition is given as:

$$\begin{aligned} p(x,t) &= \sum_{j=1}^{N} \frac{\dot{\eta}_j(t)}{j\pi} \gamma M_a \cos(j\pi x) \\ u(x,t) &= \sum_{j=1}^{N} \eta_j(t) \sin(j\pi x) \end{aligned} \tag{2.3}$$

On substituting this decomposition in acoustic momentum and energy equations (Eqn. (2.1)) and adding additive noise, we obtain,

$$\frac{\mathrm{d}\eta_j}{\mathrm{d}t} = \dot{\eta}_j \tag{2.4}$$

$$\frac{\mathrm{d}\dot{\eta}_j}{\mathrm{d}t} + \zeta_j \dot{\eta}_j + (j\pi)^2 \eta_j = \frac{2j\pi}{\gamma M a} \dot{Q}' \cos(j\pi x_f) + \xi_j \tag{2.5}$$

The damping term ζ_j is modelled as $\zeta_j = C_1 j + C_2\sqrt{1/j}$, with C_1 and C_2 following Matveev and Culick [71] and Sterling and Zukoski [37]. It is important to note here that additive noise is introduced to each mode via the ξ_j term. Such noise addition is not associated with a location. This form for the noise term is the same as in previous literature [2, 73, 76] on noisy Rijke tube simulations. Moreover, the noise terms, ξ_j, are also not dependent on the mode number – additive noise to each mode has the same intensity and color for a given simulation.

The system of equations is numerically simulated using the fourth order Runge-Kutta method. We consider K as the control parameter while choosing the values of the other Rijke tube parameters as: $\tau = 0.2, C_1 = 0.1, C_2 = 0.06$, $x_f = 0.25$ and $N = 10$ to ensure modal convergence [142]. The Hopf bifurcation diagram for the Rijke tube model in the absence of noise is shown in Fig. 2.2 by the solid lines. As the parameter K is gradually increased from 0, the system becomes unstable, and thermoacoustic instability (limit cycle oscillation) is spontaneously observed at the Hopf point. Fig. 2.2 indicates that the oscillator evolves through a subcritical Hopf bifurcation, characterized by the Hopf point and saddle-node (also fold) point at $K_H = 0.64$ and $K_{SN} = 0.44$, respectively. The region before the fold point ($K < 0.44$) is termed the subthreshold region, where the only attractor available is the stable focus, and the region beyond the Hopf point is

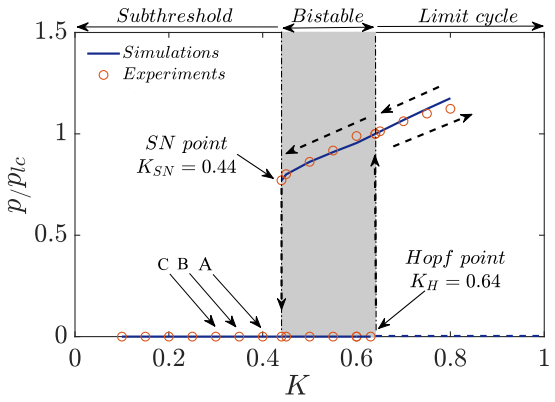

Figure 2.2: The noise-free subcritical Hopf bifurcation diagram for Rijke tube model with K as the control parameter. The bistable region is shown as the grey fill. The saddle-node and Hopf points are located at $K_{SN} = 0.44$ and $K_H = 0.64$ respectively. The dashed arrows indicate the path followed by the system as K is varied. The solid lines represent the simulation results, whereas, the markers represent the experimental data. The RMS values of the pressure oscillations (p) on y-axis is normalized by amplitude at K_H given as p_{lc}.

the linearly unstable region ($K \geq 0.64$). A bistable region, where stable focus and limit cycle oscillations coexist, is present between $0.44 < K < 0.64$. In this region, perturbations can trigger large amplitude limit cycle oscillations [73, 116, 143].

2.2.2 Noise models

The frequency spectrum of combustion noise, typically from turbulent flames as shown in Fig. 2.3(a) for varied operating conditions, exhibits the following features: the power density first increases from low frequencies, following $P \propto f^2$, up to a cut-off frequency (200Hz $\leq f_{peak} \leq$ 1000Hz) [144]) beyond which it decays following $P \propto f^{-r}$, where, $2 < r < 3.4$ [4,5]. A change in the combustor operating conditions (via parameters such as temperature (T), Reynolds number,

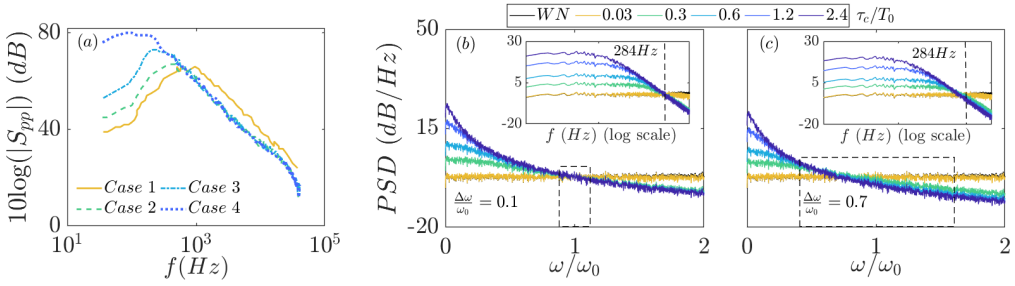

Figure 2.3: (a) Typical power spectra of combustion noise of turbulent premixed flames adapted from Rajaram and Lieuwen [4]: case 1 and 2 → fuel-acetylene at $\phi = 0.71$ and 0.64 respectively, case 3 → fuel-propane at $\phi = 1.03$ and case 4 → fuel-natural gas at $\phi = 0.95$. (b) and (c) Comparison of the power spectrum of white and OU noise for two bandwidths, $\frac{\Delta\omega}{\omega_0} = 0.1$ and $\frac{\Delta\omega}{\omega_0} = 0.7$ respectively. The y-axis shows the power spectral density of $\xi(t)$ (Eqn.(2.6)) in dB/Hz (i.e., $10\log_{10}(S_{\xi\xi}(f))$. OU noise is generated such that the powers provided by ξ and by the white noise of intensity Γ in the band around the system's natural frequency are equal. The correlation time, τ_c, is normalized by the duct acoustic time period, T_0. The inset plots show the same plot on log scale.

(Re), or equivalence ratio (ϕ)) causes a change in the amplitude, peak frequency, and decay rate r. The latter, decay rate is a representation of combustion noise correlation time. Such changes in combustion noise characteristics significantly changes system dynamics.

In combustors, additional sources of noise such as flow turbulence and cooling holes exist. Still, overall background noise is expected to have a low-pass character and ξ_j in Eqn. (2.1) can be adequately modelled by an Ornstein-Uhlenbeck (OU) process. This process has been previously employed by Ma et al. [119], Bonciolini et al. [61] and Li et al. [105] for modelling systems where external noise and heat release fluctuations are expected to have a low-pass nature. Mathematically, ξ_j when modelled as an OU process satisfies the following Langevin equation [61, 105]:

$$\dot{\xi}(t) = -\frac{1}{\tau_c}\xi(t) + \frac{\sqrt{D}}{\tau_c}\epsilon(t) \tag{2.6}$$

where τ_c denotes the noise correlation time and controls the power spectrum's cut-off frequency. D denotes the noise intensity. ϵ is Gaussian white noise (a vector of size $n \times 1$, where n is the number of samples based on sampling frequency). Thus, white noise is a limiting case of the OU noise, as $\tau_c \to 0$: the shorter τ_c, the closer ξ is to white noise. The OU noise has the following statistical properties:

$$\langle \xi(t) \rangle = 0 \quad \text{and} \quad \left\langle \xi(t)\xi\left(t'\right) \right\rangle = s^2 \exp\left(-\frac{|t-t'|}{\tau_c}\right) \tag{2.7}$$

where the parameter, $s^2 = D/\tau_c$, is the variance of the OU process given by its second moment, $\langle \xi^2 \rangle$. The power spectrum of $\xi(t)$ is given as:

$$S_{\xi\xi}(\omega) = \frac{\Gamma}{2\pi}\frac{D}{1+\omega^2\tau_c^2} \tag{2.8}$$

Γ is the measure of white noise intensity. In the limit $\tau_c \to 0$ and $D \to 1$, we get $S_{\xi\xi}(\omega) \to \Gamma/2\pi = S_{\epsilon\epsilon}(\omega)$.

The focus of the present study is to quantitatively compare white and colored noise forcing on the Rijke tube oscillator; therefore it becomes necessary to set a criterion regarding the input power. A convenient way is to keep the noise power in a band around the system's natural frequency equal for colored, ξ, and white noise, ϵ [61], i.e.,

$$\int_{\omega_1}^{\omega_2} S_{\xi\xi} d\omega = \int_{\omega_1}^{\omega_2} \Gamma/2\pi d\omega$$

In this case, the intensity of ξ is adjusted by the coefficient D, evaluated using the following expression:

$$D = \frac{\tau_c\left(\omega_2 - \omega_1\right)}{\operatorname{atan}\left(\omega_2\tau_c\right) - \operatorname{atan}\left(\omega_1\tau_c\right)} \tag{2.9}$$

We conduct our study for three bandwidths around the eigenfrequency: (i) $\Delta\omega/\omega_0 = 0.1$; (ii) $\Delta\omega/\omega_0 = 0.7$; (iii) $\Delta\omega/\omega_0 = 4.9$. The first two bandwidth cases are shown in Fig. 2.3(b)-(c). The powers in the given bandwidth (area under the PSD curves on a linear scale) for the white and OU noise are the same. In Fig. 2.3(b)-(c), the correlation time, τ_c, is normalized by the

duct acoustic time period, T_0 $(= 1/f_0)$.

It is important to note that, the increasing part of the combustion noise spectrum, controlled by f^2, can only affect the system's dynamics when $\tau_c/T_0 \leq 0.16$. In such cases, the system's eigenfrequency (f_0) sees the f^2 growth in the spectrum amplitude. The noise-induced response of the system in such cases would be nearly identical to that of white noise for all $\tau_c/T_0 \leq 0.16$; thereafter, the system's response would be controlled by the decay part (f^{-r}) of the combustion noise spectrum. This is because, within the bandwidth, the curves in the power spectrum corresponding to $\tau_c/T_0 \leq 0.16$ are similar to the white noise. The power spectrum and associated results considering the f^2 part of the combustion noise spectrum are shown in Fig. A.1 and A.2 of Appendix A. Therefore, in our study we model the additive noise with OU process which accurately models the f^{-r} part of the combustion noise.

2.2.3 Fokker Planck formulation

It is convenient to recast the Rijke tube model using the amplitude-phase coordinates. This substitution is reasonable as, in practical cases, the thermoacoustic systems are categorized as "weakly" amplified/damped systems [55]. Equations (2.4)-(2.5) can be combined and re-written as,

$$\frac{d\dot{\eta}_j}{dt} + \zeta_j\dot{\eta}_j + (j\pi)^2\eta_j = \frac{K(j\pi)\cos(j\pi x_f)}{\sqrt{3}}\left[\sqrt{|1+3\sin(j\pi x_f)\,\eta_j(t-\tau)|}-1\right] + \xi_j \tag{2.10}$$

For weakly non-linear analysis of the reduced-order Rijke tube model given by Eqn. (2.10), we assume small magnitudes of η and expand the square-root non-linearity in a Maclaurin series to obtain,

$$\begin{aligned}\frac{d\dot{\eta}_j}{dt} + \zeta_j\dot{\eta}_j + (j\pi)^2\eta_j = \frac{\sqrt{3}}{4}K(j\pi)\sin(2j\pi x_f)\,[\eta(t-\tau) - \frac{3}{4}\sin(j\pi x_f)\,\eta(t-\tau)^2 \\ +\frac{9}{8}\sin^2(j\pi x_f)\eta(t-\tau)^3] + \xi_j\end{aligned} \tag{2.11}$$

In order to simplify, we introduce the following terms in Eqn. (2.11),

$$\begin{aligned}c_1 &= \frac{\sqrt{3}Kj\pi}{4}\sin(2j\pi x_f)\\ c_2 &= -\frac{3\sqrt{3}Kj\pi}{16}\sin(2j\pi x_f)\sin(j\pi x_f)\,,\\ c_3 &= \frac{9\sqrt{3}Kj\pi}{32}\sin(2j\pi x_f)\sin^2(j\pi x_f)\end{aligned} \tag{2.12}$$

and obtain,

$$\frac{d\dot{\eta}_j}{dt} + \zeta_j\dot{\eta}_j + (j\pi)^2\eta_j + c_1\eta(t-\tau) + c_2\eta(t-\tau)^2 + c_3\eta(t-\tau)^3 - \xi_j = 0 \tag{2.13}$$

For small τ, $\eta(t-\tau)$ can be approximated as,

$$\begin{aligned}
\eta(t-\tau) &\approx \eta(t) - \tau\dot{\eta}(t) \\
\eta(t-\tau)^2 &\approx \eta^2(t) + \tau^2\dot{\eta}^2(t) - 2\tau\eta(t)\dot{\eta}(t) \\
\eta(t-\tau)^3 &\approx \eta^3(t) - \tau^3\dot{\eta}^3(t) - 3\tau\eta^2(t)\dot{\eta}(t) + 3\tau^2\eta(t)\dot{\eta}^2(t)
\end{aligned} \tag{2.14}$$

On combining Eqn. (2.13) and (2.14), we obtain the following linearized equation for j^{th} mode,

$$\begin{aligned}
\frac{d\dot{\eta_j}}{dt} + \zeta_j\dot{\eta_j} + (j\pi)^2\eta_j + c_1\eta_j - c_1\tau\dot{\eta_j} + c_2\eta^2 + c_2\tau^2\dot{\eta_j^2} - 2c_2\tau\eta_j\dot{\eta_j} + c_3\eta_j^3 - c_3\tau^3\dot{\eta_j^3} \\
-3c_3\tau\eta_j^2\dot{\eta_j} + 3c_3\tau^2\eta_j\dot{\eta_j^2} - \xi_j = 0
\end{aligned} \tag{2.15}$$

Now, we derive the Fokker-Planck equation [54] representing the probability density function (PDF) of the amplitude of the pressure fluctuations inside the Rijke tube. To obtain an explicit form of the stationary Fokker-Planck equation, we derive the Fokker-Planck equation for the j^{th} mode.

The state variable, η_j and $\dot{\eta_j}$ can be transformed into amplitude and phase equations using the following relation,

$$\begin{aligned}
\eta_j &= a_j\cos(\omega_j t + \varphi_j) \\
\dot{\eta}_j &= -a_j\omega_j\sin(\omega_j t + \varphi_j)
\end{aligned} \tag{2.16}$$

where, a_j and φ_j are the instantaneous amplitude and phase of η_j. We transform Eqn. (2.15) in terms of a_j and φ_j as,

$$\dot{a}_j\cos\phi_j - a_j\dot{\varphi}_j\sin\phi_j = 0 \tag{2.17}$$

$$\begin{aligned}
\dot{a}_j\sin\phi_j + a_j\dot{\varphi}_j\cos\phi_j = &-\zeta_j a_j\sin\phi_j + c_1\tau a_j\sin\phi_j + \frac{c_1}{\omega_j}a_j\cos\phi_j + \frac{c_2}{\omega_j}a_j^2\cos^2\phi_j \\
&+ 2c_2\tau a_j^2\sin\phi_j\cos\phi_j + c_2\tau^2 a_j^2\omega_j\sin^2\phi_j + \frac{c_3}{\omega_j}a_j^3\cos^3\phi_j \\
&+ 3c_3\tau a_j^3\sin\phi_j\cos^2\phi_j + 3c_3\tau^2 {a_j}^3\omega_j\sin^2\phi_j\cos\phi_j \\
&+ c_3\tau^3 a_j^3\omega_j^2\sin^3\phi_j + \xi_j
\end{aligned} \tag{2.18}$$

where $\phi_j = \omega_j t + \varphi_j$. The ordinary differential equations for a_j and φ_j obtained from Eqn. (2.17)-(2.18) are as,

$$\dot{a_j} = -\frac{\zeta_j a_j}{2} + \frac{c_1\tau a_j}{2} + \frac{3c_3\tau^3 a_j^3\omega_j^2}{8} + \frac{3c_3\tau a_j^3}{8} + Q_a(a,\phi) + \frac{\xi_j}{\omega_j}(\sin\phi) \tag{2.19}$$

$$\dot{\varphi}_j = \frac{c_1}{2\omega_j} + \frac{3c_3 a_j^2}{8\omega_j} + \frac{3c_3\tau^2 a_j^2\omega_j}{8} + Q_\phi(a,\phi) + \frac{\xi_j}{a_j\omega_j}(\cos\phi) \tag{2.20}$$

where, $Q_a(a,\phi)$ and $Q_\phi(a,\phi)$ are the sum of first-order sine and cosine terms that become zero after time-averaging. To derive the stochastic equations for a_j and φ_j, following the method stated in [56], we perform averaging of Eqn. (2.19) and (2.20) over one cycle of oscillation. The stochastic part of Eqn. (2.19) and (2.20) can be transformed using, $x = \xi(t)\sin\phi(t)$ and $y = \xi(t)\cos\phi(t)$. The correlation time of noise is assumed to be much smaller than the characteristic time of a_j, hence there exists a time shift $\Delta \gg \tau_c$, over which a_j and φ do not change noticeably.

We can then expand x in φ, around $\varphi(t-\Delta)=\varphi_{-\Delta}$ as,

$$x \approx -\xi(t)\sin\left(\omega_j t+\varphi_{-\Delta}\right)-\xi(t)\cos\left(\omega_j t+\varphi_{-\Delta}\right)\Delta\varphi \tag{2.21}$$

We can then integrate the fluctuating term of Eqn. (2.20) , obtain $\Delta\varphi$, and then express $\langle x\rangle$ as:

$$\langle x\rangle=-\frac{1}{\omega_j a_j}\int_0^{\Delta}\langle\xi\xi_{\tau-0}\rangle\cos\phi\cos\left(\phi-\omega_j\tau_0\right)d\tau \tag{2.22}$$

For OU noise, $\langle\xi\xi_{\tau_0}\rangle=\Gamma\frac{\gamma}{2\tau_c}e^{-\tau_0/\tau_c}$. This autocorrelation function tends to zero for time larger than τ_c. Therefore, we get,

$$\langle x\rangle/\omega_j=\dot{a_j}_{\text{stoch}}=\frac{\Gamma}{4\omega_j^2 a_j}\frac{\sqrt{D}}{\left(1+\omega_j^2\tau_c^2\right)} \tag{2.23}$$

This term exists due to the correlation between $a_j(t)$ and $\varphi(t)$, which causes the fluctuating component to have a non-zero average.
For white noise, $\tau_c\to 0$ and $D\to 1$, hence, we get,

$$\langle x\rangle/\omega_j=\dot{a_j}_{\text{stoch}}=\frac{\Gamma}{4\omega_j^2 a_j} \tag{2.24}$$

Making use of Eqn. (2.19)-(2.23), we compute the following form of Fokker Planck equation,

$$\frac{\partial}{\partial t}P\left(a_j,t\right)=-\frac{\partial}{\partial a_j}\left[m\left(a_j\right)P\left(a_j,t\right)\right]+\frac{\partial^2}{\partial a_j^2}\left[\frac{\sigma\left(a_j\right)}{2}P\left(a_j,t\right)\right] \tag{2.25}$$

where, the drift and diffusion coefficients are given as,

$$\begin{aligned} m\left(a_j\right)&=-\frac{\zeta_j a_j}{2}+\frac{c_1\tau a_j}{2}+\frac{3c_3\tau a_j^3}{8}+\frac{3c_3\tau^3\omega_j^2 a_j^3}{8}+\frac{\Gamma}{4\omega_j^2 a_j}\\ \sigma\left(a_j\right)&=\frac{\Gamma}{2\omega_j^2}\end{aligned} \tag{2.26}$$

Integration of Eqn. (2.25), will yield the following stationary PDF for OU noise,

$$P_c\left(a_j\right)=C_c a_j\exp\left[\left(-\zeta_j+c_1\tau\right)\frac{4\omega_j^2 a_j^2}{\Gamma}\frac{\left(1+\omega_j^2\tau_c^2\right)}{\sqrt{D}}+\left(1+\omega_j^2\tau^2\right)\frac{12c_3\tau a_j^4\omega_j^2}{8\Gamma}\frac{\left(1+\omega_j^2\tau_c^2\right)}{\sqrt{D}}\right] \tag{2.27}$$

and for the white noise as:

$$P_w\left(a_j\right)=C_w a_j\exp\left[\left(-\zeta_j+c_1\tau\right)\frac{4\omega_j^2 a_j^2}{\Gamma}+\left(1+\omega_j^2\tau^2\right)\frac{12c_3\tau a_j^4\omega_j^2}{8\Gamma}\right] \tag{2.28}$$

where, C_c and C_w are the normalization constants such that $\int_0^{\infty}P(a_j)da_j=1$. For a given set of parameters $(\zeta_j,\tau,\omega_j,c_1,c_3)$, $P_w\left(a_j\right)$ is dependent only on white noise intensity, Γ, whereas, $P_c\left(a_j\right)$ is also dependent on τ_c and D. Eqn. (2.27) and (2.28) differ in normalization constants,

and a factor $\frac{(1+\omega_j^2\tau_c^2)}{\sqrt{D}}$ in the exponent. For $\tau_c \to 0$ and $D \to 1$, this factor is close to 1, resulting in Eqn. (2.27) and (2.28) to be identical. The significant difference in the two expressions for P_w and P_c occur for larger values of τ_c that is investigated in detail in this study. This Fokker Planck formulation is used for system identification in section 3.3.

2.2.4 Experimental setup (electroacoustic Rijke tube simulator)

We conduct experiments in an electroacoustic Rijke tube simulator designed to mimic the classical Rijke tube with closed ends (inspired from Noiray and Schuermans [59]). Figure 2.4 illustrates the setup which consists of a cylindrical duct closed at both ends. The duct is fitted with two acoustic driver units connected to an amplifier, a condenser microphone combined with a signal conditioner, and a real-time controller (RTC). An electroacoustic feedback loop is generated in this simulator by routing the microphone to loudspeaker 1 (LS 1) through a real-time controller (RTC) (shown by the blue dashed lines). The Rijke tube model (given by Eqn. (2.5)) is simulated in the RTC. Pressure fluctuations, (p), acquired from the microphone are employed to obtain velocity fluctuations, u_f, via Eqn. (2.3). The noise is fed into the simulator through Loudspeaker 2 (LS 2). All the conversion factors/calibration of loudspeakers, microphone and amplifier are accounted for in the experiments. We consider K as the control parameter for the simulator while choosing the values of the other Rijke tube parameters as: $\tau = 0.2, C_1 = 0.1, C_2 = 0.06$, $x_f = 0.25$ and $N = 1$.

Some of the experiments were repeated multiple times to check for repeatability. Prior to experiments with the Rijke tube simulator and noise, the *cold* decay rate (with $K = 0$) of Rijke

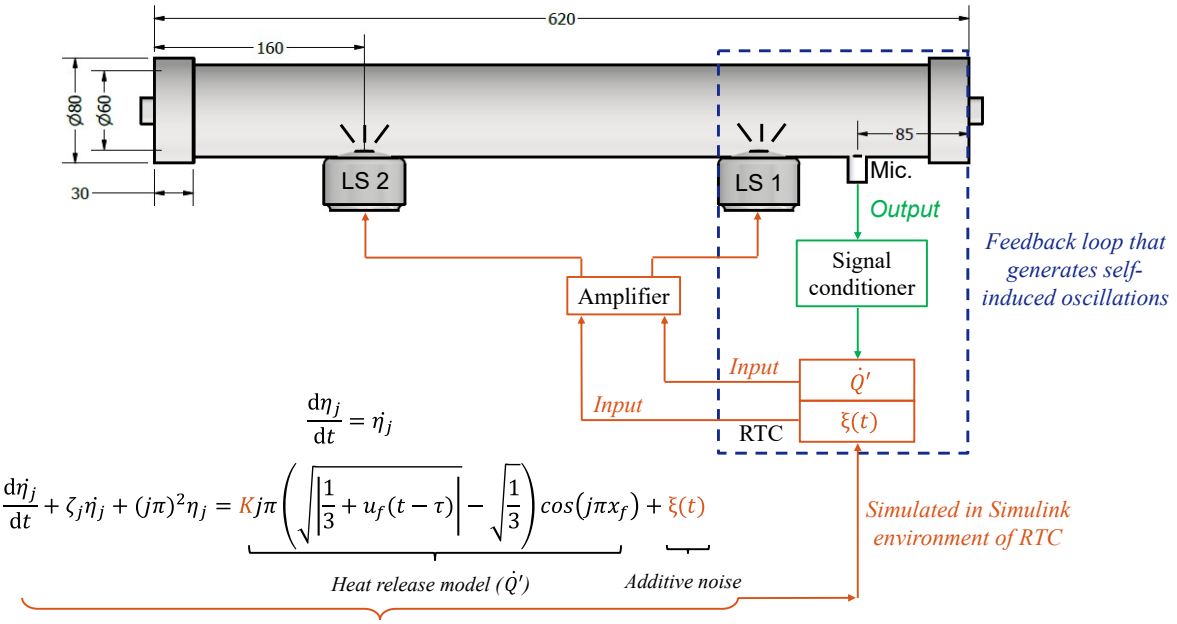

Figure 2.4: Schematic of the electroacoustic Rijke tube simulator. It is a cylindrical duct closed at both ends and is fitted with acoustic driver units and a microphone. A feedback loop inducing electroacoustic oscillations is generated by routing the microphone to loudspeaker 1 (LS 1) via a real-time controller wherein the Rijke tube model is simulated and the control parameter, K, is varied. Noise is fed through loudspeaker 2 (LS 2). All dimensions in the schematic are in mm.

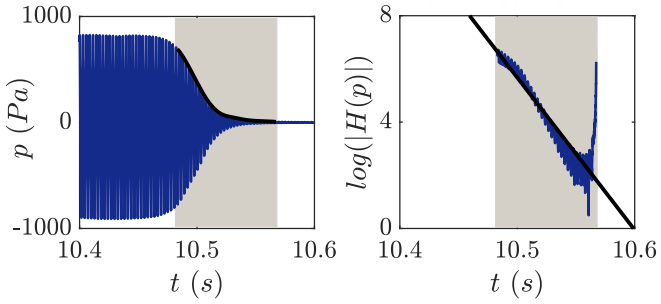

Figure 2.5: Estimation of cold damping rate, ν, of electroacoustic Rijke tube simulator. The decay rate is estimated by curve fitting a straight line to the logarithmic of pressure amplitude (obtained via Hilbert transform). The value of decay rate is found to be $\nu = 11 \pm s^{-1}$ in all reported experiments.

tube simulator was checked; in all tests, the exponential decay rate was consistently obtained with a value $\nu = 11 \pm 1s^{-1}$. For the cold decay rate measurements, the noise-free simulator was excited with the fundamental duct frequency (284 Hz) for a short duration through loudspeaker 1 after which the loudspeaker was turned off. The decay rates were estimated by curve fitting a straight line to the logarithm of the amplitude (obtained in turn using the Hilbert transform of the acoustic pressure signal). A sample result is presented in Fig. 2.5.

For the noise-free system (LS 2 switched off), as the parameter K is gradually increased from 0, thermoacoustic instability spontaneously appears in the initially stable system; a stable limit cycle is observed. The bifurcation plot, pressure-time traces, and corresponding power spectrum

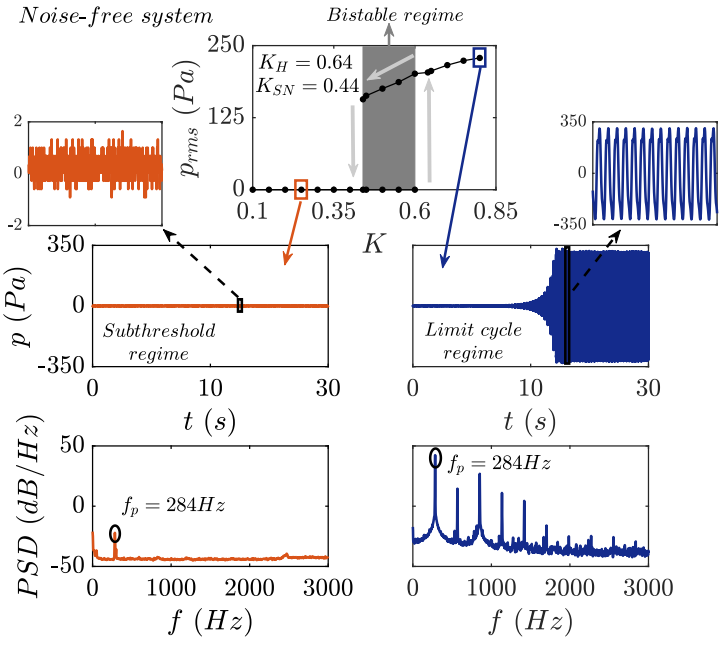

Figure 2.6: Top: The subcritical Hopf bifurcation with bistable zone as the grey fill; Center: Pressure-time traces; Bottom: Power spectrum obtained from noise-free electroacoustic Rike tube simulator. The saddle-node and Hopf points are located at $K_{SN} = 0.44$ and $K_H = 0.64$ respectively. The frequency peak is at $284Hz$.

are presented in Fig. 2.6. The simulator exhibits subcritical Hopf bifurcation with Hopf and saddle-node points at $K_H = 0.64$ and $K_{SN} = 0.44$ respectively. The peak frequency is observed at $f_0 = 284$Hz. The validation of experimental results with simulations is shown in Fig. 2.2, where the markers represents the experimental data and the lines represent the simulation results.

For the noise-free system, the growth rate of oscillations can be estimated by fitting a straight line to the logarithmic plot of the magnitude of Hilbert transform of the acoustic pressure signal. An overview of the estimated values of growth/decay rates for a noise-free system is represented in Fig. 2.7 as a function of the parameter K. To determine the decay rates in the bistable

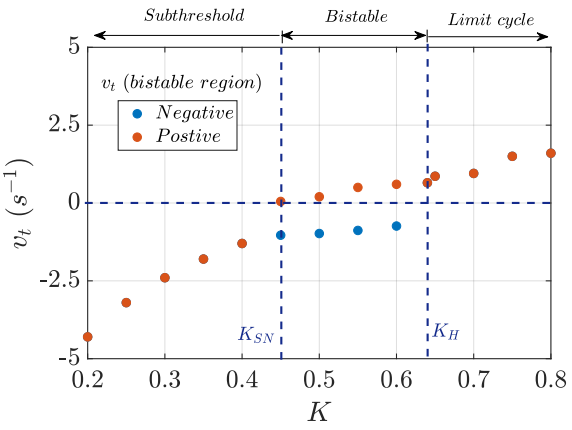

Figure 2.7: An overview of the estimation of growth rates of acoustic oscillations for a noise-free simulator as a function of K.

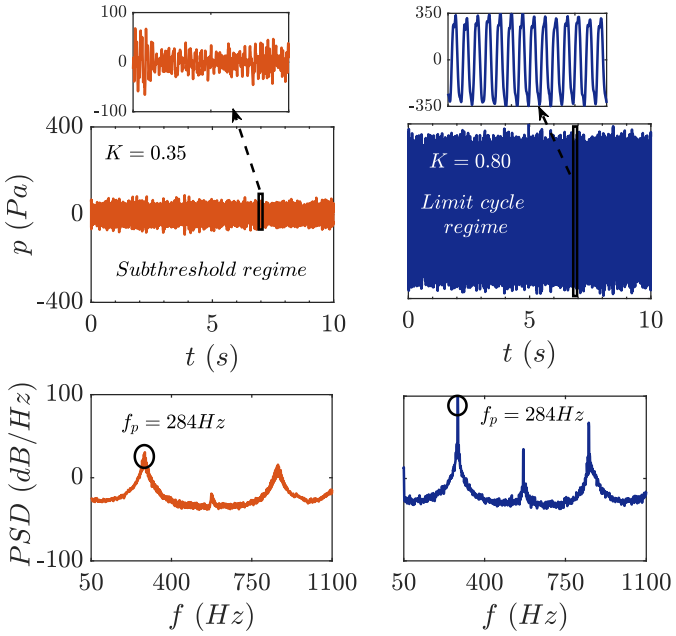

Figure 2.8: An illustration of noisy pressure-time series and corresponding power spectrum in subthreshold and limit cycle regions acquired from electroacoustic Rijke tube simulator for σ =17 Pa and $\tau_c = 0.9$ ms.

region, the initially-stable system was subjected to a small perturbation to cause the oscillations to decay.

In the present work, we conduct two sets of experiments: (i) noise modelled as white noise and (ii) noise modelled as Ornstein-Uhlenbeck (OU) process. Figure 2.8 shows an example of a noisy pressure-time series with the corresponding power spectrum in the subthreshold and linearly unstable regimes of the bifurcation plot for σ =17 Pa and $\tau_c = 0.9$ ms acquired from the Rijke tube simulator.

In the next section, we present the results obtained from our experimental investigation. Firstly, we will discuss the effect of white noise approximation on the estimation of system identification parameters and the importance of data pre-processing for analysis. Subsequently, we will examine the effects of varying colored noise parameters on these estimations.

2.3 Noise and growth rate estimation (system identification)

Accurate estimates of stability margins and linear growth rates of self-sustained oscillations is important for designing the damping devices for the control of thermoacoustic instabilities. The dynamics of a thermoacoustic system consists of non-linear and stochastic effects and for accurate estimates of the growth rates, the system identification methods (SI) must take into account these aspects [55]. The SI methods developed are based on approximating the stochastic forcing as white noise (zero correlation time), however, in a real system, the stochastic forcing has a finite correlation time. In case of experimental data analysis, a theoretical "white noise PDF" given by the expression, P_w (Eqn. (2.28)), is fitted on the experimental one, which by nature is "colored", in order to identify the growth rates. However, if the effect of noise color is not negligible in a system, the curve fit based on P_w will lead to an inaccurate parameter estimation. Here, we will investigate this deviation in the estimated growth rates when the system is subjected to both white and colored noise.

2.3.1 Effects of white noise approximation on estimation of growth rates

The concern that the noise driving a thermoacoustic system is never white in practice can bring the growth rates estimation based on white noise assumption into question. Therefore, we first estimate the growth rates using the white-noise approximation to have a comparison with the values estimated using colored noise model. By making use of the theoretical expression for $P_w(a_j)$, given by Eqn. (2.28), to curve fit on the PDF distribution of colored noise driven simulator (shown in Fig. 2.11), we estimate the growth rates in all the three regions of the subcritical Hopf bifurcation. The term $(-\zeta_j + c_1\tau)$ in the expressions for P_c and P_w (Eqn. (2.27)-(2.28)) is the measure for growth rate estimation. We will present the overview of the estimated growth rates for the noise driven Rijke tube simulator as a 2D map between noise intensity (σ) and the control parameter (K). The contours of the map will represent the relative deviation of the estimated values of the growth rates from the true values (obtained from noise-free system, given in Fig. 2.7).

The left plot of Fig. 2.9 shows the values of the estimated growth rates using the white-noise

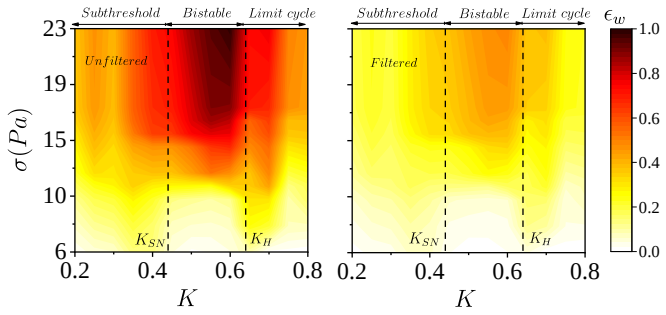

Figure 2.9: Map of the deviation in estimated growth rates as a function of noise intensity (σ) and control parameter (K) considering the white noise assumption using the unfiltered (left) and bandpass filtered pressure-time series (right). The contours represent the relative deviation of the estimated growth rates from the true value, given as, $\epsilon = |(\nu_t - \nu_e)|/\nu_t$. ϵ_w indicates the estimation of deviation for white noise.

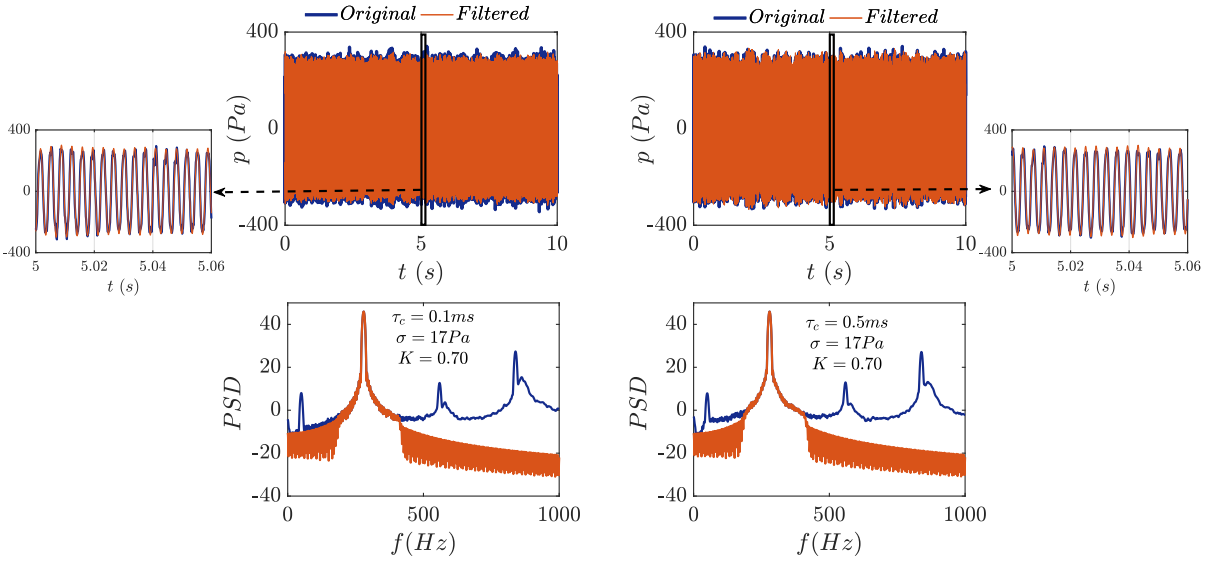

Figure 2.10: An illustration of bandpass filtering of pressure-time series and its corresponding power spectrum obtained from colored noise driven Rijke tube simulator.

approximation on the unfiltered data for the OU noise driven simulator. As can be seen from the contours, the identified values of growth rates differ significantly from the actual values. This deviation in the values becomes more prominent (leading to a deviation of $\sim 100\%$) with increasing noise intensities. The reason for such deviation can be understood from the fact that the system identification methods for the growth rate estimation are derived based on the assumption of a single mode in the frequency spectrum. However, the power spectrum from the Rijke tube simulator (or real system) will consist of several excited duct acoustic modes (shown in Fig. 2.8) which will be mutually coupled and will be influencing the response of each other. Therefore, we can say that the system parameter identification failed because of the lack of pre-processing of the data. To reduce the observed deviation in the estimated growth rates, we need to analyse one mode at a time. This can be easily done by bandpass filtering the data around the dominant mode. Therefore, we apply a bandpass filter around the eigenmode of the simulator ($f_0 = 284Hz$) such that the filter discards the neighbouring peaks while keeping the

main peak and its tails. An example plot for applying bandpass filtering is shown in Fig. 2.10. We then estimate the growth rates using white-noise approximation on the bandpass filtered data. The plot on the right side of Fig. 2.9 presents the estimation of growth rates. As we can observe, the deviation in the estimated values have considerably reduced by a factor of 4 in all the three regimes. In the plot, we can observe two trends: (i) in the bistable region, the deviation in the estimated growth rate values is in the range of 5 % to 45 % unlike the stable and unstable region where the observed deviation is in the range of 5 % to 25 %. This higher deviation in the estimated growth rates in bistable region is expected due to noise-induced triggering and noise-induced coherence resonance as the system approaches the saddle and Hopf points; (ii) the deviation in the estimated values increases from $\sim 5\%$ to $\sim 45\%$ with increasing noise intensities. This can be explained by the fact that with increasing noise intensities, the PDF becomes broader with peak values shifting towards higher values of amplitudes (also explained in next section with the help of PDFs). As the noise intensity affects the distribution of PDF, therefore, the curve fit and hence growth rate estimation is also affected leading to higher deviation from the actual values.

2.3.2 Effects of colored noise approximation on estimation of growth rates

In this section, we now investigate the influence of colored noise parameters upon the estimation of growth rates. Figure 2.11 represents the PDF distribution obtained from the bandpass filtered noisy pressure-time trace acquired from colored noise driven Rijke tube simulator for various combinations of τ_c and σ in subthreshold and limit cycle regimes. For both subthreshold and

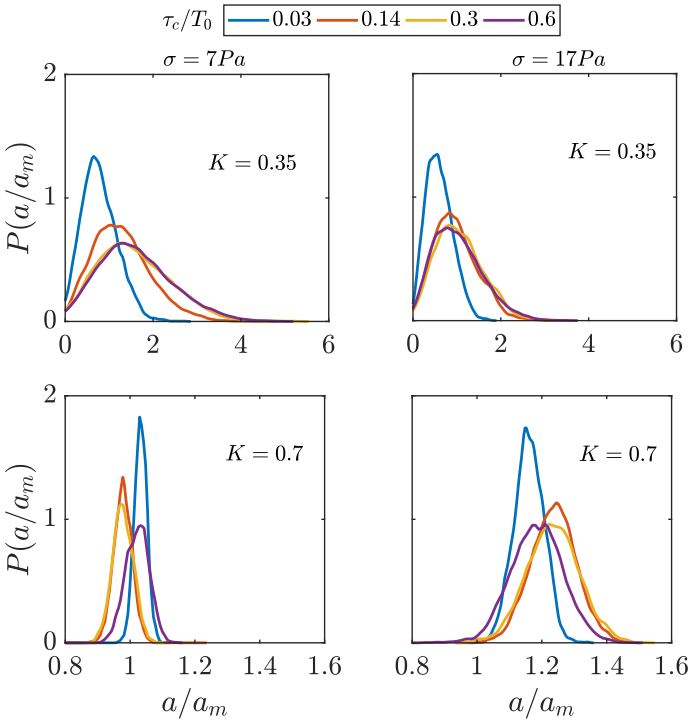

Figure 2.11: PDF distribution obtained from the Rijke tube simulator when driven by OU noise. The estimations are shown for $\Delta\omega/\omega_0 = 4.9$ at varied τ_c and σ.

limit cycle region, it can be seen that as the correlation time increases, the PDF becomes broader and the peak shifts towards the higher amplitude values for both the noise power. The shift in the peak values of PDF is small at higher correlation times ($\tau_c/T_0 \geq 0.14$) and the curves overlap each other. It can also be observed that the PDF also becomes broader with increasing noise powers leading to a decrease in the peak values. This variation of PDF distribution with τ_c and σ will affect the system identification and will lead to the deviation in the values of the estimated growth rates.

In the next step, using the theoretical expression of PDF for colored noise, $P_c(a_j)$, given by Eqn. (2.27), we further estimate the growth rates for the eigenmode by curve fitting the expression to the experimentally obtained PDF distribution from bandpass filtered data. Figure 2.12 presents the overview of the estimated growth rates for the colored noise driven Rijke tube simulator. From the contours, it can be observed that the deviation in the estimated values lies within the range of 0 % to 10 % upto $\sigma = 17Pa$. When the noise intensity, $\sigma > 17$Pa, the deviation in the estimated growth rates sharply increases from 10% to $\sim$ 30%. This can be explained through the PDF distribution curves shown in Fig. 2.11. With increasing noise intensities, the PDF becomes broader with peak values shifting towards higher values of amplitudes. As the noise intensity affects the distribution of PDF, therefore, the curve fit and hence growth rate estimation is also affected leading to higher deviation from the actual values. In order to explain the observed deviation in estimated growth rates at higher noise intensity, we studied the noise-induced response of the Rijke tube simulator in subthreshold region (discussed in subsequent section in detail). We observed the occurrence of coherence resonance [6, 47] in

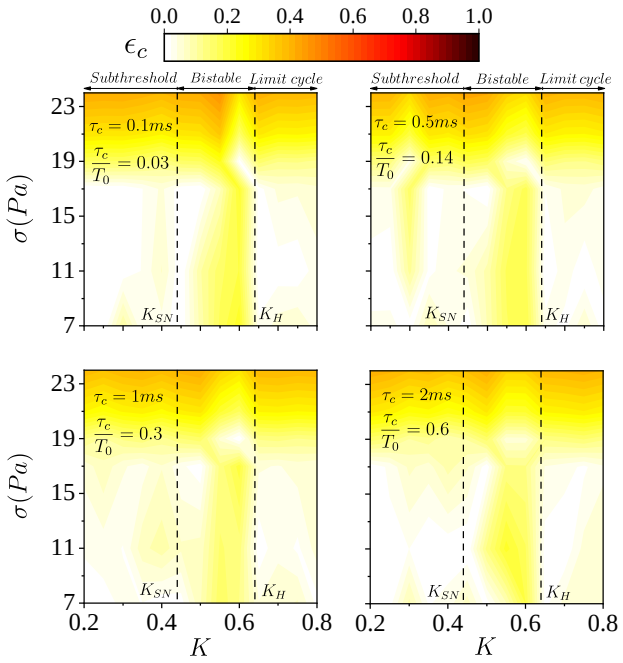

Figure 2.12: Map of the deviation in estimated growth rates as a function of noise intensity (σ) and control parameter (K) from the bandpass filtered data. The contours represent the relative deviation of the estimated growth rates from the true value, given as, $\epsilon = |(\nu_t - \nu_e)|/\nu_t$. ϵ_c indicates the estimation of deviation for OU noise.

the simulator and found that for K in the range of 0.2 to 0.4 and τ_c in the range of 0.1 ms to 10 ms, σ_{opt} at which peak coherence is induced lies within a range of 15 Pa to 30 Pa. This range of σ_{opt} is closer to the values of σ above which deviation in the estimated growth rates increases by 10 % to 20 % (Fig. 2.12). Therefore, we find that the noise intensities at which the deviation in estimated growth rates is high could be related to optimum noise intensities (σ_{opt}) at which the peak coherence is induced. Further, we can observe that the deviation in the estimated growth rates is more in the bistable region compared to the stable and unstable regions due to noise-induced triggering. If we compare the contours of right plot of Fig. 2.9 with those of Fig. 2.12, we can observe that the growth rate estimation is more accurate when the colored noise model is considered for a wider range of noise intensities.

We next investigate the influence of correlation times of the driving OU noise upon growth rate estimation. The deviation of the estimated growth rates from the true values are presented in form of a 2D map between τ_c and control parameter, K and is shown in Fig. 2.13. It can be observed from the contours that the deviation in the estimated growth rate values is in the range of 0 % to 15 % when the colored noise model is used for system identification compared to white-noise approximation, where the deviation lies within the range of 10 % to 20 %. The deviation, however, is higher in the bistable region than in the subthreshold and limit cycle regions. This could be because of the noise-induced triggering and noise-induced coherence resonance.

Summarizing, in case of the real systems, we acquire noisy pressure-time trace with no prior knowledge of the noise intensity or noise correlation time to which the system is subjected. In our study, we investigated the influence of two types of noise models: colored and white noise on growth rates estimation. We found that for a robust parameter identification, the following criteria must be taken into account: (i) pre-processing of the noisy data (applying bandpass filtering around the peak frequency); (ii) the regions of the Hopf bifurcation in which the estimation is done; (iii) using the colored noise model rather than white noise approximation for estimation; (iv) the influence of noise amplitudes on the estimated growth rates. In terms of practical implications of the study, the result that higher noise intensity can lead to inaccurate system identification is crucial to designing acoustic damping devices for the control of thermoacoustic instabilities. In particular, the deviations observed in the estimated

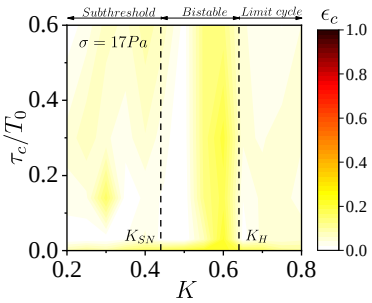

Figure 2.13: Map of the deviation in estimated growth rates as a function of correlation time (τ_c) and control parameter (K). The contours represent the relative deviation of the estimated growth rates from the true value, given as, $\epsilon = |(\nu_t - \nu_e)|/\nu_t$. $\tau_c = 0$ represents the white noise case. ϵ_c indicates the estimation of deviation for OU noise.

growth rate (or the decay rate) may lead to failure of decay-rate-based early warning indicators of thermoacoustic instabilities.

Therefore in the remainder of the Part I, we focus our investigation solely in the stable region, i.e., prior to the occurrence of the instability and investigate how changes in noise properties can affect the early warning prediction of thermoacoustic instability.

2.4 Noise-induced dynamics in subthreshold region

In this section, we first numerically investigate the influence of noise properties on coherence resonance. We then experimentally validate these results using the electroacoustic simulator (Fig. 2.4). Subsequently, we perform a multi-fractal analysis of the time series from the Rijke tube simulator to identify the effect of varying noise properties on measures of multi-fractality.

2.4.1 Effect of noise characteristics on coherence resonance

Noise induces coherent oscillations to appear in a stable oscillator prior to the Hopf bifurcation such that the relative contribution from coherent oscillations in system response (a) increases as the system is brought closer to bifurcation and (b) exhibits a resonance-like peak with increasing noise intensity. This phenomenon is known as coherence resonance (CR) [44,145] and is observed in several practical systems including thermoacoustic systems [2, 6, 95]. The noise intensity at which peak coherence is induced is the *optimum noise intensity* for CR. The phenomenon is known to be a result of nonlinear interaction between noise and the least stable mode (acoustic mode in case of thermoacoustic systems), which becomes unstable after Hopf bifurcation. The induced coherence is quantified conventionally in the form of a *coherence factor*, β, [45, 47] defined as the ratio of spectral peak height to the spectral quality factor and given as,

$$\beta = H_p \times \left(\frac{f_p}{\Delta f} \right) \tag{2.29}$$

where H_p and $f_p/\Delta f$ are the height and normalized width (normalized by the peak frequency) of a Lorentzian fit to the broad spectral peak; the width is measured at half the height of the peak of the fit as illustrated in Fig. 2.14(a).

Figure 2.14(b) presents the variation of the coherence factor against the white noise intensity for the Rijke tube system at three operating conditions (solid lines: numerical results, markers: experimental results). On the x-axis, we plot the white noise intensity within the band $\Delta\omega/\omega_0 = 4.9$, σ_b, normalized by the *optimum* noise intensity at $K = 0.40$. While on the y-axis, we plot the coherence factor (β) normalized by corresponding peak value at $K = 0.40$. The three curves correspond to control parameter $K = 0.40, 0.35$ and 0.30, all three lie in the subthreshold regime and are marked as A, B and C, respectively, in Fig. 2.2. We can observe from the plot that for each control parameter value, the induced coherent oscillations attain a peak at an optimum noise intensity which decreases as the control parameter approaches bifurcation (K increases). Furthermore, we also see that as the value of the control parameter, K, is increased towards the Hopf point, the induced coherence is higher, and the peak coherence (indicated

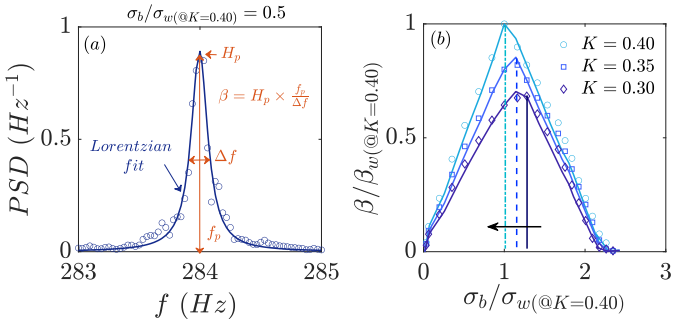

Figure 2.14: (a) An illustration for estimation of coherence factor, β from the power spectrum of noisy pressure-time series in the subthreshold regime. H_p represents the spectral peak, Δf represents the full width at half maximum, and f_p represents the peak frequency. The markers represent the simulation data while the solid black line is the Lorentzian fit to the data for estimation of β; (b) Variation of coherence factor, β, as a function of white noise intensity within $\Delta\omega/\omega_0 = 4.9$, σ_b, and control parameter, K. The solid lines represent the simulation results, whereas, the markers represent the experimental data. The x-axis and y-axis are normalized by the *optimum* white noise intensity (σ_w) and corresponding maximum coherence resonance at $K = 0.40$.

by dashed vertical lines) is induced at smaller values of noise intensity (shown by the arrow). This implies that as the system approaches its stability boundary, its noise-induced dynamics become more coherent and receptive to external noise. It can also be observed that the values of β increases as the system approaches the saddle-node point at most noise levels (except at very low ($\sigma_b/\sigma_w < 0.15$) and very high levels($\sigma_b/\sigma_w > 2$)).

Another early warning indicator directly associated with the phenomenon of CR is the autocorrelation function (ACF) with decaying amplitudes [44, 87, 94]. The coherence factor and the decay rates of ACF for a system undergoing subcritical Hopf bifurcation exhibits similar trend: the factors first increases with increase in noise levels, attains a peak at optimum noise level and then further decreases at higher noise levels. The optimum noise intensity at which both the coherence factor and the decay rate of ACF attains the peak is nearly same [94]. Besides, simple Rijke tube, the decay rates of the ACF are also employed in turbulent combustors as the early warning indicators [101]. As the system approaches the Hopf bifurcation ($K \to K_{SN}$), the coherence factor always increases which makes it an early warning indicator. Similar to the coherence factor, a consistent rise in the critical slowing down early warning indicators such as variance and cumulative number of tests for conditional heteroskedasticity is observed as the system approaches the subcritical Hopf bifurcation [87, 90]. Skewness and kurtosis [89] are another set of the precursors that could be approximately linked to the coherence factor. Skewness is a measure of the symmetric distribution of the data about its mean value. As the system approaches K_{SN}, the asymmetry of the fluctuations about the mean value increases because the probability distribution is more steeper on one side compared to the other in the vicinity of K_{SN} [146], which thereby increases the skewness. Similarly, kurtosis (k) is a measure of the tails of probability distribution which has a value of $k = 3$ for a normal distribution. In the vicinity of the Hopf bifurcation, $k > 3$ indicating a longer distribution with fat tails [89]. Thus, when background noise can be considered purely white, the coherence factor will always

increase as system is brought closer to bifurcation and related early warning indicators will exhibit monotonous trends. In case, noise intensity is varying simultaneously with changes in control parameter, the presence of an optimum noise intensity due to coherence resonance may cause deviation from monotonous trends in the coherence factor and other early warning indicators.

We show the effects of noise correlation time on the induced coherence and the optimum noise intensity and compare the findings with those obtained in Fig. 2.14(b) (when the combustion noise is white in nature). Figure 2.15 shows the variation of coherence factor with noise intensity obtained from numerical simulations for (i) $\Delta\omega/\omega_0 = 0.1$; (ii) $\Delta\omega/\omega_0 = 0.7$; (iii) $\Delta\omega/\omega_0 = 4.9$ for a constant control parameter, $K = 0.40$ (point A marked in Fig. 2.2). On the x-axis, we plot the noise intensity within the given band (σ_b) normalized by the *optimum* white noise intensity at $K = 0.40$. On the y-axis, we plot the coherence factor (β) normalized by peak β for white noise at $K = 0.40$. The hallmark of coherence resonance is clearly observed: β attains a peak value at intermediate noise levels. We observe that at $\Delta\omega/\omega_0 = 0.1$ (plot (a)), with increasing noise correlation time, the same level of β is achieved at all noise intensity (curves coincide). However, at $\Delta\omega/\omega_0 = 0.7$ and 4.9 (plots (b) and (c)), β depends on the noise intensity as well as noise color. The peak β occurs at higher noise levels with increasing correlation time. The variation of β with the bandwidth, $\Delta\omega/\omega_0$, is associated with variation in the spectral content of the signal as given in Fig. 2.3. When $\Delta\omega/\omega_0 = 0.1$, a nearly constant noise level at ω_0 is noted at all values of τ_c. Whereas when $\Delta\omega/\omega_0$ is higher (0.7 or 4.9), we observe a decrease of noise levels at ω_0 with increasing τ_c which alters the spectral content such that the peak coherence occurs at higher noise levels. The peak value of coherence factor (β_{peak}) is not affected by the noise correlation time.

This result for a constant value of the system control parameter shows that the coherence factor can change with noise color. Since it is quite likely that the correlation time of combustion noise varies while changing system control parameter, trends in coherence factor and other early warning indicators can get quite complicated; a general inference about the correlation between the proximity of the system to bifurcation (impending instability) and trends in coherence factor as well as other early warning indicators becomes elusive when system parameter and noise color

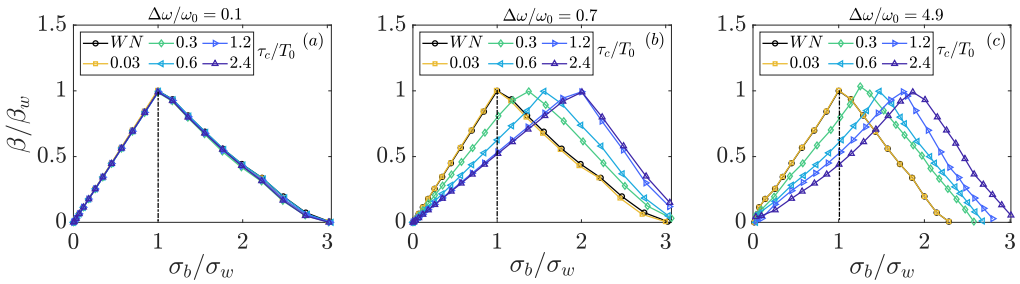

Figure 2.15: Variation of coherence factor (β) as a function of noise intensity within a given band (σ_b) and noise correlation time (τ_c) for (a) $\Delta\omega/\omega_0 = 0.1$; (b) $\Delta\omega/\omega_0 = 0.7$; (c) $\Delta\omega/\omega_0 = 4.9$ at $K = 0.40$. σ_w and β_w correspond to the *optimum* white noise intensity and corresponding maximum coherence resonance at specified control parameter values. WN represents the case when the combustion noise is modelled as the white noise.

vary simultaneously. We will elucidate this point further with data from experiments later in this section.

We further investigate the variation of β as a function of τ_c and K, while keeping a constant noise intensity within a given band corresponding to $\Delta\omega/\omega_0 = 0.1$, 0.7, and 4.9. Figure 2.16 shows 2D maps for the variation of β in the parameter space $\tau_c/T_0 - K$ for three noise intensities in numerical simulations: (a)-(c) $\sigma_b/\sigma_w = 0.57$, (d)-(f) $\sigma_b/\sigma_w = 1.57$, (g)-(i) $\sigma_b/\sigma_w = 2$ (divided as the three rows of the figure). At $\Delta\omega/\omega_0 = 0.1$ (plots (a), (d), and (g)), we observe that a change in τ_c does not significantly affect the β values for all K and σ_b/σ_w. This shows that for narrow bandwidth, the coherence factor is independent of the combustion noise model. Whereas, at $\Delta\omega/\omega_0 = 0.7$ (plots (b), (e) and (h)) and 4.9 (plots (c), (f), and (i)), we observe that β exhibits a strong dependence on τ_c, K and σ_b. At $\sigma_b/\sigma_w = 0.57$ (lower than the optimum noise intensity for white noise), β decreases monotonously with increase in τ_c for all K, with the sensitivity (how much β changes with variation in K) decreasing with increasing correlation time. At a higher intensity, $\sigma_b/\sigma_w = 1.57$, β shows a resonance-like behaviour with τ_c noise color: for a given K, β first increases sharply with increase in τ_c (till $\tau_c/T_0 \sim 0.6$ for $\Delta\omega/\omega_0 = 0.7$ and $\tau_c/T_0 \sim 1.2$ for $\Delta\omega/\omega_0 = 4.9$), attains a peak, and subsequently decreases with increase in τ_c. At an even higher intensity, $\sigma_b/\sigma_w = 2$, β increases monotonously with increase in τ_c for all K. However,

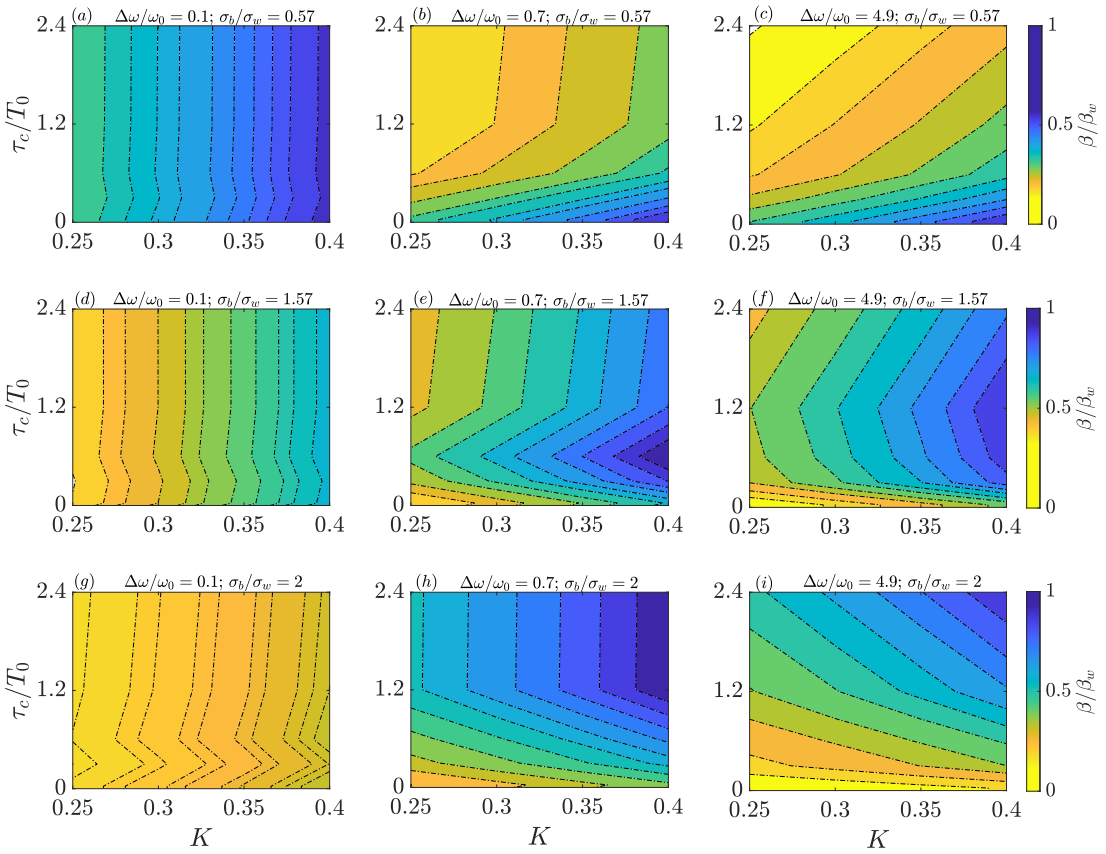

Figure 2.16: Variation of coherence factor (β) as a function of control parameter (K) and noise color (τ_c) for three noise intensities: (a)-(c) $\sigma_b/\sigma_w = 0.57$; (d)-(f) $\sigma_b/\sigma_w = 1.57$; (g)-(i) $\sigma_b/\sigma_w = 2$ for the three bandwidths: $\Delta\omega/\omega_0 = 0.1$; $\Delta\omega/\omega_0 = 0.7$; $\Delta\omega/\omega_0 = 4.9$ respectively. σ_w and β_w correspond to the *optimum* white noise intensity and corresponding maximum coherence resonance at specified control parameter values.

if the noise color and intensity can be considered constant, β is seen to increase as the system approaches thermoacoustic instability. This trend is true for combustion noise with any given correlation times. The coherence factor, therefore, indicates the approaching Hopf point when noise color and intensity do not change. The amount of increase in coherence factor, however, depends on noise intensity and color even if they do not vary and may need to be calibrated for an individual combustion system based on the characteristics of the background combustion noise for prediction purposes.

In the thermoacoustic community, Li et al. [105] have investigated the effects of noise correlation time and its intensity on the coherence factor analytically and numerically on a prototypical system (Van der Pol oscillator) undergoing the transition to thermoacoustic instability via a supercritical Hopf bifurcation. Li et al. [105] had noted two main trends: (i) the optimum noise intensity– which corresponds to peak coherence– exhibits linear dependence on τ_c: an increase in τ_c leads to an increase in the optimum noise intensity; and (ii) coherence factor decreases monotonously with increase in τ_c below a threshold noise level while it exhibits resonance-like behaviour above the threshold noise level such that the optimal τ_c increases as the system approaches the Hopf point. We can observe the same trends emerging from our findings in Fig. 2.15 and Fig. 2.16 at $\Delta\omega/\omega_0 = 0.7$ and 4.9. In addition, our results demonstrate that the threshold noise level (below which the β decreases monotonously) corresponds to low noise level cases where $\sigma_b/\sigma_w < 1$. We also find that the resonance-like behaviour of β with τ_c exists at intermediate noise levels where peak coherence is induced for some range of τ_c; whereas at high noise levels, β increases with τ_c.

To elucidate the effects of combustion noise correlation time on coherence factor in a practical

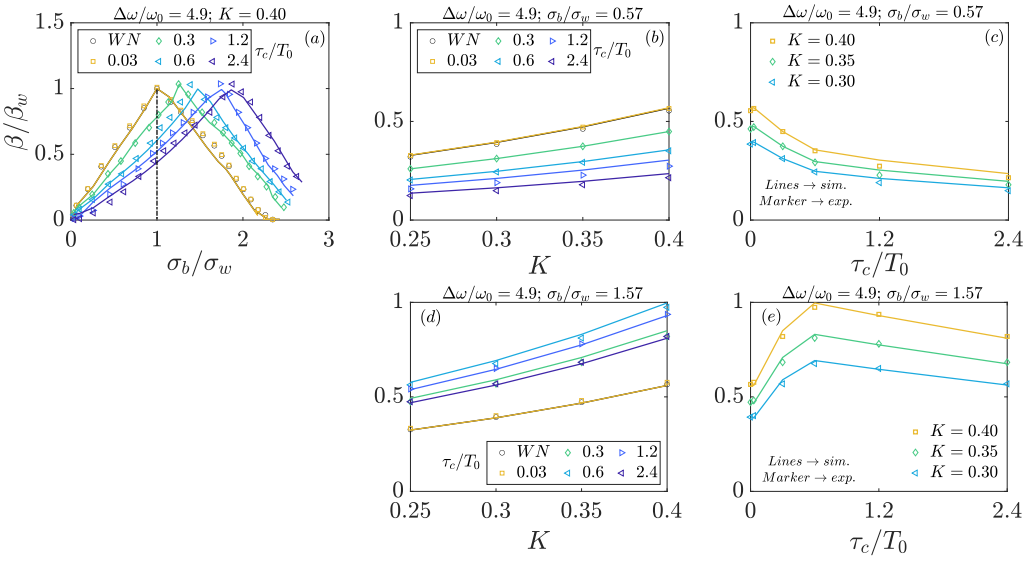

Figure 2.17: Comparison between numerical simulations and experiments: Variation of coherence factor (β) as a function of (a) noise intensity within a given band (σ_b) at $K = 0.40$; (b) and (d) control parameter (K) at $\sigma_b/\sigma_w = 0.57$ and $\sigma_b/\sigma_w = 1.57$ respectively; (c) and (e) noise color (τ_c) at $\sigma_b/\sigma_w = 0.57$ and $\sigma_b/\sigma_w = 1.57$ respectively for $\Delta\omega/\omega_0 = 4.9$. The solid lines represent the simulation results, whereas, the markers represent the experimental results. WN represents the case when the combustion noise is modelled as the white noise.

system, we further conduct experimental study using the electroacoustic Rijke tube simulator (Fig. 2.4) and validate our findings from the simulations. Figure 2.17 shows the comparative results from simulations (solid lines) and experiments (markers) for the variation of coherence factor with noise intensity, control parameter and noise correlation time at $\Delta\omega/\omega_0 = 4.9$. As can be observed from Fig. 2.17, experimental results present a good agreement with the simulations. Moreover, we can observe from Fig. 2.17(a) that with increase in noise correlation time (τ_c), the optimum noise intensity at which the induced oscillations are most coherent shifts to higher levels. Figure 2.17(b) and (d) shows that β increases as the system is brought closer to the saddle-node point for $\sigma_b/\sigma_w = 0.57$ and 1.57 respectively. Further, we observe that β decreases monotonously at $\sigma_b/\sigma_w = 0.57$ (Fig. 2.17(c)), whereas for $\sigma_b/\sigma_w = 1.57$ (Fig. 2.17(e)) the variation with correlation time is a bell-shaped curve. For $\sigma_b/\sigma_w \geq 2$, β increases monotonously with increase in τ_c (not shown here). Further, the good agreement between simulations and experiments also suggests that the noise coupling is not dependent on the mode (j). This observation is in line with Waugh and Juniper, [73]: they reported that similar results are obtained for the noisy Rijke tube oscillator regardless of whether noise is introduced at a location (they have chosen the location as same as the heater location) or introduced as additive noise to the modes. This implies that any change in the location of the noise source in the experiments will not affect affect the results and corresponding inferences.

2.4.2 Effect of noise characteristics on multi-fractality

Multi-fractal analysis of the noisy time-series acquired from a combustor is one of the recently reported strategy to identify precursors of thermoacoustic instability [96]. Two measures of multi-fractality analysis that act as the precursor to the impending instability as proposed by Nair et al. [96] are (i) generalized Hurst exponent (H_q) and (ii) multi-fractal spectrum width (D_h). For a multi-fractal signal, the values of generalized Hurst exponent (H_q) lie within the range of 0 to 1: a time series is said to have a long-range dependent structure (or correlated) when $0.5 < H_q < 1$ and an anti-correlated structure when $0 < H_q < 0.5$. For an uncorrelated time series (like Gaussian white noise), the Hurst exponent is 0.5. For the estimation of multi-fractal measures, we calculate the variation of the fluctuation function of the noisy time-series, F_w^q, at different time scales of measurement, w. We then estimate the slopes of F_w^q to obtain q-order H_q and q-order mass exponent (t_q). The reference, Gaussian white noise, exhibits a linear dependence of t_q with q, which gives a constant q-order singularity exponent, $h_q = 0.5$. In contrast, the multi-fractal time-series exhibits a non-linear variation of t_q with q. The resulting multi-fractal spectrum has a characteristic spectral width, calculated as the difference between the maximum and minimum h_q [147].

Figure 2.18 illustrates the estimations of H_q and D_h from the experiments on electroacoustic simulator when the combustion noise is modelled as the white Gaussian noise. Figure 2.18(a) presents the variation of F_w^q with w for $K = 0.25$ and $K = 0.40$ at $q = 2$ and $\Delta\omega/\omega_0 = 4.9$. The estimated generalized Hurst exponent H_q is presented in the plot (b) of Fig. 2.18 as a function of q-order. From the plot, we observe that the values of H_q lie in the range of 0 to 0.5 indicating that the time-series is anti-correlated. This implies that the time-series consists of high and low

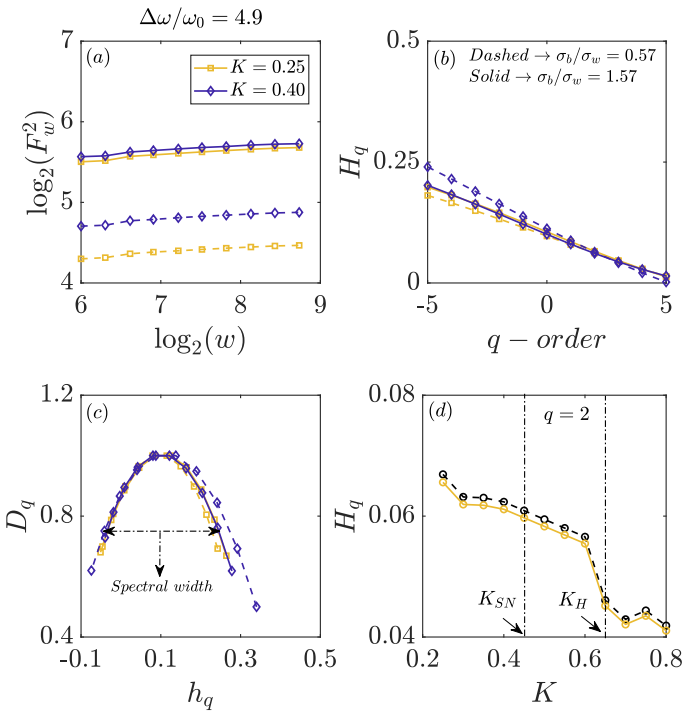

Figure 2.18: Combustion noise modelled as white noise: (a) Variation of F_w with window size (w) for $q = 2$. The slope of the various curves gives the generalized Hurst exponents (H_q) for that order, q; (b) q-order Hurst exponent (H_q) estimated in part (a); (c) Multi-fractal spectrum (D_q) at $K = 0.25$ and $K = 0.40$; (d) Variation of estimated H_q with K for $q = 2$. H_q decreases as the system are brought closer to the Hopf point. The estimations are shown for two noise intensities: $\sigma_b/\sigma_w = 0.57$ (dashed curves) and $\sigma_b/\sigma_w = 1.57$ (solid curves).

amplitude fluctuations in adjacent pairs. The high and low amplitude fluctuations in different time intervals (w) are preferentially selected by varying the order of the structure-function (q): a positive order ($q > 0$) selects high-amplitude fluctuations, whereas a negative order ($q < 0$) would select low-amplitude fluctuations. From Fig. 2.18(b), we observe that the values of H_q exhibit variations with q. This imply that the high and low amplitude fluctuations in the time series scale differently, which results in different values of H_q at different q. Hence, the time series from the simulator is multi-fractal in nature.

We now plot the multi-fractal spectrum for the time-series at $K = 0.25$ and $K = 0.40$ shown in plot (c) of Fig. 2.18. As can be seen from the plot, the multi-fractal spectrum is broadband. The width of the spectrum is expected to noticeably reduce as we approach instability. This loss of multi-fractality happens due to the predominance of a single time scale that dominates the dynamics after the onset of thermoacoustic instability. For a fractal signal, such a loss of scale variability is also known as a *loss of spectral reserve* [148]. Since this loss of spectral reserve happens gradually when the operating parameters are varied in a combustor, it acts as an early warning signal to an impending combustion instability. Next, we obtain the variation of the estimated H_q for $q = 2$ with the control parameter, K, shown in the plot (d) of Fig. 2.18. It can be observed from the plot that as the control parameter K is varied towards the Hopf point, the estimated H_q decreases gradually. Hence by estimating H_q, one can detect the system's

proximity to the thermoacoustically unstable conditions. Both these trends of H_q and D_q are consistent with the experimental studies [96].

We also investigate the effects of noise levels on the Hurst exponent and multi-fractal spectrum estimations. We find that the variations in the values of H_q lie within 0 % to 5 % at different noise levels. This can be seen in all the plots of Fig. 2.18. The dashed curves correspond to $\sigma_b/\sigma_w = 0.57$ while the solid curves represent the estimations at a noise level of $\sigma_b/\sigma_w = 1.57$. Hence, we conclude that noise levels do not significantly affect the estimations of multi-fractal measures.

A group of early warning indicators employed in turbulent combustors which could be related to the Hurst exponent are intermittency [101], permutation entropy of pressure and heat loss signals [109] and complexity-entropy causality plane (CECP) [106, 108, 110, 115]. In turbulent combustors, it is reported that a route to the thermoacoustic instability is via intermittency (an excursion of the system from low-amplitude fluctuations to high-amplitude oscillations in the stable region) [149]. The combustor loses its intermittent state upon the occurrence of the instability. Based on this fact, early warning indicators such as the recurrence rate (RR), time that a system spends in the intermittent state (τ_0) and Shannon entropy (s) of the time series (a measure of order in a system) are employed to predict the impending instability [98, 101]. Similar to the Hurst exponent, as the system approaches the Hopf bifurcation, the RR, τ_0 and s decreases and their value becomes close to 0 at the Hopf point [101]. The permutation entropy is a measure of the signal randomness based on permutation patterns of a time series [109]. A loss in permutation entropy of the pressure and heat loss signals indicate that the system is making a transition from a state of disorder (random) to a state of regularity (deterministic). Similar to the Hurst exponent, this loss in permutation entropy acts as the early warning measure in turbulent combustors. A more accurate early warning indicator based on the concept of entropy is CECP [106, 110, 115] (a combination of permutation entropy and Jensen-Shannon complexity). In the CECP plane, three zones corresponding to combustion noise, transition, and thermoacoustic instability are defined which are used to predict the instability [108]. Therefore, we speculate that the trends for the effects of correlation time variation on Hurst exponent can be used to infer approximately the behaviour of early warning indicators which decreases as the system approaches the instability.

We now investigate the effects of noise correlation time on the multi-fractality measures and compare the findings with those of white noise. We calculate the variation F_w^q with w, as a function of τ_c and obtain the q-order H_q and t_q. Figure 2.19 presents the results for the estimations at $K = 0.40$ for two bandwidths: $\Delta\omega/\omega_0 = 0.7$ (dashed curves) and $\Delta\omega/\omega_0 = 4.9$ (solid curves). When $\Delta\omega/\omega_0 = 0.1$, all the plots for varied correlation time collapse onto the white noise curve implying that at very narrow bandwidth, the H_q values are not affected by noise correlation time. When $\Delta\omega/\omega_0$ is higher (0.7 or 4.9), we observe that the slopes of F_w^q and hence estimated H_q varies with q and τ_c as shown in Fig. 2.19(a) and (b). For $q > 0$, the estimated q-order Hurst exponent lies within the range $0 < H_q < 0.5$ for all τ_c, indicating that the data is an anti-correlated fractal signal; whereas for $q < 0$, the H_q lies in the range of $0.5 < H_q < 1$ for $\tau_c/T_0 > 0.6$ indicating a change in anti-correlated nature of the signal for

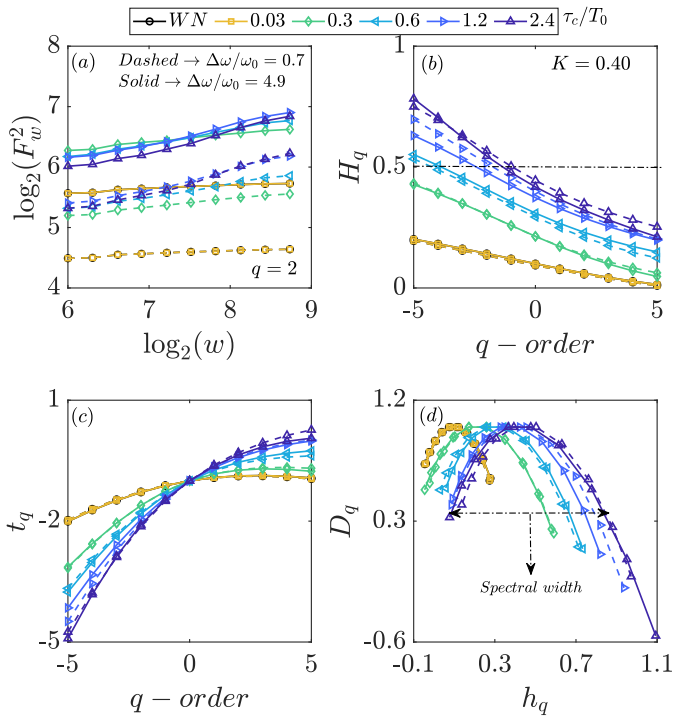

Figure 2.19: Combustion noise modelled as OU noise: (a) Variation of F_w with window size (w) for $q = 2$. The slope of the various curves gives the generalized Hurst exponents (H_q) for that order, q; (b) q-order Hurst exponent (H_q) estimated in part (a); (c) q-order mass component (t_q); (d) Multi-fractal spectrum (D_q) at $K = 0.40$. The estimations are shown for bandwidths: $\Delta\omega/\omega_0 = 0.7$ (dashed curves) and $\Delta\omega/\omega_0 = 4.9$ (solid curves). The dashed dot lines represent the Gaussian white noise.

low amplitude fluctuations. Figure 2.19(c) and (d) clearly shows the variation of t_q and D_q as a function of τ_c. The multi-fractal spectrum and its width exhibit variation with noise correlation time, τ_c: the longer the τ_c, the broader the spectrum width.

Figure 2.20 shows the variation of the estimated H_q with noise correlation time (τ_c) as a function of the control parameter K and q-order in the subthreshold region for two noise levels: (a)-(c) $\sigma_b/\sigma_w = 0.57$ and (d)-(f) $\sigma_b/\sigma_w = 1.57$. The estimations are shown for $\Delta\omega/\omega_0 = 4.9$. Figure 2.20(a) and (d) present a 2D map of the variation of H_q in the parameter space between τ_c - q-order at $K = 0.40$. We observe from the plots that for low amplitude fluctuations (i.e. $q < 0$), H_q values deviates as a function of τ_c when compared to the white noise. This deviation in the estimated H_q lies within a range of 0 % to 80 %; whereas for high amplitude fluctuations (i.e. $q > 0$), this deviation reduces and lies within a range of 0 % to 40 %. This implies that higher the noise correlation time, the higher would be the H_q for all K. When we consider a finite correlation time of combustion noise, we observe that H_q does not vary significantly as the system approaches the bifurcation point. This is illustrated in Fig. 2.20(b) and (e) where we plot a 2D map for the variation of H_q with K as a function of τ_c. We observe an almost flat curve of H_q instead of a gradual decrease as the system is brought closer to the saddle point ($K = 0.44$). This suggests that the noise correlation time affects the multi-fractal measures in such a way that H_q can no longer predict the impending instability. Recently, Waxenegger-Wilfing et al. [98]

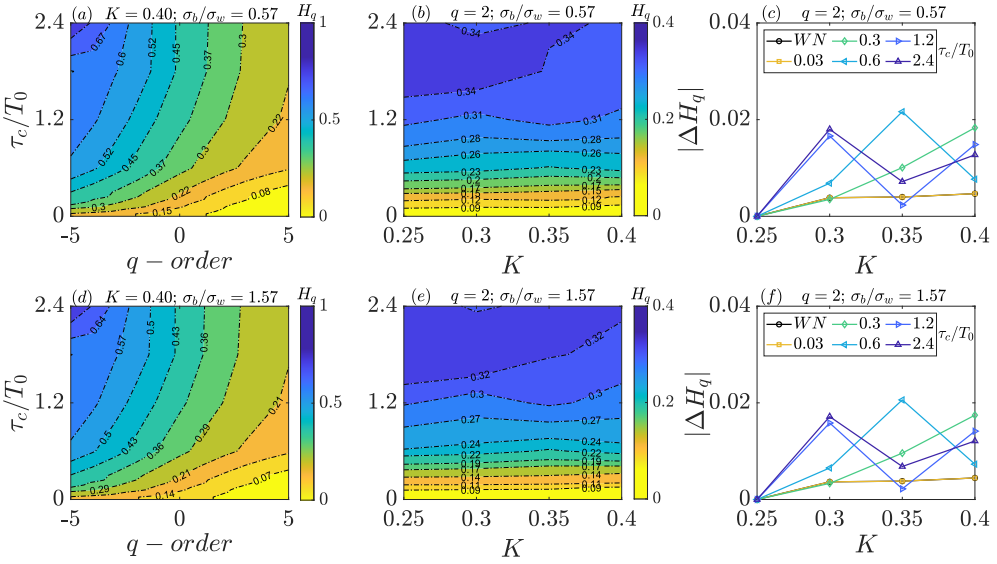

Figure 2.20: Effect of noise correlation time on H_q for two noise levels: (a)-(c) $\sigma_b/\sigma_w = 0.57$; (d)-(f) $\sigma_b/\sigma_w = 1.57$. (a), (d) Variation of q-order Hurst exponent, H_q with q-order and τ_c at $K = 0.40$; (b)-(c) and (e)-(f) Variation of estimated H_q with K and τ_c at for $q = 2$. The estimations are shown for $\Delta\omega/\omega_0 = 4.9$. $|\Delta H_q|$ represents the difference in H_q with K such that all the lines start from close to a point at $K = 0.25$.

have also showed that fluctuations in Hurst exponent to combustion noise in a rocket thrust chamber lead to false alarms and inaccurate predictions. We further plot the difference in H_q with K given as $|\Delta H_q|$ such that all the lines start from close to a point at $K = 0.25$ as shown in Fig. 2.20(c) and (f). We observe that when the combustion noise has zero correlation time (i.e. white in nature), $|\Delta H_q|$ increases with increase in K. This is expected as with increase in K (system $\rightarrow$ bifurcation point), H_q decreases thereby increasing the difference. If we now consider the curves corresponding to the finite correlation times of combustion noise, we observe that for $\tau_c/T_0 < 0.3$, the trends agree with those of white noise i.e. $|\Delta H_q|$ increases with increase in K. However, for longer correlation times, i.e. $\tau_c/T_0 > 0.3$, no such particular trend in the curves could be observed. For the electroacoustic simulator, $\tau_c/T_0 = 0.3$ correspond to the combustion noise with a correlation time of 1ms. Our results imply that the trends in multi-fractal measure such as Hurst exponent are highly sensitive to changes in noise color.

Thus, variation in the coherence factor, fractal measures, and other early warning indicators will not follow trends identified in thermoacoustic models with white noise. When noise color varies with operating parameters, trends in early warning indicators become non-monotonous and consequently, the EWIs become unreliable.

Chapter 3

Stochastic Modelling of Thermoacoustic Instability: Effect of Additive Correlated Noise Characteristics on Early Warning Prediction

3.1 Overview

A limitation of the Rijke tube model is that it exhibits instability only via subcritical Hopf bifurcation, whereas practical combustors also experience supercritical Hopf bifurcation. Therefore, it is essential to investigate the effects of noise in both types of systems. In this chapter, we present a detailed numerical investigation into the noise-induced dynamics of thermoacoustic coupling using stochastic Van der Pol oscillators (a reduced-order combustion dynamics model) that exhibit both supercritical and subcritical Hopf bifurcations. Motivated from the investigations on early warning prediction of thermoacoustic instability using electroacoustic Rijke tube simulator in Chapter 1, in this chapter, we elucidate a systematic assessment of application and limitations of different classes of early warning indicators (EWIs) as a function of noise color and intensity. We model the inherent (background/combustion) noise as an additive Ornstein-Uhlenbeck (OU) process. Specifically, we address the following questions: (i) how variations in noise characteristics influence the effectiveness of different classes of early warning indicators and (ii) which EWIs are most reliable considering that noise characteristics depend on the system and may even change with control parameters within a specific system. We investigate the various early warning indicators based on statistical measures (variance, skewness, and kurtosis), autocorrelation and spectral properties (coherence factor), multi-fractality (Hurst exponent and multi-fractal spectrum width), and time series complexity (permutation entropy and Jensen Shannon complexity). This investigation provides a comprehensive overview of the influence of additive noise characteristics on a wide range of early warning indicators, demonstrating their applicability across diverse fields.

The motivation for choosing the stochastic Van der Pol oscillator is that this model has been employed previously to model a wide range of real-world phenomena exhibiting bifurcations, such as those observed in power electronics [150], electrical engineering [151], neurology [152], biology [153], seismology [154], optics [155], and thermoacoustic instability in combustors [59, 61]. The stochastic Van der Pol oscillator has also been previously employed for understanding various nonlinear phenomena and synchronization effects such as stochastic P bifurcations [104, 127, 156], rate-tipping delay phenomenon and bifurcation dodging [123, 125], and stochastic/coherence resonance [47, 105, 157]. Therefore, with applications spanning across diverse fields of science and engineering, the stochastic Van der Pol oscillator serves as an ideal test case for understanding the interplay between system's deterministic dynamics and

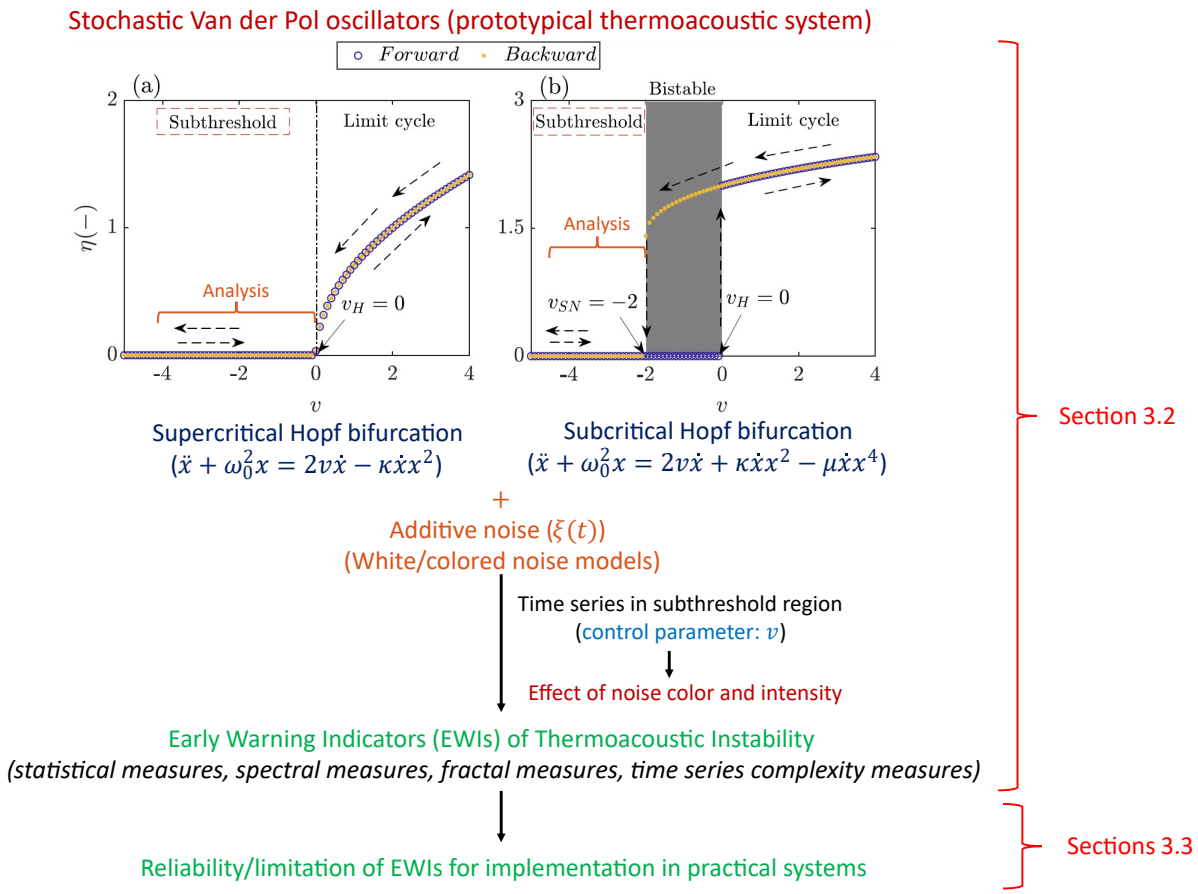

Figure 3.1: Visual summary of the contents for Chapter 3.

stochastic fluctuations (noise).

This chapter is further divided into two sections. Section 3.2 describes the mathematical model of stochastic Van der Pol oscillators and colored noise; validation of numerical simulations with analytical results and the methodology to estimate various EWIs. Section 3.3 shows the effects of correlated noise characteristics on the estimated EWIs and discuss their reliability when implemented in real systems. A brief overview of the summary for the contents of the chapter is shown in Fig. 3.1.

3.2 Model description and methodology

3.2.1 Stochastic classical Van der Pol oscillators

In this work, we employ the Van der Pol oscillator model, which is well-established for capturing the occurrence of thermoacoustic instability within combustion chambers. Van der Pol oscillator has been previously employed to study system identification [59, 61, 117], stochastic bifurcations [127], rate-tipping delay phenomenon [123, 125, 158] and noise-induced coherence resonance [2, 105]. The classical Van der Pol model describes a harmonic oscillator with linear feedback and

nonlinear damping given as [159],

$$\ddot{x} + \mu(x^2 - 1)\dot{x} + x = 0 \tag{3.1}$$

where, x represents the state of the system, $\mu \geq 0$ is the control parameter and $\mu(x^2-1)\dot{x}$ is the nonlinear damping term. This damping term acts like ordinary positive damping for $|x| > 1$, but like negative damping for $|x| < 1$. This classical Van der Pol oscillator system transitions to limit cycle oscillations via a supercritical Hopf bifurcation at $\mu = 0$.

We use the extended versions of the classical Van der Pol oscillator obtained by modifying the nonlinear damping term, which can exhibit both supercritical and subcritical Hopf bifurcations, given as [48, 160]

$$\ddot{x} + (\kappa x^2 - 2v)\dot{x} + \omega_0^2 x = 0 \tag{3.2}$$

for supercritical system, and

$$\ddot{x} + (\mu x^4 - \kappa x^2 - 2v)\dot{x} + \omega_0^2 x = 0 \tag{3.3}$$

for subcritical system. Here, v is the control parameter given as $v = (\beta^* - \alpha)/2$ in rad/sec, where α is the damping coefficient and β^* is the driving parameter. κ and μ are positive constants that define the nonlinear component of the oscillator response.

In this chapter, we investigate the noise-induced response of Van der Pol oscillators in the stable region. The corresponding stochastic differential equations for the two Van der Pol oscillators are given as [61],

$$\ddot{x} + (\kappa x^2 - 2v)\dot{x} + \omega_0^2 x = \xi(t) \tag{3.4}$$

$$\ddot{x} + (\mu x^4 - \kappa x^2 - 2v)\dot{x} + \omega_0^2 x = \xi(t) \tag{3.5}$$

where, $\xi(t)$ represents the additive noise.

The Van der Pol systems (Eqn. (3.4) and (3.5)) are numerically simulated using the fourth-order Runge-Kutta method for ODE and Euler-Maruyama method for $\xi(t)$ in Matlab. The detailed algorithm employed is given in Appendix B. We use the time step of $\mathrm{d}t = 0.0001$ s in the time span of $0 \leq t \leq 1000$ s. We choose the system parameters as $\omega_0/2\pi = 120$ s^{-1}, $\kappa = 8$ s^{-1} and $\mu = 2$ s^{-1} following Bonciolini et al. [61, 118]. For the analysis, we use data for the last 500 s. In the absence of noise, as the control parameter, v is varied from $v = -4$ to $v = 4$, the systems exhibit limit cycle oscillations via supercritical and subcritical Hopf bifurcations with the Hopf and saddle-node points observed at $v_H = 0$ and $v_{SN} = -2$ respectively, as shown in Fig. 3.2(a) and (c). The dashed arrows indicate the path the system follows as v is varied in forward (red markers) and backward (blue markers) direction. The region before the Hopf point in Fig. 3.2(a) and the saddle-node point in Fig. 3.2(c) is known as the stable (or *subthreshold* [48]) region. In case of the subcritical system, a bistable region is present for $-2 < v < 0$ where two stable states (focus and limit cycle oscillations) coexist (highlighted in grey in Fig. 3.2(c)). We have verified the numerical simulations by comparing the results for amplitude distribution with analytical solution. The associated derivation and results are shown in section 3.2.3.

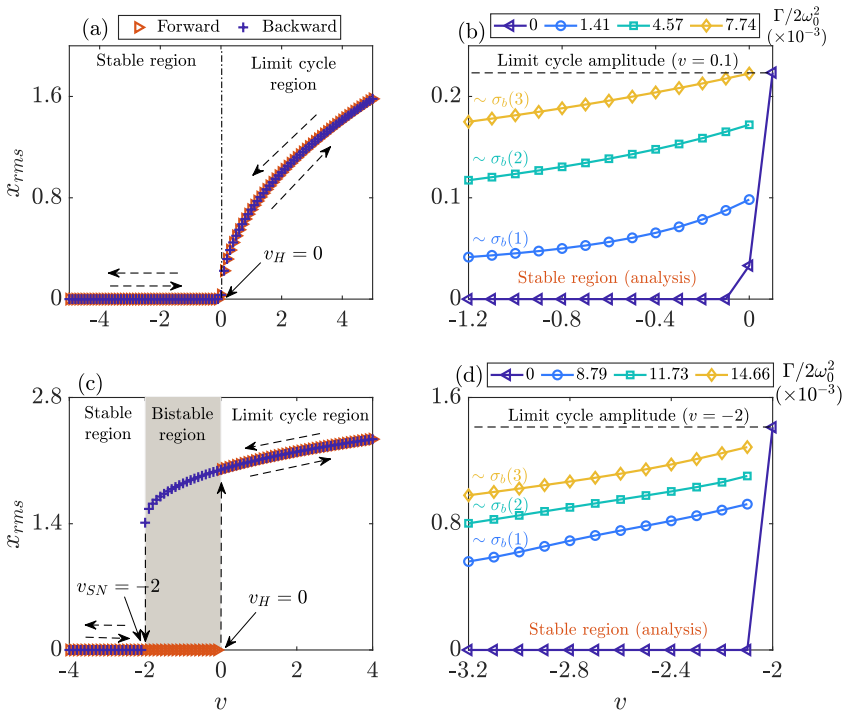

Figure 3.2: Bifurcation diagram for Van der Pol oscillators with v as the control parameter in the absence of noise: (a) supercritical Hopf bifurcation and (c) subcritical Hopf bifurcation. The dashed arrows indicate the path the system follows as v is varied in forward (red markers) and backward (blue markers) direction. The Hopf point in plots (a) and (c) and the saddle-node point in plot (c) are observed at $v = 0$ and $v = -2$, respectively. The grey area in plot (c) shows the bistable region ($-2 < v < 0$). The stable region is the area before the Hopf point in plot (a) and the saddle-node point in plot (c). Plots (b) and (d) show the system's response in the stable region when driven by white noise of intensity, Γ (normalized by eigenfrequency, $\omega_0 = 2\pi f_0$). The various EWIs are estimated in the stable region at $-1.2 \leq v \leq -0.2$ and $-3.2 \leq v \leq -2.2$ for supercritical and subcritical systems respectively.

3.2.2 Noise models

We first model $\xi(t)$ as the delta correlated white Gaussian noise of intensity Γ. Figure 3.2(b) and (d) shows the response of the two classical Van der Pol systems (Eqn. (3.4)-(3.5)) in the stable region when driven with white noise at three noise levels (low, intermediate and high). We can observe that as the system approaches the Hopf bifurcation, in the stable region, its amplitude (or response) increases for all noise intensities regardless of the nature of Hopf bifurcation. This noise-induced response of the system is responsible for changing certain parameters before the occurrence of the Hopf bifurcation, which are employed as the EWIs.

To investigate the effects of correlated noise characteristics on the system's response, we then model $\xi(t)$ as the Ornstein Uhlenbeck (OU) process which satisfies the following Langevin equation,

$$\dot{\xi}(t) = -\frac{1}{\tau_c}\xi(t) + \frac{\sqrt{D}}{\tau_c}\epsilon(t) \tag{3.6}$$

as described in section 2.2.2. We generate OU noise such that the powers provided by $\xi(t)$ and $\epsilon(t)$ in a band, $\Delta\omega = \omega_2 - \omega_1$, around the system's eigenfrequency—denoted by σ_b—are

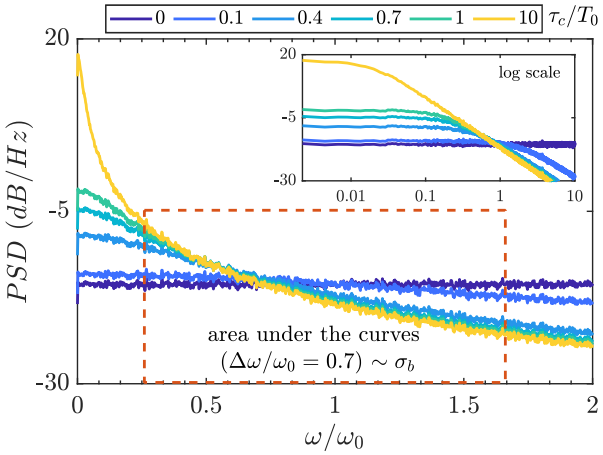

Figure 3.3: Power spectrum of white ($\tau_c/T_0 = 0$) and OU noise. The OU noise is generated such that the powers provided by $\xi(t)$ and $\epsilon(t)$ within $\Delta\omega/\omega_0 = 0.7$ are equal (area under the curve on a linear scale denoted by σ_b). τ_c is normalized by the time period of acoustic oscillations at Hopf point ($T_0 = 2\pi/\omega_0$). The inset plot show the same curves on log scale.

equal [61], i.e.,

$$\sigma_b = \int_{\omega_1}^{\omega_2} S_{\xi\xi} \mathrm{d}\omega = \int_{\omega_1}^{\omega_2} S_{\epsilon\epsilon} \mathrm{d}\omega \tag{3.7}$$

While employing this method for noise generation, the choice of bandwidth around the system's fundamental frequency plays a crucial role [61,161,162], as discussed in sections 2.3-2.4: a small bandwidth (e.g., $\Delta\omega/\omega_0 = 0.1$) may lead to loss of information from the time series, thereby failing to capture the effect of noise color on various EWIs (in this case, all the curves from colored noise cases will collapse on the white noise case). This effect of noise color variation can be observed more accurately with broader bandwidths, ranging from $\Delta\omega/\omega_0 = 0.4$ to 1.4. However, if the bandwidth is still narrower, for instance $\Delta\omega/\omega_0 = 0.4$, information loss can still occur, leading to underestimation of EWIs. We find that after $\Delta\omega/\omega_0 = 0.7$, the deviation in estimated EWIs becomes significantly less, hence, for the present study, we choose $\Delta\omega/\omega_0 = 0.7$. The corresponding power spectrum for white and OU noise are shown in Fig. 3.3. The noise correlation time, τ_c, is normalized by the time period of acoustic oscillations at Hopf point ($T_0 = 2\pi/\omega_0$). The range of the normalized noise correlation time chosen for the present work is 0 to 10. The various EWIs are estimated at three noise intensities: low $\sim \sigma_b(1)$), intermediate ($\sim \sigma_b(2)$) and high ($\sim \sigma_b(3)$), for which the systems' responses are shown in Figs. 3.2(b) and (d).

3.2.3 Validation of numerical simulations with analytical results

The stochastic classical Van der Pol oscillators (Eqn. (3.4)-(3.5)) can be re-written as,

$$\ddot{x} + \omega_0^2 x = f(x, \dot{x}) + \xi(t) \tag{3.8}$$

It is convenient to recast the Van der Pol model using amplitude-phase coordinates. This substitution is valid under the assumption of weakly amplified/damped systems [159], which

implies that $|v| \ll \omega_0$ and hence the right-hand side of the above equation is small compared to the left-hand side. Assuming,

$$x = A(t)\cos[\omega_0 t + \varphi(t)] = A(t)\cos\phi(t) \tag{3.9}$$

the amplitude-phase coordinates can be given as,

$$A = \sqrt{x^2 + (\dot{x}/\omega_0)^2} \tag{3.10}$$

$$\varphi = -\arctan\left(\frac{\dot{x}}{\omega_0 x}\right) - \omega_0 t \tag{3.11}$$

Taking the time derivative of Eqn. (3.10) and (3.11) and considering Eqn. (3.8), we obtain,

$$\begin{aligned} \dot{A} &= \overbrace{-\frac{\sin\phi}{\omega_j} f\left(A\cos\phi, -A\omega_j \sin\phi\right)}^{f_1(A,\phi)} \overbrace{-\frac{\sin\phi}{\omega_j}\xi}^{f_2(A\phi)}, \\ \dot{\varphi} &= \underbrace{-\frac{\cos\phi}{A\omega_j} f\left(A\cos\phi, -A\omega_j \sin\phi\right)}_{f_3(A,\phi)} \underbrace{-\frac{\cos\phi}{A\omega_j}\xi}_{f_4(A\phi)}. \end{aligned} \tag{3.12}$$

This is a generic expression that is valid for any nonlinear function f. Now considering the case of Van der Pol oscillators, for supercritical system

$$f(x, \dot{x}) = (2v - \kappa x^2)\dot{x} \tag{3.13}$$

and for subcritical system,

$$f(x, \dot{x}) = (2v + \kappa x^2 - \mu x^4)\dot{x} \tag{3.14}$$

Performing deterministic and stochastic averaging [56] for the two oscillators, yield the following stochastic differential equations (SDE) for the amplitude A,

$$\dot{A} = A\left(v - \frac{\kappa}{8}A^2\right) + \frac{\Gamma_e}{4\omega_0^2 A} + \zeta \tag{3.15}$$

$$\dot{A} = A\left(v + \frac{\kappa}{8}A^2 - \frac{\mu}{16}A^4\right) + \frac{\Gamma_e}{4\omega_0^2 A} + \zeta \tag{3.16}$$

where,

$$\langle \zeta\zeta_\tau \rangle = \frac{\delta(\tau)\pi S_{\xi\xi}(\omega_0)}{\omega_0^2} = \frac{\Gamma_e}{2\omega_0^2}\delta(\tau) \tag{3.17}$$

and

$$\Gamma_e = \Gamma \tag{3.18}$$

for white noise driven systems, while

$$\Gamma_e = \Gamma\frac{D}{1 + \omega_0^2\tau_c^2} \tag{3.19}$$

for OU noise driven systems.

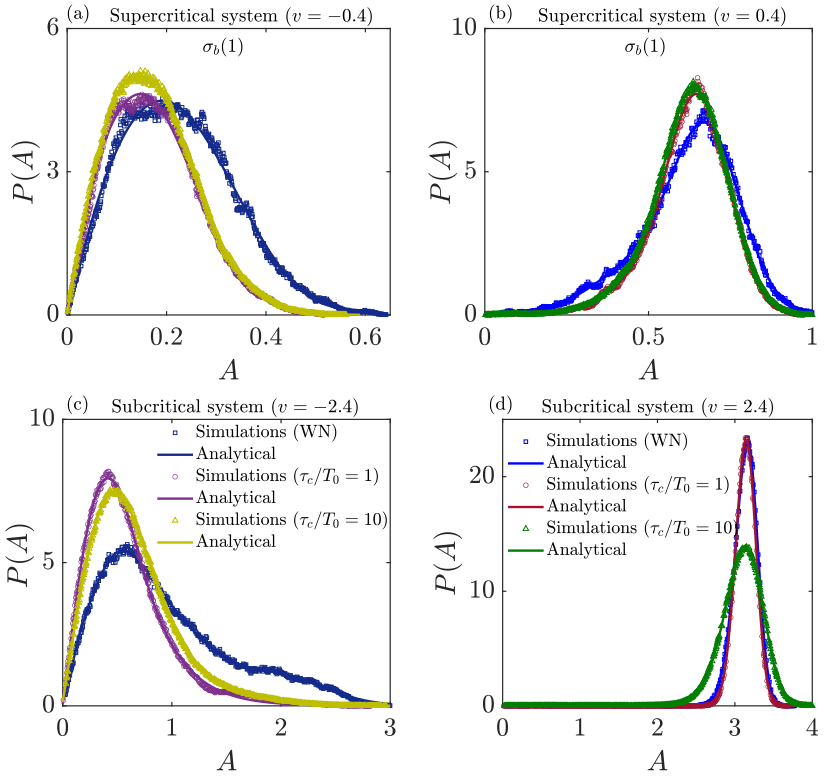

Figure 3.4: Comparison between numerical (markers) and analytical (lines) results for amplitude distribution supercritical (a,b) and subcritical (c,d) systems respectively in the stable (a,c) and limit cycle (b,d) regions.

The Eqn. (3.15) and (3.16) can be re-written as,

$$\begin{aligned} \dot{A} &= -\frac{\partial \mathscr{V}}{\partial A} + \zeta \\ -\frac{\partial \mathscr{V}}{\partial A} &= \mathscr{F}(A) \end{aligned} \tag{3.20}$$

where, $\mathscr{V}(A)$ is the potential governing the amplitude dynamics. We now compute the Fokker Planck equation [54] associated with the amplitude equation as,

$$\frac{\partial}{\partial t}P(A,t) = -\frac{\partial}{\partial A}[\mathscr{F}(A)P(A,t)] + \frac{\Gamma_e}{4\omega_0^2}\frac{\partial^2}{\partial A^2}P(A,t) \tag{3.21}$$

Considering that when $A \to \infty$, the probability density vanishes, we can write that the stationary probability density of the acoustic envelope is solution of the following equation,

$$\frac{d}{dA}P(A) - \frac{4\omega_0^2}{\Gamma_e}\mathscr{F}(A)P(A) = 0 \tag{3.22}$$

The analytical solution for stationary probability density can be then computed as,

$$P(A) = \mathscr{N} \exp\left(-\frac{4\omega_0^2}{\Gamma_e}\mathscr{V}(A)\right) \tag{3.23}$$

For supercritical system

$$\mathscr{V}(A) = -\frac{v}{2}A^2 + \frac{\kappa}{32}A^4 - \frac{\Gamma_e}{4\omega_0^2}\ln A \tag{3.24}$$

and for subcritical system

$$\mathscr{V}(A) = -\frac{v}{2}A^2 - \frac{\kappa}{32}A^4 + \frac{\mu}{96}A^6 - \frac{\Gamma_e}{4\omega_0^2}\ln A \tag{3.25}$$

where, $\mathscr{N}$ is the normalization constant given as $\int_0^\infty P(A)dA = 1$.
To verify the numerical simulations, Fig. 3.4 shows the comparison between the amplitude distribution from simulations (markers) and analytical expression (lines) given by Eqn. (3.23)-(3.25) for the two Van der Pol systems in stable and limit cycle regions when driven by both white and OU noise. We can observe good agreement between simulations and analytical results which provides confidence in the simulations performed in the present work.

3.2.4 Methodology

In this section, we present the methodology to estimate the various early warning indicators (EWIs) from the noisy time-series obtained from stochastic Van der Pol oscillator systems in the stable region. We investigate the EWIs based on statistics (variance, skewness and kurtosis), autocorrelation function (decay rate), spectral properties (coherence factor), multi-fractality (Hurst exponent and spectral width) and entropy/complexity measures.

3.2.4.1 Variance

Variance (V) is the expectation value of the squared deviation of the system variable from its mean. It indicates how the data is spread from the mean value and is the second moment of the distribution given as [163],

$$V = \frac{1}{N}\sum_{i=1}^{N}(x_i - \bar{x})^2 \tag{3.26}$$

where, x_i is the time-series data, N is the number of data points and $\bar{x}$ is the mean of x calculated as, $\bar{x} = \frac{1}{N}\sum_{i=1}^{N} x_i$. Variance is reported to increase as the system approaches the Hopf bifurcation (or critical transition) [87, 146].

3.2.4.2 Skewness

Skewness (S) is the measure of the asymmetric probability distribution of system variable about its mean value. The skewness can be positive, negative or zero and is defined as the third moment of the distribution given as [163],

$$S = \frac{\frac{1}{N}\sum_{i=1}^{N}(x_i - \bar{x})^3}{\left[\sqrt{\frac{1}{N}\sum_{i=1}^{N}(x_i - \bar{x})^2}\right]^3} \tag{3.27}$$

where, N is the number of data points and $\bar{x}$ is the mean of x_i. For a normal distribution, $S = 0$, which indicates that the probability distribution of the system variable is symmetric

about its mean. The probability distribution is negatively skewed when the left tail is longer than the right tail, while it is positively skewed when the right tail is longer than the left. It is reported that the probability distribution becomes asymmetric near the Hopf bifurcation, leading to either monotonous rise [89] or decrease in skewness [80, 92].

3.2.4.3 Kurtosis

Kurtosis (k) is the measure of the tailedness in the probability distribution of the system variable and is defined as the fourth moment of the distribution given as [163],

$$k = \frac{\frac{1}{N}\sum_{i=1}^{N}(x_i - \bar{x})^4}{\left[\sqrt{\frac{1}{N}\sum_{i=1}^{N}(x_i - \bar{x})^2}\right]^4} \tag{3.28}$$

Kurtosis is said to be mesokurtic (medium-tailed) when $k = 3$ (e.g., normal distribution), platykurtic (thin-tailed) when $k < 3$ (e.g., Bernoulli distribution) and leptokurtic (fat-tailed or super-Gaussian) when $k > 3$ (e.g., Rayleigh or Laplace distribution) [91]. In the vicinity of the Hopf bifurcation (or critical transition), the probability distribution is reported to become more leptokurtic or platykurtic [89, 91].

3.2.4.4 Autocorrelation function

Autocorrelation is a measure of the correlation between the data points in a time series that are some time steps apart (also called as time-lag). Autocorrelation at any lag is estimated using the following expression [164],

$$AC = \frac{E\left[(x_{t_1} - \bar{x})(x_{t_2} - \bar{x})\right]}{V} \tag{3.29}$$

where, x_{t_1} and x_{t_2} represents the data value at time t_1 and t_2, $\bar{x}$ is the mean of x_i and V is the variance of x_i estimated by Eqn. (3.26). The autocorrelation function (ACF) is obtained as the sequence of AC as a function of time lags. The decay rate (α) of ACF can then be estimated by fitting an exponential decay over the magnitude of its Hilbert transform. As the system approaches the Hopf bifurcation (or critical transition), it is reported that the decay rates of ACF becomes increasingly smaller in magnitude [86, 146].

3.2.4.5 Coherence factor

In the stable region, noise induces random bursts of periodic oscillations such that the coherence in the time trace is maximum at an intermediate level of noise intensity [47]. This phenomenon is known as coherence resonance (CR) and has been shown to occur in systems undergoing supercritical and subcritical Hopf bifurcation [2, 6, 47]. The phenomenon of CR arises from the interaction between noise and the least stable eigenmodes of a system, which becomes unstable after Hopf bifurcation [2]. Noise-induced coherence in a system can be quantified by the coherence factor (β) [6,47], defined as the ratio of spectral peak height to the spectral quality

factor and given as,

$$\beta = H_p \times \left(\frac{f_p}{\Delta f} \right) \tag{3.30}$$

where H_p and $f_p/\Delta f$ represent the height and normalized width of a Lorentzian fit to the broad spectral peak; the width is measured at half the height of the peak of the fit. It is reported that for a constant noise intensity, β always increases as the system approaches the Hopf bifurcation (or critical transition) [2, 6].

3.2.4.6 Fractal measures

Multi-fractal Detrended Fluctuation Analysis (MFDFA) [165] is performed to study the fractal signature of the noisy time series. In this analysis, we first obtain a mean subtracted deviate of noisy time series as,

$$Y(N) = \sum_{t=1}^{N} (x_t - \bar{x}) \tag{3.31}$$

where, x_t is the time series and $\bar{x}$ is its mean. We then divide the deviate series, $Y(N)$, into n_w non-overlapping windows (segments) of size w. We then subtract a polynomial fit of order m from the profile of each window (also known as detrending). The choice of polynomial order m for detrending is important for the accurate estimation of the Hurst exponent. The Hurst exponent is sensitive to the trend removal method, making the selection of an appropriate m essential. Using a lower order m, such as $m = 1$ (linear detrending) or $m = 2$ (quadratic detrending), can lead to significant errors by underestimating the trend. This underestimation fails to capture the data's complexity, resulting in systematic deviations. These deviations artificially lower the root mean square (RMS) of the fluctuations, leading to inaccurate Hurst exponent values. Conversely, a higher order m introduces a more complex trend shape, which might seem beneficial but can cause overfitting, particularly for time series with small segment sizes. Overfitting occurs when the polynomial trend mimics the noise in the data, reducing the fluctuations to nearly zero. This distortion makes the time series appear smoother than it is, skewing the Hurst exponent calculation. To prevent these issues, it is crucial that the smallest segment size (i.e., scale) is much larger than the polynomial order m. A practical guideline is that the segment size w should be at least $w \geq m + 2$. This ensures that the polynomial trend does not overly conform to short-term variations in the data, preserving the integrity of the fluctuation function used for Hurst exponent estimation. For the smallest segment sizes containing $10 - 20$ samples, an appropriate choice of m is typically between 1 and 3. This range is supported by Ihlen et al. [147], who suggest that a lower-order polynomial is sufficient to capture the main trend without overfitting for short time series. It is important to note that the choice of m affects only the quantitative values, while the trends in the Hurst exponent remain unaffected. In this study, we found that $m = 3$ provided a good balance, effectively removing the trend while maintaining the statistical properties of the fluctuations. We then compute a q-order RMS for each window to capture the magnitude of the local fluctuations in the signal

and obtain a q-order fluctuation function as [165],

$$F_w^q = \left[\frac{1}{n_w} \sum_{i=1}^{n_w} \left(\sqrt{\frac{1}{w} \sum_{t=1}^{w} (y_i(t) - \bar{y}_i)^2} \right)^q \right]^{1/q} \tag{3.32}$$

F_w^q is plotted as a function of scale, w, for different q-orders in a log-log plot; the slope of which gives a generalized q-order Hurst exponent (H_q). In general, the value of H_q lies within the range of 0 to 1. A time series will have a correlated structure when $0.5 < H_q < 1$ and an anti-correlated structure when $0 < H_q < 0.5$. The white Gaussian noise has an uncorrelated structure for which $H_q = 0.5$. If the time series is multi-fractal, then H_q will vary with q, and this variation can be manifested in the form of a multi-fractal spectrum (D_q) which will have a characteristic spectral width (w_D) [147]. In this work, we estimate the Hurst exponent at $q = 2$ (H^2 or H) which scales the rms of the standard deviation of fluctuations with the length of the data. As the system approaches the Hopf bifurcation (or critical transition), both H and w_D are reported to reduce and become close to zero [89, 96].

3.2.4.7 Permutation entropy

Permutation entropy (PE) is a measure of randomness in a time series. We employ the algorithm proposed by Bandt and Pompe [114] for the estimation of PE from the noisy time series. In this algorithm, we first identify the embedding dimension, d_E, which represents the number of data points in each vector required for analysis. We then choose a time delay, τ_{dE}, which represents the spacing between the data points in each vector. The time delay determines the sensitivity to patterns over different time scales. We then construct a d_E dimensional embedded vectors by selecting data points at regular intervals based on the chosen τ_{dE}, for e.g., for a time series $x(t)$, the embedded vector at time t would be $(x(t), x(t + \tau_{dE}), x(t + 2\tau_{dE}), ..., x(t + (d_E - 1)\tau_{dE}))$. For each d_E length vector in the time series, we create a permutation (rearrangement of the data points) of its elements. We then calculate all possible permutations (π) for the chosen d_E. For each vector in the time series, we then count the number of times each permutation appear ($q(\pi)$) and keep track for each unique permutation. We then determine the relative frequency of each permutation ($p(\pi)$) by dividing its count ($q(\pi)$) by the total number of d_E length vectors, which is represented as, $N - d_E + 1$, where N is the total number of data points. The permutation entropy (PE) can be then computed using [114],

$$PE = -\sum_{\pi} p(\pi) \log_2 p(\pi) \tag{3.33}$$

We can estimate the normalized permutation entropy by dividing the calculated PE by the maximum possible permutation entropy ($PE(max.)$) for the given embedding dimension (d_E) as, $PE' = PE/(\log_2(d_E)!)$. The maximum PE estimate occurs when the time series contains the most complex and random patterns for the given d_E. The value of PE' lies in the range of $0 - 1$. A high value of PE' indicates complex dynamics, while PE' close to zero indicates a periodic signal [166]. It is important to select appropriate value of d_E and τ_{dE} to effectively

show the dynamics of a system. In literature [114, 167, 168], detailed investigations have been shown on varied dynamical systems to provide the acceptable ranges for d_E and τ_{dE}. d_E should be chosen such that $N \gg d_E!$. In general, the studies have reported that for any practical system, $3 \leq d_E \leq 7$ and $\tau_{dE} = 1$ would be most suitable. Figure 3.5 shows the variation of the estimated PE' with the embedding dimension, d_E, at $v = -2.2$. We find that, for a fixed noise color and intensity, PE' decreases with increase in the embdedding dimension. This trend concurs with the previous studies of acoustic emission by an anomalous discharge in a plasma system [169], flame front instability induced by radiative heat loss [170] and prediction of combustion instability in gas turbine combustors [109]. For the present analysis, we choose $d_E = 5$ and $\tau = 1$, as null hypotheses can be accepted by a two-sided t-test for PE' at 5% reliability [109, 114]. The normalized permutation entropy is reported to decrease as the system approaches the Hopf bifurcation (or critical transition) [108, 109, 171].

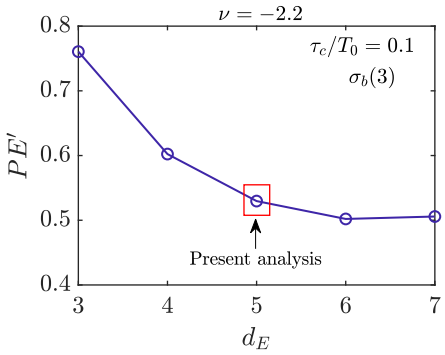

Figure 3.5: Noisy system: variation of permutation entropy (PE') as a function of the embedding dimension (D) at $v = -2.2$ for subthreshold Van der Pol system.

3.2.4.8 Jensen-Shannon complexity

The Jensen-Shannon complexity is a measure that quantifies the complexity of a probability distribution. It is derived from the Jensen-Shannon divergence, a symmetric and smoothed version of the Kullback-Leibler divergence, which is used to measure the difference between two probability distributions [172]. To estimate Jensen-Shannon complexity, first we need to represent the data as probability distribution (P). This distribution can be represented as a vector of probabilities, where each element corresponds to the probability of a particular outcome occurring (Q which represents the uniform distribution whose every element is $1/(d_E)!$, where d_E is the embedding dimension [114]). We then compute the average distribution by taking the weighted average of two probability distributions, P and Q. We compute Jensen-Shannon divergence using,

$$JSD\,[P,Q] = \frac{PE'\left[\frac{P+Q}{2}\right] - \frac{PE'[P]}{2} - \frac{PE'[Q]}{2}}{JSD_{\max.}} \tag{3.34}$$

where

$$JSD_{\max.} = -\frac{1}{2}\left[\frac{d_E!+1}{d_E!}\log(d_E!+1) - 2\log 2d_E! \quad + \log d_E!\right] \tag{3.35}$$

$JSD(P,Q)$ can then be used as the measure of the complexity by quantifying the differences/similarities between P and Q as,

$$C_P = JSD(P,Q)PE'(P) \tag{3.36}$$

A higher value of C_P indicates greater algorithmic complexity between the two distributions. Jensen-Shannon complexity is reported to increase as the system approaches the Hopf bifurcation (or critical transition) [108].
A summary of the relationship between each measure and their phenomenon to serve as an early warning indicator is tabulated in Table 3.1.

Table 3.1: Types of early warning measures along with their trend (consistent increase or decrease as the system approach the critical transition) to serve as EWIs to predict the approaching critical transition.

EWI class	EWI	Trend	
		Increase	Decrease
Statistical measures	Variance (V)	✓	
	Skewness (S)	✓	✓
	Kurtosis (k)	✓	✓
Spectral measures	ACF (α)	✓	
	Coherence factor (β)	✓	
Fractal measures	Hurst exponent (H)		✓
	Multi-fractal spectrum width (w_D)		✓
Entropy/complexity measures	Permutation entropy (PE')		✓
	Jensen-Shannon complexity (C_P)	✓	

3.3 Effect of additive noise characteristics on early warning indicators

In this section, we discuss the effects of noise color and intensity on the various EWIs (estimated in the stable region) for both supercritical and subcritical Van der Pol systems.
The results corresponding to each EWI are presented as 2D contour maps in the parameter space (τ_c – v) at three noise intensities: $\sigma_b(1)$ (column 1), $\sigma_b(2)$ (column 2) and $\sigma_b(3)$ (column 3). The Hopf and saddle-node points occur at $v_H = 0$ and $v_{SN} = -2$ respectively. To illustrate whether the variation in an EWI is more sensitive to changes in noise color or control parameter, vertical and horizontal arrows are provided in each plot respectively. In each plot, a 4x4 grid (16 points in τ_c – v) is chosen, and the arrows are placed at those 16 points.
Figure 3.6 illustrates the effect of control parameter (v), noise color (τ_c/T_0) and intensity (σ_b) on variance for both supercritical (plots (a)-(c)) and subcritical (plots (d)-(f)) Van der Pol

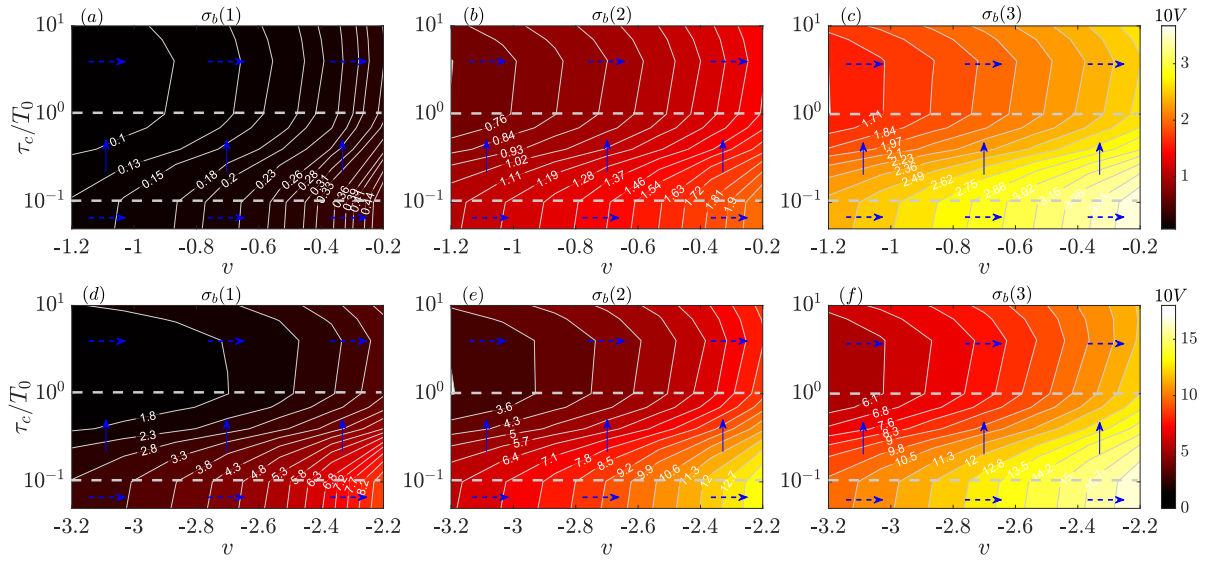

Figure 3.6: 2D contour map of variance (V) as the control parameter (v) and noise correlation time (τ_c/T_0) are varied at three noise intensities ($\sigma_b(1)$ (a, d), $\sigma_b(2)$ (b, e) and $\sigma_b(3)$ (c, f)) for supercritical (a)-(c) and subcritical (d)-(f) Van der Pol systems. The dashed grey lines separate the plots into categories of low, moderate, and high noise correlation times. The arrows roughly indicate whether the variation in V is greater in the direction of control parameter (dashed) or in the direction of noise correlation time (solid).

systems. The dashed grey lines separate the plots into categories of low ($\tau_c/T_0 \leq 0.1$), moderate ($0.1 < \tau_c/T_0 \leq 1$), and high ($\tau_c/T_0 > 1$) noise correlation times. We observe that, for a fixed noise intensity and control parameter, V decreases with increase in noise color up to $\tau_c/T_0 = 1$ and then becomes relatively constant. We observe that V increases monotonously with increase in control parameter at all noise correlation times and noise intensities. However, when noise color spans the range 0.1 to 1, variance is more sensitive to changes in noise color than changes in control parameter value. This could result in a non-monotonous behaviour of variance in practical systems, where noise color is expected to change with change in control parameter. Therefore, variance can be employed as an effective early warning indicator, either at very small noise correlation times, i.e. $\sim$ white noise or very large correlation times ($\tau_c/T_0 > 1$) (shown by the dashed blue arrows). We also observe that variance increases with increase in noise intensity for each noise color and control parameter. These observed trends for variance are qualitatively similar in both the Van der Pol systems.

Figure 3.7 shows the variation of skewness (S) with v, τ_c/T_0 and σ_b for the two Van der Pol systems. In case of supercritical system (Figs. 3.7(a)-(c)), we observe that, for each v, skewness decreases with increase in noise color. When noise color is kept constant, skewness exhibits an oscillatory behaviour at $\sigma_b(1)$, while decreases consistently at $\sigma_b(2)$ and $\sigma_b(3)$, as the control parameter is increased towards the Hopf point. In case of subcritical system (Figs. 3.7(d)-(f)), for each v, skewness increases with increase in noise color at $\sigma_b(1)$. Whereas, at $\sigma_b(2)$ and $\sigma_b(3)$, skewness increases with increase in noise color for $v < -2.5$ while it decreases for $-2.5 < v < -2$. Near the saddle-node point, for all $\tau_c/T_0 > 4$, we observe that skewness increases at low noise intensity while it decreases at intermediate and high intensities.

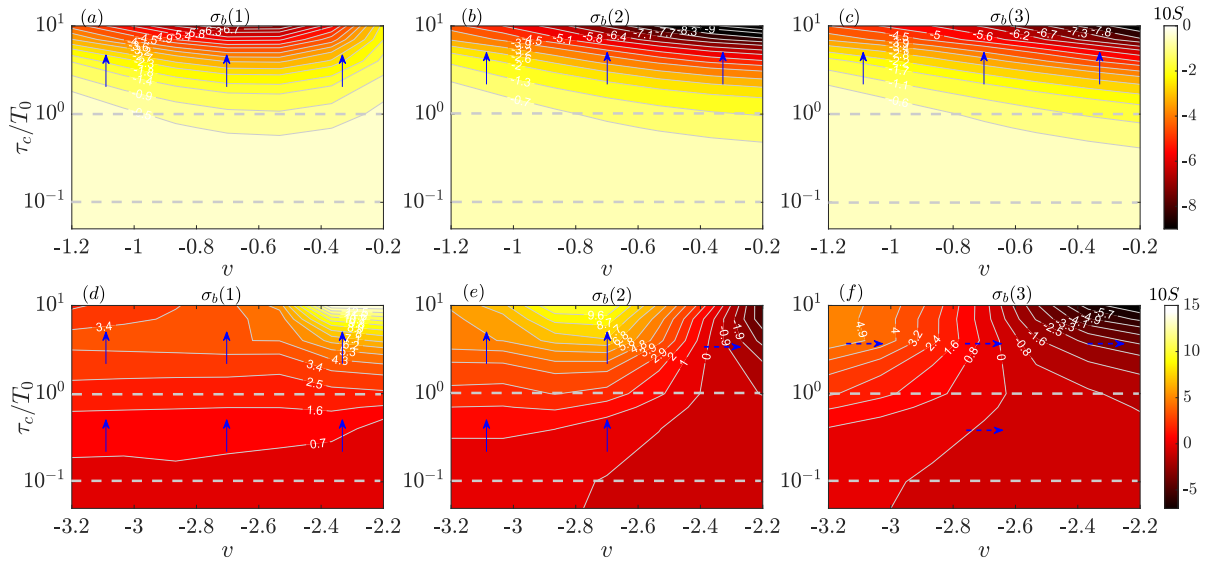

Figure 3.7: 2D contour map of skewness (S) as the control parameter (v) and noise correlation time (τ_c/T_0) are varied at three noise intensities ($\sigma_b(1)$ (a, d), $\sigma_b(2)$ (b, e) and $\sigma_b(3)$ (c, f)) for supercritical (a)-(c) and subcritical (d)-(f) Van der Pol systems. The dashed grey lines separate the plots into categories of low, moderate, and high noise correlation times. The arrows roughly indicate whether the variation in S is greater in the direction of control parameter (dashed) or in the direction of noise correlation time (solid).

In both systems (Fig. 3.7), the primary factor driving changes in skewness is the variation in noise color rather than the control parameter, except close to the saddle-node point at large correlation times and moderate to high noise intensities in subcritical system, as highlighted by the blue dashed arrows. Hence skewness is not suitable as an early warning indicator for practical systems.

Figure 3.8 shows the variation of kurtosis (k) with v, τ_c/T_0 and σ_b for both the Van der Pol systems. In case of supercritical system (Figs. 3.8(a)-(c)), we observe that, for each v, kurtosis increases with increase in noise color, whereas it decreases with increase in noise intensity. When noise color and intensity are kept constant, kurtosis decreases as the system approaches the Hopf bifurcation. However, for all $\tau_c/T_0 > 0.1$, the changes in kurtosis are mostly influenced by changes in noise color than the control parameter, specifically at intermediate and high noise intensity, as indicated by blue solid arrows. In case of subcritical system (Figs. 3.8(d)-(f)), we observe the following trends for kurtosis: (i) at $\sigma_b(1)$, k decreases with increase in τ_c/T_0 for all $v < -2.3$, while shows an oscillatory response with noise color for all $-2.3 < v < -2$; (ii) at $\sigma_b(2)$ and $\sigma_b(3)$, k shows an oscillatory response with noise color at each v and (iii) for each v and τ_c/T_0, kurtosis decreases with increase in noise intensity. As the system approaches the saddle-node point, k increases at low noise intensity while it decreases for intermediate to high noise intensities. When noise color span the range 0.1 to 1, no clear monotonous trend for kurtosis can be expected as the changes in its values are mostly influenced by the noise color (see blue solid arrows).

Hence, Fig. 3.8 shows that the implementation of kurtosis as an early warning indicator has limitations. It can work well for both the type of Van der Pol systems if noise has very small

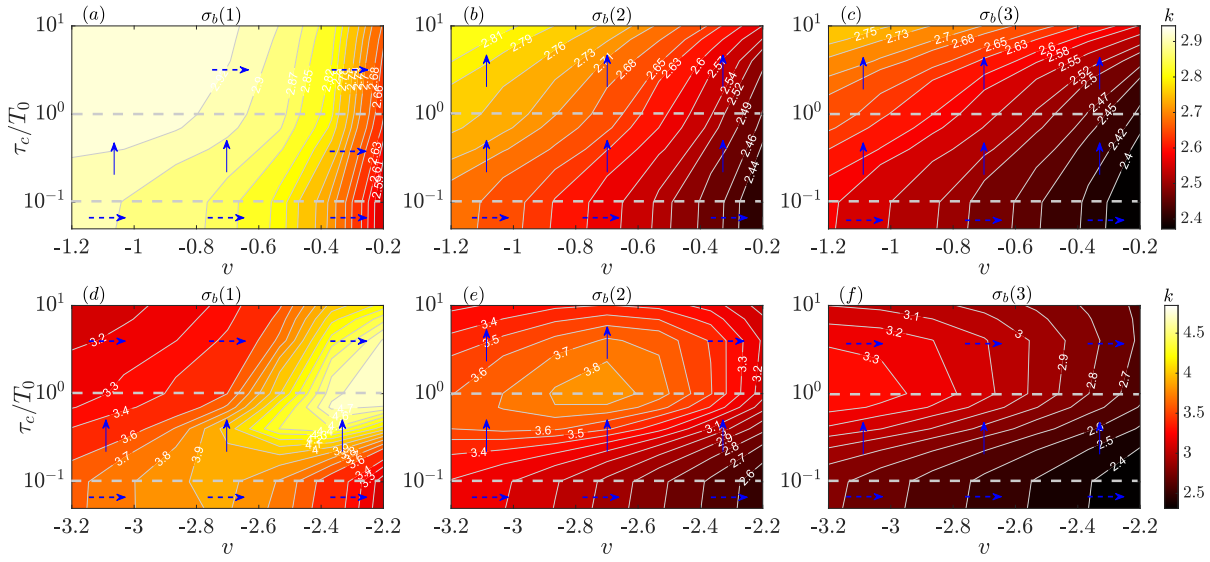

Figure 3.8: 2D contour map of kurtosis (k) as the control parameter (v) and noise correlation time (τ_c/T_0) are varied at three noise intensities ($\sigma_b(1)$ (a, d), $\sigma_b(2)$ (b, e) and $\sigma_b(3)$ (c, f)) for supercritical (a)-(c) and subcritical (d)-(f) Van der Pol systems. The dashed grey lines separate the plots into categories of low, moderate, and high noise correlation times. The arrows roughly indicate whether the variation in k is greater in the direction of control parameter (dashed) or in the direction of noise correlation time (solid).

correlation time, i.e. when white noise approximation is acceptable. For $\tau_c/T_0 > 0.1$, kurtosis could be employed for supercritical systems with low noise intensity; while for subcritical system, it may only work when the noise correlation time is high ($\tau_c/T_0 > 4$) and the system is already in the vicinity of the saddle-node point.

It should be noted that in case of the subcritical Van der Pol system, the trends in skewness and kurtosis are also influenced by the changes in the κ value in Eqn. (3.5). κ influences the width of the bistable region: smaller (or larger) the κ value, smaller (or larger) the bistable region. This change in the bistable region, causes a qualitative change in the trends of skewness and kurtosis (shown in appendix C). Any changes in κ value results in different trends in the variation of skewness and kurtosis with v, τ_c/T_0 and σ_b. Thus, these two measures are not suitable as early warning indicators.

Figure 3.9 shows the variation of decay rates (α) of ACF as a function of v, τ_c/T_0 and σ_b for the two Van der Pol systems. In case of supercritical system (Figs. 3.9(a)-(c)), we observe that, for each v, α remains relatively constant with increase in noise color at $\sigma_b(1)$, whereas α shows an oscillatory response with noise color at $\sigma_b(2)$ and $\sigma_b(3)$. We further observe that, for each τ_c/T_0 and v, α decreases with increase in noise intensity. When noise color and intensity are kept constant, α increases as the system approaches the Hopf point; however, changes in α are influenced by noise color in the range of 0.1 to 1, specifically from intermediate to high noise intensities (blue solid arrows). In case of subcritical system (Figs. 3.9(d)-(f)), for each v, we observe that α decreases at $\sigma_b(1)$ and $\sigma_b(2)$, while it increases at $\sigma_b(3)$ with increase in noise color up to $\tau_c/T_0 = 1$, after which α becomes relatively constant. When noise color and intensity are constant, α increases as the system approaches the saddle-node point.

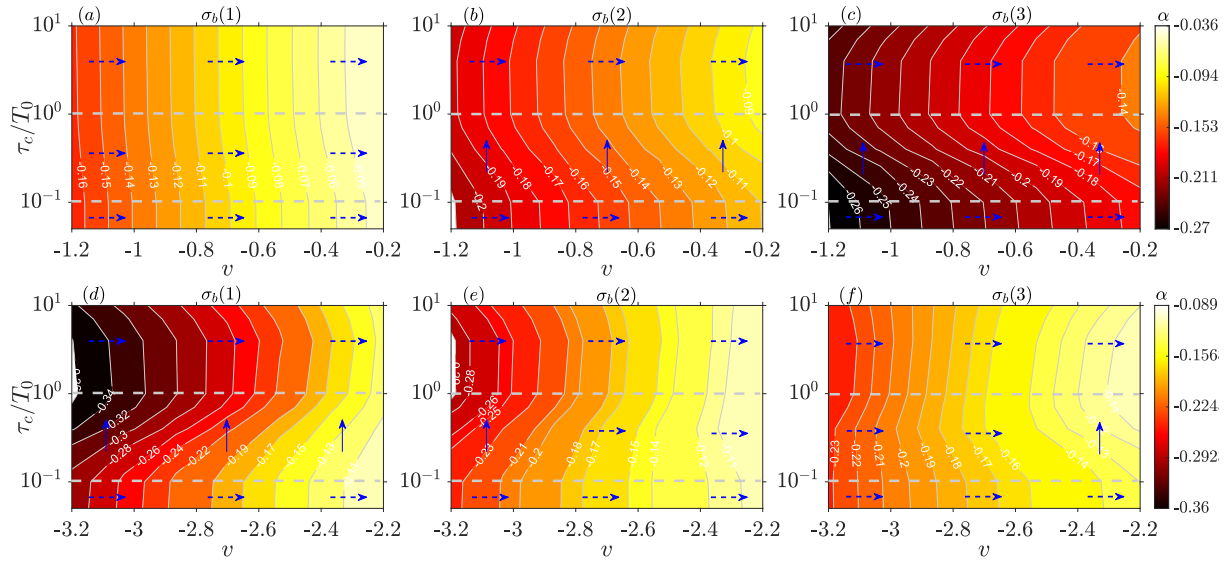

Figure 3.9: 2D contour map of the decay rates (α) of ACF as the control parameter (v) and noise correlation time (τ_c/T_0) are varied at three noise intensities ($\sigma_b(1)$ (a, d), $\sigma_b(2)$ (b, e) and $\sigma_b(3)$ (c, f)) for supercritical (a)-(c) and subcritical (d)-(f) Van der Pol systems. The dashed grey lines separate the plots into categories of low, moderate, and high noise correlation times. The arrows roughly indicate whether the variation in α is greater in the direction of control parameter (dashed) or in the direction of noise correlation time (solid).

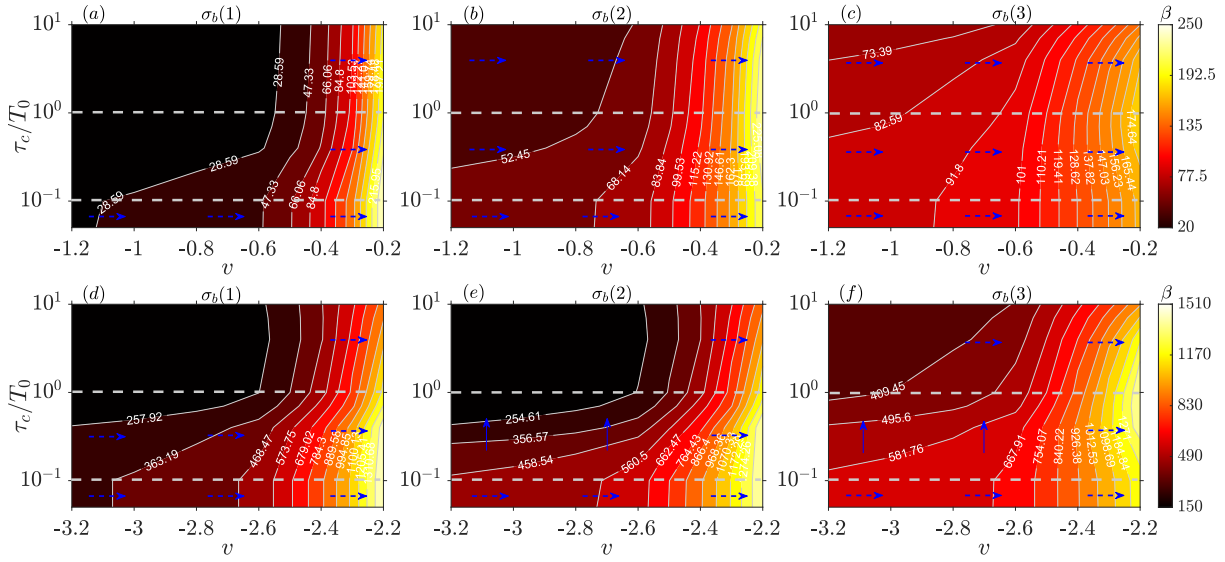

Figure 3.10: 2D contour map of coherence factor (β) as the control parameter (v) and noise correlation time (τ_c/T_0) are varied at three noise intensities ($\sigma_b(1)$ (a, d), $\sigma_b(2)$ (b, e) and $\sigma_b(3)$ (c, f)) for supercritical (a)-(c) and subcritical (d)-(f) Van der Pol systems. The dashed grey lines separate the plots into categories of low, moderate, and high noise correlation times. The arrows roughly indicate whether the variation in β is greater in the direction of control parameter (dashed) or in the direction of noise correlation time (solid).

Overall, Fig. 3.9 indicates that the decay rate of ACF can serve as reliable early warning indicator in systems where noise correlation time is either minimal ($\tau_c/T_0 \leq 0.1$) or larger than the system time scale ($\tau_c/T_0 \geq 1$), as indicated by blue dashed arrows.

Figure 3.10 shows the variation of coherence factor (β) with v, τ_c/T_0 and σ_b for both the Van

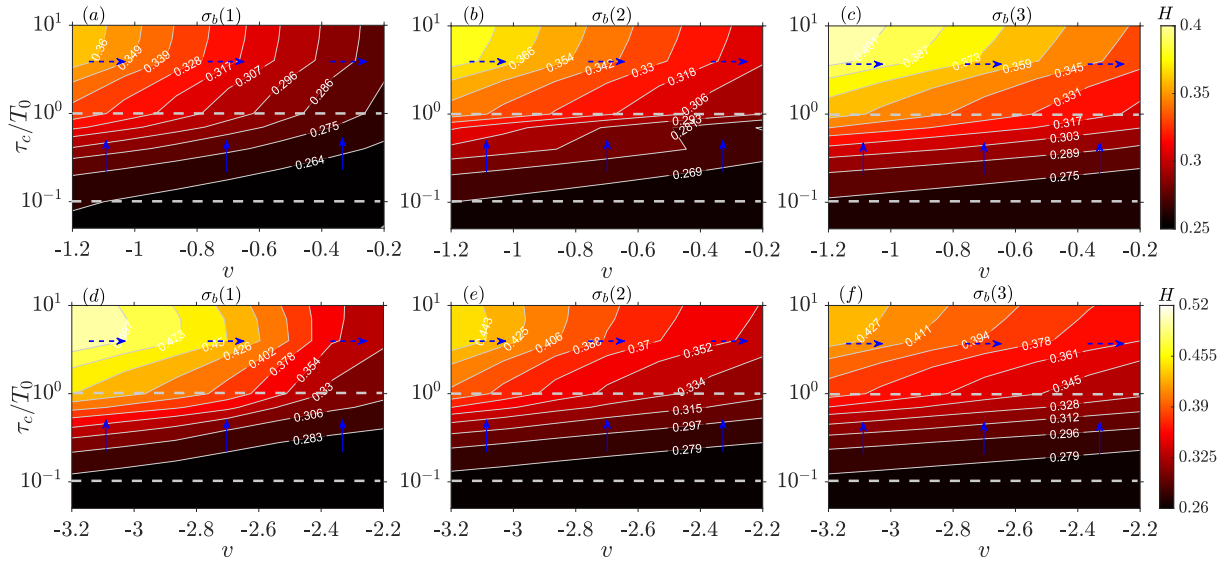

Figure 3.11: 2D contour map of Hurst exponent (H) as the control parameter (v) and noise correlation time (τ_c/T_0) are varied at three noise intensities ($\sigma_b(1)$, $\sigma_b(2)$ and $\sigma_b(3)$) for supercritical (a)-(c) and subcritical (d)-(f) Van der Pol systems. The dashed grey lines separate the plots into categories of low, moderate, and high noise correlation times. The arrows roughly indicate whether the variation in H is greater in the direction of control parameter (dashed) or in the direction of noise correlation time (solid).

der Pol systems. We observe that coherence factor decreases with increase in noise color up to $\tau_c/T_0 = 1$ and then becomes relatively constant. This trend is true for each v at $\sigma_b(1)$ and $\sigma_b(2)$. At $\sigma_b(3)$, in the vicinity of the Hopf and saddle-node points, β exhibits an oscillatory behaviour with noise color. Further, at each τ_c/T_0 and v, we can observe the phenomenon of coherence resonance: β attains a peak value at an *optimum* noise intensity, which shift towards lower values as the system approach the Hopf bifurcation. When noise correlation time and intensity are considered constant, coherence factor increases as the two systems approach the Hopf bifurcation (Fig. 3.10). The variation in β is dominated by the changes in control parameter than the noise characteristics (blue dashed arrows). Thus, coherence factor can serve as an effective early warning indicator even when noise characteristics vary simultaneously with the system parameter. These trends are qualitatively true for both supercritical and subcritical Van der Pol systems.

Figure 3.11 shows the variation of Hurst exponent (H) with v, τ_c/T_0 and σ_b for both the Van der Pol systems. We can note that the value of H falls within the range of 0 to 0.5 This suggests that the time series from both systems exhibit an anti-correlated signature. We observe that, for each σ_b and v, Hurst exponent increases with increase in noise color up to $\tau_c/T_0 = 4$, after which it becomes relatively constant. Hurst exponent does not exhibit significant variation with noise intensity. When noise color and intensity are considered constant, Hurst exponent decreases as the two systems approach the Hopf bifurcation. However, the degree of variation in H with the control parameter is significantly less than with variations in noise correlation times up to $\tau_c/T_0 = 1$ (blue solid arrows). Consequently, if both noise correlation time and intensity vary simultaneously with the control parameter, the trends in the Hurst exponent (H) could become

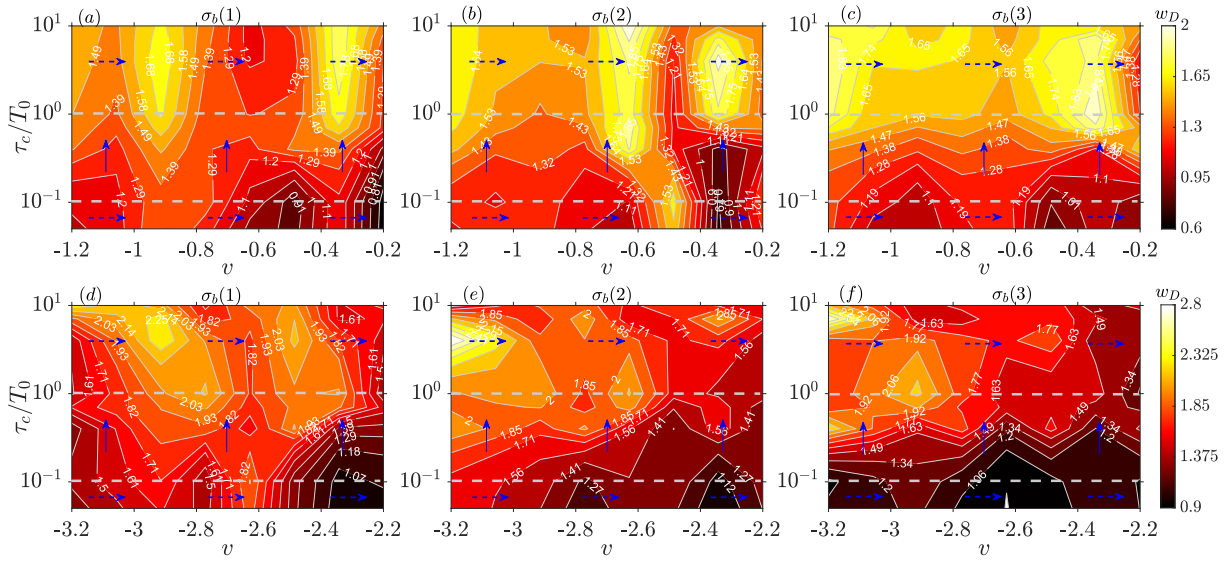

Figure 3.12: 2D contour map of multi-fractal spectrum width (w_D) as the control parameter (v) and noise correlation time (τ_c/T_0) are varied at three noise intensities ($\sigma_b(1)$, $\sigma_b(2)$ and $\sigma_b(3)$) for supercritical (a)-(c) and subcritical (d)-(f) Van der Pol systems. The dashed grey lines separate the plots into categories of low, moderate, and high noise correlation times. The arrows roughly indicate whether the variation in w_D is greater in the direction of control parameter (dashed) or in the direction of noise correlation time (solid).

non-monotonous. Thus, Hurst exponent can be considered as a reliable early warning indicator in systems where the noise correlation time is larger than the system time scale, i.e., $\tau_c/T_0 > 1$ (blue dashed arrows). Examples for previous successful implementation of the Hurst exponent as a precursor include Nair et al. [96,173], Unni et al. [174], and Fu et al. [99], where the transition to periodic oscillations is reported to occur via intermittency. In these aforementioned studies, noise color may have satisfied the criterion for correlation time. It is also possible that the change in Hurst exponent is due to a combined effect of noise color variation and parameter variation, but was ascribed to the parameter. For instance, with reference to Fig. 3.11(f), simultaneous increase in control parameter and decrease in noise color will result in a prominent monotonous decrease in the Hurst exponent. Whereas, the use of the Hurst exponent in an experiment where noise color increases with increase in parameter will lead to a much smaller decrease – or even an increase – in the Hurst exponent with increase in control parameter as observed in Fig. 2.20 with electroacoustic simulator. Such an experiment on the Hurst exponent as an instability precursor would likely be considered as inconclusive, but as we see here, such trends are a manifestation of the effects of noise characteristics.

Another early warning measure associated with fractal signature of the time series is the multi-fractal spectrum width. Figure 3.12 shows the variation of spectrum width (w_D) with v, τ_c/T_0 and σ_b for both the Van der Pol systems. We observe that no consistent trend is apparent in the plots with respect to noise color and control parameter for any σ_b. We also observe that w_D does not show variations with noise intensity. Although for low ($\tau_c/T_0 < 0.1$) and high ($\tau_c/T_0 > 1$) noise color, the blue dashed arrows indicates that variation in w_D is mostly influenced by control parameter than the noise color, however, it does not display any

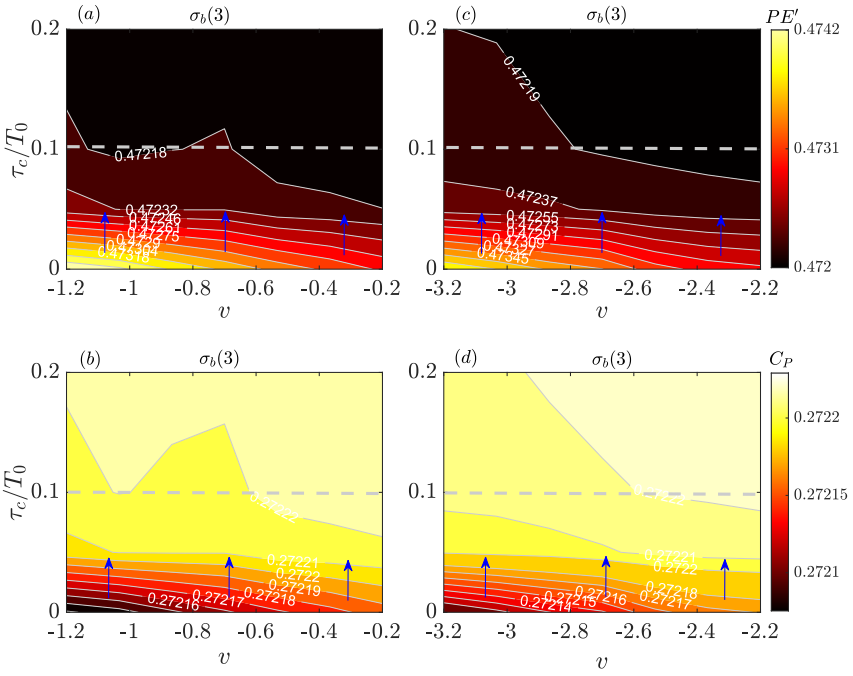

Figure 3.13: 2D contour map of (a), (c) permutation entropy (PE') and (b), (d) Jensen-Shannon complexity (C_P) as the control parameter (v) and noise correlation time (τ_c/T_0) are varied at $\sigma_b(3)$ for supercritical (a)-(b) and subcritical (c)-(d) Van der Pol systems. The dashed grey line separate the plots into categories of low and moderate to high noise correlation times. The arrows roughly indicate whether the variations in PE' and C_P are greater in the direction of control parameter (dashed) or in the direction of noise correlation time (solid).

monotonous trend and may either increase or decrease as the two systems approach the Hopf bifurcation. This indicates that the multi-fractal spectrum width is not a suitable choice as an early warning indicator.

Figure 3.13 shows the variation of entropy/complexity measures of time series with v and τ_c/T_0 at $\sigma_b(3)$ for the two Van der Pol systems. We observe that, for each v, permutation entropy (Figs. 3.13(a) and (c)) decreases, while Jensen-Shannon complexity (Figs. 3.13(b) and (d)) increases with increase in noise color up to $\tau_c/T_0 = 0.1$, after which they become constant. As no variations in PE' and C_P after $\tau_c/T_0 > 0.1$ are observed, the limits of y-axis are restricted to $\tau_c/T_0 = 0.2$ for clear visualization of trends. Although not shown here, but, we find that noise intensity does not influence these measures. When noise color and intensity are considered constant, PE' decreases while C_P increases as the two systems approach the Hopf bifurcation. Even within the span of $0 < \tau_c/T_0 < 0.1$, the variation in PE' and C_P are more responsive to changes in noise correlation time than the control parameter, as indicated by the blue solid arrows. Consequently, entropy/complexity measures can only be employed as early warning indicators in systems where the white noise approximation is acceptable.

Figures 3.6-3.13 illustrated the characteristics and limitations of various EWIs with respect to control parameter, noise color and intensity. In order to summarize and recommend the most reliable indicators for implementation in practical systems, we estimate the % change in each EWI as the control parameter is varied towards the Hopf bifurcation. The % change (χ) in each

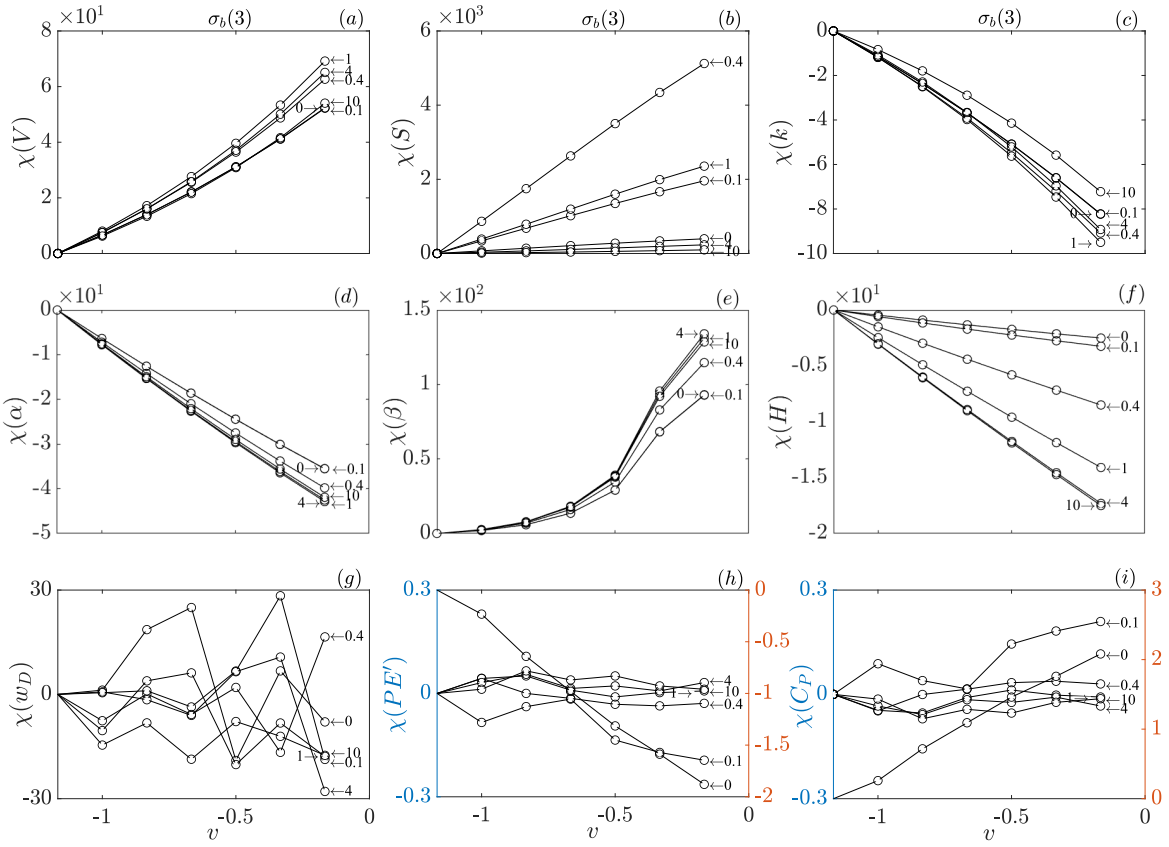

Figure 3.14: Summary of the reliability of various EWIs represented as the % change in each indicator (χ) as the control parameter (v) is increased towards the supercritical Hopf bifurcation for varied noise color (τ_c, marked with arrows) at $\sigma_b(3)$.

EWI is calculated as,

$$\chi = \frac{\text{EWI} - \text{EWI}_{ref}}{\text{EWI}_{ref}} \times 100 \tag{3.37}$$

where, EWI_{ref} is the value of EWI at the far away point from the Hopf bifurcation for each noise color, i.e., $v = -1.2$ for supercritical system and $v = -3.2$ for subcritical system. The advantage of such normalization is that all the curves in the plot will start from zero, indicating the maximum change in an EWI near the Hopf or saddle-node point.

Figures 3.14 and 3.15 show a comparative analysis of the various EWIs in terms of χ for varied noise correlation times at $\sigma_b(3)$ for supercritical and subcritical Van der Pol systems respectively. We find that among the investigated EWIs, variance (Figs. 3.14(a) and 3.15(a)), ACF decay rates (Figs. 3.14(d) and 3.15(d)) and coherence factor (Figs. 3.14(e) and 3.15(e)) are the most reliable indicators, as they exhibit a monotonous trend regardless of noise characteristics and bifurcation variant. The Hurst exponent (Figs. 3.14(f) and 3.15(f)) falls next on the reliability index but the trends are distinguishable only when $\tau_c/T_0 \geq 1$. The entropy/complexity measures (Figs. 3.14(h-i) and 3.15(h-i)) can be only reliable in systems approximated by white noise. Multi-fractal spectrum width (Figs. 3.14(g) and 3.15(g)) is not suitable as an EWI. Although, we can observe that the % change in skewness (Figs. 3.14(b) and 3.15(b))) and kurtosis (Figs. 3.14(c) and 3.15(c)) is high, but the trends are not consistent with change in system parameter, as can be compared between Figs. 3.14-3.15 and Figs. C.1-C.2. Hence, these are also deemed unsuitable

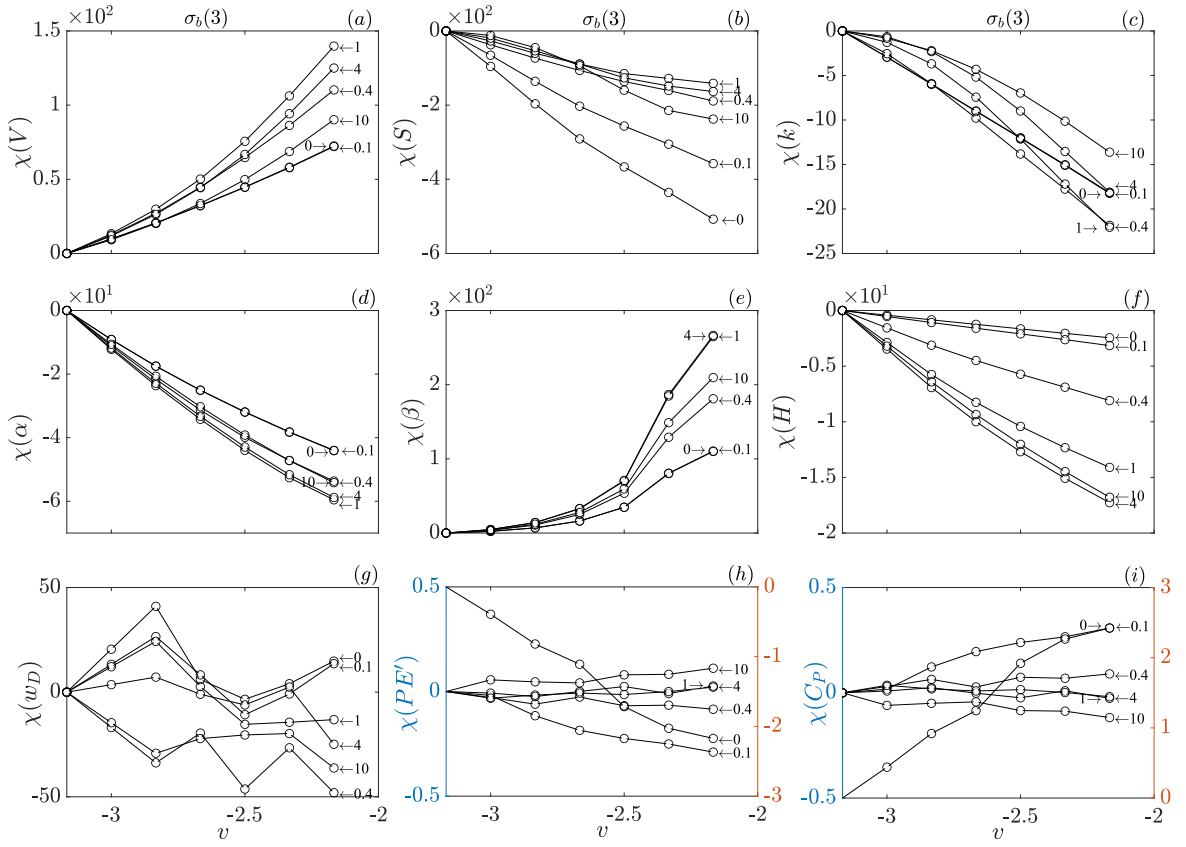

Figure 3.15: Summary of the reliability of various EWIs represented as the % change in each indicator (χ) as the control parameter (v) is increased towards the subcritical Hopf bifurcation for varied noise color (τ_c, marked with arrows) at $\sigma_b(3)$.

as early warning indicators.

Implementation of any early warning indicator in practical system is based on detecting the changes in the EWI and relating them with whether the system is moving closer to or away from the critical point. In our numerical study, the closest point to limit cycle oscillations is $v = -0.2$ *and* $v = -2.2$ *for supercritical and subcritical systems respectively. Despite their sensitivity to changes in noise characteristics, indicators such as* V, α, β *and* H *consistently exhibit a monotonous trend up to* $v = -0.2$ *and* $v = -2.2$*, suggesting their efficacy as EWIs. However, when applying these indicators for prediction, it is crucial to calibrate them for individual systems based on the noise characteristics.*

In practical combustion systems, the flame response to the acoustic forcing can occur after a time delay (τ), as shown in Bonciolini et al. [175–177]. In Appendix D, we show the effect of the time delay on the trends of two noise-induced precursors: coherence factor and Hurst exponent. In case the time delay of flame response is not negligible, we find that the coherence factor will work at most time delays and noise color, while the trends in the Hurst exponent are mostly dependent on the noise color of additive noise (i.e., $\tau_c/T_0 \geq 1$) than the time delay. Although introducing time delay as a parameter complicates the stochastic dynamics of the system–due to the addition of multiplicative noise from variations in the time delay–our conclusions for non-time delay oscillators remain applicable.

An important note here is that we have conducted the analysis in the subthreshold region,

where the system is linearly stable. In bistable region, noise-induced triggering (also known as noise-induced flickering [178]) is challenging for EWIs to detect because the system transitions to an alternative state due to strong external disturbances, without approaching or crossing the bifurcation point. Dakos et al. [80] have conducted extensive investigations into this phenomenon using the same framework as that for linearly stable systems. They analyzed two datasets for an ecosystem: one where the control parameter is slowly increased towards the Hopf point (critical slowing down) and another where both the control parameter and stochastic fluctuations are increased to induce triggering within a bistable region (flickering). They found that traditional EWIs like autocorrelation and skewness showed an increasing trend even after the critical transition, making them unreliable. Variance, however, displayed an increasing trend until it began to decrease near the transition point due to more frequent excursions to the alternative attractor, indicating its potential as a reliable EWI in these contexts. Similarly, the spectral exponent was found to be a reliable indicator. On the other hand, the Hurst exponent exhibited a non-monotonic trend, offering no clear indication of an impending transition. This suggests that missed alarms are more likely in triggered cases, as EWIs typically signal transitions when the system gradually approaches a bifurcation. In situations where external forcing changes faster than the system's response rate, variance or spectral exponent can still function as indicators, but they may not be entirely reliable. In such scenarios, novel approaches like potential analysis may be more effective in assessing bistability [84,179]. This method allows for a better understanding of the system's potential landscape and can provide insights into the likelihood of transitions even in the presence of strong perturbations.

In this chapter, we investigate the effect of noise characteristics—correlation time and intensity—on commonly employed early warning indicators (EWIs) of critical transition in dynamical systems. We assess the reliability of these indicators via numerical simulations using a generalized Van der Pol oscillator which undergoes both supercritical and subcritical Hopf bifurcation. We model correlated noise in the system as an additive Ornstein Uhlenbeck (OU) process. The study is performed in the subthreshold regime such that the stable focus is the only possible asymptotic state. We thus have three primary parameters in this study: the control parameter which controls the proximity of the system to the Hopf bifurcation, the noise correlation time, and the noise intensity. We have applied various measures – statistical, spectral, fractal, and entropy/complexity-related – while varying the parameters. Unlike most previous investigations, the objective is to systematically assess whether a given measure can be employed reliably as an early warning indicator. A reliable EWI would follow a monotonous trend as the system is brought close to the Hopf point. In addition, it is desired that the measure vary predominantly in response to variation in the control parameter. Such criteria for an EWI is relevant in a practical setting where noise characteristics may vary simultaneously with the operating/ambient conditions or the control parameter. For instance, in combustors, both inherent noise and the control parameter is linked to the properties of the flame driving combustors. As a consequence, as the control parameter is varied, the noise characteristics (in particular, noise color) also varies. An EWI such as kurtosis in the normalized noise color range of 0.1–1 (see Fig. 3.8) will vary due to changes in the color and control parameter. Depending

Table 3.2: Summary of results obtained in this work in the stable region along with comparisons from existing literature.

EWIs	Types of noise			Results (literature)	Results (this work)	Limitations (this work)
	White noise or type undefined	Colored noise				
		Correlation time	Intensity			
Variance	Ref. [80, 86, 87, 89, 91, 180]	Ref. [181–184], this work	Ref. [181], this work	Robust with limitations (time delays)	Reliable with limitations	$0.1 \leq \tau_c/T_0 \leq 1$
Skewness	Ref. [80, 89, 91, 180]	Ref. [183], this work	this work	Mixed trends	Not reliable	Bifurcation type, τ_c and σ_b
Kurtosis	Ref. [89, 91]	this work	this work	Mixed trends	Reliable with limitations	$\tau_c/T_0 \geq 1$, σ_b
ACF	Ref. [80, 86, 87, 89, 91, 180, 185]	Ref. [181–184], this work	Ref. [181], this work	Robust with limitations (time lags) (type of noise)	Reliable with limitations	$0.1 \leq \tau_c/T_0 \leq 1$
Coherence factor	Ref. [2, 6, 186]	Ref. [186], this work	Ref. [186], this work	Robust	Reliable	–
Hurst exponent	Ref. [89, 96]	Ref. [184, 186], this work	Ref. [186], this work	Robust	Reliable with limitations	$\tau_c/T_0 \leq 1$
Multi-fractal spectrum width	Ref. [96]	this work	this work	–	Not reliable	Bifurcation type, τ_c and σ_b
Permutation entropy	Ref. [108, 109]	this work	this work	Robust	Reliable with limitations	$\tau_c/T_0 \geq 1$
Jensen Shannon complexity	Ref. [108, 109]	this work	this work	Robust	Reliable with limitations	$\tau_c/T_0 \geq 1$

on the variation in noise color, the desired monotonous trend may not be obtained. Kurtosis in such a scenario would be unreliable. Coherence factor (Fig. 3.10) on the other hand will still vary monotonously in response to control parameter variation – except for a subcritical system at large noise intensity and far away from bifurcation (Fig. 3.10f).

Thus, conclusions from investigations conducted in the absence of information on how noise varies with control parameter will differ depending on the noise intensity, noise color, and control parameter. A summary comparing the findings in this study and conclusions from previous studies on the various classes of investigated EWIs is tabulated in Table 3.2.

Chapter 4

Effect of Multiplicative Correlated Noise Characteristics on Early Warning Prediction

4.1 Overview

The background noise in a combustor features contributions not only from additive sources arising from aerodynamics and combustion but also from multiplicative sources arising from coupling mechanisms such as velocity, pressure and mixture coupling [1,33,36]. In this chapter, we numerically investigate the effects of noise characteristics of combined multiplicative and additive noise sources on the reliability/efficacy of different classes of EWIs using the stochastic Van der Pol oscillator. We investigate the EWIs based on spectral properties (coherence factor), statistical measures (variance), multi-fractality (Hurst exponent), and time series complexity (permutation entropy). This investigation provides more detailed insights on the most reliable EWIs that should be employed for accurate prediction of instability, considering variations in noise sources and characteristics expected in practical gas turbine combustors.

In dynamical systems theory, a subcritical Hopf bifurcation is known as a catastrophic critical transition, characterized by the system abruptly transitioning to limit cycle oscillations upon variation of the control parameter. This phenomenon is particularly important due to the presence of hysteresis, which leads to a bistable region where noise-induced transitions can occur. In practical gas turbine combustors, thermoacoustic instability is frequently observed to arise through subcritical Hopf bifurcation [67,149,187,188]. In Chapter 2, we observed that the trends in EWIs for both supercritical and subcritical bifurcations are largely similar. Therefore, in the subsequent chapters of PART I, we will focus on systems exhibiting subcritical Hopf bifurcation.

This chapter is further divided into two sections. Section 4.2 describes the mathematical model of stochastic Van der Pol oscillator and colored noise and the methodology to estimate various EWIs. Section 4.3 shows the effects of correlated noise characteristics on the estimated EWIs and discuss their reliability when implemented in real systems. A brief overview of the summary for the contents of the chapter is shown in Fig. 4.1.

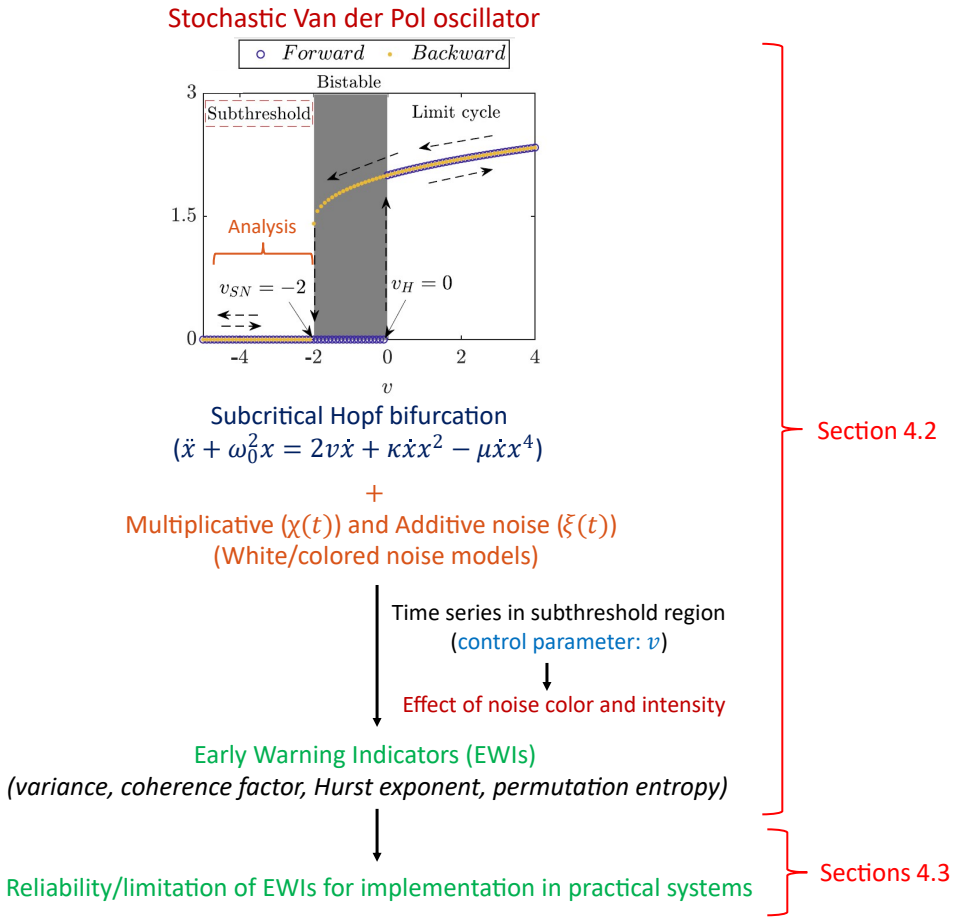

Figure 4.1: Visual summary of the contents for Chapter 4.

4.2 Model description and methodology

4.2.1 Stochastic Van der Pol oscillator

For this investigation, we employ the extended version of Van der Pol oscillator model (discussed in section 3.2.1) which exhibits instabilities via subcritical Hopf bifurcation, given as

$$\ddot{x} + (\mu x^4 - \kappa x^2 - 2v)\dot{x} + \omega_0^2 x = 0 \tag{4.1}$$

The corresponding stochastic differential equation is given as,

$$\ddot{x} + \omega_0^2 x = \left(2v + \kappa x^2 - \mu x^4\right)\dot{x} + \chi(t)\dot{x} + \xi(t) \tag{4.2}$$

where, $\chi(t)$ is the velocity coupled multiplicative noise and $\xi(t)$ is the additive noise. We numerically simulate this model using the fourth-order Runge-Kutta method in Matlab using a time step of $dt = 0.0001$ s in the time span of $0 \leq t \leq 1000$ s. We choose the system parameters as $f_0 = \omega_0/2\pi = 100$ Hz, $\kappa = 8$ s^{-1} and $\mu = 2$ s^{-1} following the experimental validation of Bonciolini et al. [158]. For the analysis, we use data for last 500 s. In the absence of noise, as the control parameter, v, is varied from $v = -4$ to $v = 4$, the oscillator undergoes transition

to instability via a subcritical Hopf bifurcation as shown in Fig. 3.2(c), with the Hopf and saddle-node points observed at $v_H = 0$ and $v_{SN} = -2$ respectively. The analysis for estimating various EWIs to detect the approaching instability is carried out in the subthreshold region where the control parameter varies from $-3.2 \leq v \leq -2.2$.

4.2.2 Noise models

We first model $\chi(t)$ and $\xi(t)$ in Eqn (4.2) as the white Gaussian noise of intensity Γ, as discussed in section 3.2.2. To investigate the effect of noise color, we then model $\chi(t)$ and $\xi(t)$ based on the following spectral features [4]: (i) the power spectrum for flow (velocity coupled) noise remains constant (or flat) up to a cutoff frequency and then decays following the power law ($P \propto f^{-r}$) – OU noise and (ii) the power spectrum of additive (combustion) noise increases at low frequencies up to a cutoff frequency following $P \propto f^2$, attains a maximum and then decays following $P \propto f^{-r}$. Here, r represents the decay rate of power spectrum and is proportional to the noise color (or correlation time), P is the power spectral density and f is the frequency. The corresponding mathematical expressions for $\chi(t)$ and $\xi(t)$ in the frequency domain are given as [61],

$$\frac{\widehat{\chi}(s)}{\widehat{\epsilon}(s)} = H_m(s) = \frac{\sqrt{\mathrm{D_m}}}{(1+\tau_m s)} \tag{4.3}$$

whose power spectrum can be given as,

$$S_{\chi\chi}(\omega) = |H_m|^2 S_{\epsilon\epsilon} = \frac{\Gamma}{2\pi}\frac{D_m}{1+\omega^2\tau_{\mathrm{m}}^2} \tag{4.4}$$

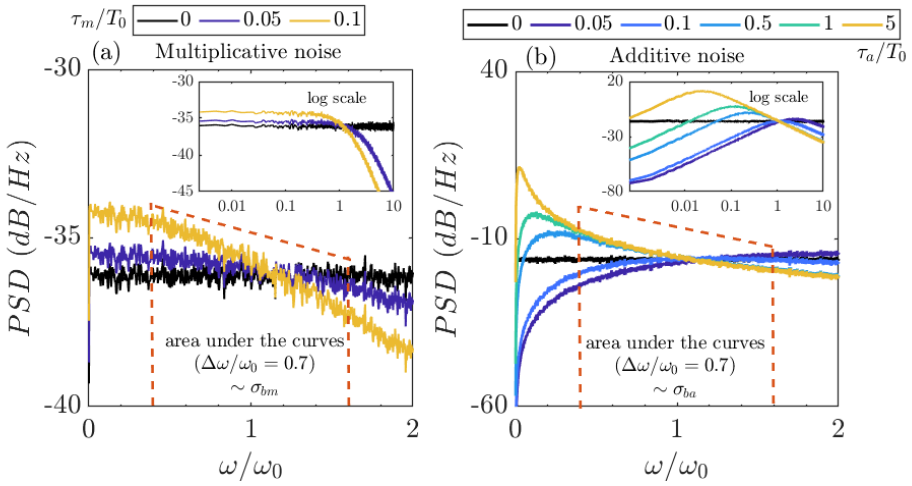

Figure 4.2: Power spectrum for colored (a) multiplicative noise and (b) additive noise. The black curves correspond to white Gaussian noise in each case. The colored noises are generated such that the powers provided by $\chi(t)$, $\xi(t)$ and $\epsilon(t)$ within $\Delta\omega/\omega_0 = 0.7$ are equal (area under the curve on a linear scale denoted by σ_{bm} and σ_{ba} respectively). τ_m and τ_a are normalized by the time period of acoustic oscillations at Hopf point ($T_0 = 2\pi/\omega_0$). The inset plots show the same curves on log scale.

and,

$$\frac{\widehat{\xi}(s)}{\widehat{\epsilon}(s)} = H_a(s) = \frac{\sqrt{\mathrm{D_a}}\tau_a^2 s}{(1+\tau_a s)^2} \tag{4.5}$$

whose power spectrum can be given as,

$$S_{\xi\xi}(\omega) = |H_a|^2 S_{\epsilon\epsilon} = \frac{\Gamma}{2\pi}\frac{\mathrm{D_a}\omega^2\tau_a^4}{(1+\omega^2\tau_a^2)^2} \tag{4.6}$$

which features f_{peak} at,

$$f_{peak} = \frac{1}{2\pi\tau_a} \tag{4.7}$$

where, $s = i\omega$ is the Laplace variable, $\epsilon(s)$ is the white noise, τ_m and τ_a are the respective noise correlation times, D_m and D_a are the respective noise intensities.

Here as well, we generate the two types of colored noises in such a way that the powers provided by $\chi(t)$, $\xi(t)$ and $\epsilon(t)$ in a band, $\Delta\omega = \omega_2 - \omega_1$, around the system's eigenfrequency are equal [61], i.e.,

$$\sigma_{bm} = \int_{\omega_1}^{\omega_2} S_{\chi\chi}\mathrm{d}\omega = \int_{\omega_1}^{\omega_2} S_{\epsilon\epsilon}\mathrm{d}\omega \tag{4.8}$$

and

$$\sigma_{ba} = \int_{\omega_1}^{\omega_2} S_{\xi\xi}\mathrm{d}\omega = \int_{\omega_1}^{\omega_2} S_{\epsilon\epsilon}\mathrm{d}\omega \tag{4.9}$$

For the present study, we choose $\Delta\omega/\omega_0 = 0.7$, as discussed in section 3.2.2. The corresponding power spectrum for both the types of noises at varied noise correlation times are shown in Fig. 4.2. The noise correlation times are normalized by the time period of acoustic oscillations at Hopf point ($T_0 = 2\pi/\omega_0$).

4.2.3 Methodology

In this chapter, we investigate the EWIs based on spectral properties (coherence factor), statistical measures (variance), multi-fractality (Hurst exponent) and time series complexity measures (permutation entropy). The detailed methodology along with the specifications of parameters for estimation of these EWIs are discussed in section 3.2.4. A brief summary of the formulations to estimate various EWIs along with their monotonic trend is illustrated in Fig. 4.3. Figure 4.4 shows the variation of β with noise intensity (σ_b) and control parameter (v) when

EWI class	EWI	Formulation	Trend
Statistical measures	Variance	$V = \frac{1}{N}\sum_{i-1}^{N}(x_i - \bar{x})^2$	Increases
Spectral measures	Coherence factor	$\beta = H_P \times (f_P/\Delta f)$	Increases
Fractal measures	Hurst exponent	$F_q \sim w^{H_q}$	Decreases
Entropy measures	Permutation entropy	$PE = -\sum_{\pi} p(\pi)\log_2 p(\pi)$	Decreases

Figure 4.3: A brief summary of methodology to estimate various early warning indicators in the subthreshold region along with their monotonic trend.

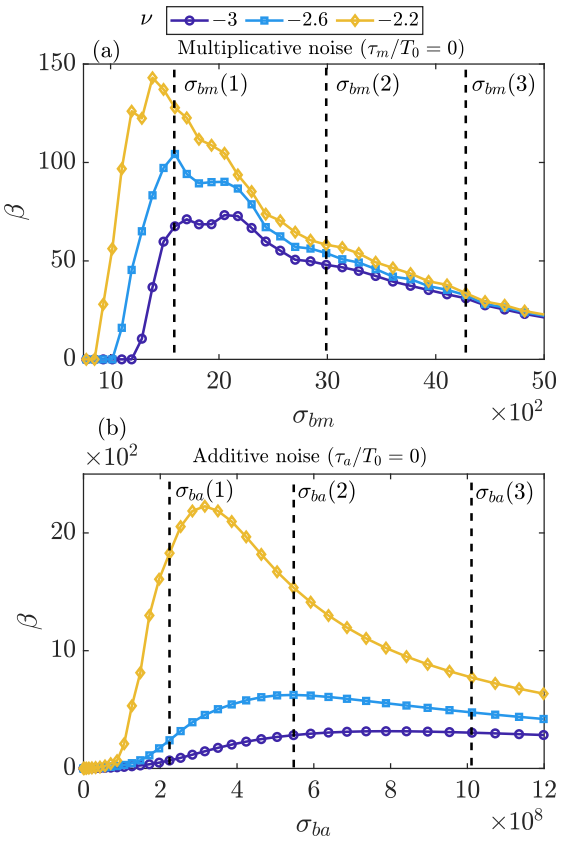

Figure 4.4: Coherence resonance: variation of coherence factor (β) as a function of white noise intensity within $\Delta\omega/\omega_0 = 0.7$ and control parameter v for the system when excited by (a) only multiplicative noise and (b) only additive noise. The results are presented at three noise intensities (low, intermediate and high) marked by dashed lines for respective cases.

the nonlinear oscillator is excited by only white multiplicative noise (plot (a)) and only white additive noise (plot (b)). We can observe the hallmark of coherence resonance in the two cases: (i) for each v, β attains a peak value at an intermediate noise level (or optimum noise intensity). This optimum noise intensity shifts to lower values as the control parameter is increased towards the saddle-node point ($v_{SN} = -2$). (ii) β increases as the system approaches the saddle-node point at most noise intensities, except for very low or very high noise levels where the variation in β is too small to distinguish a trend. This consistent increase in β as the system approaches the instability serve as an EWI.

In case of multiplicative noise driven oscillator (Fig. 4.4(a)), we observe that as v is decreased from $v = -2.2$ to $v = -3$, there appear two distinct peaks for β. This indicates that multiplicative noise changes qualitative characteristics in a system such that a transition from one peak to two peaks in coherence resonance is induced. This phenomenon is also observed by Luo and Zhu [189] for bistable systems. No such qualitative characteristics are observed/reported for additive noise driven systems.

Figure 4.4 also shows that noise intensity plays an important role in affecting the system dynamics in the subthreshold region. Therefore, in addition to noise color variations, we also investigate the effects of noise intensity on the trends of various EWIs. In section 4.3, we will

present the results at three noise intensities (low, intermediate and high) marked in Fig. 4.4 for respective cases.

4.3 Effect of background noise characteristics on EWIs

In this section, we will discuss the effects of stochastic features (noise correlation time and intensity) of background noise on the various EWIs estimated in the subthreshold region. The results are presented as a 2D contour map in the parameter space between noise color (τ) and control parameter (v) at low (column 1), intermediate (column 2) and high (column 3) noise intensities. The saddle-node point occurs at $v_{SN} = -2$. The dashed lines in the contour plots separate it into categories of low, moderate, and high noise correlation times. The arrows roughly indicate whether the variation in the EWI is greater in the direction of control parameter (horizontal) or in the direction of noise correlation time (vertical).

4.3.1 Effect of multiplicative colored noise

Figure 4.5 shows the variation of coherence factor (β), variance (V), Hurst exponent (H) and permutation entropy (PE') as a function of noise color (τ_m/T_0), noise intensity (σ_{bm}) and control parameter (v) when the system is excited by only multiplicative noise (i.e. $\xi(t) = 0$ and $\chi(t) \neq 0$ in Eqn. (4.2)). We observe from Fig. 4.5(a)-(c) that for each v, coherence factor decreases with increase in noise color at $\sigma_{bm}(1)$ and $\sigma_{bm}(2)$. At high noise levels ($\sigma_{bm}(3)$), β exhibits an oscillatory behaviour (first increases, attains a peak value and then decreases–a bell-shaped curve behaviour) with noise color up to $\tau_m/T_0 = 0.05$, after which it consistently decreases with increase in τ_m. When noise color and intensity are considered fixed, β increases as the system approaches the saddle-node point, as illustrated in Fig. 4.5(d). The amount of increase in β, however, depends on the noise color and intensity even if they do not vary. We observe that the changes in β are more sensitive to changes in noise color rather than the control parameter, as indicated by the arrows in the contour plots, except at $\sigma_{bm}(1)$ for $\tau_m/T_0 \leq 0.05$. This indicates that even a slight change in noise color with variations (or fluctuations) in operating condition, will cause a significant change in the values of coherence factor and hence, the corresponding trend in β can deviate from monotonous behaviour.

Similarly, variance (Fig. 4.5(e)-(g)) also decreases with increase in noise color at all v and σ_{bm}. Whereas for a fixed τ_m and v, variance increases with increase in noise intensity. If noise color and intensity are fixed, variance also increases as the system approaches the saddle-node point (Fig. 4.5(h)), however, the changes in V are more sensitive to changes in noise color and intensity than the control parameter, as indicated by the arrows.

We observe that the Hurst exponent (Fig. 4.5(i)-(k)), on the other hand, increases with increase in both noise color and intensity at each v. While, it remains relatively constant as the system approaches the saddle-node point at all τ_m and σ_{bm}, as illustrated in Fig. 4.5(l). Further, changes in H are also predominantly influenced by noise properties than the control parameter. Permutation entropy (Fig. 4.5(m)-(o)) decreases with increase in noise color, while it exhibits an oscillatory behaviour with noise intensity at all v. Similar to the Hurst exponent, PE' also

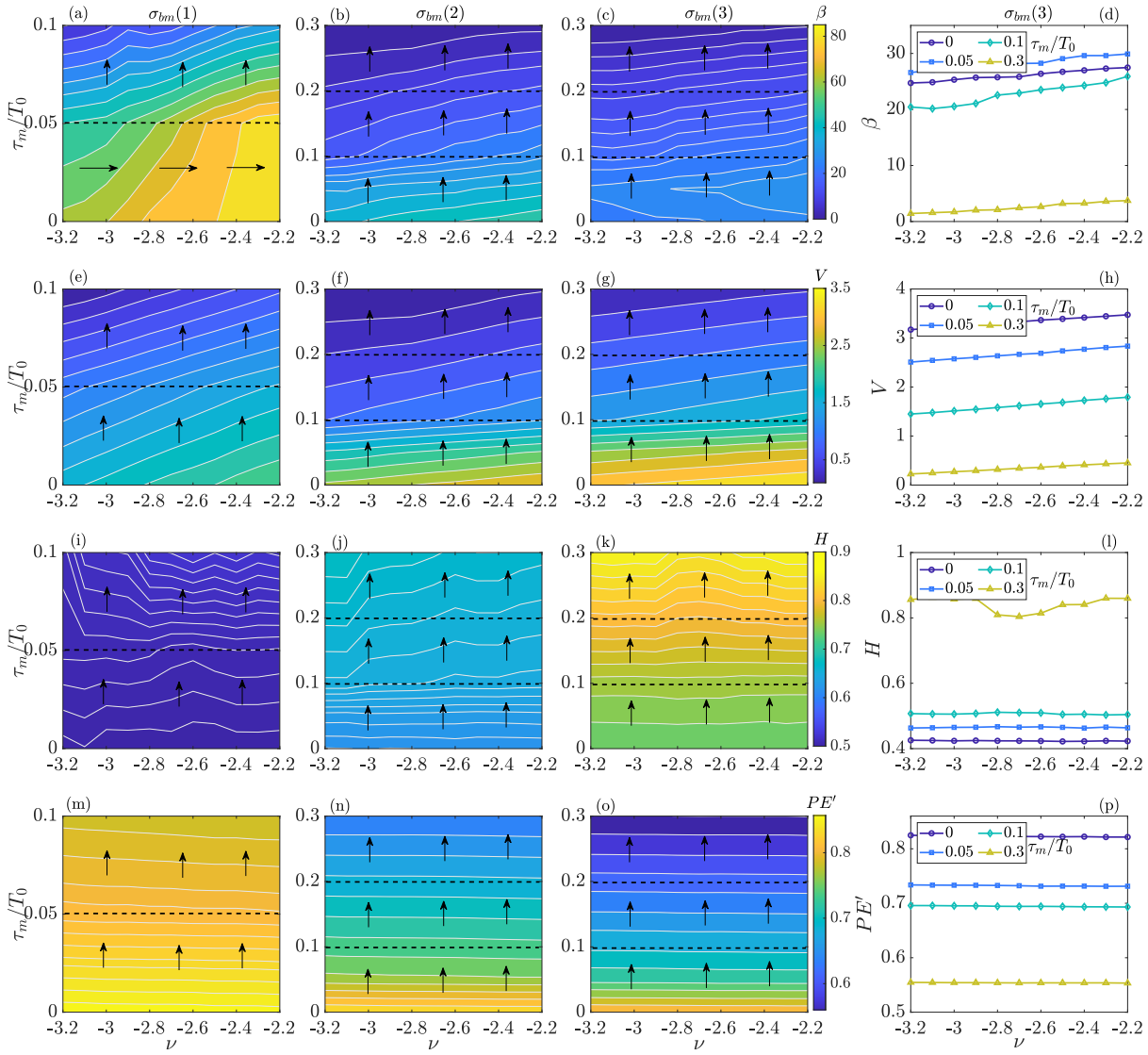

Figure 4.5: Multiplicative noise driven system: variation of (a)-(d) coherence factor (β), (e)-(h) variance (V), (i)-(l) Hurst exponent (H) and (m)-(p) permutation entropy (PE') as a function of noise color (τ_m) and noise intensity (σ_{bm}). The dashed lines in the contour plots separate it into categories of low, moderate, and high noise correlation times. The arrows roughly indicate whether the variation in the EWI is greater in the direction of control parameter (horizontal) or in the direction of noise correlation time (vertical). The line plots in column 4 illustrates the general trend in each EWI as a function of control parameter at $\sigma_{bm}(3)$.

remains constant as the system approaches the saddle-node point at all τ_m and σ_{bm}, as illustrated in Fig. 4.5(p) and changes in PE' are governed only by noise color.

Therefore, Fig. 4.5 indicates that if noise properties change simultaneously with the control parameter, trends in coherence factor and variance can become non-monotonous, specifically at moderate to high noise levels, if the background noise has major contributions from velocity coupling sources. Whereas, as the Hurst exponent and permutation entropy do not exhibit any trend with the control parameter these parameters can not be employed as EWIs.

It should be noted that at low noise levels ($\sigma_{bm}(1)$), multiplicative noise affects the system's response such that the noise-induced fluctuations in the system becomes nearly zero for all

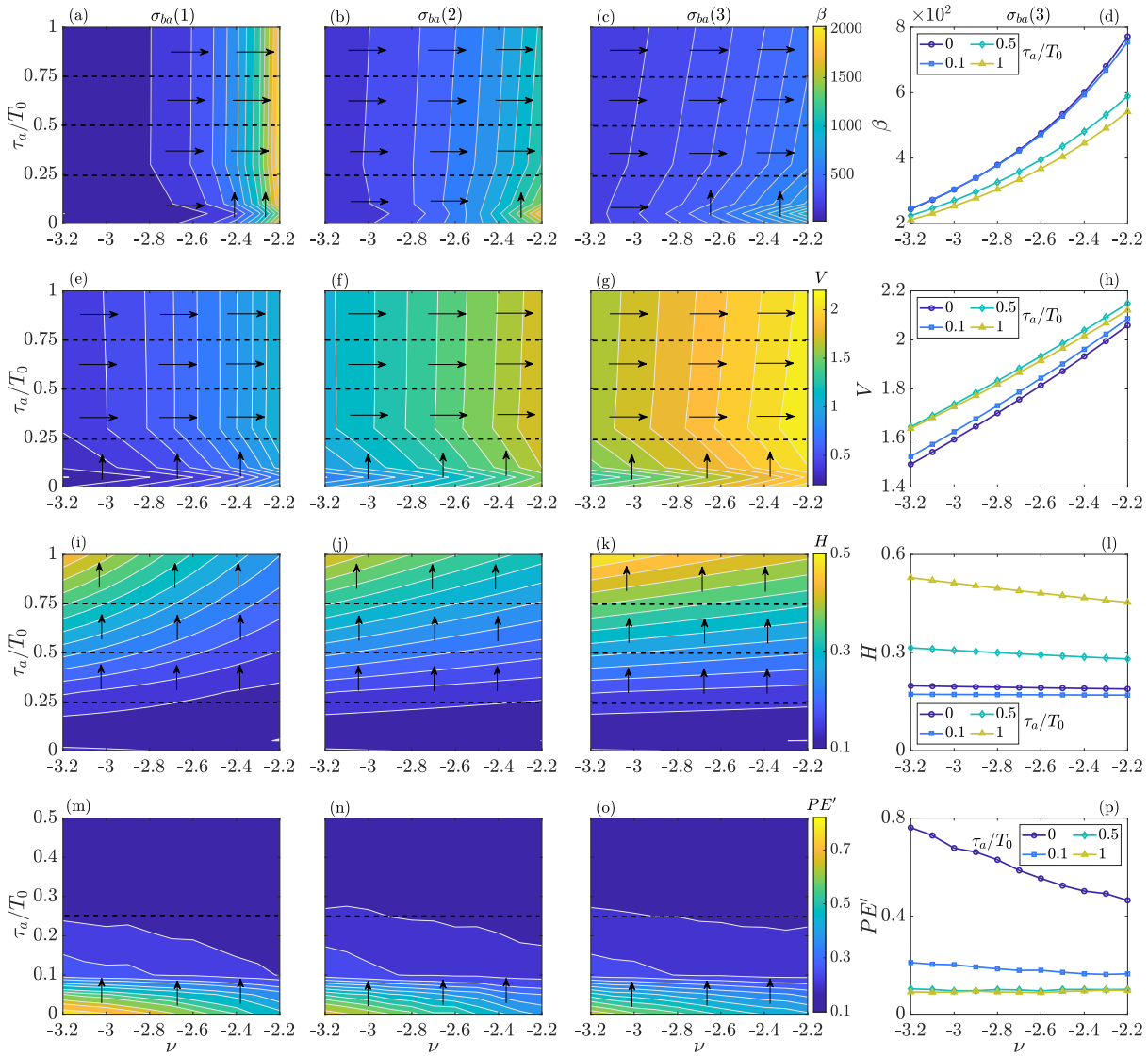

Figure 4.6: Additive noise driven system: variation of (a)-(d) coherence factor (β), (e)-(h) variance (V), (i)-(l) Hurst exponent (H) and (m)-(p) permutation entropy (PE') as a function of noise color (τ_a) and noise intensity (σ_{ba}). The dashed lines in the contour plots separate it into categories of low, moderate, and high noise correlation times. The arrows roughly indicate whether the variation in the EWI is greater in the direction of control parameter (horizontal) or in the direction of noise correlation time (vertical). The line plots in column 4 illustrates the general trend in each EWI as a function of control parameter at $\sigma_{ba}(3)$.

$\tau_m/T_0 > 0.1$. Hence, EWIs can not be estimated for small noise levels at large correlation times.

4.3.2 Effect of additive colored noise

Figure 4.6 shows the variation of coherence factor (β), variance (V), Hurst exponent (H) and permutation entropy (PE') as a function of noise color (τ_a/T_0), noise intensity (σ_{ba}) and control parameter (v) when the oscillator is excited by only additive noise (i.e. $\xi(t) \neq 0$ and $\chi(t) = 0$ in Eqn. (4.2)). An excitation by additive noise does not change the qualitative characteristics of the system, hence, we can investigate wide ranges of noise color for this case. We find that for a fixed v and σ_{ba}, coherence factor (Fig. 4.6(a)-(c)) exhibits an oscillatory behaviour with noise

color up to $\tau_a/T_0 = 0.05$. For $\tau_a/T_0 > 0.05$, β remains relatively constant with noise color at low (Fig. 4.6(a)) and moderate (Fig. 4.6(b)) noise intensities, while it consistently decreases with increase in noise color at $\sigma_{ba}(3)$ (Fig. 4.6(c)). If noise color and intensity are fixed (Fig. 4.6(d)), coherence factor increases as the system approaches the saddle-node point. This trend holds for the entire range of investigated noise color and intensity. Majorly, the changes in β are more sensitive to changes in v than τ_a, making it a reliable EWI except at low noise correlation times ($\tau_a/T_0 \leq 0.05$) in the vicinity of saddle-node point where changes in β are more influenced by τ_a than v (as indicated by arrows).

We observe that variance (Fig. 4.6((e)-(g)) also exhibits an oscillatory behaviour with noise color up to $\tau_a/T_0 \leq 0.05$ for all v and σ_{ba}, after which it becomes constant. Variance increases with increase in noise intensity at all v and τ_a. Further, when noise color and intensity are fixed (Fig. 4.6(h)), variance increases as the system approaches the saddle-node point. For all $\tau_a/T_0 > 0.05$, the changes in V are mostly influenced by the changes in control parameter than the noise color, as illustrated by the arrows.

We observe that the Hurst exponent (Fig. 4.6(i)-(k)) increases with increase in noise color at all v and σ_{ba}. We also observe that noise intensity do not significantly affect the values of Hurst exponent. When noise color and intensity are fixed (Fig. 4.6(l)), Hurst exponent decreases as the system approaches the saddle-node point, however, the amount of decrease in H is dependent on the noise intensity: H decreases faster at low noise levels (Fig. 4.6(i)) and relatively slower at high noise levels (Fig. 4.6(k)). Further, in this case as well, changes in H are more sensitive to changes in noise color than the control parameter at all σ_{ba} (indicated by the vertical arrows).

We observe that for a fixed v and σ_{ba}, permutation entropy (Fig. 4.6(m)-(o)) consistently decreases with increase in noise color up to $\tau_a/T_0 = 0.3$, after which it becomes constant (hence the contour plots extend only up to $\tau_a/T_0 = 0.5$). Similar to H, permutation entropy does not exhibit significant variations with noise intensity. We observe that as the system approaches the saddle-node point (Fig. 4.6(p)), PE' decreases for all $\tau_a/T_0 < 0.1$. At high correlation times ($\tau_a/T_0 \geq 0.1$), permutation entropy remains relatively constant with increase in v towards the saddle-node point. In this case as well, we observe that changes in PE' are influenced significantly by noise color than the control parameter (indicated by the vertical arrows).

Therefore, Fig. 4.6 indicates that a monotonous increase in coherence factor and variance as the system approaches the instability can be considered as effective EWIs in practical combustion systems when the background noise has significant contributions from additive sources, except when the noise color is very small, i.e. close to white noise approximation. Whereas, Hurst exponent can act as an effective EWI in systems where the noise correlation time is very large, i.e., $\tau_a/T_0 > 0.5$. Permutation entropy, on the other hand, can be employed as an EWI only in the systems featuring minimal correlation time i.e., where white noise approximation is acceptable.

4.3.3 Effect of multiplicative and additive colored noise

Figure 4.7 shows the variation of β, V, H and PE' as a function of noise color (τ_m and τ_a) and control parameter (v) at $\sigma_{bm}(3)$ and $\sigma_{ba}(3)$ when the system is excited by both multiplicative and additive noises (i.e. $\xi(t) \neq 0$ and $\chi(t) \neq 0$ in Eqn. (4.2)). In the figure, columns $1-3$ show

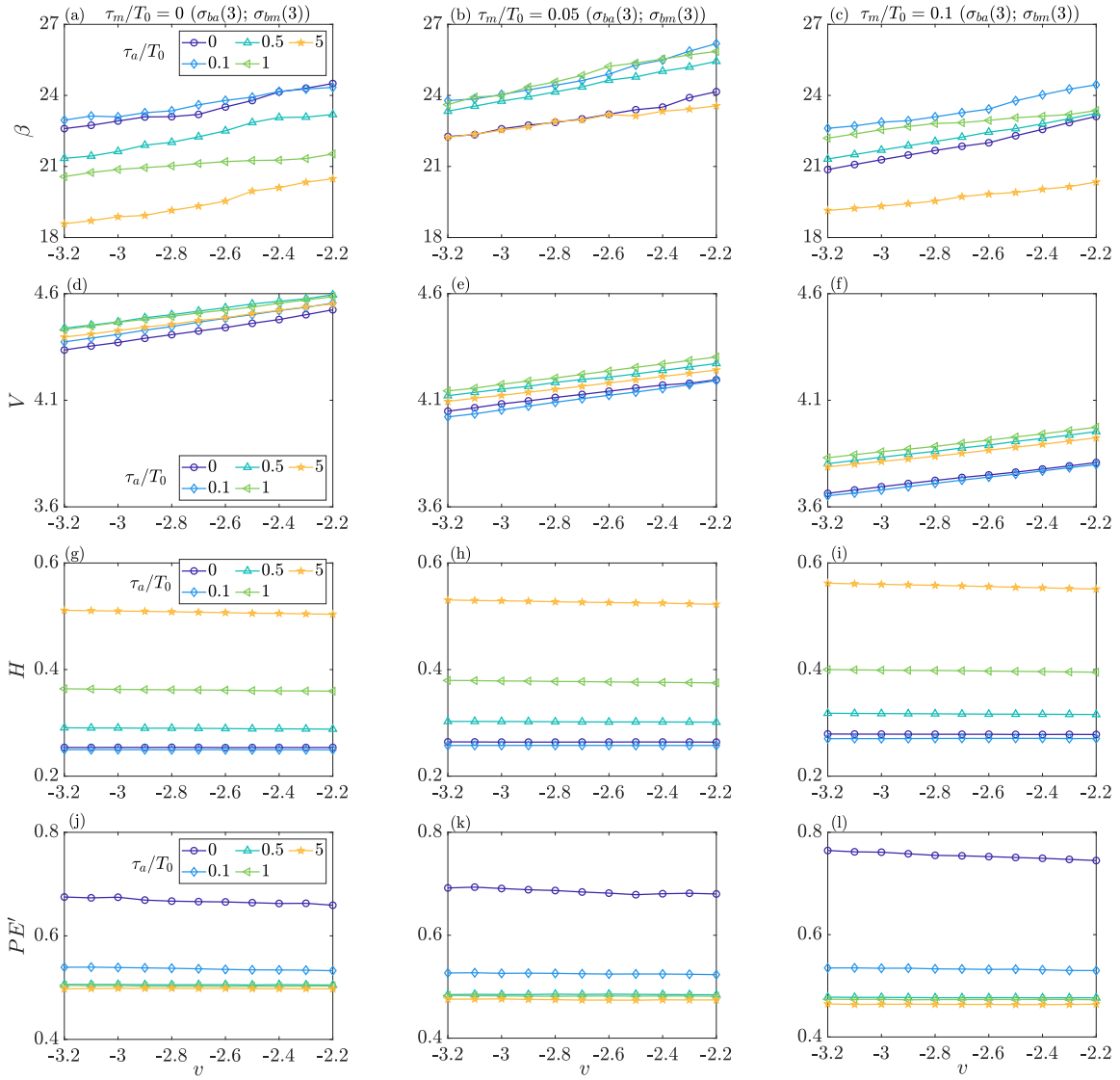

Figure 4.7: Multiplicative and additive noise driven system: variation of (a)-(c) coherence factor (β), (d)-(f) variance (V), (g)-(i) Hurst exponent (H) and (j)-(l) permutation entropy (PE') as a function of noise color (τ_m and τ_a) at $\sigma_{bm}(3)$ and $\sigma_{ba}(3)$.

the variation of EWIs with τ_m, while the individual curves inside each plot show the variation of EWIs with τ_a. We find that for a fixed v and σ, the coherence factor (Fig. 4.7(a)-(c)) exhibits an oscillatory behaviour with both τ_m and τ_a: β first increases with increase in τ, reaches a peak value at an optimum τ and after which it decreases with a further increase in τ. This optimum value of τ_m and τ_a at which peak β is observed, changes with change in the control parameter. We observe that for each τ, β increases monotonously as the system approaches the saddle-node point. We observe that changes in coherence factor are influenced equally by changes in both τ_a/T_0 and v when $\tau_m/T_0 = 0$, whereas for $\tau_m/T_0 > 0$, changes in β are more sensitive to the changes in control parameter than τ_a/T_0. Therefore, when noise color changes simultaneously with operating conditions, the trends in coherence factor can still be employed as effective EWIs.

We observe the following trends for variance (Fig. 4.7(d)-(e)): (i) for fixed τ_m and v, variance

exhibits oscillatory behaviour τ_a, (ii) for fixed τ_a and v, variance decreases consistently with increase in τ_m, and (iii) variance increases monotonously as the system approaches the saddle-node point at all τ_a and τ_m. We can observe that the deviation in the values of V with changes in noise color is less compared to its deviation with changes in the control parameter, therefore, in cases where noise color changes simultaneously with the operating conditions, the trends in variance can serve as reliable EWIs.

We observe that the Hurst exponent (Fig. 4.7(g)-(i)) increases with increase in both τ_a and τ_m at each v. Whereas, permutation entropy (Fig. 4.7(j)-(l)) decreases with increase in τ_a up to $\tau_a/T_0 = 1$, after which it becomes constant. While PE' increases with increase in τ_m at all τ_a/T_0 and v. A slight decrease in the Hurst exponent, as the system approaches the saddle-node point, can be observed when $\tau_a/T_0 \geq 0.5$ at all τ_m/T_0. On the other hand, the decrease in permutation entropy, as v is increased towards v_{SN}, is evident only when $\tau_a/T_0 < 0.1$ at all τ_m/T_0. For all other noise color values, these two indicators, do not show variations with changes in the control parameter. We can observe that the changes in the Hurst exponent and permutation entropy are predominantly influenced only by noise color. Therefore, in scenarios when noise color changes with operating conditions, these EWIs would be less reliable in predicting the impending instability.

Noise introduces both coherent and incoherent fluctuations, leading to a competition that results in coherence resonance (CR). This phenomenon is characterized by changes in spectral peak features, which become more pronounced as the system approaches the saddle-node point. The coherence factor, by analyzing these spectral characteristics, effectively tracks the system's approach to instability. It measures the degree to which the system's response is periodic and coherent, providing a clear signal as the system nears the Hopf bifurcation. Similarly, variance captures stochastic fluctuations by measuring deviations of data from their mean value. As stochastic fluctuations vary with changes in the control parameter, variance becomes a reliable predictor of impending limit cycle oscillations. This reliability stems from the fact that as the system approaches a bifurcation point, the increased sensitivity to perturbations results in larger deviations, which are well-captured by the variance. Other EWIs such as the Hurst exponent and entropy/complexity measures have limitations in their implementation for systems with dominant oscillations. The Hurst exponent, which measures the long-term memory of time series data, can be less effective in detecting the approach of instability in oscillatory systems because it is more sensitive to trends and long-term correlations rather than periodic changes. Similarly, entropy/complexity measures, which quantify the unpredictability and structural complexity of the time series, may not capture the regular periodic patterns associated with oscillatory systems. These metrics are more suited for systems where changes are not primarily driven by oscillatory dynamics.

Therefore, while coherence factor and variance provide robust and reliable early warning indicators for systems exhibiting oscillatory behavior and approaching bifurcation points, the Hurst exponent and entropy/complexity measures may have limitations in their implementation due to their design and sensitivity characteristics. This distinction is crucial for accurately predicting and managing thermoacoustic instability in practical applications, such as gas turbine

combustors, where noise and oscillations play significant roles.

4.3.4 Reliability of EWIs: recommendations for use in practical combustion systems

The background noise in a combustion system can exert various qualitative and quantitative effects on a combustor's dynamics. As the noise properties such as correlation time and intensity often vary alongside changes in system operating conditions, trends in several EWIs can become intricate and may exhibit non-monotonic trends, potentially resulting in inaccurate predictions of impending thermoacoustic instability.

In this study, the addition of noise aims to model the inherent noise—originating from fluctuations in fuel-air supply systems, variations in heat release due to unsteady combustion, fluctuations in the flow field, and aerodynamic noise—present in various combustion systems. To recommend the most reliable indicators for practical implementation, we perform the following sensitivity analysis for each EWI.

4.3.4.1 Sensitivity to variations in control parameter

For this investigation, we estimate the percentage change in each EWI as the control parameter approaches the Hopf bifurcation. The percentage change (Δ) in each EWI is calculated as follows:

$$\Delta = \frac{\text{EWI} - \text{EWI}_{ref}}{\text{EWI}_{ref}} \times 100 \tag{4.10}$$

where, EWI_{ref} is the value of EWI at the far away point from the Hopf bifurcation for each noise color, i.e., $v = -3.2$. This normalization ensures all curves in the plot begin at zero, highlighting

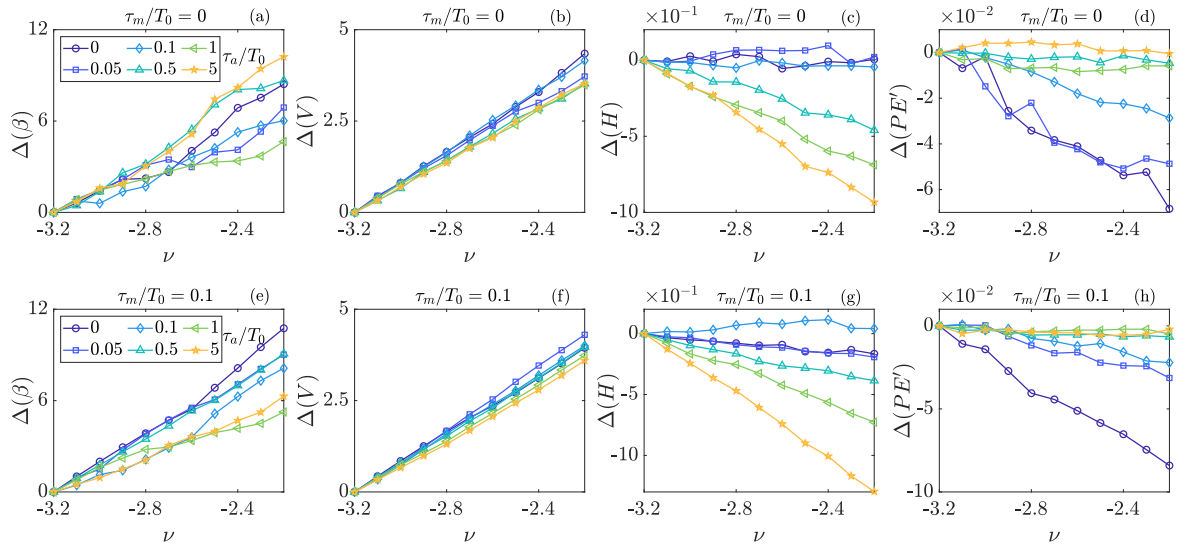

Figure 4.8: Multiplicative and additive noise driven system: Reliability of the various EWIs represented as the % change in each indicator (Δ) as the control parameter (v) is increased towards the saddle-node point ($v_{SN} = -2$) as a function of noise color (τ_m and τ_a) at $\sigma_{bm}(3)$ and $\sigma_{ba}(3)$. The top and bottom rows correspond to the cases when $\tau_m/T_0 = 0$ and $\tau_m/T_0 = 0.1$ respectively.

the maximum change in an EWI as the system approaches the saddle-node point.

Figure 4.8 show a comparative analysis of the various EWIs in terms of Δ as a function of noise color (τ_m and τ_a) at $\sigma_{bm}(3)$ and $\sigma_{ba}(3)$. We find that among the investigated EWIs, coherence factor (Fig. 4.8(a),(e)) and variance (Fig. 4.8(b),(f)) exhibit a consistent increasing trend at all combinations of τ_m and τ_a as the system approaches the saddle-node point, making them the most reliable EWIs for practical implementation. The implementation of a decrease in Hurst exponent (Fig. 4.8(c),(g)) and permutation entropy (Fig. 4.8(d),(h)) has limitations: Hurst exponent can work effectively when $\tau_a/T_0 > 0.5$, whereas permutation entropy can work in cases when additive noise has minimal correlation time ($\tau_a/T_0 < 0.1$), i.e. when white noise approximation is acceptable. These trends are true for all τ_m/T_0.

4.3.4.2 Sensitivity to variations in time series length

We examined how sensitive the estimated early warning indicators (EWIs) are to the length of the time series. Figure 4.9 illustrates the variation of different EWIs as a function of time series length and the control parameter (v) as a function of noise color (τ_a and τ_m) at $\sigma_{ba}(3)$ and $\sigma_{bm}(3)$. Our findings reveal that among the investigated EWIs, Hurst exponent (plots (c,g)) and permutation entropy (plots (d,h)) are most sensitive to the changes in time series length. These metrics show considerable variation with changes in the time series length, which can affect their reliability in real-time applications. Conversely, coherence factor (plots (a,e)) and variance (plots (b,f)) exhibit relatively stable trends regardless of the time series length, making them more dependable for accurate prediction.

In practical combustor configurations, the onset of instability can occur rapidly, often within a few seconds. Given this time constraint, we recommend using β and V as they provide

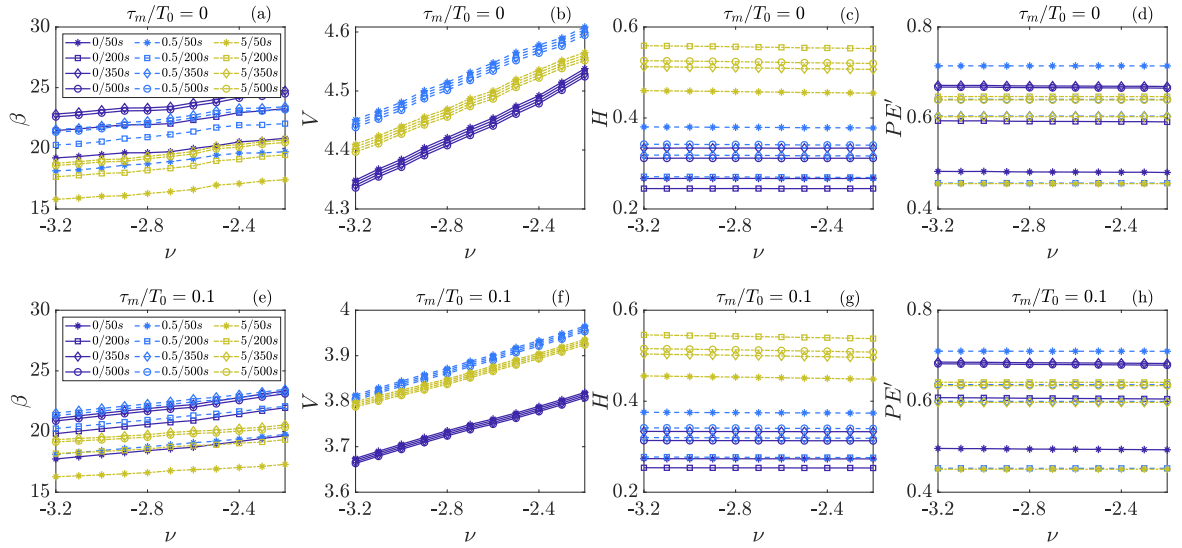

Figure 4.9: Multiplicative and additive noise driven system: Sensitivity of the various EWIs to the length of the time series as the control parameter (v) is increased towards the saddle-node point ($v_{SN} = -2$) as a function of noise color (τ_m and τ_a) at $\sigma_{bm}(3)$ and $\sigma_{ba}(3)$. The top and bottom rows correspond to the cases when $\tau_m/T_0 = 0$ and $\tau_m/T_0 = 0.1$ respectively.

reliable predictions even with shorter time series lengths. Their estimation process is also faster and less sensitive to variations in noise characteristics, making them suitable for real-time monitoring. On the other hand, EWIs such as the Hurst exponent and entropy/complexity measures require longer time series for accurate estimation and are more reliable at higher noise correlation times. This limitation hinders their effectiveness in real-time scenarios where quick decision-making is critical. Overall, while various EWIs offer different insights, our study highlights the importance of selecting appropriate indicators like the coherence factor and variance for real-time applications due to their robustness, quick estimation, and minimal sensitivity to time series length and noise characteristics. This approach ensures timely and accurate detection of thermoacoustic instability.

An important note here is that as per the nature of the EWIs, a unique correlation between the absolute value of EWIs and the Hopf or saddle node points cannot be obtained. Thus, to identify the stability boundary, a calibration is necessary — regardless of the chosen EWI. If inconsistencies and errors in system input or system control are present, such issues will have to be either addressed (removed) or incorporated in the calibration to ensure safe system operation — the latter strategy will lead to a smaller system operating envelope. This might not always be feasible. In such cases, the observation that reliable EWI measures (as identified in our work) are changing with a prominent trend is an indication that the system is approaching a bifurcation as sufficiently far away, changes in EWI will be minimal and without a monotonous trend. The phrase 'sufficiently far away' will be system-dependent but as per previous reports on noise-induced coherence, the efficacy of noise to cause noise-induced oscillations is expected to decay rapidly with increasing separation from the stability boundary.

Chapter 5

Implementation of Early Warning Indicators (EWIs) in Experiments

5.1 Overview

In this work, we extend the numerical investigations discussed in Chapters 2-4 and show the practical implementation of the recommended EWIs on a laminar combustion system operating on lean premixed natural gas-air mixtures (shown in Fig. 5.2). This lean premixed combustion system undergoes transition to thermoacoustic instability via a subcritical Hopf bifurcation. We choose noise intensity to be the varying parameter for this investigation as intensity of noise (whether white or colored), has been reported to play crucial roles in changing the stability margins of the system [76], causing noise-induced transitions to instability in bistable region [3, 73] and affecting the estimation growth/decay rates of thermoacoustic oscillations [161, 190]. The primary objective of this study is to test the reliability of various EWIs discussed in chapters 2-4, in a practical combustion system. This investigation provides practical insights for choosing appropriate EWIs in systems where noise characteristics can change with changes in operating conditions, specifically in turbulent combustors, to accurately detect the system's proximity to the impending thermoacoustic oscillations.

This chapter is further divided into two sections. Section 5.2 describes experimental setup and brief methodology to estimate various EWIs. Section 5.3 shows the effects of noise intensity

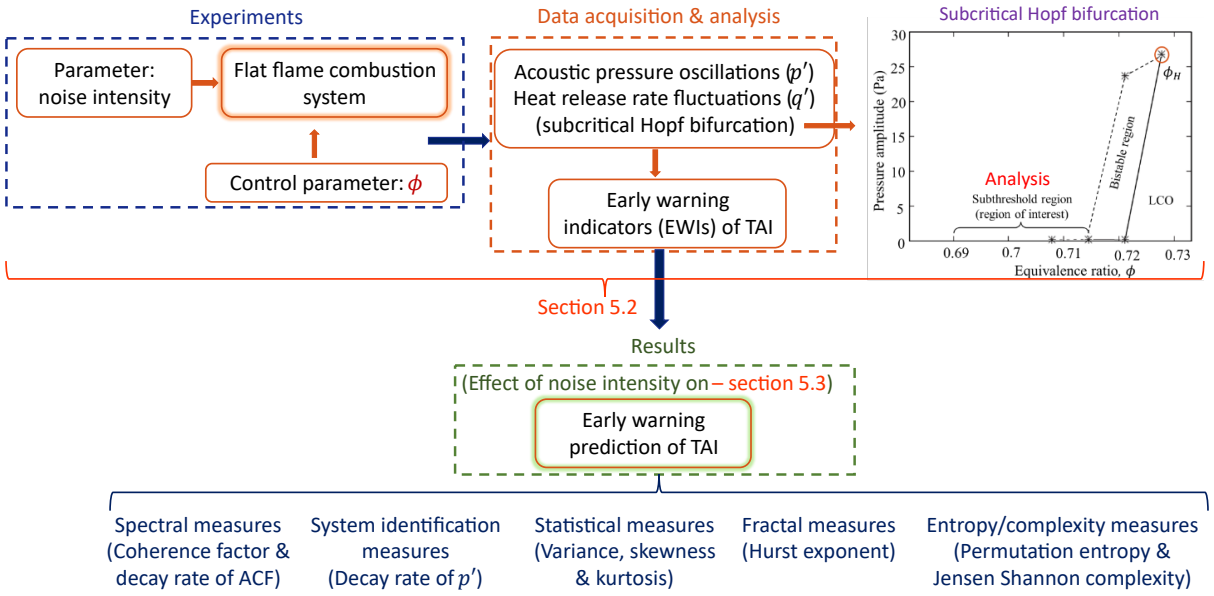

Figure 5.1: Visual summary of the contents for Chapter 5. TAI stands for thermoacoustic instability.

on the estimated EWIs and discuss their reliability when implemented in real systems. A brief overview of the summary for the contents of the chapter is shown in Fig. 5.1.

5.2 Experimental setup and methodology

5.2.1 Experimental setup

In this work, experiments are conducted using a prototypical combustor, schematically shown in Fig. 5.2, which operates on premixed natural gas-air mixtures under lean conditions. The combustor (inner diameter = 105 mm) consists of an upstream plenum (length = 570 mm), a combustion source (laminar quasi flat 50 mm diameter conical flame stabilized on a perforated copper plate), a quartz duct (length = 300 mm) for optical access of flame and a downstream exhaust (length = 315 mm). The plenum is mounted with two acoustic actuators and an inlet for premixed fuel-air mixtures, while the exhaust is mounted with thermocouples and water-cooled microphones for temperature and acoustic pressure measurements, respectively. A silencing device consisting of three alternating layers of aluminium discs and fire proof foam which reduces the flow noise due to the entering fuel-air mixture to $p'_0 = 0.18$ Pa(rms). The upstream and downstream ducts are separated by a perforated brass plate which acts as a flame

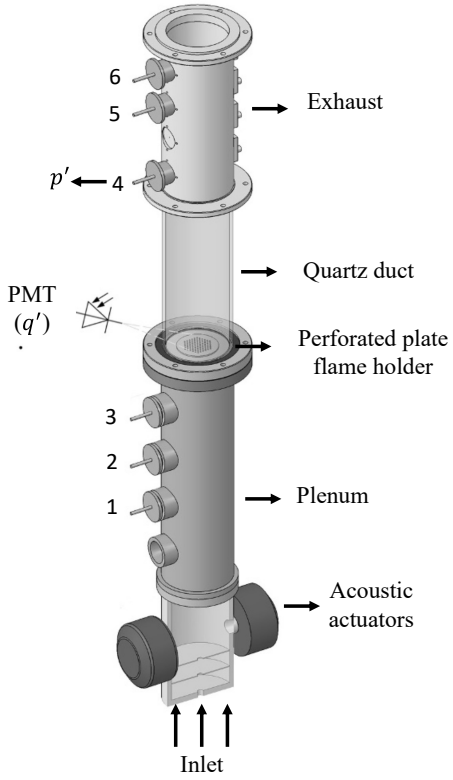

Figure 5.2: Flat flame combustion system operating on lean premixed natural gas-air mixtures. The setup consists of a plenum mounted with two acoustic actuators and upstream pressure microphones (1 to 3), a quartz duct for acquiring q' with the help of photo-multiplier tube (PMT) and an exhaust duct mounted with downstream pressure microphones (4 to 6). Analysis based on p' from microphone 4 and q' from PMT are presented in subsequent sections.

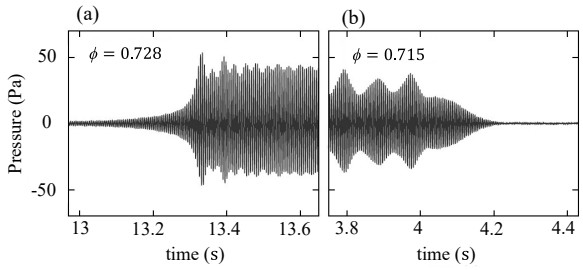

Figure 5.3: Noise-free system (no acoustic excitation through loudspeakers): Transition to (a) self-excited limit cycle oscillations at $\phi = 0.728$ and (b) to stable state at $\phi = 0.715$.

holder. It has 91 holes with a diameter of $d_h = 2$ mm which are arranged in a hexagonal shape with a circumscribing circle with a diameter of $d_c = 50$ mm. The flow passes the holes with a mean velocity of $u = 1.13$ m/s, resulting in a Reynolds number of $Re = 147$ and thus providing a laminar flow.

In the experiments, the airflow rate is kept constant at 0.36 g/s and the equivalence ratio, ϕ, is chosen as the control parameter, whose values are varied in the range 0.688 to 0.735 in steps of 0.007 (standard deviation in ϕ, calculated from air/fuel measurements is 0.002). Given the dimensions of the upstream plenum, and low values of the air/fuel flow rates, fluctuations in ϕ are expected to be lower than the measured error in ϕ, upstream of the flame. The corresponding fuel flow rates are in the range 0.0144 g/s to 0.0154 g/s. The air/fuel mass flow rates are measured using coriolis flow meters, regulated by PID valves: an Endress + Hauser PROMASS A80 (nominal uncertainty $\pm 0.5\%$) is used for air and a Bronkhorst mini CORI-FLOW (nominal uncertainty $\pm 0.2\%$) integrates both flow meter and valve for fuel.

The setup consists of a total of 6 microphones mounted in normal direction with respect to the setup, three (mic. $1-3$) are located in the upstream plenum and three (mic. $4-6$) are located in downstream exhaust duct. All the microphones are calibrated to account for phase and magnitude. For microphones $1-3$, the calibration is conducted on a separate tube of wall thickness equal to that of the plenum, while for microphones $4-6$, the calibration is conducted at the exhaust duct itself by flush mounting a reference microphone to its inner surface opposite to each microphone. We present here the analysis based on acoustic pressure oscillations (p') acquired in the exhaust duct through microphone 4 at a sampling rate of 8192 Hz as this microphone featured the smallest deviation from the reference microphone and is located closest to the flame. The heat release rate fluctuations (q') are also acquired from CH chemiluminescence using a photo-multiplier tube (PMT) at the flame through the quartz glass duct. Each measurement is recorded for 32 s. Using a K-type thermocouple (measurement error $\pm 2.2°$C), the temperature at the interface between the quartz duct and the perforated plate flame holder is monitored. Experiments are performed after the measured temperature reaches a steady state.

We first perform the bifurcation experiments in the noise-free system to track the system's transition to thermoacoustic instability and identify the stability margins. In the absence of external acoustic excitation, as the control parameter, ϕ is varied in forward and backward direction, the system transitions between steady state and limit cycle oscillations (LCO). An

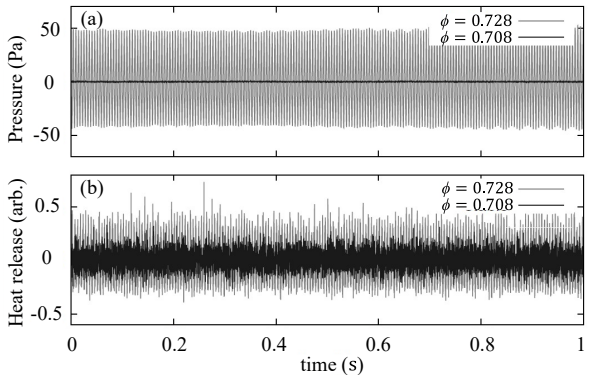

Figure 5.4: Noise-free system (no acoustic excitation through loudspeakers): Exemplary time series of (a) acoustic pressure oscillations (p') and (b) heat release rate fluctuations (q') at $\phi = 0.728$ (limit cycle oscillations) and $\phi = 0.708$ (stable system).

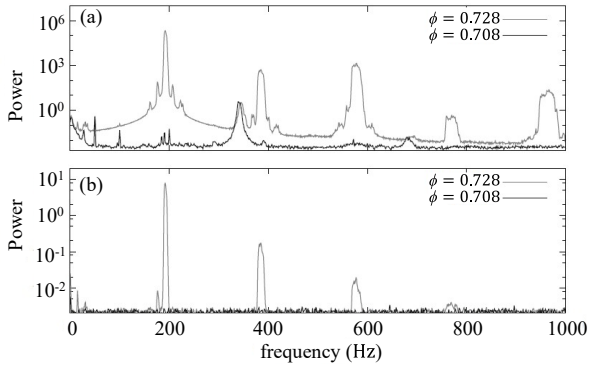

Figure 5.5: Noise-free system (no acoustic excitation through loudspeakers): Exemplary frequency spectrum of (a) acoustic pressure oscillations (p') and (b) heat release rate fluctuations (q') at $\phi = 0.728$ (limit cycle oscillations) and $\phi = 0.708$ (stable system).

exemplary illustration of transition between two states (steady and LCO), time series and corresponding power spectra for both p' and q' are shown in Fig. 5.3-5.5 respectively. The maximum instantaneous pressure amplitude of instability observed is 52.10 Pa. As the control parameter, ϕ is varied, the system undergoes a transition to self-induced limit cycle oscillations via a subcritical Hopf bifurcation with Hopf and saddle-node points observed at $\phi_H = 0.728$ and $\phi_{SN} = 0.715$ respectively, shown in Fig. 5.6. The solid and dashed curves represent the forward and reverse directions of the bifurcation analysis, respectively. The region before the saddle-node point is termed as the subthreshold region, where the only attractor available is the stable focus, and the region beyond the Hopf point is the linearly unstable region (thermoacoustic instability). A bistable region exists between $0.715 \leq \phi \leq 0.728$. In this region, small perturbations can trigger large amplitude limit cycle oscillations [73, 116]. Therefore, the EWIs are of practical relevance only till the saddle-node point. Hence, we focus our investigation on the subthreshold region where the system is in a stable state. Multiple realizations of the experiments are performed to ensure the accuracy of the saddle-node point (see Fig. E.1 in Appendix E). The frequency spectrum of oscillations in p' and q' during limit cycle peaks at 191 Hz.

The present investigation aims to study the effect of noise intensity on the early warning

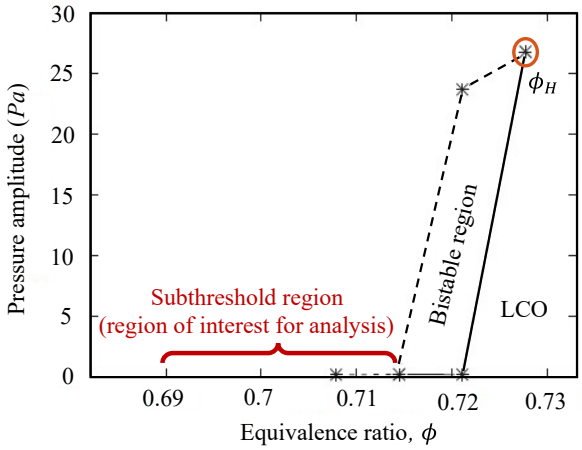

Figure 5.6: Subcritical Hopf bifurcation in the noise-free system. The solid line connects experimental points obtained by increasing ϕ, while the dashed line indicates translation in the reverse direction. The Hopf and saddle-node points are observed at $\phi_H = 0.728$ and $\phi_{SN} = 0.715$ respectively. A bistable region exists between $0.715 \leq \phi \leq 0.728$. LCO represents the limit cycle oscillations. The analysis is performed in the subthreshold region with ϕ varying in the range 0.695 to 0.714.

indicators of thermoacoustic instability. For this purpose, external excitation is added to the system through the two acoustic actuators, driven by white Gaussian noise voltage signals generated at 16384 Hz. The noise intensity, σ, is systematically varied in the range 5.7 Pa to 17 Pa in steps of 1.4 Pa. σ is the root mean square value of the acoustic noise level measured at the microphone location. The power spectrum of the input white noise signals at varied intensities is shown in Fig. 5.7. σ is interchangeably termed either the noise level or the noise intensity, as appropriate, in the subsequent sections. All the measurements are taken 30 s after the noise intensity is increased. The experiments are repeated seven times for each equivalence ratio. As the noise intensity increases, stochastic fluctuations in the system also increase.
The corresponding system's response to varied noise levels in the subthreshold region in amplitude and frequency domains is shown in Fig. 5.8 and Fig. 5.9 respectively. Figure 5.8 shows

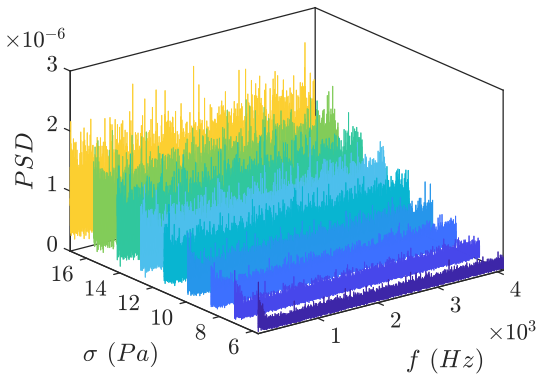

Figure 5.7: Power spectrum of white noise input given to the speaker at varied intensities on y-axis.

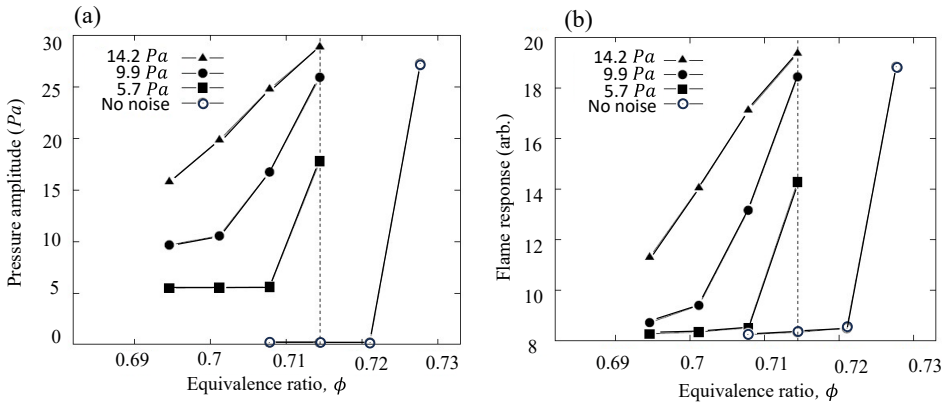

Figure 5.8: Noisy system: (a) Pressure (p'_{rms}) and (b) flame (q'_{rms}) response to noisy excitation in subthreshold region. The noise levels represent the measurements without the flame (reproduced from Kabiraj et al. [6]).

the rms values of acoustic pressure (p') and heat release rate (q') fluctuations as a function of ϕ in the stable region at varied noise intensities. Each data value represents the average of 7 measurements at same operating condition. The vertical line in the plots separate the stable and bistable regions. We can observe from the plots that the response of both p' and q' increases with increase in both noise intensity and equivalence ratio. However, at $\sigma = 5.7$ Pa, p' does not depend on ϕ until saddle-node point is reached. Figure 5.9 shows the waterfall plots for power spectrum of system's response as a function of noise intensity (on y-axis) at two equivalence ratios, $\phi = 0.708$ (left plot) and $\phi = 0.714$ (right plot) respectively. As noise intensity increases, the spectral peak, observed at 191 ± 3 Hz, initially rises with increasing noise intensity, reaches a maximum at intermediate noise levels, and then decreases. These fluctuations, caused by the introduction of noise in the stable system, are used to estimate various Early Warning Indicators (EWIs) for predictive purposes. The width of the spectral peak also changes with noise intensity. The variation in the peak height and width with control parameter and noise variation is best captured in the coherent factor (β) as reported in Kabiraj et al. [6].

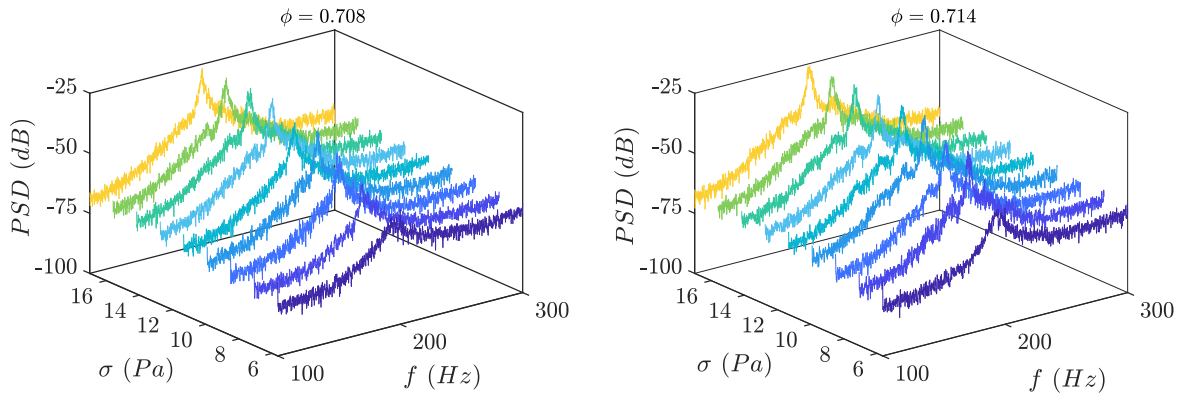

Figure 5.9: Noisy system: Frequency spectra of p' for the system excited by noise at $\phi = 0.708$ (left) and $\phi = 0.714$ (right). The different colors in the plots (ranging from blue to yellow) correspond to increasing noise intensities marked on y-axis.

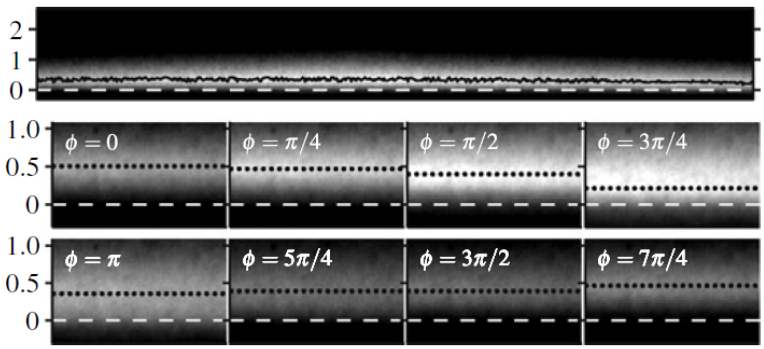

Figure 5.10: Top: mean image of the flame. The black solid line represents the maximum intensity along the vertical direction, while the dashed white line marks the location of the perforated plate. The vertical scale is in mm (true aspect ratio). Bottom: Phase-averaged images of the center part of the flame subjected to harmonic forcing are presented. The black dotted lines denote the vertical location of the maximum intensity integrated along the horizontal direction (adapted from Moeck et al. [7]).

Along with the time series signals and corresponding power spectrum, we also show the kinematics of a flat flame during thermoacoustic instability in the subthreshold regime in Fig. 5.10. Acoustic noise is introduced into the system. The system itself comprises of the combustor acoustics and the flame. The flame responds to acoustic fluctuations and acoustic fluctuations are generated as per flame response. The flame response to noise will be kinematically similar. In Fig. 5.10, the top image correspond to the mean image of the side-view of the flame and bottom images correspond to its response to acoustic excitation. The horizontal extent corresponds to approximately half of the burner plate. Based on the maximum intensity along every image column, the flame can be considered flat. The intensity has a larger vertical extent in the middle due to the flame's circular shape. The two bottom frames show phase-averaged intensity distributions for forcing at the fundamental frequency and a velocity fluctuation amplitude of 0.5 m/s. These phase-averaged images reveal that the flame reaches its maximum intensity while moving upstream to the burner. At the minimum stand-off distance, the intensity drops and remains low while moving back downstream.

5.2.2 Methodology

In this chapter, we investigate the practical implementation of the various EWIs based on spectral properties (coherence factor), autocorrelation (decay rate), system identification (growth/decay rates of p'), statistical measures (variance, skewness and kurtosis), multi-fractality (Hurst exponent) and time series complexity measures (permutation entropy and Jensen-Shannon complexity). The detailed methodology along with the specifications of parameters for estimation of these EWIs are discussed in section 3.2.4. A brief summary of the formulations to estimate various EWIs along with their monotonic trend is illustrated in Fig. 5.11.

EWI class	EWI	Formulation	Trend
Spectral measures	Coherence factor	$\beta = H_P \times (f_P/\Delta f)$	Increases
	Decay rate of ACF (α)	$AC = (E[(x_{t1} - \bar{x})(x_{t2} - \bar{x})])/V$	
System Identification measures	Decay rates of p' (v)	Fokker Planck equation	Increases
Statistical measures	Variance	$V = \frac{1}{N}\sum_{i-1}^{N}(x_i - \bar{x})^2$	Increases
	Skewness	$S = \left(\sum_{i=1}^{N}(x_i - \bar{x})^3/N\right)/V^{3/2}$	
	Kurtosis	$k = \left(\sum_{i=1}^{N}(x_i - \bar{x})^4/N\right)/V^2$	
Multi-fractal measures	Hurst exponent	$F_q \sim w^{H_q}$	Decreases
Entropy measures	Permutation entropy	$PE = -\sum_{\pi} p(\pi)\log_2 p(\pi)$	Decreases
	Jensen-Shannon complexity	$C_P = Q_j[P, P_e]PE[P]$	Increases

Figure 5.11: A brief summary of methodology to estimate various early warning indicators in the subthreshold region along with their monotonic trend (marked in Fig. 5.6).

5.3 Effect of noise characteristics on EWIs

This section discusses the effects of noise intensity on the various early warning indicators estimated in the subthreshold region (marked in Fig. 5.6). The saddle-node point occur at $\phi_{SN} = 0.715$ respectively. The results corresponding to each EWI are presented as 2D contour maps in the parameter space ($\sigma - \phi$). Each plot is subdivided into categories of low, moderate, and high noise levels by dashed lines. To illustrate whether the variation in an EWI is more sensitive to changes in noise intensity or control parameter, vertical and horizontal arrows are provided in each plot respectively. In each plot, a 4x4 grid (16 points in $\sigma - \phi$) is chosen, and the arrows are placed at those 16 points.

5.3.1 Effects of noise intensity on coherence factor and autocorrelation

Figure 5.12 shows the variation of coherence factor (β) and decay rates (α) of ACF as a function of noise intensity (σ) and control parameter (ϕ), estimated from p'. We can observe the occurrence of coherence resonance [6, 47] from Fig. 5.12(a): (i) for each ϕ, β attains a peak value at intermediate noise levels, and (ii) peak coherence is induced at a lower noise level as ϕ approaches the Hopf bifurcation. We observe that for a fixed noise level, β increases as the system approaches the instability. This monotonous increasing trend of β is observed at most noise levels, except for 15.58 Pa $< \sigma <$ 11.33 Pa, where peak coherence is induced (as indicated by black (dashed) and red (solid) arrows). We can also observe that far away from the Hopf bifurcation ($\phi < 0.701$), the variation in β is too small to distinguish a trend. This is because, at low ϕ, the peak coherence is induced at significantly large noise intensities.

Noise induces both coherent and incoherent fluctuations in the system, a competition between these fluctuations result in the occurrence of coherence resonance (CR). This is manifested by

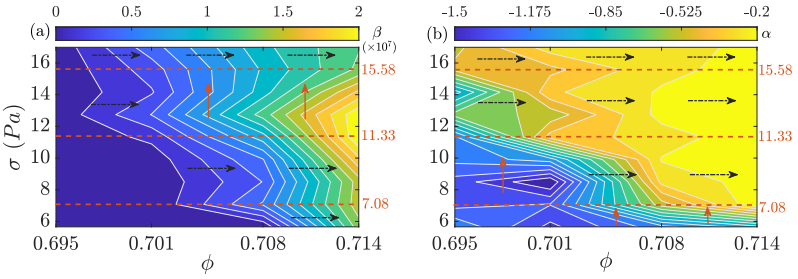

Figure 5.12: 2D contour map of (a) coherence factor (β) and (b) decay rates of ACF (α) as the control parameter (ϕ) and noise intensity (σ) are varied. The arrows roughly indicate whether the variation in β and α is greater in the direction of control parameter (horizontal black dashed arrows) or in the direction of noise intensity (vertical red solid arrows). The red dashed lines separate the plots into categories of low, moderate, and high noise levels.

changes in spectral peak characteristics, which become more distinct as ϕ increases towards the saddle-node point. As coherence factor is estimated using the spectral features, it effectively tracks the approaching instability. Thus, in a combustion system, the coherence factor will always increase as the system is brought closer to bifurcation. In case noise intensity is varying simultaneously with changes in control parameter, the presence of an optimum noise intensity due to coherence resonance can cause deviation from monotonous trends in the coherence factor at intermediate noise levels (indicated by red arrows).

Similar to the coherence factor, the decay rates (α) of ACF also exhibit oscillatory behaviour with noise intensity (Fig. 5.12(b)): α increases at low noise levels, attains a peak value at intermediate level and after that decreases with a further increase in the noise level; however, the oscillatory response is not as prominent as that of β. We further observe that α increases as the system approaches the instability at most noise levels except for $\sigma < 7.08$ Pa, where the variation in the values of α are more sensitive to changes in σ than ϕ (as shown by the red (solid) arrows). Also, for 7.08 Pa $< \sigma <$ 11.33 Pa, far away from the Hopf bifurcation ($\phi < 0.701$), changes in α depend on noise level than ϕ. This implies that when noise intensity changes with the control parameter, trends in α can become non-monotonous.

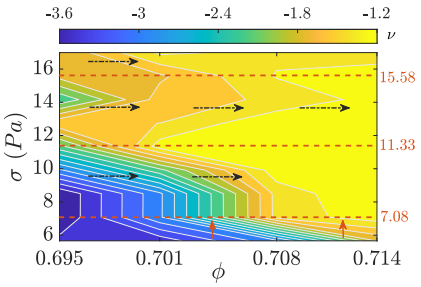

Figure 5.13: 2D contour map of decay rates of acoustic oscillations (ν), as the control parameter (ϕ) and noise intensity (σ) are varied. The arrows roughly indicate whether the variation in ν is greater in the direction of control parameter (horizontal black dashed arrows) or in the direction of noise intensity (vertical red solid arrows). The red dashed lines separate the plots into categories of low, moderate, and high noise levels.

5.3.2 Effects of noise intensity on decay rates of acoustic oscillations

Figure 5.13 shows the variation of decay rates of p' with noise intensity (σ) and control parameter (ϕ). We observe that the estimation of decay rates is influenced by noise intensity, causing a deviation from the true values (ν at $\sigma = 0$). Specifically, for each ϕ, an increase in σ leads to an increase in ν. This deviation in the estimation of ν with varying σ has been previously reported by Vishnoi et al. [161,190] across all three regions of the Hopf bifurcation. We further find that ν increases as the system approaches the saddle-node point at most noise levels (depicted by black (dashed) arrows). However, when noise levels are low ($\sigma < 7.08$ Pa) and cover the range of 8.5 Pa to 11.33 Pa, the deviations in ν are more contingent on changes in σ than ϕ (illustrated by red (solid) arrows). Thus, an increase in ν can be employed as an EWI for systems with moderate or high noise levels.

5.3.3 Effects of noise intensity on statistical measures

Figure 5.14 shows the variation of variance, skewness and kurtosis with noise intensity (σ) and control parameter (ϕ), estimated from p'. We observe that for each ϕ, variance and skewness increase with an increase in noise intensity, whereas kurtosis does not exhibit any specific trend with noise intensity. We can observe from Fig. 5.14(a) that variance increases as the system approaches the instability; however, the amount of increase in variance depends on noise level and distance from Hopf bifurcation (shown by black (dashed) and red (solid) arrows): (i) for low noise levels, i.e., $\sigma < 7.08$ Pa, variance shows no significant changes with ϕ; (ii) for noise levels ranging between 7.08 Pa $< \sigma <$ 10 Pa and 11.33 Pa $< \sigma <$ 12.74 Pa, changes in variance are more sensitive to changes in σ than ϕ, implying non-monotonous trends in cases where noise intensity will change with control parameter. Also, far away from Hopf bifurcation, i.e., $\phi < 0.701$, changes in V mostly depend on noise intensities. Thus, an increase in variance can be employed as an effective early warning indicator for combustion systems featuring high noise levels (in our case for $\sigma > 12.74$ Pa).

Figure 5.14(b) shows that skewness increases as the system approaches the instability at most noise levels except for $\sigma < 7.08$ Pa (shown by black (dashed) and red (solid) arrows). At low

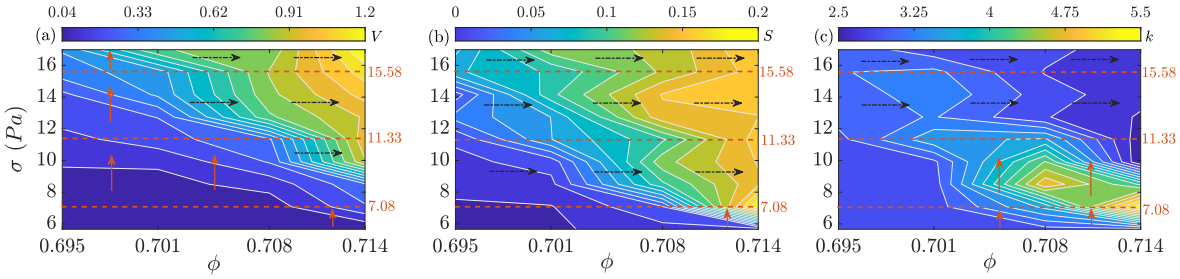

Figure 5.14: 2D contour map of (a) variance (V), (b) skewness (S) and (c) kurtosis (k) as the control parameter (ϕ) and noise intensity (σ) are varied. The arrows roughly indicate whether the variation in V, S and k is greater in the direction of control parameter (horizontal black dashed arrows) or in the direction of noise intensity (vertical red solid arrows). The red dashed lines separate the plots into categories of low, moderate, and high noise levels.

noise levels, changes in skewness are dominated by changes in σ, leading to non-monotonous trends in a real system. Figure 5.14(c) shows that for noise levels up to $\sigma = 8.5$ Pa, kurtosis increases close to the Hopf bifurcation. In contrast, for 8.5 Pa $< \sigma <$ 11.33 Pa, kurtosis gradually increases as ϕ is increased up to $\phi = 0.708$ and then decreases near the saddle-node point. For all $\sigma >$ 11.33 Pa, kurtosis decreases as the system approaches the instability. In all cases, kurtosis exhibits no clear trend with either noise intensity or control parameter, which implies its inaccuracy as an early warning measure.

5.3.4 Effects of noise intensity on multi-fractal and time series complexity measures

Figure 5.15 shows the variation of Hurst exponent, permutation entropy and Jensen-Shannon complexity with noise intensity (σ) and ϕ estimated from p'. We find from Fig. 5.15(a) that for a fixed ϕ, the Hurst exponent does not exhibit a specific trend with an increase in noise intensity. At the same time, it decreases monotonously as ϕ is increased towards instability at most noise levels except for $\sigma <$ 11.33 Pa (as indicated by black (dashed) arrows). For noise levels, $\sigma <$ 7.08 Pa, and 8.5 Pa $< \sigma <$ 11.33 Pa, H is more sensitive to changes in σ than ϕ (indicated by red (solid) arrows). Therefore, a decrease in H as an early warning measure is suitable for systems featuring high noise levels. Waxenegger-Wilfing et al. [98], in their experiments on a rocket thrust chamber, have also reported that increased fluctuations in the Hurst exponent lead to false alarms and inaccurate predictions.

Figure 5.15(b) and (c) show that permutation entropy increases while Jensen-Shannon complexity decreases with an increase in noise intensity for each ϕ up to $\phi = 0.708$. Near the saddle-node point, PE and CP show non-monotonic response with σ. We observe that PE decreases while CP increases as the system approaches the instability for high noise levels, i.e., for all $\sigma >$ 11.33 Pa (indicated by black (dashed) arrows). Similar to Hurst exponent, at $\sigma <$ 7.08 Pa and 8.5 Pa $< \sigma <$ 11.33 Pa, PE and CP are also more sensitive to changes in σ than ϕ (red (solid) arrows), making them unsuitable early warning measures at such noise levels.

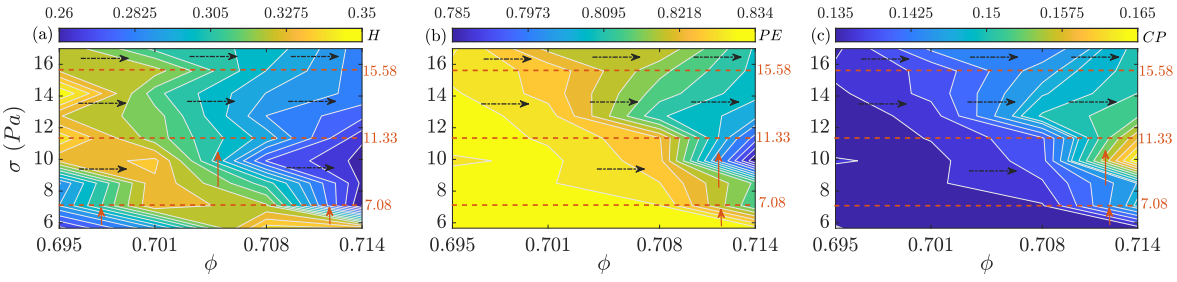

Figure 5.15: 2D contour map of (a) Hurst exponent (H), (b) permutation entropy (PE) and (c) Jensen-Shannon complexity (CP) as the control parameter (ϕ) and noise intensity (σ) are varied. The arrows roughly indicate whether the variation in H, PE and CP is greater in the direction of control parameter (horizontal black dashed arrows) or in the direction of noise intensity (vertical red solid arrows). The red dashed lines separate the plots into categories of low, moderate, and high noise levels.

5.3.5 Reliability of early warning indicators

Figures 5.12-5.15 illustrated the characteristics and limitations of various EWIs at varied noise levels. We now discuss the reliability of employing these EWIs in practical combustors to predict thermoacoustic instability accurately. Figure 5.16 shows a comparative analysis (or cross-analysis) of the various EWIs in normalized form as the system approaches the instability. The normalization in each EWI is calculated as,

$$\chi = \left| \frac{\text{EWI} - \text{EWI}_{@5.7\text{Pa};\phi=0.695}}{\text{EWI}_{@5.7\text{Pa};\phi=0.695}} \right| \tag{5.1}$$

The error-bars in each plot in Fig. 5.16 represent the standard deviation observed in estimated EWIs over multiple experiments. However, please note that the methods considered have never been used previously with error bounds/uncertainty due to the nature and purpose of EWIs. Therefore, we emphasize on the uncertainty associated with the experiments. We find that among all the EWIs investigated, the coherence factor (Fig. 5.16(a)) shows the maximum variation ($\sim$ order of 10^3) in its value as the system approaches the Hopf bifurcation at all noise levels, making it the most reliable early warning indicator for practical combustors. Variance (Fig. 5.16(d)) and skewness (Fig. 5.16(e)) shows a variation of the order of $\sim$ 30 and $\sim$ 10

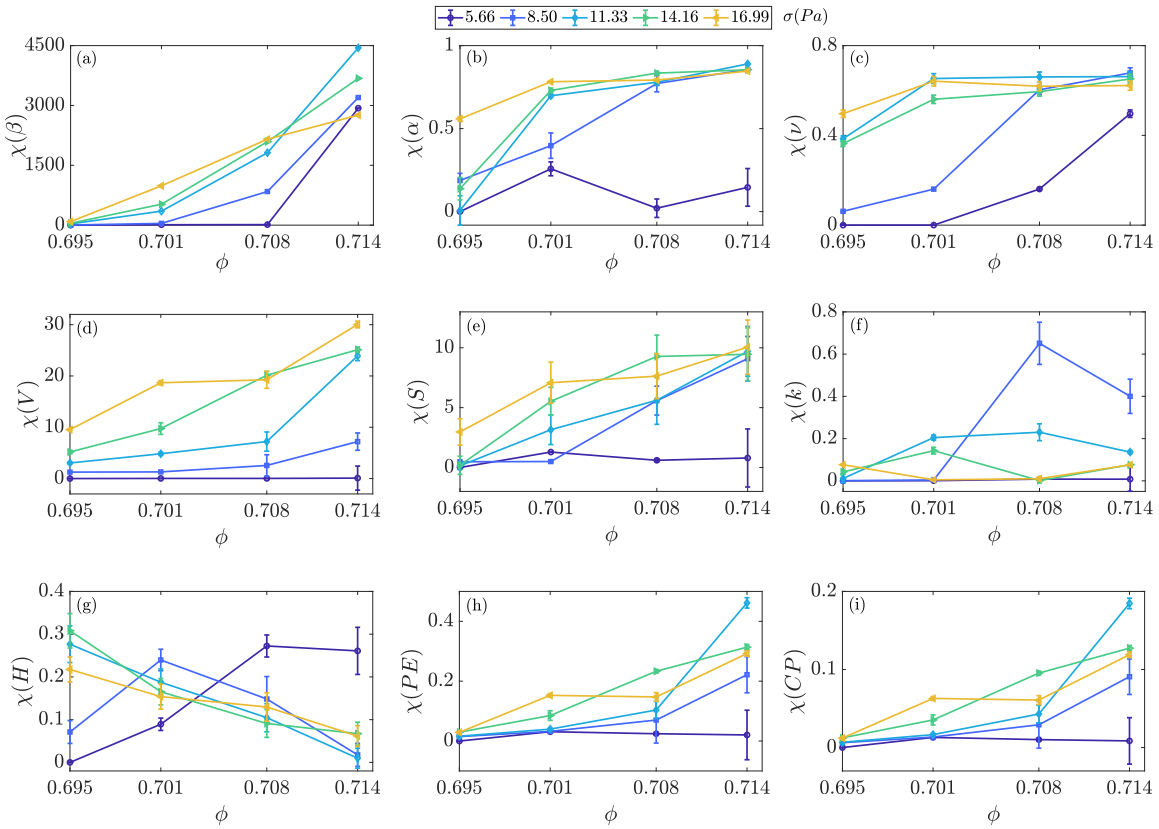

Figure 5.16: Reliability of various EWIs, estimated using p' data, represented in normalized form as the control parameter (ϕ) is increased towards the Hopf bifurcation at varied noise levels (σ). The error-bars represent the standard deviated observed in estimated EWIs over multiple experiments.

respectively, which makes them robust indicators as well. The decay rates of ACF (Fig. 5.16(b)), decay rates of acoustic oscillations (Fig. 5.16(c)) and Hurst exponent (Fig. 5.16(g)) falls next on the reliability index as the maximum variation in their values are between 0.3 and 0.8. The maximum changes in entropy/complexity measures (Fig. 5.16(h)-(i)) are below 0.2, indicating lower reliability compared to other EWIs. It is important to note that indicators such as α, V, S and H prove effective only above a certain threshold of noise level in the system, for example, when $\sigma > 8.50$ Pa in our experiments. Finally, kurtosis ((Fig. 5.16(f))) can not be used as an early warning measure under any condition.

Implementing any early warning measure in practical combustion systems requires defining a minimum threshold value at a suitable distance from the saddle-node point to monitor the system's proximity to instability. This threshold will be based on how close to the bifurcation the system may be allowed to get. The definition of 'how close' and, therefore, the corresponding threshold is system dependent and is to be identified by the user. Our findings imply that this threshold will also be affected by noise in the system. In this work, we consider variation in the EWIs vary as the control parameter is modified. The observed trends in EWI variation is the most important aspect to consider when evaluating EWIs. We show how trends in EWI are affected in the presence of noise: if the variation in EWI is prominently along the variation of control parameter then it is reliable. If the variation of the EWI is prominent along the noise intensity, then it is not a reliable EWI. Additionally, if the trend is non-monotonic or if relative changes are small then also the EWI is not reliable. These variations in trends are shown with the help of horizontal and vertical arrows in the contour plots. In our experimental study, the closest point to instability is $\phi = 0.714$. Despite their sensitivity to changes in noise characteristics, indicators such as β, α, ν, V, and S consistently exhibit a monotonous trend up to $\phi = 0.714$, suggesting their efficacy in predicting impending instability.

It is important to note that the length of the time series used for estimating various Early Warning Indicators (EWIs) is a crucial parameter when assessing the system's proximity to instabilities. We conducted an additional investigation to examine the impact of time series length on different EWIs. The corresponding results are shown in Fig. F.1 in Appendix F. Our findings indicate that EWIs such as skewness (S), kurtosis (k), and Hurst exponent (H) are significantly influenced by the time series length, especially at low and intermediate noise intensities. These metrics show considerable variation with changes in the time series length, which can affect their reliability in real-time applications. Whereas, coherence factor (β) and variance (V) exhibit relatively stable trends regardless of the time series length, making them more dependable for accurate prediction.

5.3.6 Estimation of early warning indicators using heat release rate fluctuations (q')

Since self-excited thermoacoustic oscillations arise due to the coupling of p' and q', we further investigate the q' time series data, which is obtained by capturing fluctuations in CH chemiluminescence, to estimate various Early Warning Indicators (EWIs). The methodology for estimating these EWIs remain the same as mentioned in section 2.2. We find that only

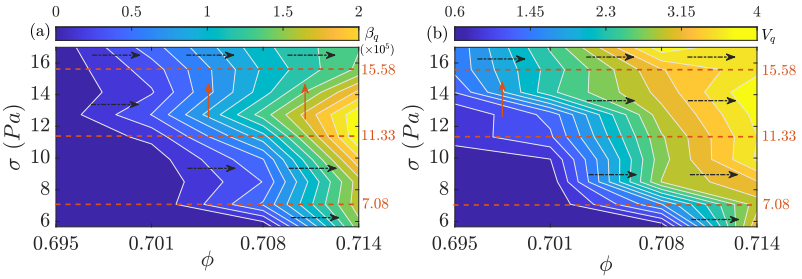

Figure 5.17: 2D contour map of (a) coherence factor (β_q) and (b) variance (V_q), estimated using heat release rate (q') measurements (hence the subscript q), as a function of control parameter (ϕ) and noise intensity (σ). The arrows indicate whether the variation in β_q and V_q is greater in the direction of control parameter or in the direction of noise intensity. The red dashed lines separate the plots into categories of low, moderate, and high noise levels.

the coherence factor (β_q) and variance (V_q) can be reliably estimated using q', results shown in Fig. 5.17. Both β_q and V_q exhibit a monotonous increase as the system approaches the saddle-node point at most noise levels, highlighting their robustness as EWIs. The subscript q is added to these indicators to differentiate it from those estimated from acoustic pressure oscillations (β in Fig. 5.12(a) and V in Fig. 5.14(a)). Among other indicators, we find that the ACF decay rates and skewness can be effective, but only in systems with very high noise levels (for example, $\sigma > 14$ Pa in our experiments). However, kurtosis, Hurst exponent, and entropy/complexity measures cannot be estimated using q'.

The acquisition of q' data depends on various factors such as efficacy of CH filter and PMT, hence fluctuations observed in q' are very low compared to fluctuations in p', as shown in Fig. 5.4(b). Hence, all the EWIs can not be reliably estimated from q' data.

Therefore, in practical systems, when monitoring the onset of instability tracking either p' or q' time series, coherence factor and variance should be the best choices as early warning indicators. In practical turbulent combustion systems, noise may stem from fluctuations in the fuel-air supply systems, variations in heat release caused by unsteady combustion, fluctuations in flow field caused by turbulence, flow separation and aerodynamic noise. Further in these systems, the noise characteristics are expected to vary simultaneously with the changes in operating condition (temperature, Reynolds number, equivalent ratio, etc.), specifically noise intensity increases as the system becomes more turbulent. In such situations, for an accurate prediction of impending thermoacoustic oscillations, it becomes crucial to utilize early warning indicators that demonstrate a consistent trend with the control parameter and remain largely unaffected by fluctuations in noise characteristics. Based on our controlled experimental investigation, employing the analysis of both acoustic pressure oscillations (p') and fluctuations in heat release rate (q'), we recommend coherence factor and variance to be the best choices as early warning indicators for application in gas turbine engines.

The present analysis, conducted on a simple flat flame laminar combustor (a prototypical thermoacoustic system), provides insights that are applicable to real systems. Further studies on the effects of noise spectra, the mode of noise introduction, and other factors will still need to be tested on such simplified systems rather than the complex combustors, to derive useful

and general conclusions. This is expected, as most seminal results on combustor dynamics (bifurcations, system identification, stochastic dynamics, flame response, and others) are based on simple cases. Moreover, the novel methodology employed in this study will serve as a foundation for future investigations into stochastic dynamics and early warning indicators for combustor dynamics.

Conclusions - PART I

In this part of the thesis, we examine how different types of noise, i.e. additive and multiplicative and their characteristics–correlation time and intensity–impact the reliability of various early warning indicators. Key questions addressed include (a) the existence of comparative reliability assessments among different EWIs, (b) how variations in noise properties affect EWI effectiveness, and (c) which EWIs are most reliable considering that noise characteristics can change with the system and its operating conditions. This information is essential for engine designers and users to develop robust monitoring systems for gas turbine combustors. The range of EWIs studied includes statistical measures (variance, skewness,kurtosis), spectral measures (coherence factor, autocorrelation), system identification measures (growth/decay rates of acoustic pressure oscillations), fractal measures (Hurst exponent, multi-fractal spectrum width), and time series complexity measures (permutation entropy, Jensen-Shannon complexity). The investigation uses three types of systems: (i) an electrically driven Rijke tube simulator (a prototypical thermoacoustic system), (ii) reduced-order combustion dynamics model (stochastic Van der Pol oscillators), and (iii) a lean premixed flat flame combustion system operating on natural gas-air mixtures. In all cases, we subjected the systems to two types of noise: (i) white noise and (ii) colored noise at varied noise correlation times and intensity.

- **Electroacoustic modelling:** The investigation using an electroacoustic simulator formed the foundation for our study. This simulator employs electroacoustic feedback to replicate the nonlinear flame response to acoustic perturbations. Such a practical setup is advantageous for conducting detailed investigations and understanding how the system responds to varying noise properties before integrating the flame. We primarily examined how changes in inherent noise properties can affect system identification (growth/decay rates of oscillations), which is crucial for designing acoustic dampers and the system's response in the stable region (coherence resonance and fractal behavior). From this investigation, we draw the following conclusions:

    1. Increasing the correlation time and noise intensity leads to an increase in the deviation of the estimated growth rates from the true values. For $\sigma < \sigma_{opt}$, the deviation in the estimated values lies within the range of 0 % to 10 % but when $\sigma > \sigma_{opt}$, the deviation increases from 10% to 30%. A sharp increase in the deviation of the estimated growth rates above σ_{opt} can be attributed to the fact that higher noise intensities affects the non-linear and stochastic dynamics of the system thus affecting the system identification. This optimum value of noise intensity above which the deviation in the estimated growth rates sharply increases is close to the value at which the peak coherence is induced in the system.
    2. For colored noise model, the deviation in the estimated growth rates lies within the range of 0 % to 10 % compared to the deviation of 5 % to 25 % observed considering the white noise approximation.

3. The accuracy in the estimated growth rates can be increased by (i) applying a bandpass filter around the frequency of interest; (ii) using the Fokker Planck equation based on colored noise model for growth rate estimation rather than white noise model; (iii) when the noise intensities are lower that the optimum value at which the peak coherence is induced.
4. Concerning noise-induced coherence, noise correlation time affects the system response in such a way that peak coherence is induced at higher noise intensities compared to white noise forcing. The peak coherence factor also reduces in magnitude with correlation time.
5. When noise intensity and correlation time (color) are kept constant, the coherence factor (β) always increases as the system is brought closer to the Hopf bifurcation at most noise levels (except at very small or very large noise levels, where β variation is too small to distinguish a trend); which makes it a reliable early warning indicator. Even for constant noise intensity and color, the increase in the value of coherence factor, depends on noise correlation time, intensity, and in our experiments, the choice of bandwidth. When employing coherence resonance and related indicators for prediction, precursors would have to be calibrated for individual combustion system based on the characteristics of the background combustion noise.
6. Increasing noise correlation time increases the Hurst exponent and width of the multi-fractal spectrum.
7. Fractal measures are observed to be insensitive to noise intensity.
8. We find that there are limitations for loss of multi-fractality (indicated by the gradual decrease of the Hurst exponent) to act as the reliable early warning indicator.
9. Thus, variation in the coherence factor, fractal measures, and other early warning indicators will not follow trends identified in thermoacoustic models with white noise. When noise color varies with operating parameters, trends in early warning indicators become non-monotonous and consequently, the EWIs become unreliable.

- **Stochastic modelling:** Building on the results from the electroacoustic system, we then employed the most commonly used reduced-order combustion dynamics model to mimic thermoacoustic instability as described in the literature—stochastic Van der Pol oscillators (exhibiting both supercritical and subcritical Hopf bifurcation). We performed detailed numerical simulations to assess the reliability of a wide spectrum of early warning indicators (EWIs) as a function of noise color and intensity. The objective was to identify the most reliable indicators that consistently show a trend with the control parameter (operating condition) and remain largely unaffected by fluctuations in noise characteristics. For this investigation, we modeled the background noise as purely additive, purely multiplicative, and a combination of additive and multiplicative. The specific effects of noise on the efficacy of the various EWIs identified in our study are as follows:

For purely additive noise:

1. Variance and decay rate of ACF increases as the systems approach the Hopf bifurcation, hence can serve as reliable EWIs, but only in systems where noise has either minimal correlation time ($\tau_c/T_0 < 0.1$) or has high correlation time ($\tau_c/T_0 > 1$). When noise color is of the order of system's time scale, i.e. $0.1 < \tau_c/T_0 \leq 1$, the degree of changes in these indicators are predominantly influenced by changes in noise color than the control parameter.
2. Skewness can not be employed as an EWI, as it varies more with noise color compared to the control parameter.
3. Kurtosis can be a reliable EWI in the systems characterized by minimal noise correlation time, i.e., $\tau_c/T_0 \leq 0.1$ regardless of bifurcation variant and noise intensities. For large correlation times ($\tau_c/T_0 > 1$), kurtosis can be suitable at low noise intensity for supercritical systems and at high noise intensity for subcritical systems.
4. Coherence factor increases as the systems approach the Hopf bifurcation, regardless of simultaneous changes in noise characteristics and bifurcation variant. Hence, it emerges as one of the most reliable early warning indicators.
5. Among the fractal measures, for low to moderate noise correlation times, i.e. $0 \leq \tau_c/T_0 \leq 1$, Hurst exponent is strongly dependent on noise color than the control parameter. Hence, a decrease in Hurst exponent can be employed as reliable EWI only when the noise correlation time is much larger than the system's time-scale ($\tau_c/T_0 > 1$). Whereas, the loss in spectral reserve, indicated by a decrease in the width of the multi-fractal spectrum, is unsuitable as an EWI at all investigated conditions.
6. The entropy/complexity measures are highly sensitive to changes in noise color, therefore they can serve as reliable EWIs only for systems where white noise approximation is acceptable.

For purely multiplicative noise:

1. When noise is solely multiplicative, for a fixed control parameter, coherence factor, variance, and permutation entropy decrease while the Hurst exponent increases with increasing noise correlation time. However, variability in multiplicative noise color alongside the control parameter renders all investigated EWIs more sensitive to noise color than to the control parameter, challenging their reliability as EWIs.

For combination of both additive and multiplicative noise:

1. In case when background noise has contributions from both multiplicative and additive sources, then coherence factor and variance are observed to always increase as system is brought closer to the Hopf bifurcation, irrespective of the background noise characteristics, making them the most reliable EWIs. Nevertheless, the extent of increase in these EWIs depends on noise characteristics, even when considered as

constants. Hence, calibration may be necessary for individual systems based on the specific attributes of the background noise.

2. The implementation of the decrease in Hurst exponent and permutation entropy as EWIs has limitations. These indicators are applicable only in systems where the background noise has major contribution from additive sources. Specifically, the Hurst exponent is effective when the noise correlation time is large ($\tau_a/T_0 > 0.5$), while permutation entropy is reliable in systems with small noise correlation times ($\tau_a/T_0 < 0.1$), i.e. where white noise approximation is acceptable.

- **Practical implementation:** We then demonstrate the practical implementation of the recommended EWIs from numerical simulations on a flat flame combustion system operating on lean premixed natural gas-air mixtures, which exhibits subcritical Hopf bifurcation. Through this investigation, we showcase the limitations and robustness of EWIs for application in practical gas turbine combustors. Here, noise intensity is the varying parameter. From our study, we draw the following conclusions:

  1. Coherence factor increases as the system approaches the Hopf bifurcation under most noise levels, indicating its effectiveness as an EWI. Further, the coherence factor is quite sensitive when the system is close to the Hopf bifurcation. So, in addition to whether we are moving close or away from the Hopf point, it also indicates if we are close or far away from the saddle-node point.
  2. The ACF decay rates, variance and skewness increase as the system approaches the Hopf bifurcation, making them reliable indicators except at very low noise levels, $\sigma < 7.08$ Pa in our experiments.
  3. We find that an increase in kurtosis is not a suitable early warning measure under any condition.
  4. Hurst exponent and entropy/complexity measures can effectively work as early warning indicators in combustion systems with high noise intensities, $\sigma > 12.74$ Pa in our experiments.

Based on our extensive investigation on the reliability and efficacy of EWIs, we provide a ranking

Early warning indicator	Reliability index	Limitations
Coherence factor	Rank 1 (most reliable)	
Variance Decay rates of ACF Decay rates of p'	Rank 2	Moderate noise color ($0.1 \leq \tau_c/T_0 \leq 1$) and low noise intensity
Hurst exponent	Rank 3	Low noise color ($\tau_c/T_0 < 1$)
Permutation entropy Jensen-Shannon complexity	Rank 4	Moderate to high noise color ($\tau_c/T_0 > 0.1$) and low noise intensity
Skewness, kurtosis	Rank 5 (least reliable)	Noise properties, bifurcation variant
Multifractal spectrum width	Rank 6	Cannot serve as an EWI

Ranking order of EWIs based on their reliability index.

order for employing in practical systems (illustrated in the table above). An important point to note is when applying these indicators for prediction, it is crucial to calibrate precursors for individual combustion systems based on background noise characteristics.

In conclusion, coherence factor and variance emerge as robust choices for EWIs in engine monitoring applications, particularly in the absence of detailed information on noise properties and their variations with operating conditions. These measures demonstrate consistent behavior with respect to changes in the control parameter, offering reliable insights into the prediction of impending thermoacoustic instability in gas turbine combustors.

PART II: Noise Interaction with Turbulent Swirling Flows

Part contents

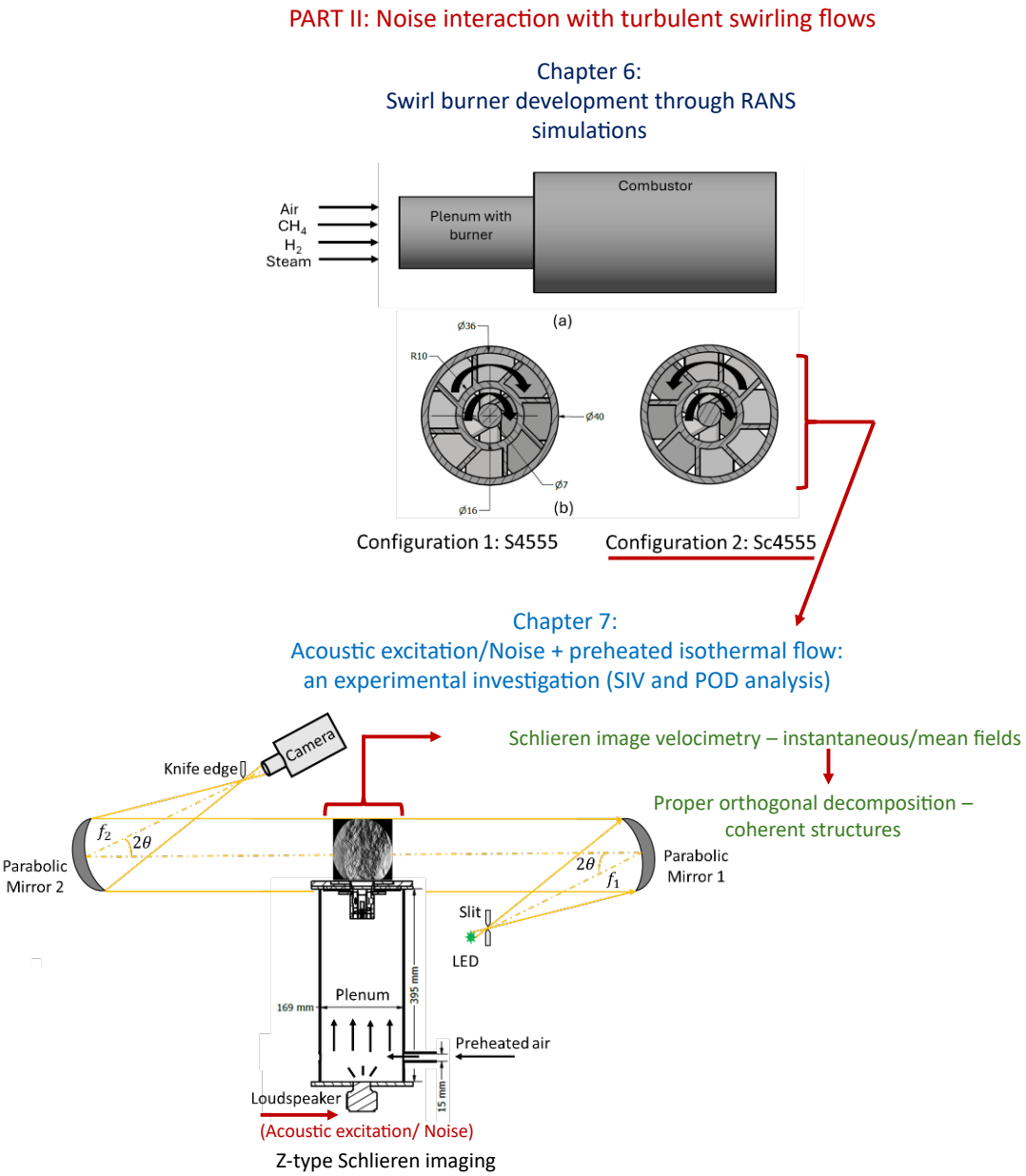

Overview of the contents of PART II: this part is divided into two chapters, (i) Top (chapter 6): swirl burner development, where RANS simulations are performed to develop a novel fuel flexible multi-swirl burner and (ii) Bottom (chapter 7): where experimental investigation is conducted on the developed swirl burner to investigate the interaction between noise and swirling flow fields.

Summary

The objective of this part of the thesis is to investigate how the coherent structures associated with global instability of swirling flows interact with inherent noise inside the combustor.

The hypothesis is that introducing a broad range of frequencies may suppress or excite the coherent structures associated with instability. This information is significant for developing mitigation and control strategies for thermoacoustic instability in practical combustion systems. Here, first design and develop a swirl burner comprising of multiple swirling passages through numerical RANS simulations. We perform extensive simulations with a variety of fuel/air mixtures and study the flow/flame characterization. After finalizing the burner configuration, we experimentally investigate the associated typical flow features and coherent structures. The objective is to study the interaction between large-scale coherent structures, specifically the PVC and acoustic excitation using time-resolved Schlieren imaging. We investigate three distinct excitation ranges: (i) a frequency lower than the natural frequency of PVC, (ii) a frequency higher than the natural frequency of PVC, and (iii) broad-band excitation (white noise). We first obtain the mean flow characteristics of the burner through Schlieren images and, subsequently, employ proper orthogonal decomposition (POD) analysis to identify and extract the dominant coherent structures in the flow.

We demonstrate the usage of Schlieren image velocimetry (SIV) for turbulent swirling flows. The demonstration of this diagnostic technique is less explored in the field of gas turbine combustors. Schlieren image velocimetry (SIV), first proposed by Townend [191], is a non-intrusive diagnostic method utilized for visualizing and quantifying fluid flow velocities based on schlieren imaging principles. SIV capitalizes on changes in refractive index that cause light deviation due to optical inhomogeneities within the medium. Unlike particle image velocimetry (PIV), SIV doesn't require seeding particles; instead, turbulent eddies within the flow serve as "particles." As turbulent eddy length scales become increasingly smaller with rising Reynolds numbers, successive Schlieren images, with slight time delays, can be correlated to extract velocity field data. This method is suitable during initial phase of burner design and development on laboratory scale as it does not require expensive laser sources and seeding particles. In literature, SIV has been successfully implemented for capturing flow features in high speed Helium jets [192], synthetic jets [193], gas fires and explosions [194], subsonic and supersonic turbulent boundary layer [195–198], sweeping jets [199] and swirling sprays [200]. Consequently, analyzing Schlieren images is invaluable in fluid mechanics, facilitating the visualization and calculation of flow fields in unseeded flows [201,202]. Recently Schlieren imaging showed promising results to characterize non-MILD distributed combustion in a swirl burner [203]. The challenging task is to obtain the velocity fields from the Schlieren images. For this, we followed the image pre-processing techniques proposed in the studies of Kegerise and Settles [204], Hargather et al. [197], Biswas and Qiao [192], Ozawa et al. [198], Machado et al. [200] and Józsa et al. [203], where the authors have shown a close agreement between SIV and PIV results for their respective experimental setups. The maximum deviation reported in the studies is $\sim 15\%$. SIV strongly depend on the flow topology and the scale of the visualized turbulent structure. Therefore, we also support the obtained velocity profiles from SIV with RANS simulations.

Apart from estimating velocity, Schlieren images have also proven to be useful in obtaining the symmetric/anti-symmetric structures in a flow by performing modal decomposition study. A

few studies where the successful implementation of Schlieren-POD has been reported are Berry et al. [205], Pellessier et al. [193] and Wen et al. [199]. Hence, Schlieren visualization can serve as a powerful tool to qualitatively investigate swirling flow features.

This part of the thesis include two chapters. In chapter 6, we develop the swirl burner based on the RANS simulations. In chapter 7, we perform the experimental investigation of the developed burner and study the interaction of noise with the flow fields. This is the first study in gas turbine community where the application of SIV and corresponding modal decomposition is extended to a turbulent swirling flow, hence, the discussions on the methodology and results are crucial.

Chapter 6

Swirl Burner Development

6.1 Overview

In this chapter, we aim to develop a novel fuel-flexible multiple swirl burner to achieve stable combustion, enhanced flashback resistance, and low emissions (carbon and NOx). To this end, we propose the design of triple and dual swirl burners and investigate the flow, flame, and flashback characteristics within the burner passages and inside the combustor using the Reynolds Averaged Navier-Stokes (RANS) simulation approach. We test a wide range of fuel/air mixtures, from methane-air mixtures to methane-hydrogen-steam-air mixtures, at varied equivalence ratios and power levels. Our results are based on the characterization of mean velocity (axial, radial, and tangential), vorticity, temperature fields, and emissions, and we validate the RANS simulation results with Laser Doppler Anemometry (LDA) experiments.

We began our investigation by designing a triple swirl burner, comprising three coaxial swirling passages: inner and intermediate axial swirlers, and an outer radial swirler, inspired by the TARS (Triple Annular Research Swirler) concept [206]. TARS is a fuel injector developed by Goodrich Corporation in collaboration with General Electric Aircraft Engines (GEAE) for research purposes. TARS has a complex geometry with design features analogous to an aero-engine application and has been studied extensively in both experimental and numerical contexts [18, 207, 208]. In this configuration, we tested isothermal flow (pure air), methane-air mixtures, and two methane-hydrogen blends: (i) $90\% - 10\%$ and (ii) $60\% - 40\%$, with and without steam dilution at an equivalence ratio of $\phi = 0.75$. Our investigation found that the flow fields for methane-air mixtures were stable with no flashback. However, adding hydrogen caused an upstream propagation of the reaction zone and central recirculation zone (CRZ), leading to flame flashback at 40% hydrogen content. Higher flame temperatures up to 2200 K were also observed with hydrogen addition, resulting in increased NOx emissions. The flame temperatures decreased to 1800 K under humidified conditions, reducing the flashback propensity and NOx emissions by a factor of 5 for methane-hydrogen blends. The mass flow rates and inlet temperature of the air were kept constant at 8.73 g/s, 40 g/s and 300 K, respectively.

When we increased the hydrogen content to a $50\% - 50\%$ blend and, instead of humidification (moisture at 300 K), diluted the mixture with steam (inlet temperature increased to 623 K), the burner experienced flashback through the radial slots of the outer swirler. Consequently, we modified the burner design to a dual swirler configuration by blocking the radial slots. This chapter presents the detailed results from the investigation of the dual swirl burner, examining the effect of steam dilution and swirling direction on the flow and flame characteristics for

methane-hydrogen-air mixtures at an equivalence ratio of $\phi = 0.9$ with a power of around $131kW$. This burner configuration is identified as a more suitable candidate for next-generation fuel-flexible gas turbines.

This chapter is further divided into two sections. Section 6.2 describes the burner geometry, RANS configuration, and operating/boundary conditions used for the simulations. Section 6.3 presents the comparative flow and flame features within the burner and inside the combustor.

6.2 Burner geometry and RANS configuration

6.2.1 Dual Swirl Burner

In the present study, the investigated burner is characterized by two co-axial mixture passages: outer and inner axial swirlers as shown in Fig. 6.1(a). The dashed-dot red lines represent the cross-wise planes at which the velocity fields are discussed in the subsequent sections. Several configurations of the burner can be obtained by varying the vane angles or changing the swirling direction (co- or counter-rotating). In the present work, the swirling direction is considered to be the main focus as counter-rotating swirling streams have been reported to form intense shear stresses that affect the combustion processes significantly [209]. In this study, we are presenting the numerical investigation of two burner configurations as shown in Fig. 6.1(b):

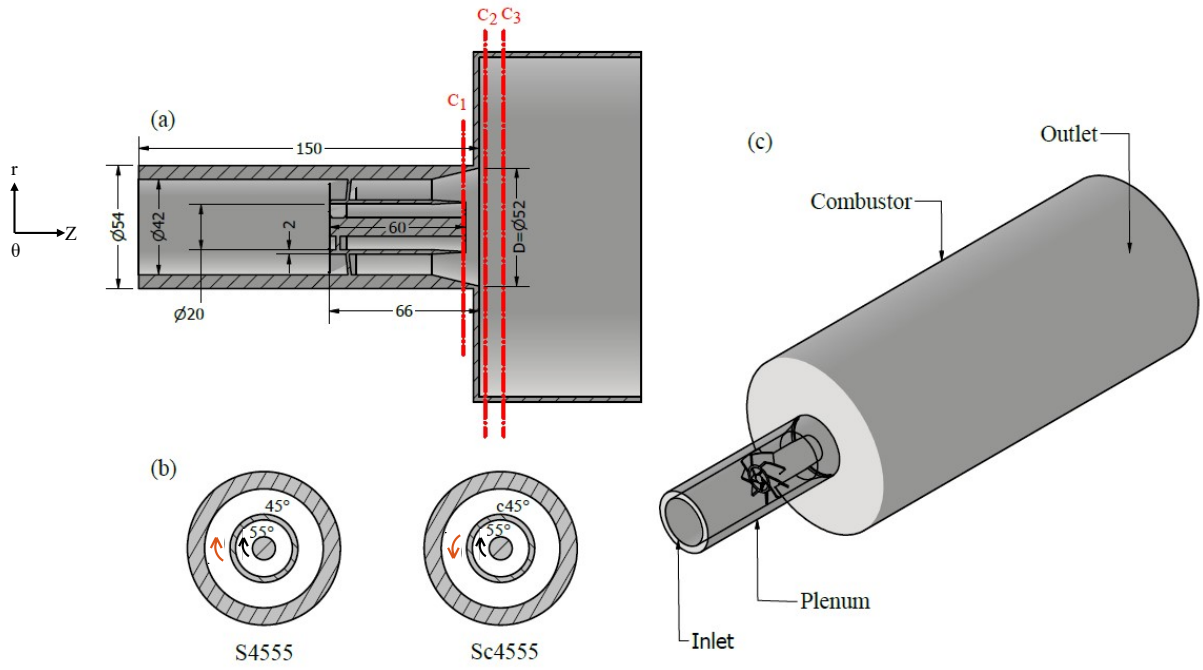

Figure 6.1: (a) Half-section view; (b) Cross-sectional view of the dual swirl burner and its configurations (Swirler 1: S4555; Swirler 2: Sc4555) respectively; (c) Computational domain for RANS simulations. All dimensions are in mm. The burner exit diameter (D) is chosen to be the normalizing parameter for the coordinates. The dashed-dot red lines represent the cross-wise planes at which the velocity fields are discussed later.

Table 6.1: Geometric details of the swirlers.

Swirler	Vane angle (deg.)	Number of vanes	Swirl number	Swirl direction
Outer	45	8	0.77	co- and counter- rotating
Inner	55	5	1.06	co- rotating

S4555 (Swirler 1) and Sc4555 (Swirler 2), where the swirlers are defined by their respective vane angles: 45° outer, and 55° inner swirlers and "c" indicates the counter-rotating direction. The outer and inner axial swirl numbers are 0.77 and 1.06 respectively. The thickness of the intermediate swirler body is 2 mm; while the inner diameter of the inner swirler is 7 mm. The overall length and exit diameter of the dual swirl burner for two configurations are $L = 66$ mm and $D = 52$ mm respectively. The exit diameter (D) is chosen as the reference length for normalization against each case. The geometric details of the two swirlers are tabulated in Table 6.1. Figure 6.1(c) shows the computational domain that we are employing for carrying out the numerical simulations. The domain consists of a plenum with a dual swirl burner flush mounted to cylindrical confinement, which acts as the combustor. The inlet is located at $\sim$ 3D upstream of the dump plane. The cylindrical confinement is $\sim$ 7D long and $\sim$ 3D in diameter. The origin of the coordinates is placed at the centre of the plenum inlet.

6.2.2 RANS configuration

Reynolds Averaged Navier Stokes (RANS) simulation approach employing SST $k-\omega$ model and Flamelet Generated Manifold combustion (FGM) model [210] is used to predict the flow and temperature fields within the burner and inside the combustor. The SST $k-\omega$ turbulence model, in addition to solving the conservation equations, also solves the transport partial differential equations for turbulent kinetic energy (k) and specific rate of turbulent dissipation (ω). The SST $k-\omega$ turbulence model amongst other RANS turbulence models (such as $k-\omega$, $k-\epsilon$ (where ϵ is the turbulent dissipation), RNG, etc.), provides a better prediction of complex swirling flows and flow separation as it accounts for the transport of the principal shear stress in adverse pressure gradient boundary layers [211]. The SST (shear stress transport) formulation aids in combining the standard $k-\omega$ and $k-\epsilon$ models through a blending function. This function activates the standard $k-\omega$ model in the viscous sub-layer the wall and $k-\epsilon$ model in the

Table 6.2: Summary of FGM and TFSC parameters.

Parameter	Approach or Value
Flamelet type	Premixed
Flamelet solution method	Progress variable space
Energy treatment	Non-adiabatic
Flamelet grid points	32×32
Flamelet refinement	Stoichiometric mixture fraction
Turbulent Schmidt number	0.7
Turbulence-chemistry interaction	Turbulent flame speed
Variance method	Transport equation

free stream, thereby ensuring utilization of appropriate model throughout the flow field. We employ the SST $k-\omega$ model in conjunction with Kato Launder production limiter (production limiter clip factor = 10) on turbulent viscosity which avoids the build up of excessive k near the stagnation points in the flow, thereby preventing the overestimation of shear stress. To account for roughness of walls through roughness correlations [212], γ transport equation model including the cross-flow transition model is employed. The SST $k-\omega$ turbulence model also has a high accuracy to expense ratio in wide range of flows which makes it the most popular model in engineering computations [211].

We employ the progress variable approach with the FGM model and Zimont's Turbulent Flame Speed Closure model (TFSC) [213] to incorporate the detailed chemistry mechanism in turbulent flows. The progress variable approach tracks the global progress of the combustion reaction and the flame using the premixed adiabatic flamelet library generated by the FGM model [210,213]. This eliminates the need for computationally expensive evaluation of transport equations for each species. A summary of FGM and TFSC parameters Incorporated in the present work is tabulated in Table 6.2. The simulations are carried out in Ansys Fluent 2022 R1 employing GRI-Mech 3.0 [214] reaction mechanism (325 reactions and 52 species) for combustion. GRI-Mech 3.0 provides better predictions of laminar and turbulent flame speeds for combustion of hydrocarbons [214]. The conservation and transport equations are discretized using a second-order upwind scheme and COUPLED algorithm [215,216] has been employed to account for pressure-velocity coupling. The criteria for achieving the convergence of the solution of all the equations is set to a value of 10^{-9} [210]. The under-relaxation factors (α) for turbulent kinetic energy, pollutant NO, progress variable and mean mixture fraction are chosen to be $\alpha = 0.75$ to ensure the stability of the solution [215,216].

6.2.2.1 Mesh sensitivity

We conduct the mesh (or grid) independence study to ensure that the solution obtained is not sensitive to mesh size. We generated an unstructured polyhedral mesh with its size varying from 1.9 million to 9.6 million cells which corresponds to a base size ($\sim$ smallest size of the mesh) varying from 10 mm to 0.9 mm. The growth rate of the mesh is kept constant at a value of 1.2 ensuring a constant aspect ratio with an increase in mesh elements. Figure 6.2(a) and (b) shows the effects of variation of mesh size on the mean axial and tangential velocities of air (cold flow case shown in Table 6.3) at the dump plane inside the combustor. We can observe that the mesh sizes, $1.9M$ and $3.9M$ cells, under-predicts the peak annular jet velocities and over-predicts the recirculation zones resulting from complex swirling flow and flow separation in the combustor. Additionally, these mesh sizes are unable to capture the variation in the peak annular velocities occurring due to the presence of multiple swirling passages. The variation in the axial and tangential velocities is significantly small (a relative difference of $\sim 5\%$ is observed) when mesh size is varied between $4.6M$ and $9.6M$. As the computational time required significantly increases with mesh sizes of $9.6M$, therefore, we choose the mesh size of $4.6M$ for the present study (shown in Fig. 6.2(c)) to ensure the balance between accuracy and computational time. The chosen mesh size also shown accuracy for both non-reacting and reacting flows.

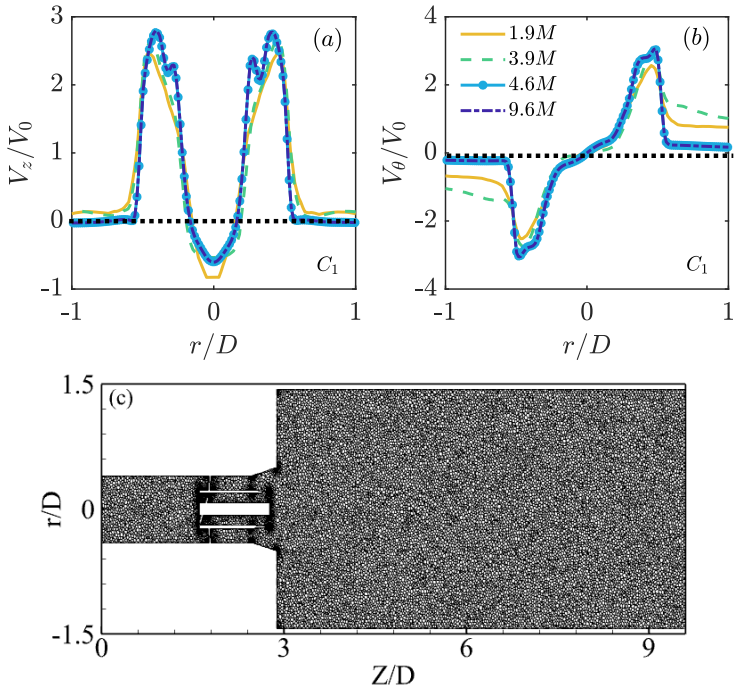

Figure 6.2: Grid independence test: (a) and (b) mean axial and tangential velocity profiles at C_1 plane respectively for 4 different mesh sizes ranging from 1.9 million to 9.6 million cells; (c) the stream-wise plane showing the chosen mesh size ($4.6M$) at which the results are presented.

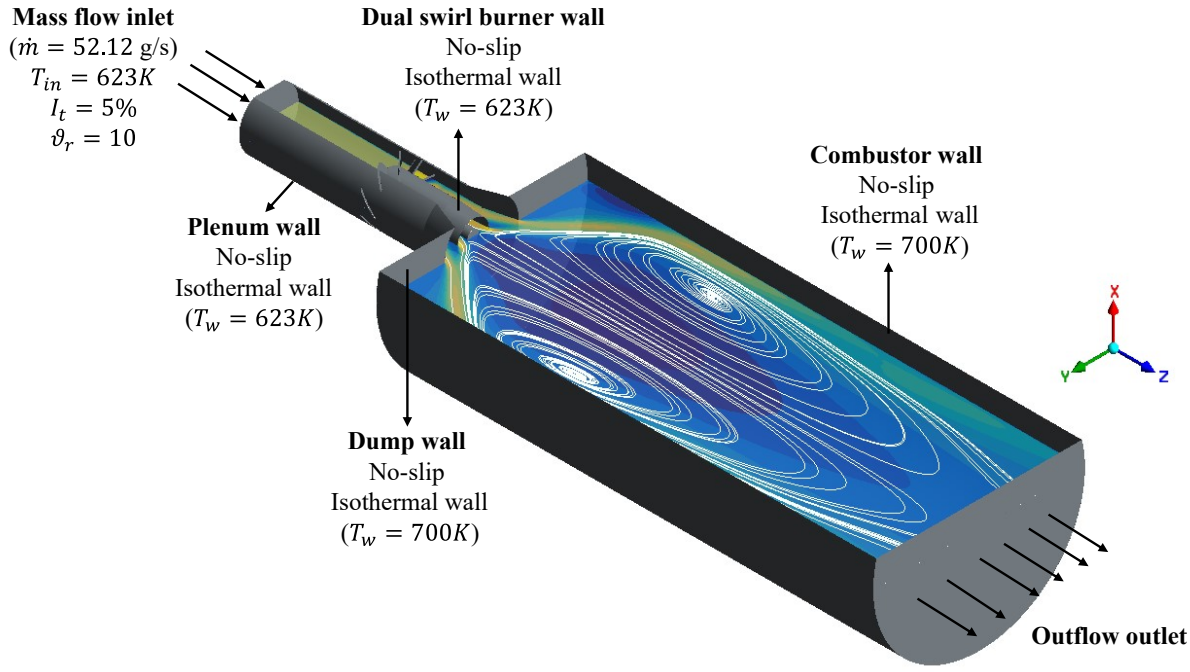

Figure 6.3: An illustration of the computational domain with the boundary conditions for the RANS simulations.

Table 6.3: Operating conditions for RANS simulations

Case description	T_{in} (K)	$\dot{m}_{air}$ (g/s)	$\dot{m}_{CH_4}$ (g/s)	$\dot{m}_{H_2}$ (g/s)	Ω	ϕ	P (kW)
Cold flow (for validation)	300	9	–	–	–	–	–
Non-reacting flow	623	42	1.77 (80%)	0.35 (20%)	0, 0.2	0.9	–
Reacting flow	623	42	1.77 (80%)	0.35 (20%)	0, 0.2	0.9	131

6.2.2.2 Boundary and operating conditions

Figure 6.3 shows the schematic of the computational domain illustrating the boundary conditions (details tabulated in Table 6.3) employed.

1. Inlet: The total mass flow rate ($\dot{m}$), species mass fractions, temperature (T_{in}), reaction progress variable, and pressure (p = 101kPa) are specified at the inlet. To account for turbulence at the inlet, a turbulence intensity (I_t) of 5% and a turbulent viscosity ratio (ν_r) of 10 are specified [216]. The Damköhler number (Da), defined as the ratio of a characteristic flow time to a characteristic chemical time, is $Da > 1$, indicating that the chemical reaction rates are faster than the fluid mixing rates, resulting in a fast-chemistry region. Conversely, the Karlovitz number (Ka), defined as the ratio of the Kolmogorov timescale to the chemical timescale, is $Ka < 1$, placing the flame in the "thin reaction zone" [217]. On the Borghi-Peters combustion diagram [217, 218] for premixed turbulent flows, these parameter values represent wrinkled and corrugated flames. The turbulent Reynolds number at the inlet is $Re_t = 1365$.

2. Outlet: The outflow boundary condition is specified such that the pressure and temperature gradients are zero.

3. Wall: An isothermal boundary condition is imposed with a temperature of 623K specified on the plenum and swirler walls and 700K specified on the combustor wall. This setup captures the heat losses through convection and radiation from the walls and adequately represents the overall flame shape and structure [210, 219]. All walls are stationary with a no-slip condition.

The operating conditions for the present investigation are tabulated in Table 6.3. We first provide an experimental validation of the code using air at the flow rate of $\dot{m}_{air}$ = 9g/s) and inlet temperature of $T_{in} = 300K$. We then conduct the numerical investigations for non-reacting (isothermal) and reacting (combustion of premixed methane-hydrogen-steam-air mixtures) flows at an inlet temperature of $T_{in} = 623K$. The total mass flow rate of air and steam is kept constant at 50g/s, while fuel flow rates are varied. The steam content, Ω, is defined as the ratio of mass flow rate of steam to that of air ($\Omega = \dot{m}_{steam}/\dot{m}_{air}$).

6.2.2.3 Validation: cold flow case

We validate our RANS solver setup by comparing the isothermal flow fields of the cold case (tabulated in Table 6.3) with experiments from a slightly different burner configuration: a triple swirl burner. This burner, in addition to the two axial swirling passages shown in Fig. 6.1, also

features an outer radial swirling passage, and is denoted as S504555, where the vane angle of the radial slots is 50°. The experiments were conducted at Cardiff University using an atmospheric test rig, which consists of a vertical airflow conditioning chamber and a funnel extension for mounting the triple swirl burner. Mean axial, radial, and tangential velocity data were acquired using the LDA (Laser Doppler Anemometry) diagnostic technique at various planes downstream of the burner exit (inside the combustor). A 3D Dantec traverse system, mounted with the laser head, was employed for measurements in vertical and horizontal planes relative to the burner. The airflow rate was controlled by a Platon flow meter (accuracy: ±1.25% FSD) at a constant pressure of $p = 2$bar. Aluminium dioxide particles with a nominal size of 5 μm were used as seeding particles for flow visualization.

Figure 6.4 shows the stream-wise contours of mean axial and tangential velocity obtained from experiments (plots (a) and (c)) and RANS simulations (plots (b) and (d)). The coordinates and velocities are normalized by the burner exit diameter ($D = 52$mm) and average exit velocity ($V_0 = 20.15$m/s), calculated by volumetric flow rate at $T_{in} = 300K$, respectively. Figure 6.4(a)

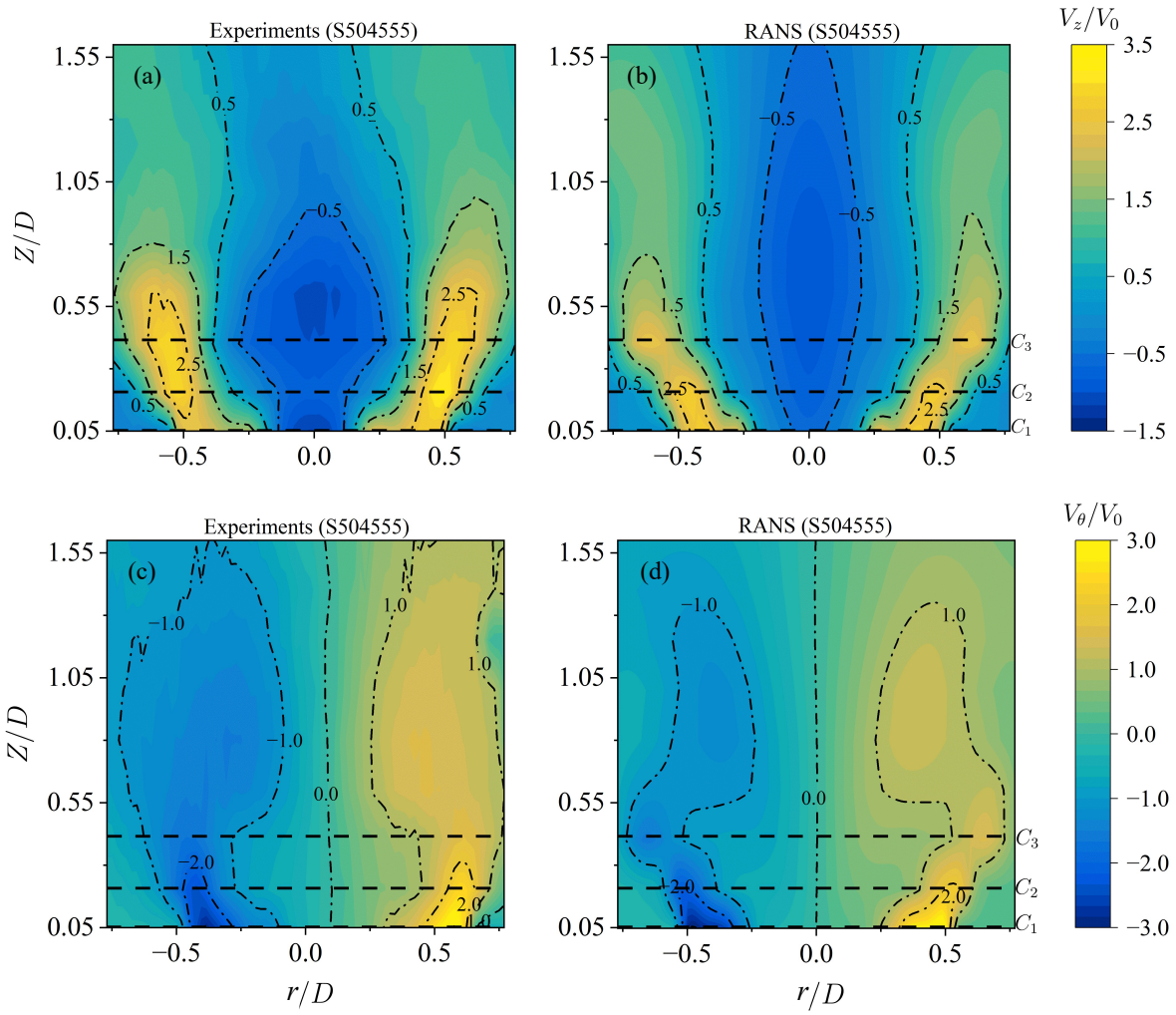

Figure 6.4: Validation: Stream-wise contours of mean (a), (b) axial velocity (V_z) and (c), (d) mean tangential velocity (V_θ) from experiments (a, c) and RANS simulations (b, d) for a triple swirl burner (S5045555). The coordinates and velocities are normalized by D and V_0 respectively.

and (b) illustrate an annular jet with a peak velocity of approximately $2.5V_0$ emanating from the burner exit, separating the central recirculation zone (CRZ), which has a width of about 0.5D and a length of approximately 1.45D, from the two outer recirculation zones (ORZ). The CRZ dominates the central flow region with a maximum negative velocity of around $0.5V_0$. Figure 6.4(c) and (d) show that the tangential velocity also reaches its highest magnitude, around $2V_0$, at a similar location as the axial velocity. As V_θ is the out-of-plane circumferential component, the contours show opposite directions on the two sides of the centerline. The RANS simulations exhibit significant similarity with the experiments in terms of magnitudes and locations of peak axial velocities and recirculation zones.

Further, in Fig. 6.5, we plot the mean axial and tangential velocity profiles at three planes ($C_1 \rightarrow Z/D = 0.05$, $C_2 \rightarrow Z/D = 0.2$, and $C_3 \rightarrow Z/D = 0.4$), marked by black dashed lines in Fig. 6.4. The RANS simulations show good agreement with the experiments, particularly at planes C_2 and C_3. At plane C_1, RANS under-predicts the central recirculation zone and the location of peak tangential velocity, with a relative deviation of around 9.5% observed between RANS and experiments. Due to the triple swirl burner exhibiting flashback under the reacting conditions tabulated in Table 6.3, we present the investigation on the dual swirl burner. Given that the RANS solver setup can predict the flow fields with an accuracy of over 90%, we employ it to predict the flow fields for the dual swirl burner.

6.3 Results and Discussions

In this section, we present the results and observations obtained from the RANS simulations of the non-reacting and reacting flows in the dual swirl burner. We provide comparative results for co- and counter-swirl configurations, analyzing velocity, turbulence, temperature, and combustion species distribution in both the burner and the combustor.

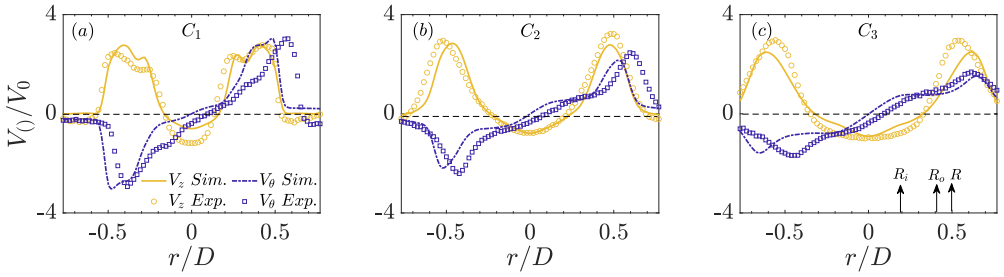

Figure 6.5: Validation: mean axial (V_z) and tangential (V_θ) velocity profiles at (a) $C_1 \rightarrow Z/D = 0.05$; (b) $C_2 \rightarrow Z/D = 0.2$; (c) $C_3 \rightarrow Z/D = 0.4$ inside the combustor of S504555. The Y coordinate and velocities are normalized by D and V_0 respectively. The lines represent the RANS simulation results, whereas, the markers represent the experimental results. The exit radii of each swirler is marked by the arrows.

6.3.1 Non-reacting Flow Fields

6.3.1.1 Velocity fields

A swirling motion is imparted to the incoming flow by the stationary vanes of the swirlers. Therefore, the flow that emanates from the burner exit, in addition to axial and radial velocity, also has a tangential velocity component. The presence of the swirling motion creates radial and axial pressure gradient which influences the flow field. The central core of the rotating flow has low pressure which recovers as the flow emanates from the burner leads to the creation of adverse axial pressure gradients such that when $S > 0.6$, the flow reverses its direction along the burner axis and forms a central torroidal recirculation zone (CRZ). This CRZ causes the expansion of the annular jet emerging from the burner. The length of the CRZ, defined as the distance from the burner exit to the point where the flow reverses its direction, depends on the swirl number: the length increases with increase in swirl number. The recirculation zones promotes the fuel/air mixing and helps in stabilizing the combustion. The sudden expansion of the jet due to the area change and the confinement of the combustion chamber results in the formation of outer recirculation zones (ORZ). Figure 6.6 presents an illustration of the typical flow field emerging from the co-rotating dual swirl burner $\Omega = 0$. Two annular jets that separates the central and the outer recirculation zones emanates from the outer and inner swirling passages. Regions of strong velocity gradients, known as the shear layers, exist between the incoming annular jet and the formed recirculation zones (CRZ and ORZ). These regions are highly unstable and turbulent and are associated with the vortex roll-up and form concentrated regions of vorticity [220]. The flame is expected to stabilize or anchor at these inner (between annular jet and CRZ) and outer (between annular jet and ORZ) shear layers. Further, we can observe small regions of reversed flow attached to the inner walls of the two swirlers. These

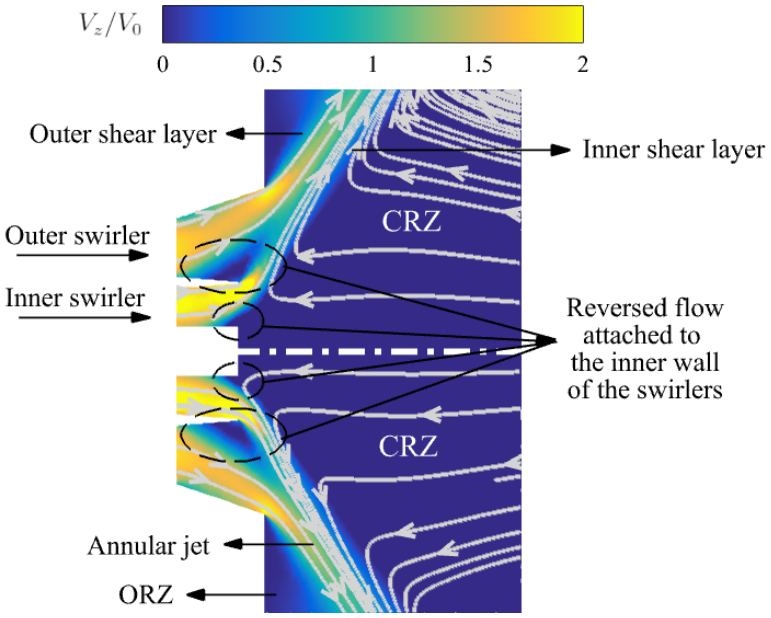

Figure 6.6: Non-reacting flow: illustration of the typical flow features from the dual swirl burner by stream-wise contours of mean axial velocity (V_z), normalized by V_0.

regions of the reversed flow favour the merging of the two incoming jets of the swirlers [18]. The reversed flow region attached to the walls of the inner swirler predominantly acts as the flame attachment (or anchoring) point. Additionally, this is also a potential region for the occurrence of the boundary layer flashback due to the upstream propagation of CRZ.

To study the effects of swirler configurations and steam dilution on the non-reacting flow fields, we present the comparative results for co- and counter-rotating burner. We find that steam dilution does not affect the non-reacting flow fields significantly, therefore, we present the results in this section at $\Omega = 0.2$. Figure 6.7 shows the stream-wise (r–z plane) contours for the mean axial velocity (a, b) and mean tangential velocity (c, d) for swirler 1 (S4555) and swirler 2 (Sc4555) respectively. Coordinates and velocity are normalized by the burner exit diameter (D) and the plug flow velocity at burner exit ($V_0 = 52.71\,\mathrm{m/s}$) estimated for $T_{in} = 623\mathrm{K}$. From Fig. 6.7(a) we find that in case of the co-flow (swirler 1), the CRZ that dominates the central core region inside the combustor has a maximum width of $\sim$ 2D, a length of $\sim$ 6.8D and a maximum negative velocity of $\sim 0.33\mathrm{V}_0$ ($\sim -17\,\mathrm{m/s}$). The maximum width of the CRZ is observed at $\sim$ 3.73D inside the combustor; whereas, in case of the counter-rotating flow (Fig. 6.7(b)), we observe that the width of the CRZ is increased by $\sim$ 5% ($\sim$ 2.1D), while its length is reduced by $\sim$ 0.15%. The peak negative velocity is increased by $\sim$ 11% ($\sim -19.5\,\mathrm{m/s}$) when compared to the co-rotating flow (Fig. 6.7(a)). The occurrence of a shorter CRZ in the case of counter-rotating

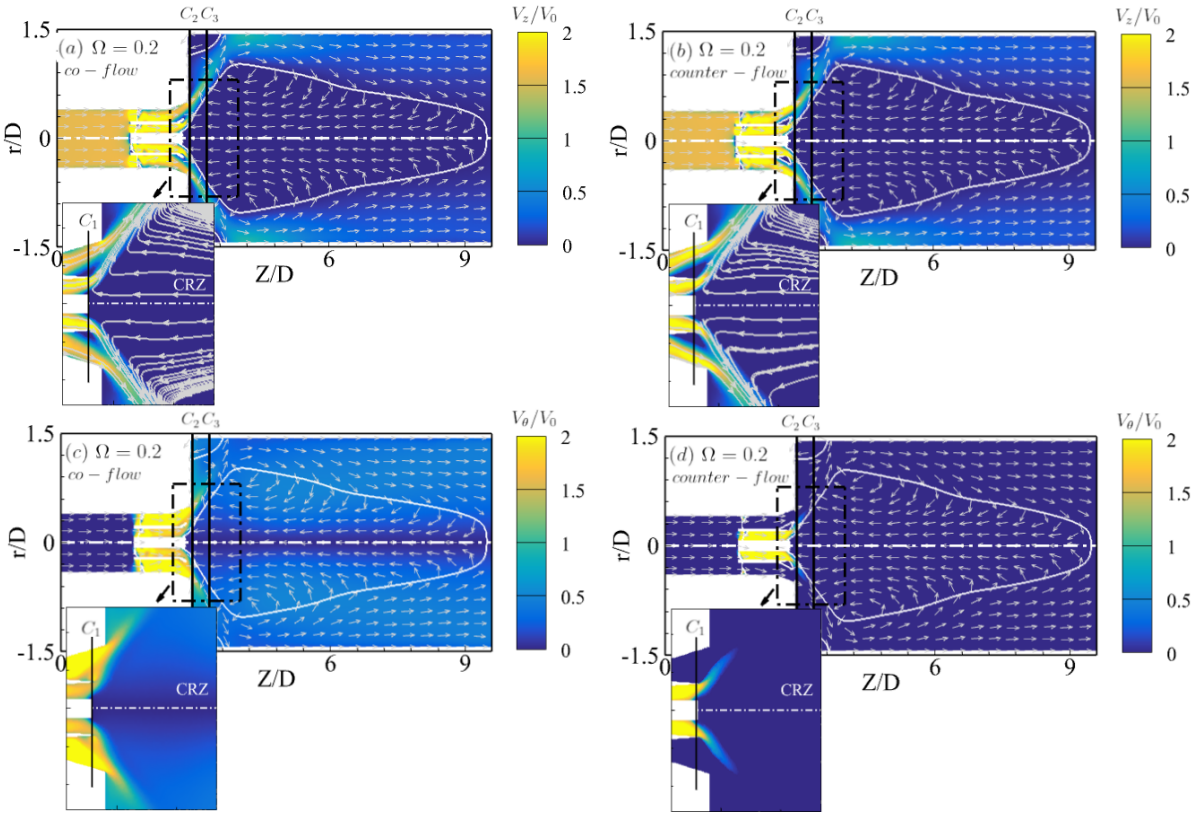

Figure 6.7: Non-reacting flow: stream-wise contours of mean (a, b) axial velocity (V_z) and (c,d) tangential velocity for swirler 1: S4555 (a, c) and swirler 2: Sc4555 (b, d) respectively. The coordinates and velocities are normalized by D and V_0 respectively. The contour lines for zero axial velocity are indicated by solid white lines. The arrows indicate the direction of flow.

flow makes it less susceptible to flame oscillations [221] and increases the pressure gradient and turbulence in the combustor which aids in enhanced mixing of cold reactants and hot combustion gases [222]. The reduction in the length of the CRZ in case of counter-rotating flow has also been observed in TARS [209] and in the GTMC dual swirl burner [222–224]. The strongest annular jet with a peak axial velocity of $\sim 1.95V_0$ and $\sim 2.1V_0$ emanates from swirling passages extends up to $\sim 3.73D$ in the combustor for co- and counter- rotating flows respectively, after which it reattaches to the combustor walls. The annular jet of the counter-rotating flow has a larger divergence angle than the co-rotating flow. This is because of the increased width of the CRZ observed in the counter-flow. This increase width of the CRZ is attributed to the fact that the opposing sense of direction of the two swirling passages increases the magnitudes of the radial velocity which leads to a wide expansion of the annular jet. Therefore, we can expect a shorter and a wider flame in case of counter-flow as compared to the co-flow. From the zoomed inset of Fig. 6.7(a) and (b) we observe that the maximum negative velocity of reversed flow regions attached to the inner walls of the two swirlers is increased from $0.12V_0$ (~ -6.5m/s) in co-flow to $\sim 0.34V_0$ (~ -17.85m/s) in counter-flow. Further, the flow fields indicate that the flame is likely to attach to the center body of the inner swirler. From the stream-wise contours of mean tangential velocity of swirler 1 (S4555) and swirler 2 (Sc4555) (Fig. 6.7(c) and (d) respectively), we can observe that the flow inside the combustor is dominated by the swirl direction of the outer swirler. The tangential velocity have the highest magnitude at about a similar location as the axial velocity for both the configurations inside the combustor and extend up to $\sim 3.2D$ for co-rotating flow and up to $\sim 3.13D$ for counter-rotating flow. In swirler 2, at the burner exit near the centerline, the magnitudes of tangential velocity are smaller than the swirler 1 due to opposing sense of rotation about burner axis for the inner and outer swirlers of the counter-rotating configuration.

To identify the impact of each swirler on the flow field, Fig. 6.8 shows the cross-wise contours of mean axial velocity (a, e), tangential velocity (b, f), radial velocity (c, g) and turbulent kinetic energy (d, h) at plane C_1 inside the burner (shown in the zoomed inset of Fig. 6.7 for swirler 1 ((a)-(d)) and swirler 2 ((e)-(h)). From Fig. 6.8(a) and (e), we observe the presence of a larger reversed flow region attached to the inner wall of the outer swirler in case of counter-rotating flow in comparison to the co-flow. This is because of the increased magnitudes of velocity in the radial direction (Fig. 6.8(c) and (g)) in case of counter-flow which causes the higher expansion of the flow emerging from the outer swirler thereby resulting in increased recirculation near the wall. This leads to increased turbulence near the burner exit inside the outer swirler in case of counter-flow (Fig. 6.8(h)). The increased turbulence will cause more entrainment of recirculating gases in the incoming flow and therefore increases the probability of boundary layer flashback through outer shear layer. Further, we can observe from Fig. 6.8(c) and (g), that the shearing is prominent in the counter-rotating case due to presence of a positive velocity jet followed by a negative velocity jet near the burner exit which leads to more turbulence in counter-rotating case.

We next discuss the comparative circumferentially averaged axial velocity, tangential velocity, radial velocity and turbulent kinetic energy profiles at planes C_2 and C_3 inside the combustor of swirler 1 (S4555-lines) and swirler 2 (Sc4555-markers) (Fig. 6.9). The presence of multiple

peaks at plane C_2 in Fig. 6.9(a) and (c) indicates the presence of multiple swirling passages in the burner. The outer swirler is observed to significantly affect the flow in the combustor: the counter-rotating flow has increased the width of the CRZ and increased the peak axial velocity

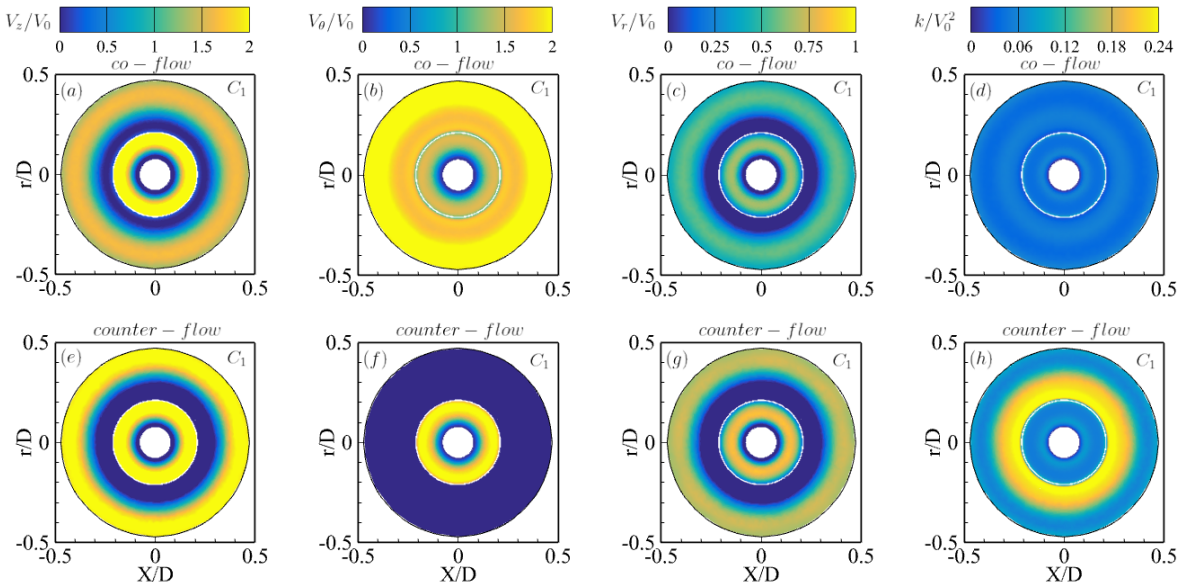

Figure 6.8: Non-reactng flow: cross-wise contours of mean axial velocity (a, e), tangential velocity (b, f), radial velocity (c, g) and turbulent kinetic energy (d, h) at plane C_1 inside the burner for swirler 1 ((a)-(d)) and swirler 2 ((e)-(h)). The coordinates, velocities and k are normalized by D, V_0 and V_0^2 respectively.

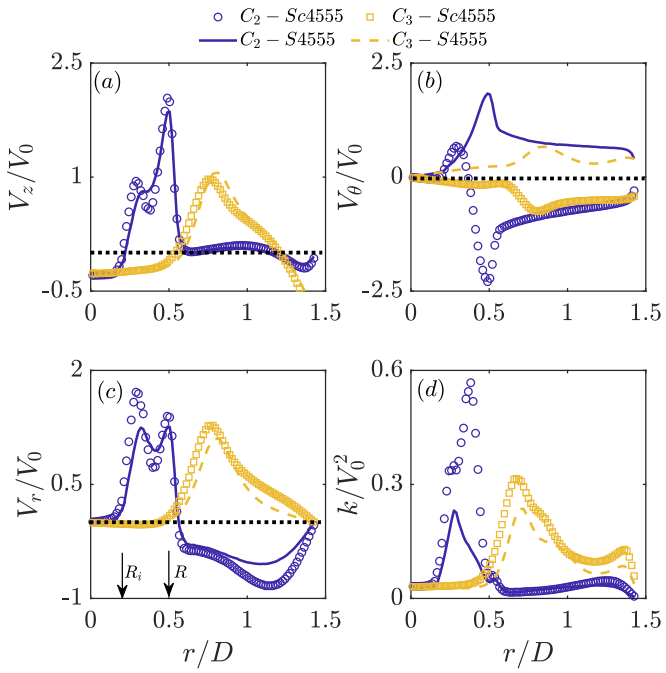

Figure 6.9: Non-reacting flow: circumferentially averaged (a) axial velocity (V_z); (b) tangential velocity (V_θ); (c) radial velocity (V_r); (d) turbulent kinetic energy (k) profiles at planes C_1 ($Z/D = 0.05$), C_2 ($Z/D = 0.4$) and C_3 ($Z/D = 0.8$) inside the combustor of swirler 1 (S4555-lines) and swirler 2 (Sc4555-markers). The coordinates and velocities are normalized by D and V_0 respectively. The exit radii of each swirler is marked by the arrows.

magnitude (Fig. 6.9(a)), has reversed the direction of tangential velocity (Fig. 6.9(b)) and has increased the turbulence at the burner exit in both axial and tangential direction. These effects are attributed to the interaction between co- and counter- rotating swirling flows in the inner and outer passages. We can observe in the downstream direction (from $C_1 \rightarrow C_3$), the magnitudes of the axial, tangential and radial velocity decreases for both the burner configurations. The magnitudes of the radial velocity of counter-rotating case at C_2 and C_3 is 13% and 8% higher than the co-rotating case (Fig. 6.9(c)) which indicates that the divergence angle of the annular jet of the counter-flow is greater than the co-flow that causes the faster re-attachment of the flow to the combustor wall for swirler 2. From Fig. 6.9(d), we observe that the turbulence intensity is highest in the shear layers for both the configurations. The maximum turbulent kinetic energy for counter-rotating case observed near the burner exit is $\sim$ 23% greater than the co-rotating flow. This higher turbulence in the shear layer of the counter-flow can be utilized for better mixing [224].

6.3.2 Reacting Flow Fields

6.3.2.1 Velocity fields

The heat release from combustion results in temperature jump and a corresponding density drop, which in turn causes the flow fields for the reacting case to differ from those of the non-reacting conditions. We now discuss the effects of combustion on the flow-fields of the co- and counter-rotating flows at $\Omega = 0$ and $\Omega = 0.2$ respectively. Figure 6.10(a, d) and Fig. 6.11(a, d) shows the stream-wise (r–z plane) contours for the mean axial velocity for swirler 1 and swirler 2 at $\Omega = 0$ and $\Omega = 0.2$ respectively. In comparison to the non-reacting flow (Fig. 6.7), we observe a reduction in the size of the CRZ with increased maximum negative velocity and increased peak annular velocity in reacting flow for both the swirler configurations: the width of CRZ reduces by $\sim$0.7 % for co-rotating flow and $\sim$ 5% for counter-rotating flow compared to the non-reacting flow. The length of the CRZ reduces by 7.5% for co-rotating case, while it reduces by 10% for counter-rotating case. The maximum negative velocity of the CRZ increases by $\sim$ 28 % ($\sim -24\,\mathrm{m\,s^{-1}}$) for co-rotating case and by $\sim$ 21% (~ -25m/s) for counter-rotating case; whereas the maximum velocity of the annular jet emanating from the burner exit increases by $\sim$5 % for the co-rotating flow and by $\sim$ 8% for the counter-rotating flow compared to the non-reacting case. The steam dilution does not affect the velocity field significantly. From the velocity fields of both the swirlers, we can expect two types of flame stabilized in either of the shear layers (high velocity gradient regions between annular jet and recirculation zones): (i) a V-shaped flame or (ii) an M-shaped flame anchored to the center body of the inner swirler.

6.3.2.2 Temperature distribution and flame shape

Figure 6.10(b, e) and Fig. 6.11(b, e) shows the stream-wise (r–z plane) contours for the temperature distribution for swirler 1 and swirler 2 at $\Omega = 0$ and $\Omega = 0.2$ respectively. We can observe two high temperature regions at near the burner exit inside the combustor: (i) the center region wherein the hot combustion gases are recirculated through the CRZ; (ii) the outer

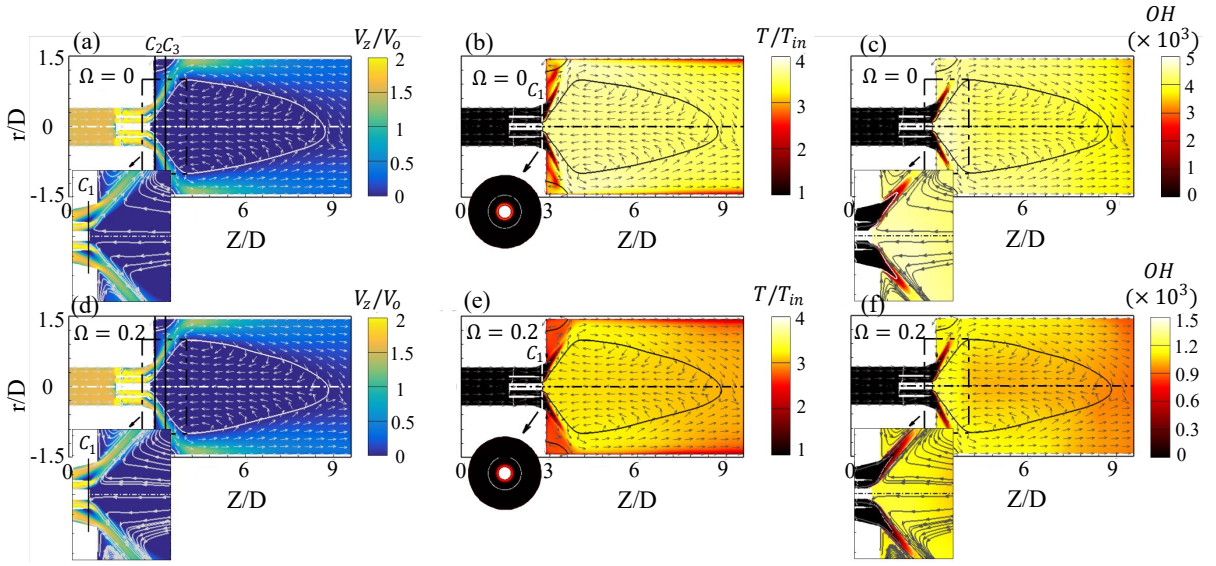

Figure 6.10: Reacting flow: stream-wise contours of (a, d) mean axial velocity, (b, e) temperature distribution and (c, f) OH species mass fraction for swirler 1 (S4555) at $\Omega = 0$ and $\Omega = 0.2$ respectively. The coordinates, velocity and temperature are normalized by D, V_0 and T_{in} respectively. The contour lines for zero axial velocity are indicated by solid lines. The arrows indicate the direction of flow.

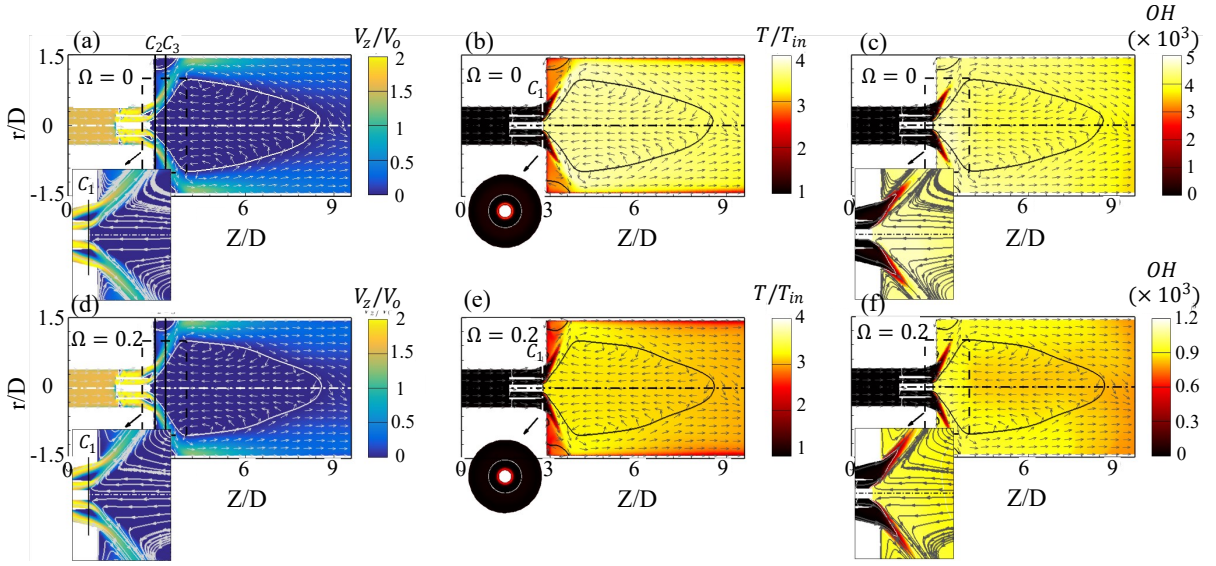

Figure 6.11: Reacting flow: stream-wise contours of (a, d) mean axial velocity, (b, e) temperature distribution and (c, f) OH species mass fraction for swirler 2 (Sc4555) at $\Omega = 0$ and $\Omega = 0.2$ respectively. The coordinates, velocity and temperature are normalized by D, V_0 and T_{in} respectively. The contour lines for zero axial velocity are indicated by solid lines. The arrows indicate the direction of flow.

region near the combustor walls wherein the ORZ is located. At $\Omega = 0$, a flame temperature of 2400 K ($\sim 3.85 T_{in}$) is observed inside the combustor for both the configurations. When the fuel-air mixture is diluted with steam (i.e. at $\Omega = 0.2$), we observe that the flame temperature reduces to 1994 K for both the swirlers. This is because the steam absorbs the energy from the combustion to heat up. Further, steam dilution also increases the heat loss of the flame due

to its stronger radiation ability [225]. At the combustor walls, we observe low temperatures due to the heat-loss (constant wall temperature boundary condition). These trends can also be observed from the distribution of temperature along the centerline of the combustor for both the swirlers shown in Fig. 6.12(a). The temperature profiles have a steep gradient in the reaction zone. The similarity in the peak temperatures between co- and counter- configurations has also been reported by Li and Gutmark [209] for TARS when operating on gaseous fuel. We can observe that in both the configurations, the flame is attached to the inner wall of the inner swirler as expected from the velocity field (the location of flame attachment is shown by the cross-wise contours for each configuration).

The flame shape and structure for swirler 1 and swirler 2 at $\Omega = 0$ and $\Omega = 0.2$ is represented by the distribution of OH species mass fraction in Fig. 6.10(c, f) and Fig. 6.11(c, f) respectively. We can observe that the steam dilution decreases the concentration of the OH species mass fractions for both co-and counter-rotating flows. This is because the steam addition decreases the concentration of all the reactants which leads to a lower reaction rate for the same ϕ and also decreases the flame residence time by increasing the mass flow rates. We observe an M-shaped flame anchored to the inner wall of the inner swirler in both the configurations. The M-shaped flame observed at intermediate steam content ($\Omega = 0.1 - 0.2$) can transition to a short V-shaped flame at higher steam content ($\Omega = 0.3 - 0.4$) [226]. From the zoomed inset of Fig. 6.10(c, f) and Fig. 6.11(c, f), we can observe that steam dilution causes the flame to move in the downstream direction. The superimposition of the streamlines of axial and radial velocity components on the OH distribution shows that the M-shaped flame is stabilized in the outer shear layer in both the swirlers. Further, in case of counter-rotating flow, we can observe that the flame is stretched in radial and confined in axial direction which results in a wider and shorter flame when compared to co-flow. The existence of the flame divides the combustor in three regions as shown in Fig. 6.12: (I) pre-flame region; (II) in-flame region or the reaction zone which is dominated by the mixing, and (III) post-flame or burn-out region which is dominated by the chemistry. All the combustion species mass fractions such as OH, CH_2O, CO, NO, etc. first increases

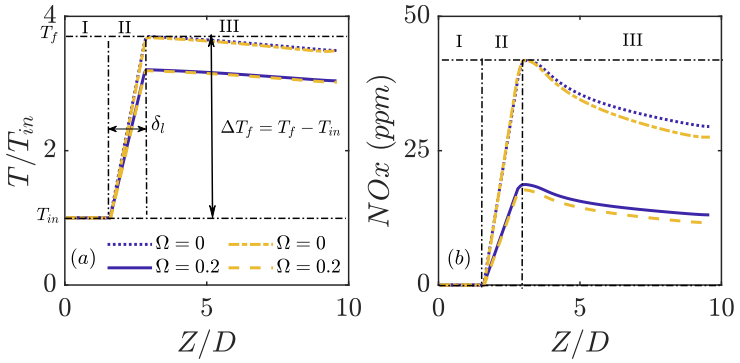

Figure 6.12: Reacting flow: centerline profiles of (a) temperature and (b) NOx emissions formed by thermal pathway for swirler 1 (yellow) and swirler 2 (blue) at $\Omega = 0$ and $\Omega = 0.2$ respectively. The coordinate and temperature are normalized by D and T_{in}. δ_l represents the flame thickness; T_f represents the flame temperature. I →pre-flame region; II →in-flame region (or reaction zone) and III →post-flame region (or burn-out).

sharply from pre-flame region to the reaction zone, attains a maximum in the reaction zone and then decreases in the burn-out region to attain equilibrium through a series of recombination reactions with the other species. The sharp gradients observed in the reaction zone correspond to the flame edge indicating the location of the flame front and gives an estimate of the flame thickness (δ_l).

6.3.2.3 Emissions

It has been reported previously that NOx emissions in a premixed flame depends on temperature and equivalence ratio: NOx emissions are low at low temperatures and equivalence ratios and increases rapidly with increase in equivalence ratios [8]. There are 4 conventional pathways for NOx formation [8]: (i) thermal pathway (Zeldovich) which is the strongest pathway for NOx formation when the temperatures are above 1700K. In this case, the concentration of the equilibrium NO is the highest due to increased residence time of gases in high temperature regions; (ii) prompt NO pathway where NO results from CH radicals, therefore are higher in concentration in rich mixtures. These NOx occurs at temperatures below 1000K due to their lower activation energy compared to the thermal NOx; (iii) NO formation via N_2O which is the source of NOx formation at lean conditions; (iv) NO formation via NNH radical pathway is prominent for flames where hydrogen content is high due to more H radicals. For dry methane flames, the flame adiabatic temperature lies within 1350 K to 1950 K depending on the equivalence ratios. The addition of hydrogen increases the flame temperatures due to higher flame speed and reaction rates. The flame temperature observed in the dual swirl burner for methane-hydrogen mixture is 2400K at $\Omega = 0$ and 1994K at $\Omega = 0.2$ which indicates that the thermal NOx pathway dominates the NO formation. We estimate the NOx emissions from the burner by choosing the thermal NOx model in Ansys solver setup. This pathway of NOx model estimates the pollutant that is formed after combustion. Figure 6.12(b) shows the distribution of NOx formed by the thermal pathway along the centerline of the combustor for both the swirlers. We can observe that the highest NOx concentration occurs in the reaction zone in the CRZ where the incoming reactants interact with the recirculating hot combustion products. The addition of the steam decreases the temperatures inside the combustor and thereby reduces the NOx emissions. The overall NOx emissions from both the configurations are below 45ppm at $\Omega = 0$ and 15ppm at $\Omega = 0.2$ which is expected for a lean premixed gas turbine combustor [227]. At the combustor exit, the average NOx emission for co-flow is 24ppm, whereas it is 25.1ppm in the counter-flow at $\Omega = 0$. With the steam dilution, the NOx emission reduces to 10.4ppm

Table 6.4: Comparison of NOx and CO emissions from dual swirl burner with Göke [8]

Burner	T_{in} (K)	$\dot{m}_t$ (kg/h) $(air + steam)$	$\%CH_4, \%H_2$	Ω	ϕ	NOx (ppm) $(15\%O_2, \text{dry})$	CO (ppm) $(15\%O_2, \text{dry})$
Premixed combustor [8]	623	180	80, 20	0.2	0.9	3.2	1.3
Swirler 1 (co-flow)	623	180	80, 20	0	0.9	7.3	1.26
				0.2		3.0	1.26
Swirler 2 (counter-flow)	623	180	80, 20	0	0.9	7.5	1.26
				0.2		3.3	1.26

for co-flow and 11.5ppm for counter-flow. We present the comparison of the estimated NOx ($@15\%O_2$, dry) in the dual swirl burner with the experimental study of Göke [8] on a premixed combustor employing a single swirler at the same operating conditions shown in Table 6.4. The flame temperature observed in Göke [8] is $\sim 1750 - 1850$K which is $\sim 12 - 15\%$ lower than the flame temperature attained in the dual swirl burner. We observe that the estimated NOx for both co-rotating flow and counter-rotating flow are similar to the values reported by Göke [8].
CO emissions for pure methane-air mixtures at dry conditions show dependence on the equivalence ratios [8]: near the lean blowout limit ($\phi \sim 0.2 - 0.3$), CO emissions are $\sim$ 5ppm($@15\%\mathrm{O}_2, \mathrm{dry}$) due to flame instability and low temperatures; at $\phi \sim 0.5 - 0.6$, CO emissions are extremely low ($\sim 0.2 - 0.3$ppm($@15\%\mathrm{O}_2, \mathrm{dry}$)). This is the range where the lean premixed gas turbines operate; Further increase of ϕ, increases the CO emissions due to increase in CO_2 and temperature. The hydrogen addition to the methane-air mixture reduces the CO emissions due to reduction in the concentrations of CO_2 [8], increase in OH concentration [228] and increase in global reaction rate [229]. Steam dilution does not affect the trend of CO emissions except that the same trends are observed at high equivalence ratios. The estimated CO emissions ($@15\%\mathrm{O}_2, \mathrm{dry}$) from co-flow and counter-flow along with the comparison with Göke [8] are tabulated in Table 6.4. The estimated CO emissions from both the configurations is below 5ppm and a deviation of only 4% is observed from the experiments. We observe that the CO emissions are not affected by the swirler configurations.
Our results indicates that GRI-Mech 3.0 provides relatively good prediction of NOx and CO emissions for methane-hydrogen flames. The accuracy in the prediction of emissions employing GRI-Mech 3.0 reaction mechanisms has also been confirmed by the numerical study by Göke [8]. From Table 6.4, we also observe that the swirler configurations (co- and counter-flow) at high inlet temperatures does not significantly affect the NOx and CO emissions, despite having differences in the flame structure. This is because gaseous fuel at high temperatures require lesser mixing time within highly turbulent flow [209].

Chapter 7

Schlieren Image Velocimetry and Modal Decomposition Study of Preheated Swirling Flows

7.1 Overview

In this chapter, we experimentally investigate the typical flow features and coherent structures of the counter-rotating dual swirl burner developed in chapter 6. Here, the objective is to study the interaction between large-scale coherent structures, specifically the PVC and acoustic excitation using time-resolved Schlieren imaging. The hypothesis is that introducing a broad range of frequencies may suppress or excite the coherent structures associated with instability. This information is significant for developing mitigation and control strategies for thermoacoustic instability in practical combustion systems. This study encompasses three distinct excitation ranges: (i) a frequency lower than the natural frequency of PVC, (ii) a frequency higher than the natural frequency of PVC (motivated from the work of Lacarelle et al. [129]), and (iii) broad-band excitation (white noise). We first perform Schlieren image velocimetry to obtain the mean flow characteristics of the burner, compare the velocity fields with RANS simulations and, subsequently, employ proper orthogonal decomposition (POD) analysis to identify and extract the dominant coherent structures in the flow.

This chapter is further divided into two sections. Section 7.2 discusses the details of experimental setup and data pre-processing, followed by the procedure for performing SIV and POD analysis. In section 7.3, we present the results and discuss the effects of different acoustic actuation on the flow.

7.2 Experimental setup and methodology

7.2.1 Experimental setup

This study conducts experiments using an unconfined multi-swirler jet setup, schematically shown in Fig. 7.1, together with the Schlieren imaging configuration. The investigated burner (half-section view shown as a zoomed inset) is characterized by three co-axial air passages: outer radial swirler ($S = 0.8$), intermediate ($S = 0.8$) and inner ($S = 1.08$) axial swirlers, discussed and developed in section 6.2. Multiple realizations of the burner can be obtained by varying the vane angles, swirling direction (co- or counter-rotating) or blocking varied swirling passages. For the present work, radial slots are blocked to obtain a dual-swirl burner configuration (as discussed in chapter 6), where intermediate and inner swirlers have counter- and co-rotating vanes (45° and 55°), respectively. We chose counter-rotating swirling direction of the burner as counter-flow is reported to create high turbulence in the shear layers and enhance mixing [224].

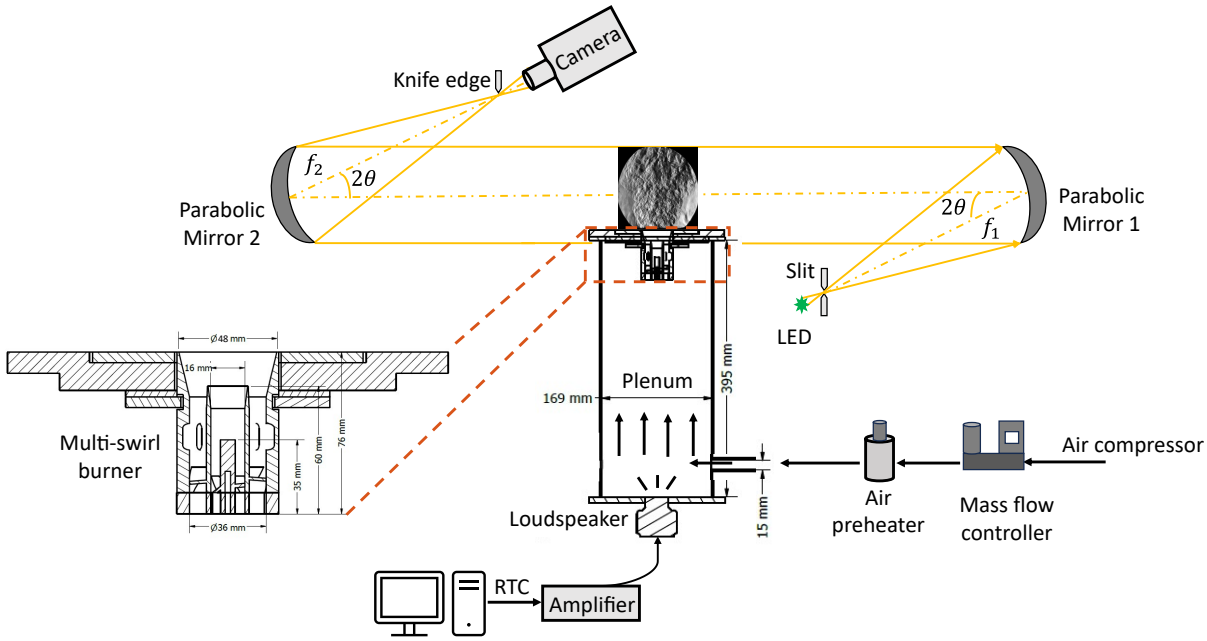

Figure 7.1: Schematic diagram of the unconfined experimental test rig with Z-type Schlieren imaging system.

The dual swirl burner configuration is asymmetric, with 8 and 5 vanes in intermediate and inner swirlers, respectively. The overall length and exit diameter of the dual swirl burner are $L = 76$ mm and $D = 48$ mm. The bulk velocity corresponding to the burner exit diameter is $u_{bulk} \sim 1.34$ m/s.

Preheated air (100°C) at a constant flow rate of 150 SLPM is fed to the burner via a cylindrical duct of 169 mm diameter. The test rig also allows for the actuation of stream-wise acoustic waves using the loudspeaker (Ahuja AU60 unit) mounted upstream of the burner. In this work, we present the comparative results for flow fields and coherent structures between the natural flow and acoustically forced flow with two types of actuation: (i) a sinusoidal excitation of constant amplitude at two different frequencies corresponding to the Strouhal numbers (defined as, $St = fD/u_{bulk}$) of $St = 0.46$ (frequency lower than the natural frequency of observed PVC, see section 3.2) and $St = 2$ (frequency much larger than the natural frequency of PVC) and (ii) a white noise excitation.

A time-resolved Z-type Schlieren imaging system captures the flow field emerging from the swirling jet (illustrated in Fig. 7.1). This setup consists of two identical parabolic mirrors (6" diameter with a focal length of 609.6 mm), a green LED point source (CBT120 luminous device), a source slit and a knife edge [201]. The instantaneous flow snapshots were captured using a high-speed camera (Photron Fastcam mini AX100 with F2.8/100 mm macro lens) at a frame rate of 1000 FPS with a resolution of 8250 px/m. 1800 images of size 1024×1024 are acquired for each flow condition. The average pixel shift between two consecutive images is ~ 12 pixels. Note that in case of high speed flows, where bulk velocity at the burner/nozzle exit is greater than 300 m/s, an extremely high framing rate is required to capture such flow details and extract a meaningful correlation between consecutive images [192]. For example, to observe a 10×10 cm^2 region of interest in a flow field flowing at a velocity of 500 m/s, a minimum of

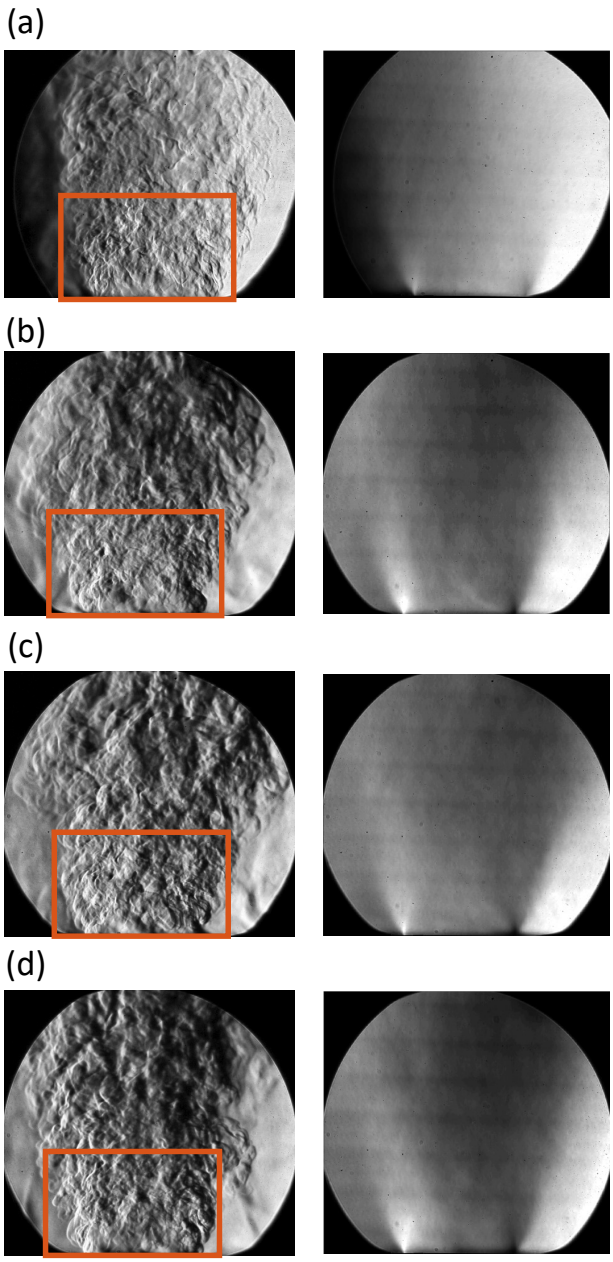

Figure 7.2: Instantaneous (left) and mean (right) Schlieren images captured at varied flow conditions: (a) natural flow; forced flow with acoustic excitation of (b) $St = 0.46$, (c) $St = 2$ and (d) white noise. The region of interest for the subsequent analysis is highlighted by the rectangle.

80 kHz frame rate is required for an optimum 10 to 12 pixel shift [192]. Also, in such high speed flows, camera exposure time should be less than frame-to-frame time delay to reduce the integration effect, which requires involvement of two cameras (master and slave). In this work, as the velocity is low ($\sim$ 1.34 m/s), a dt = 1 ms is sufficient to capture the flow effectively. An illustration of the acquired instantaneous flow images (left column) and corresponding mean intensity (right column) for each flow condition is shown in Fig. 7.2. The rectangular red boxes indicate the chosen region of interest for the subsequent analysis. The instantaneous Schlieren images (Fig. 7.2) show the temporal and spatial flow structures (turbulent eddies) of varied length scales, while the mean intensity images show the two annular jets emerging from the

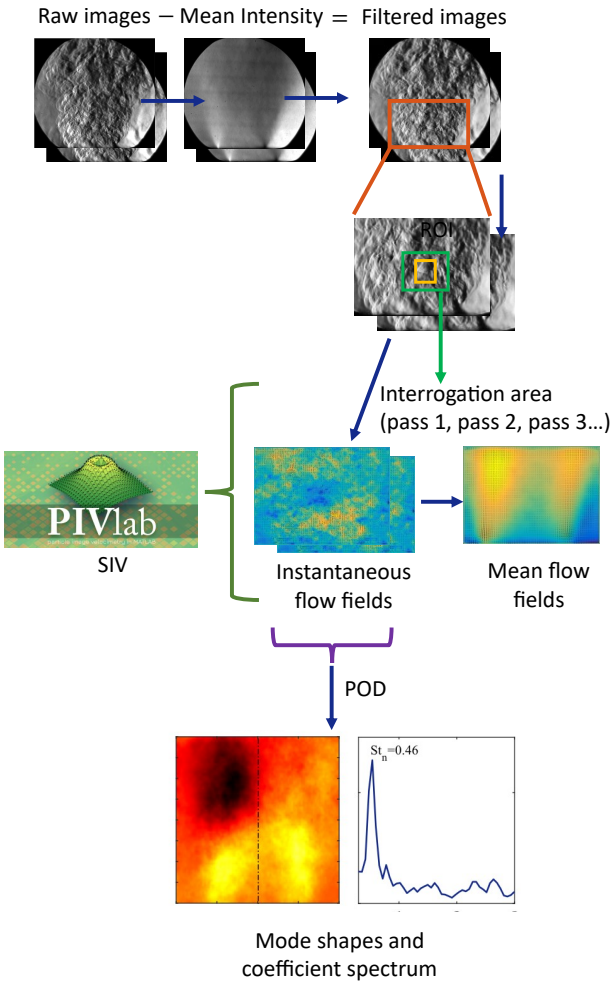

Figure 7.3: An illustration of the image pre-processing employed for Schlieren image velocimetry (SIV) and proper orthogonal decomposition (POD) study.

swirl burner. We can also observe that acoustic excitation of the flow causes increased vortical fluctuations, indicating an increase in the energy of the turbulent eddies.

7.2.2 Methodology

7.2.2.1 Image pre-processing

Schlieren imaging shows the density gradients in the line of sight. Hence, the results are the projections of 3D structures with temporal evolution characterized by high density and temperature gradients. Therefore, image restoration and enhancement play a significant role in obtaining the flow fields and properties from Schlieren images. Figure 7.3 shows an illustration of image pre-processing employed for performing Schlieren image velocimetry (SIV) and Proper orthogonal decomposition (POD) analysis. The visualization of structures (or turbulent eddies) in the images is enhanced by subtracting the mean intensity from the instantaneous snapshots (image re-construction) followed by an intensity capping [230], which significantly improves the image contrast for cross-correlation. Note that, mean intensity subtraction does not necessarily always work when dealing with Schlieren images: it can also lead to loss of actual signals [192]. Noise filters are applied to remove image outliers caused by camera shot noise, pixel anomalies,

and digitization artefacts. Lastly, a Laplace filter was also applied to enhance the edges of the turbulent structures, which reduces the so-called peak-locking effect [231]: long camera exposure time could blur turbulent structures and create an under-sampled image segment. A region of interest (ROI), as shown in Fig. 7.3, was then chosen to perform the SIV and POD analysis.

7.2.2.2 Schlieren image velocimetry (SIV)

SIV is performed using the PIVLab application [232] to estimate the instantaneous and mean flow fields emerging from the burner at varied flow conditions. The velocity vectors are obtained using the FFT window deformation cross-correlation algorithm, wherein the size of the interrogation windows changes from coarse to fine in various passes (shown by green and yellow squares in Fig. 7.3). A large interrogation window in the first pass, on the one hand, enhances the signal-to-noise ratio (SNR) and estimates the displacement of pixels reliably, but also gives low vector resolution. Therefore, the size of the interrogation windows is reduced in the subsequent passes, where the pixel displacement information from the initial pass is used to offset the interrogation areas in the next pass. Thereby yielding high vector resolution, SNR and dynamic velocity range. For the present analysis, we chose 4 passes of the window sizes as 128×128, 64×64, 32×32 and 16×16 respectively. The estimated velocity vectors are then calibrated using 8250 px/m resolution with the time step of 1 ms between the images. The post-processing of the estimated vector fields includes data filtering to remove any erroneous vectors occurring due to outliers or poor illumination using a standard deviation filter followed by the interpolation of missing data.

An important note here is SIV offers integrated velocity fields along the line of sight, therefore, it mostly provides qualitative characteristics of the flow features. Achieving precise quantitative accuracy for velocity fields can be challenging, especially in regions of uniform density or where density gradients are weak. There are several key considerations: (i) spatial resolution of SIV limited by the optical setup and resolution of the imaging system. This means that small-scale flow structures (smallest eddies) may not be fully resolved, particularly in high-speed flows where rapid changes occur over short distances. In such cases, it may be challenging to distinguish between turbulent fluctuations and true flow velocities, leading to inaccuracies in the measurements. (ii) Optical distortions, such as aberrations in the imaging system or non-uniform illumination, can introduce errors into the schlieren images. These distortions can make it difficult to accurately interpret the density gradients and can affect the precision of the velocity measurements. (iii) limited depth of field of SIV, which makes it challenging to fully characterize complex three-dimensional flows. Given these factors, it is crucial to report the expected uncertainty limits in SIV results: the mean uncertainties in axial (V_y) and radial (V_x) velocities observed are 1.24 ± 0.13 m/s and 0.6 ± 0.03 m/s, respectively. These values are derived from statistical measurements (histogram plots) in PIVLab. In summary, Schlieren imaging velocimetry serves as a valuable tool for visualizing and quantifying fluid flow velocities, offering valuable insights into complex flow phenomena. However, one must carefully consider its limitations and uncertainties when interpreting the results.

7.2.2.3 Proper orthogonal decomposition (POD)

Proper Orthogonal Decomposition (POD) is a technique used to extract dominant patterns or modes from a set of data (spatial snapshots of a field variable such as velocity) [233]. A brief methodology for obtaining POD modes is as follows [233]: (i) the spatial snapshots are firstly arranged into a matrix, U, where each column corresponds to a snapshot, and each row corresponds to a spatial location. For N snapshots and M spatial locations, U is an $M \times N$ matrix; (ii) then a singular value decomposition (SVD) on U is performed to obtain $U = A \sum W^T$, where A is the matrix of spatial modes (POD modes), $\sum$ is a diagonal matrix of singular (or eigen) values and W is the matrix of temporal coefficients; (iii) a certain number n of dominant modes, based on the magnitude of the eigenvalues, are selected. Typically, n is chosen to capture a significant amount of the total energy or variability in the data. The reconstructed field variable is then given as, $u_n(x,t) = \sum_i^n w_{ri}\phi_i(x)$, where, w_{ri} are the temporal coefficients and $\phi_i(x)$ are the spatial modes. The POD modes represent the spatial structures, and the temporal coefficients provide the time evolution.
We estimate the POD modes from the instantaneous axial velocity snapshots and identify the dominant coherent structures and the corresponding peak frequency at all flow conditions.

7.3 Results and discussions

7.3.1 Velocity fields

Figure 7.4 shows the stream-wise 2D contours in the x-y plane for mean velocity magnitude (left) and vorticity (right) fields obtained from SIV at varied flow conditions. Typical features associated with the swirling flow are observed: two annular jets, separating the central (CRZ) and the outer (ORZ) recirculation zones, emanate from the intermediate and inner swirling passages. Regions of strong velocity gradients, known as the shear layers, exist between the incoming annular jet and the formed recirculation zones. These regions are highly unstable and turbulent and are associated with the vortex roll-up, forming concentrated vorticity regions, as shown in the right plots. The flame is expected to stabilize or anchor at these inner (between annular jet and CRZ) and outer (between annular jet and ORZ) shear layers. We observe a short central recirculation zone –a typical feature associated with counter flow configuration– which indicates that the flow will be less susceptible to flame oscillations [221], thereby increasing pressure gradient and turbulence. We observe that acoustic excitation of the flow reduces the magnitude of both velocity and vorticity fields. This implies that acoustic perturbations cause fluctuations in the vortical structures, which may, in turn, affect the frequency and energy level of global flow instabilities, as also reported by Chen et al. [234].
Figure 7.5 shows the mean axial and radial velocity profiles near the burner exit ($y/D = 0.05$) for all investigated cases. We can observe the presence of negative velocities in the central and outer recirculation zones. Downstream this plane, negative velocities at the center are not observed (see, Fig. 7.6). This implies that the CRZ is mostly propagated upstream inside the burner passages, specifically through the inner swirler, owing to its short length. The

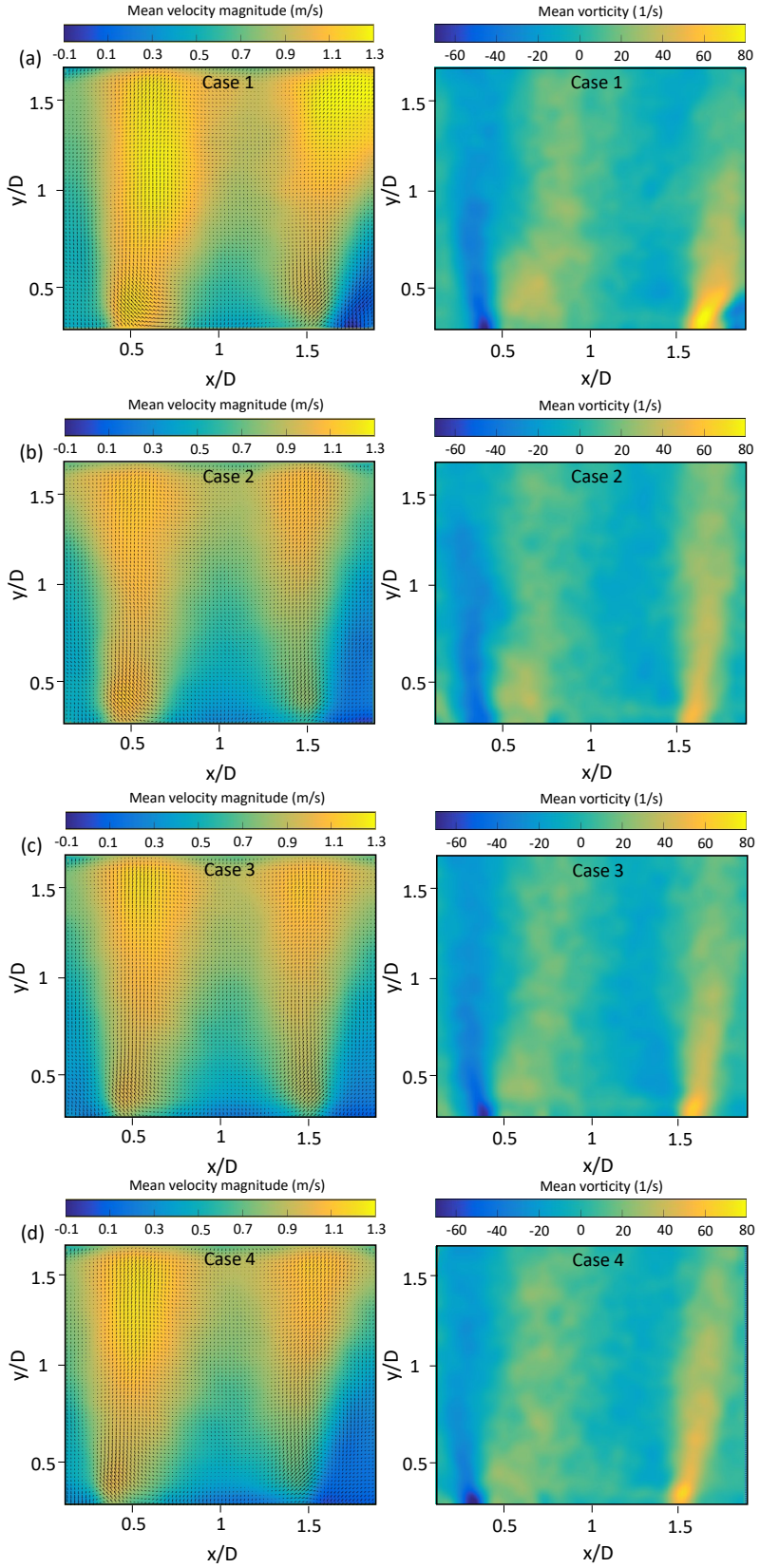

Figure 7.4: Mean velocity magnitude (left) and vorticity (right) fields estimated from SIV at varied flow conditions: (a) natural flow; forced flow with acoustic excitation of (b) $St = 0.46$, (c) $St = 2$ and (d) white noise. The coordinates are normalized by burner exit diameter (D).

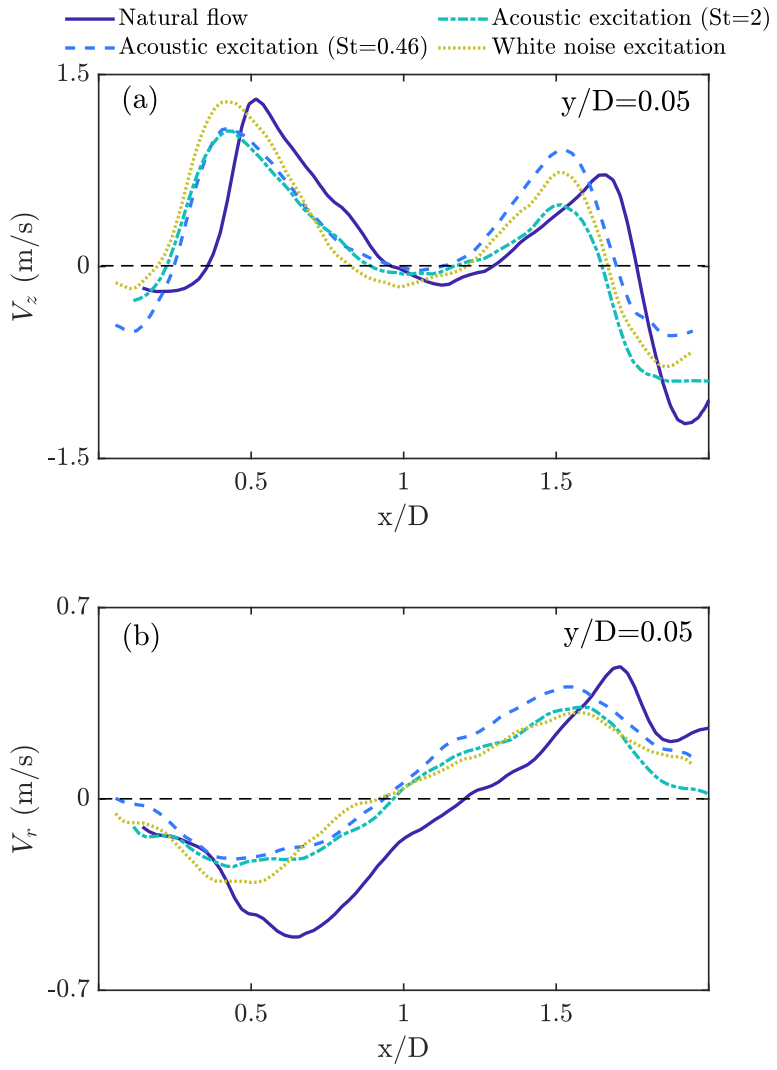

Figure 7.5: (A) Mean axial (V_z) and (b) radial (V_r) velocity profiles at $y/d = 0.05$ obtained from SIV at varied flow conditions (natural flow; forced flow with acoustic excitation of $St = 0.46$, $St = 2$ and white noise). The coordinates are normalized by burner exit diameter (D).

upstream propagation of CRZ indicates the potential occurrence of flame flashback under reactive conditions. We can observe the asymmetry in the flow fields in terms of peak annular jet velocities arising due to asymmetric burner geometry. The intermediate and inner axial swirlers in the burner have 8 and 5 vanes, respectively. The flow from the burner hence would not be symmetric around the center axis. Such asymmetry in the axial velocities were also reported through LES and PIV results in TARS (Triple Annular Research Swirler) by Iudiciani [18].
In addition to the experimental results, we conducted RANS simulations to validate the trends observed in the SIV data. The comparison between SIV and simulations is presented in Fig. 7.6. We observe a similarity in the qualitative trends between SIV and RANS. Although SIV offers integrated velocity fields along the line of sight, it accurately captures the characteristic flow features qualitatively provided the Schlieren images are pre-processed (restoration, enhancement and filtering) adequately, as evident from Fig. 7.6.

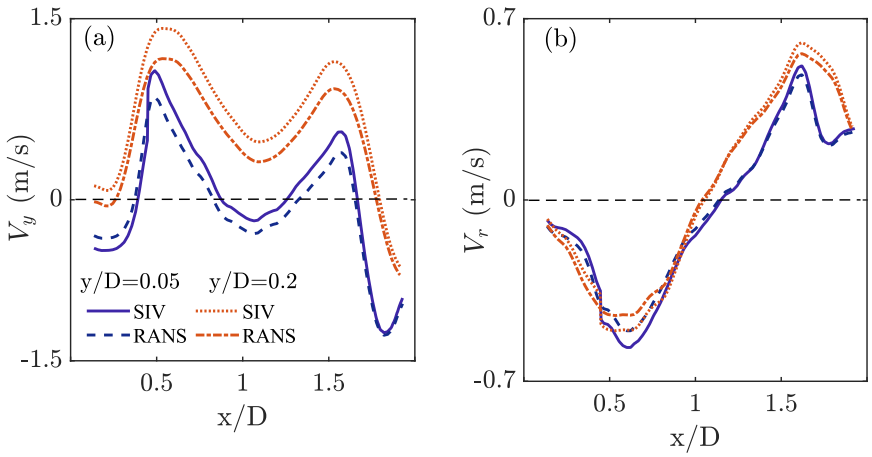

Figure 7.6: Comparison between rans and SIV results: (a) mean axial (V_z) and (b) radial (V_r) velocity profiles at $y/d = 0.05$ and $y/d = 0.2$. The coordinates are normalized by burner exit diameter (D).

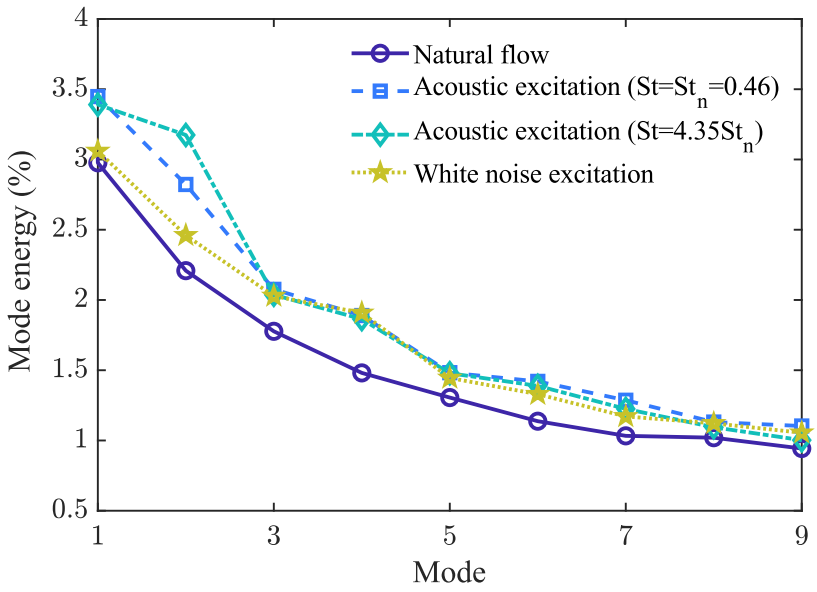

Figure 7.7: Mode energy fraction for first 9 modes drawn in descending order at all flow conditions (natural flow; forced flow with acoustic excitation of $St = 0.46$, $St = 2$ and white noise).

7.3.2 Flow structures identified from Schlieren image velocimetry

Figure 7.7 shows the energy of first 9 POD modes drawn in descending order for all flow conditions. In the energy spectra, modes $1 - 6$ have the highest energy content and hence represent dominating large-scale structures in the flow field. The energy content for modes greater that 7 is too low ($< 1\%$) for the POD to separate it from other dynamical structures and noise in the data. Acoustic forcing of the flow increases the mode energies regardless of the type of excitation. The energy level of acoustic excitation with $St = 0.46$, $St = 2$, and white noise are relatively similar for all modes, compared to the natural flow.

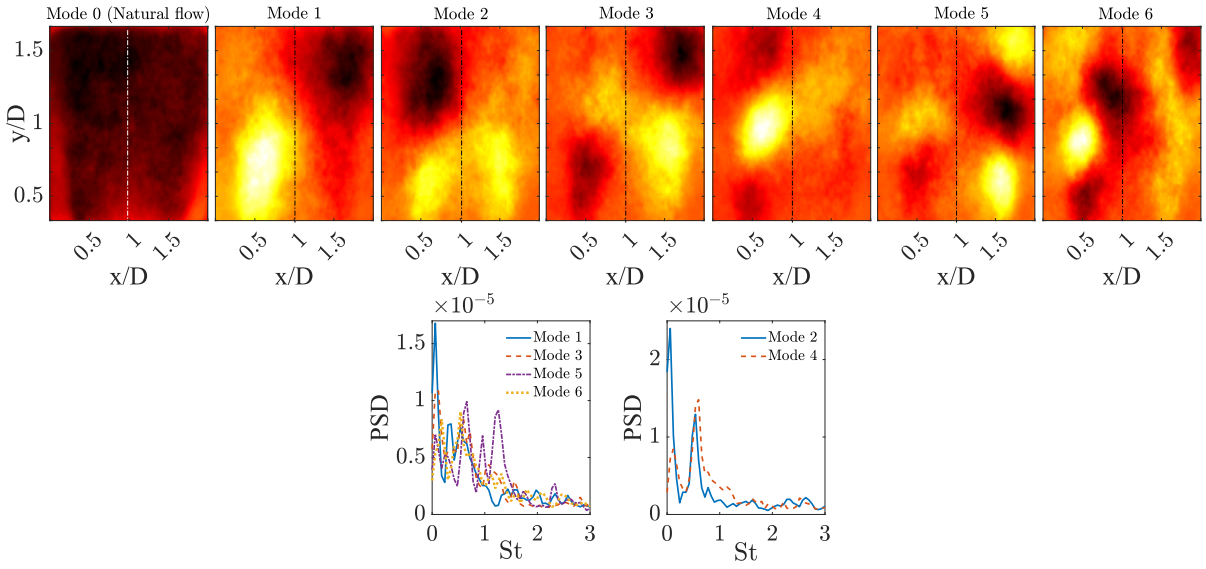

Figure 7.8: POD modes 0−6 in the stream-wise direction (top) and corresponding power spectra of time coefficients (bottom) of natural flow. The dashed dot line indicates the burner axis. The solid line corresponds to first mode of the pair and dashed line to the second.

We performed a sensitivity analysis, similar to Lacarelle et al. [129], for identifying the minimum number of instantaneous axial velocity snapshots required to effectively capture the mode shapes. We performed this analysis on the natural flow case, where we varied the number of snapshots ranging from 100 to 1800 in steps of 400. We find that for the analysis of POD modes from SIV data, a minimum of 1000 to 1200 snapshots are required. Here we show the analysis of POD modes obtained from 1500 snapshots of axial velocity.

Figure 7.8 shows the POD modes (0-6) and corresponding power spectra of time coefficients for the natural flow (unforced case). Mode 0 represents the mean axial flow from the burner. It is important to mention here that the sign of cross-wise velocity shows an opposed symmetry than the azimuthal velocity, such that modes $(2, 4)$ have anti-symmetric structure while modes $(1, 3, 5, 6)$ have symmetric structures. This implies helical fluctuations of an azimuthal order of $|m| = 2$ and higher are present in the flow [235]. When we consider the frequency spectra of the temporal coefficients of the mode pairs (modes $1, 3, 5, 6$) and (modes $2, 4$), we can observe multiple distinct peaks. This indicates that contributions from several different structures in the flow with their own dynamics are present in a mode pair. In other words, POD spreads out the coherent structures across multiple modes. The presence of similar double or triple helical structures in the swirling jet flow has been previously reported by Percin et al. [236], Vanierschot et al. [237,238] and Vignat et al. [239]. The frequency of the dominant anti-symmetric structures is observed at $St = 0.53 \pm 0.03$. The symmetric modes correspond to a double helical PVC, while the anti-symmetric modes correspond to single helical PVC [238].

Figure 7.9 shows the effect of excitation at $St = 0.46$ on the flow structures and corresponding power spectrum. When the flow is excited with $St = 0.46$, the symmetric modes $(1, 3, 5, 6)$ exhibit strong similarities with a phase shift in the axial direction compared to the natural flow. They indicate counter-rotating vortices at the burner exit. The anti-symmetric structures of

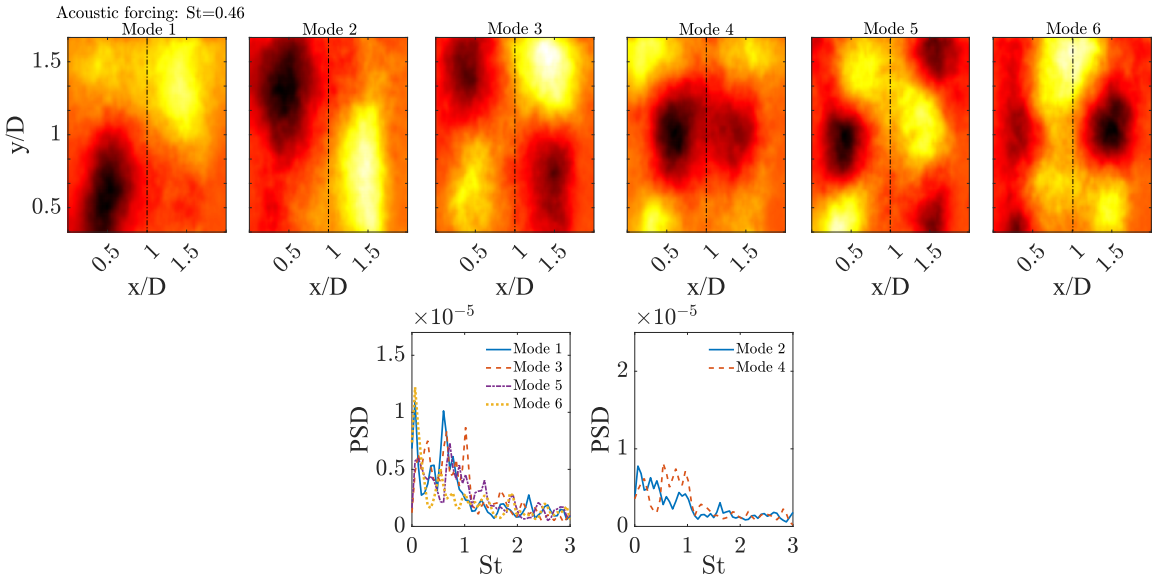

Figure 7.9: POD modes $1-6$ in the stream-wise direction and corresponding power spectra of time coefficients of forced flow at $St = 0.46$. The dashed dot line indicates the burner axis. The solid line corresponds to first mode of the pair and dashed line to the second.

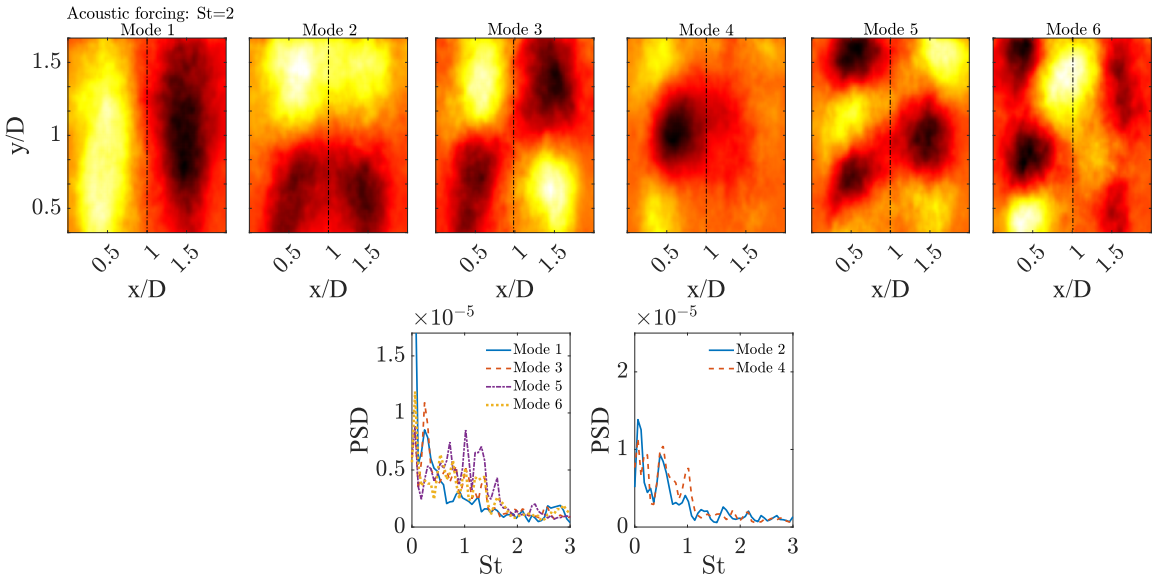

Figure 7.10: Pod modes $1-6$ in the stream-wise direction and corresponding power spectra of time coefficients of forced flow at $St = 2$. The dashed dot line indicates the burner axis. The solid line corresponds to first mode of the pair and dashed line to the second.

modes $(2, 4)$, on the other hand, changes to the symmetric ones and power spectra no longer show a peak frequency. This implies that the acoustic forcing of $St = 0.46$ which is lower than the natural frequency of the helical instability causes a suppression of single helical PVC. In this case, axial fluctuations are more energetic than the PVC. These results are in agreement with the experimental works of Moeck et al. [134], Lacarelle et al. [129] and numerical work of Iudiciani et al. [132].

We find that when the flow is forced with a frequency twice the natural frequency of PVC (i.e., $St = 1.06$), the helical structures becomes more energetic than the excitation, while maintaining

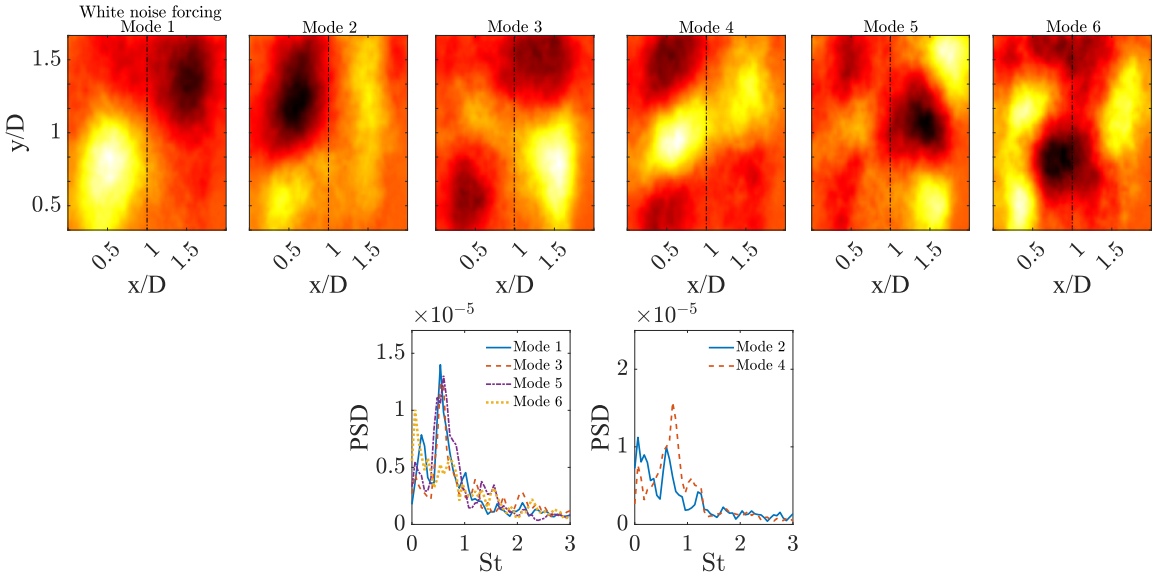

Figure 7.11: Pod modes $1-6$ in the stream-wise direction (top) and corresponding power spectra of time coefficients (bottom) of forced flow: white noise excitation. The dashed dot line indicates the burner axis. The solid line corresponds to first mode of the pair and dashed line to the second.

a peak at $St = 0.53$ as for the unforced case (not shown here). We now look at the structures when the flow is forced with $St = 2$ a higher frequency other than the PVC harmonics, shown in Fig. 7.10. We can observe that all the modes retain their symmetric/anti-symmetric structures as that of the natural flow with a phase shift in the axial direction. Thus, this forcing does not suppress the structures, but redistributes the modal contribution on the energy content. These trends concur with the experimental work of Lacarelle et al. [129].

From Fig. 7.8 and 7.10, we see that single frequency excitation of the flow fields either stabilizes or suppresses the single helical PVC depending on the excitation frequency, while it causes no major change to the double helical PVC. Figure 7.11 show the effect of broadband excitation, i.e., white noise, on the flow structures. We observe the following two main trends: (i) symmetric and anti-symmetric flow structures remain same as that of the natural flow case with no phase shift and (ii) white noise excites double helical PVC at $\sim St = 0.53$, while stabilizing the single helical PVC in the flow, evident from the frequency spectrum for the two cases. The observed trends holds for two different excitation amplitudes: 10% and 40% of bulk velocity. This excitation of the helical instabilities could be attributed to the amplification of shear layer (convective instability) caused by flow fluctuations, leading to the growth of coherent structures. These structures generate coherent Reynolds stresses and substantially modify the mean flow leading. This phenomenon is expected to become more pronounced in reactive cases. Further, from the mean axial velocity fields (Fig. 7.5), we noted upstream propagation of CRZ inside the burner. Therefore, these helical instabilities are expected to originate inside the burner passages, specifically in the inner swirler, due to its short length.

The POD analysis on raw Schlieren images did not provide the information on the presence of symmetric or anti-symmetric structures in the flow. The main reason behind this is that the flow had propagated upstream inside the burner, where most of the structures are formed. On

the other hand, POD analysis on the instantaneous axial velocity snapshots from SIV revealed the dominant structures along with the types of PVC and associated frequencies. Hence, this latter approach (POD-SIV) is better suitable for extracting more qualitative information on the flow.

In addition to the POD analysis, we also perform spectral proper orthogonal decomposition (SPOD) analysis [240] on the instantaneous axial velocity snapshots from SIV. The corresponding results are presented in Fig. G.1 of Appendix G. We find a qualitative agreement between the two analysis for the observed frequency of the dominant anti-symmetric mode pair (2-4). Further, from the temporal evolution of mode coefficients, we observe that the dominant mode is marginally stable for natural flow and an excitation with white noise forcing stabilizes this mode in the flow.

Conclusions - PART II

Swirling flows in gas turbine (GT) combustors are highly susceptible to precessing vortex core (PVC), a self-excited global hydrodynamic instability associated with vortex breakdown. This instability creates large-scale coherent structures and significant flame fluctuations, potentially causing thermoacoustic instability. While previous studies have examined PVC excitation and suppression under single-frequency acoustic excitation, GT combustors inherently exhibit noise dynamics that vary with operating conditions and combustor designs. It is crucial to investigate how these coherent structures interact with the inherent combustor noise, which is the focus of this part of the thesis. We derive the following conclusions:

1. We begin by developing a multiple swirl burner using RANS simulations, capable of operating with various hydrogen-enriched fuel blends. This burner, designed to exhibit reduced flame flashback and NOx emissions, considers parameters such as swirling direction (co- and counter-rotating), fuel blends, equivalence ratios, and the number of swirling passages. We report the comparative insights from RANS investigation of co- and counter-rotating configurations of a dual-swirl burner operating on lean premixed methane-hydrogen-steam-air mixture. We find that the two configurations can lead to important differences in the flow field and the flame structure. From the non-reacting and reacting velocity fields, we observe that in comparison to the co-rotating case, the counter-rotating swirl case has a shorter and wider CRZ located slightly further downstream in the combustor. The annular jet emerging from the burner exit has a wide divergence angle in case of counter-rotating flow than the co-flow. We observe that the counter-rotating flow increases the magnitudes of axial, radial and tangential velocity with increased turbulence in the shear layers. From the reacting flow-fields, we observe that steam dilution decreases the flame temperature from $\sim 3.85\mathrm{T_{in}}$ to $\sim 3.2\mathrm{T_{in}}$ inside the combustor and also shifts the flame slightly in the downstream direction for both the swirlers. We observe the existence of an M-shaped flame, stabilized in the outer shear layer, anchored to the center body of the inner swirler for both the configurations. The counter-rotating case has a short and wide flame. In terms of NOx and CO emissions, significant differences between co-flow and counter-flow are not observed (a 9% increase in NOx emission is observed in case of counter-flow); however, steam dilution ($\Omega = 0.2$) reduces the NOx emissions by 57% for both the swirlers. The flow-fields, temperature distribution and emissions from the dual swirl burner compare well with the literature. Our results indicate that counter-rotating configuration offers enhanced mixing between cold reactants and hot products, as well as enhanced mixing upstream of the flame (in case the configuration is employed for non-premixed or technically/partially-premixed combustion).

2. We then experimentally investigate the effects of acoustic excitation on the swirling flow field from the counter-rotating dual swirl burner using Schlieren image velocimetry (SIV). Subsequently, we perform Proper Orthogonal Decomposition (POD) and Spectral Proper Orthogonal Decomposition (SPOD) analyses using the SIV snapshots of instantaneous

axial velocity field to identify dominant coherent structures and their interactions with acoustic excitations. Analysis of the velocity fields reveals that the central recirculation zone moves upstream within the burner passages, suggesting a potential risk of flashback. Moreover, the external forcing of the natural flow induces a reduction in both velocity and vorticity magnitudes, causing fluctuations in the energy levels of turbulent eddies. The POD analysis confirms the presence of the PVC (Precessing Vortex Core) in the swirl burner flow field, which was observed as a marginally stable mode excited by turbulent fluctuations. The spatial modes of the natural flow revealed the occurrence of single and double helical PVC at $St = 0.53$. Acoustic actuation at $St = 0.46$ (frequency lower than the PVC frequency) effectively suppresses single helical instability. Acoustic actuation at $St = 2$ (higher frequency unrelated to PVC harmonics) acoustic actuation stabilizes the single helical PVC while altering the modal contribution of double helical instability on the energy spectrum. Broadband forcing, however, is observed to excite both single and double helical instabilities.

In summary, we recommend the dual swirl burner with a counter-rotating configuration as a promising candidate for next-generation fuel-flexible gas turbine combustors. We demonstrate the implementation of Schlieren image velocimetry (SIV) for analyzing turbulent swirling flow. SIV analysis successfully characterizes the typical flow features and coherent structures qualitatively. Additionally, we find that inherent noise in the combustor can lead to the excitation or stabilization of the PVC, thereby increasing the probability of thermoacoustic instability. Future work will involve identifying interaction mechanisms leading to the observed suppression and excitation of helical instabilities by acoustic oscillations.

References

[1] Timothy C. Lieuwen and Vigor Yang. *Combustion Instabilities In Gas Turbine Engines*. American Institute of Aeronautics and Astronautics, 1 2006.

[2] Vikrant Gupta, Aditya Saurabh, Christian Oliver Paschereit, and Lipika Kabiraj. Numerical results on noise-induced dynamics in the subthreshold regime for thermoacoustic systems. *Journal of Sound and Vibration*, 390:55–66, 3 2017.

[3] Vivekanandan Jegadeesan and R. I. Sujith. Experimental investigation of noise induced triggering in thermoacoustic systems. *Proceedings of the Combustion Institute*, 34:3175–3183, 1 2013.

[4] Rajesh Rajaram and Tim Lieuwen. Acoustic radiation from turbulent premixed flames. *Journal of Fluid Mechanics*, 637:357–385, 10 2009.

[5] Holger Nawroth, Christian O. Paschereit, Feichi Zhang, Peter Habisreuther, and Henning Bockhorn. Flow investigation and acoustic measurements of an unconfined turbulent premixed jet flame. In *43rd Fluid Dynamics Conference*. American Institute of Aeronautics and Astronautics, 6 2013.

[6] Lipika Kabiraj, Richard Steinert, Aditya Saurabh, and Christian Oliver Paschereit. Coherence resonance in a thermoacoustic system. *Physical Review E*, 92:42909, 10 2015.

[7] Jonas Pablo Moeck, Michael Oevermann, Rupert Klein, Christian Oliver Paschereit, and Heiko Schmidt. A two-way coupling for modeling thermoacoustic instabilities in a flat flame rijke tube. *Proceedings of the Combustion Institute*, 32(1):1199–1207, 2009.

[8] Sebastian Göke. *Ultra-Wet Combustion: An Experimental and Numerical Study*. PhD thesis, Berlin, Technische Universtität Berlin, Diss., 2012, 2012.

[9] L. Rayleigh. The explanation of certain acoustical phenomena. *Roy. Inst. Proc.*, 8:536–542, 1878.

[10] Abbott Allen Putnam. *Combustion-driven oscillations in industry*. Elsevier Publishing Company, 1971.

[11] S. Candel, D. Durox, S. Ducruix, A.-L. Birbaud, N. Noiray, and T. Schuller. Flame dynamics and combustion noise: Progress and challenges. *International Journal of Aeroacoustics*, 8(1):1–56, January 2009.

[12] Shreekrishna, Vishal Acharya, and Tim Lieuwen. Flame response to equivalence ratio fluctuations — relationship between chemiluminescence and heat release. *International Journal of Spray and Combustion Dynamics*, 5(4):329–358, December 2013.

[13] Sébastien Candel, Daniel Durox, Thierry Schuller, Jean-François Bourgouin, and Jonas P. Moeck. Dynamics of swirling flames. *Annual Review of Fluid Mechanics*, 46(1):147–173, January 2014.

[14] Satyanarayanan R. Chakravarthy, Ramgopal Sampath, and Vikram Ramanan. Dynamics and diagnostics of flame-acoustic interactions. *Combustion Science and Technology*, 189(3):395–437, November 2016.

[15] T Lieuwen, H Torres, C Johnson, and BT Zinn. A mechanism of combustion instability in lean premixed gas turbine combustors. *Journal of Engineering for Gas Turbines and Power*, 123(1):182–189, 2001.

[16] Sébastien Candel. Combustion dynamics and control: Progress and challenges. *Proceedings of the Combustion Institute*, 29:1–28, 1 2002.

[17] O Lucca-Negro and T O'doherty. Vortex breakdown: a review. *Progress in energy and combustion science*, 27(4):431–481, 2001.

[18] Piero Iudiciani. *Swirl stabilized premixed flame analysis using LES and POD*. Lund University, 2012.

[19] Thoralf G Reichel, Steffen Terhaar, and Oliver Paschereit. Increasing flashback resistance in lean premixed swirl-stabilized hydrogen combustion by axial air injection. *Journal of Engineering for Gas Turbines and Power*, 137(7):071503, 2015.

[20] Christian Oliver Paschereit, Ephraim Gutmark, and Wolfgang Weisenstein. Coherent structures in swirling flows and their role in acoustic combustion control. *Physics of Fluids*, 11(9):2667–2678, 1999.

[21] PM Anacleto, EC Fernandes, MV Heitor, and SI Shtork. Swirl flow structure and flame characteristics in a model lean premixed combustor. *Combustion Science and Technology*, 175(8):1369–1388, 2003.

[22] Agustin Valera-Medina, Nicholas Syred, and A Griffiths. Visualisation of isothermal large coherent structures in a swirl burner. *Combustion and Flame*, 156(9):1723–1734, 2009.

[23] Xiangzhou Feng, Jianqin Suo, Qiandong Li, and Longxi Zheng. Modal decomposition study of the non-reactive flow field in a dual-swirl combustor. *Energies*, 16(17):6182, 2023.

[24] A. P. Dowling. A kinematic model of a ducted flame. *Journal of Fluid Mechanics*, 394:51–72, September 1999.

[25] N. Noiray, D. Durox, T. Schuller, and S. Candel. A unified framework for nonlinear combustion instability analysis based on the flame describing function. *Journal of Fluid Mechanics*, 615:139, November 2008.

[26] F. E. C. Culick and V. Yang. Instability phenomenology and case studies: Overview of combustion instabilities in liquid-propellant rocket engines. In W. E. Anderson and

V. Yang, editors, *Liquid Rocket Engine Combustion Instability*, pages 3–37. American Institute of Aeronautics and Astronautics, January 1995.

[27] B. T. Zinn and T. C. Lieuwen. Combustion instabilities: Basic concepts. In T. C. Lieuwen and V. Yang, editors, *Combustion Instabilities In Gas Turbine Engines*, pages 3–26. American Institute of Aeronautics and Astronautics, January 2006.

[28] V. S. Burnley and F. E. C. Culick. Influence of random excitations on acoustic instabilities in combustion chambers. *AIAA Journal*, 38(8):1403–1410, August 2000.

[29] C.L. Morfey. Amplification of aerodynamic noise by convected flow inhomogeneities. *Journal of Sound and Vibration*, 31:391–397, 12 1973.

[30] F. E. C. Culick, L. Paparizos, J. Sterling, and V. Burnley. Combustion noise and combustion instabilities in propulsion systems. pages 1–18. AGARD conference proceedings. No.512. Advisory Group for Aerospace Research and Development, North Atlantic Treaty Organization, 1992.

[31] Warren C. Strahle. Combustion noise. *Progress in Energy and Combustion Science*, 4:157–176, 1 1978.

[32] T. Sattelmayer. Influence of the combustor aerodynamics on combustion instabilities from equivalence ratio fluctuations. *Journal of Engineering for Gas Turbines and Power*, 125:11–19, 1 2003.

[33] Jacqueline O'Connor. Understanding the role of flow dynamics in thermoacoustic combustion instability. *Proceedings of the Combustion Institute*, 39:4583–4610, 2023.

[34] S.J. Shanbhogue, Y.S. Sanusi, S. Taamallah, M.A. Habib, E.M.A. Mokheimer, and A.F. Ghoniem. Flame macrostructures, combustion instability and extinction strain scaling in swirl-stabilized premixed ch4/h2 combustion. *Combustion and Flame*, 163:494–507, 1 2016.

[35] Wyatt Culler, Xiaoling Chen, Janith Samarasinghe, Stephen Peluso, Domenic Santavicca, and Jacqueline O'Connor. The effect of variable fuel staging transients on self-excited instabilities in a multiple-nozzle combustor. *Combustion and Flame*, 194:472–484, 8 2018.

[36] Claude N. L. Seywert. *Combustion instabilities : issues in modeling and control.* PhD thesis, 2001.

[37] J. D. Sterling and E. E. Zukoski. Nonlinear dynamics of laboratory combustor pressure oscillations. *Combustion Science and Technology*, 77:225–238, 6 1991.

[38] Lipika Kabiraj, Aditya Saurabh, Nader Karimi, Anna Sailor, Epaminondas Mastorakos, Ann P. Dowling, and Christian O. Paschereit. Chaos in an imperfectly premixed model combustor. *Chaos: An Interdisciplinary Journal of Nonlinear Science*, 25, 2 2015.

[39] N. Noiray and B. Schuermans. On the dynamic nature of azimuthal thermoacoustic modes in annular gas turbine combustion chambers. *Proceedings of the Royal Society A: Mathematical, Physical and Engineering Sciences*, 469(2151):20120535–20120535, January 2013.

[40] Roberto Benzi, Alfonso Sutera, and Angelo Vulpiani. The mechanism of stochastic resonance. *Journal of Physics A: mathematical and general*, 14(11):L453, 1981.

[41] Roberto Benzi, Giorgio Parisi, Alfonso Sutera, and Angelo Vulpiani. Stochastic resonance in climatic change. *Tellus*, 34(1):10–16, 1982.

[42] John K Douglass, Lon Wilkens, Eleni Pantazelou, and Frank Moss. Noise enhancement of information transfer in crayfish mechanoreceptors by stochastic resonance. *Nature*, 365(6444):337, 1993.

[43] Thomas Wellens, Vyacheslav Shatokhin, and Andreas Buchleitner. Stochastic resonance. *Reports on progress in physics*, 67(1):45, 2003.

[44] Arkady S Pikovsky and Jürgen Kurths. Coherence resonance in a noise-driven excitable system. *Physical Review Letters*, 78:775–778, 2 1997.

[45] Alexander Neiman, Peter I Saparin, and Lewi Stone. Coherence resonance at noisy precursors of bifurcations in nonlinear dynamical systems. *Physical Review E*, 56:270–273, 7 1997.

[46] István. Z Kiss, John L Hudson, Gerardo J Escalera Santos, and P Parmananda. Experiments on coherence resonance: noisy precursors to hopf bifurcations. *Physical Review E*, 67:35201, 3 2003.

[47] O V Ushakov, H.-J. Wünsche, F Henneberger, I A Khovanov, L Schimansky-Geier, and M A Zaks. Coherence resonance near a hopf bifurcation. *Physical Review Letters*, 95:123903, 9 2005.

[48] A Zakharova, T Vadivasova, V Anishchenko, A Koseska, and J Kurths. Stochastic bifurcations and coherencelike resonance in a self-sustained bistable noisy oscillator. *Physical Review E*, 81:11106, 1 2010.

[49] Aditya Saurabh, Lipika Kabiraj, Richard Steinert, and Christian Oliver Paschereit. Noise-induced dynamics in the subthreshold region in thermoacoustic systems. *Journal of Engineering for Gas Turbines and Power*, 139(3):031508, October 2016.

[50] Victor Scott Burnley. *Nonlinear combustion instabilities and stochastic sources*. PhD thesis, 1 1996.

[51] F. E. C. Culick. Non-linear growth and limiting amplitude of acoustic oscillations in combustion chambers. *Combustion Science and Technology*, 3(1):1–16, April 1971.

[52] Ben T. Zinn and Eugene A. Powell. Nonlinear combustion instability in liquid-propellant rocket engines. *Symposium (International) on Combustion*, 13(1):491–503, January 1971.

[53] V. S. Burnely and F. E. Culick. The influence of combustion noise on acoustic instabilities, 6 1997.

[54] Crispin W Gardiner et al. *Handbook of stochastic methods*, volume 3. springer Berlin, 1985.

[55] Giacomo Bonciolini, Edouard Boujo, and Nicolas Noiray. Effects of turbulence-induced colored noise on thermoacoustic instabilities in combustion chambers. In *International Symposium: Thermoacoustic Instabilities in Gas Turbines and Rocket Engines*, pages 1–20. ETH Zürich, 2016.

[56] Rouslan L Stratonovich. *Topics in the theory of random noise*, volume 2. CRC Press, 1967.

[57] P Clavin, J. S. Kim, and F. A. Williams. Turbulence-induced noise effects on high-frequency combustion instabilities. *Combustion Science and Technology*, 96:61–84, 1 1994.

[58] Tim Lieuwen and Andrzej Banaszuk. Background noise effects on combustor stability. *Journal of Propulsion and Power*, 21:25–31, 1 2005.

[59] Nicolas Noiray and Bruno Schuermans. Deterministic quantities characterizing noise driven hopf bifurcations in gas turbine combustors. *International Journal of Non-Linear Mechanics*, 50:152–163, 4 2013.

[60] N. Noiray and A. Denisov. A method to identify thermoacoustic growth rates in combustion chambers from dynamic pressure time series. *Proceedings of the Combustion Institute*, 36:3843–3850, 1 2017.

[61] Giacomo Bonciolini, Edouard Boujo, and Nicolas Noiray. Output-only parameter identification of a colored-noise-driven van-der-pol oscillator: Thermoacoustic instabilities as an example. *Physical Review E*, 95:62217, 6 2017.

[62] E. Boujo and N. Noiray. Robust identification of harmonic oscillator parameters using the adjoint fokker–planck equation. *Proceedings of the Royal Society A: Mathematical, Physical and Engineering Sciences*, 473:20160894, 4 2017.

[63] Xinyan Li, Dan Zhao, and Baolu Shi. Coherence resonance and stochastic bifurcation behaviors of simplified standing-wave thermoacoustic systems. *The Journal of the Acoustical Society of America*, 145(2):692–702, 2019.

[64] Lipika Kabiraj and R. I. Sujith. Nonlinear self-excited thermoacoustic oscillations: intermittency and flame blowout. *Journal of Fluid Mechanics*, 713:376–397, 12 2012.

[65] Ali H. Nayfeh and Balakumar Balachandran. *Applied Nonlinear Dynamics*, chapter 1, pages 1–34. Wiley-VCH Verlag GmbH, 1995.

[66] Luigi Crocco and Sig-I Cheng. Theory of combustion instability in liquid propellant rocket motors. Technical report, Princton Univ NJ, 1956.

[67] Lipika Kabiraj and R. I. Sujith. Investigation of subcritical instability in ducted premixed flames. pages 969–977. ASMEDC, 1 2011.

[68] Ann P. Dowling and Yasser Mahmoudi. Combustion noise. *Proceedings of the Combustion Institute*, 35(1):65–100, 2015.

[69] C. K. W. Tam, F. Bake, L. S. Hultgren, and T. Poinsot. Combustion noise: modeling and prediction. *CEAS Aeronautical Journal*, 10(1):101–122, March 2019.

[70] Isidor Elias. Acoustical resonances produced by combustion of a fuel-air mixture in a rectangular duct. *The Journal of the Acoustical Society of America*, 31(3):296–304, March 1959.

[71] Konstantin I. Matveev and F. E. C. Culick. A model for combustion instability involving vortex shedding. *Combustion Science and Technology*, 175:1059–1083, 6 2003.

[72] Iain C Waugh and Matthew P Juniper. Triggering in a thermoacoustic system with stochastic noise. *International journal of spray and combustion dynamics*, 3(3):225–241, 2011.

[73] Iain C Waugh and Matthew P Juniper. Triggering in a thermoacoustic system with stochastic noise. *International Journal of Spray and Combustion Dynamics*, 3:225–241, 9 2011.

[74] Nitin Babu George, Vishnu Unni, Manikandan Raghunathan, and Raman Sujith. Effect of varying turbulence intensity on thermoacoustic instability in a partially pre-mixed combustor. In *ICSV 23*, 2016.

[75] TC Lieuwen. Phase drift characteristics of self-excited, combustion-driven oscillations. *Journal of Sound and Vibration*, 242(5):893–905, 2001.

[76] E.A. Gopalakrishnan and R.I. Sujith. Effect of external noise on the hysteresis characteristics of a thermoacoustic system. *Journal of Fluid Mechanics*, 776:334–353, 8 2015.

[77] R Berthet, A Petrossian, S Residori, B Roman, and S Fauve. Effect of multiplicative noise on parametric instabilities. *Physica D: Nonlinear Phenomena*, 174(1-4):84–99, 2003.

[78] E A Gopalakrishnan, J Tony, E Sreelekha, and R I Sujith. Stochastic bifurcations in a prototypical thermoacoustic system. *Physical Review E*, 94:22203, 8 2016.

[79] N. Noiray and B. Schuermans. On the dynamic nature of azimuthal thermoacoustic modes in annular gas turbine combustion chambers. *Proceedings of the Royal Society A: Mathematical, Physical and Engineering Sciences*, 469(2151):20120535–20120535, January 2013.

[80] Vasilis Dakos, Stephen R. Carpenter, William A. Brock, Aaron M. Ellison, Vishwesha Guttal, Anthony R. Ives, Sonia Kéfi, Valerie Livina, David A. Seekell, Egbert H. van Nes, and Marten Scheffer. Methods for detecting early warnings of critical transitions in time series illustrated using simulated ecological data. *PLoS ONE*, 7:e41010, 7 2012.

[81] Fahimeh Nazarimehr, Sajad Jafari, Matjaž Perc, and Julien C. Sprott. Critical slowing down indicators. *Europhysics Letters*, 132:18001, 10 2020.

[82] Anthony R. Ives and Vasilis Dakos. Detecting dynamical changes in nonlinear time series using locally linear state-space models. *Ecosphere*, 3:art58, 6 2012.

[83] S. R. Carpenter, J. J. Cole, M. L. Pace, R. Batt, W. A. Brock, T. Cline, J. Coloso, J. R. Hodgson, J. F. Kitchell, D. A. Seekell, L. Smith, and B. Weidel. Early warnings of regime shifts: a whole-ecosystem experiment. *Science*, 332:1079–1082, 5 2011.

[84] Valerie N Livina, F Kwasniok, and Timothy M Lenton. Potential analysis reveals changing number of climate states during the last 60 kyr. *Climate of the Past*, 6(1):77–82, 2010.

[85] S. R. Carpenter and W. A. Brock. Rising variance: a leading indicator of ecological transition. *Ecology Letters*, 9:311–318, 3 2006.

[86] Vasilis Dakos, Egbert H. van Nes, Paolo D'Odorico, and Marten Scheffer. Robustness of variance and autocorrelation as indicators of critical slowing down. *Ecology*, 93:264–271, 2 2012.

[87] E. A. Gopalakrishnan, Yogita Sharma, Tony John, Partha Sharathi Dutta, and R. I. Sujith. Early warning signals for critical transitions in a thermoacoustic system. *Scientific Reports*, 6:35310, 10 2016.

[88] Qiang An, Adam M. Steinberg, Sandeep Jella, Gilles Bourque, and Marc Füri. Early warning signs of imminent thermoacoustic oscillations through critical slowing down. *Journal of Engineering for Gas Turbines and Power*, 141:054501, 5 2019.

[89] Induja Pavithran and R. I. Sujith. Effect of rate of change of parameter on early warning signals for critical transitions. *Chaos: An Interdisciplinary Journal of Nonlinear Science*, 31:013116, 1 2021.

[90] Kento Baba, Sena Kishiya, Hiroshi Gotoda, Takeshi Shoji, and Seiji Yoshida. Early detection of thermoacoustic instability in a staged single-sector combustor for aircraft engines using symbolic dynamics-based approach. *Chaos: An Interdisciplinary Journal of Nonlinear Science*, 33, 7 2023.

[91] Reinette Biggs, Stephen R. Carpenter, and William A. Brock. Turning back from the brink: Detecting an impending regime shift in time to avert it. *Proceedings of the National Academy of Sciences*, 106:826–831, 1 2009.

[92] Vishwesha Guttal and Ciriyam Jayaprakash. Changing skewness: an early warning signal of regime shifts in ecosystems. *Ecology Letters*, 11:450–460, 5 2008.

[93] David A. Seekell, Stephen R. Carpenter, and Michael L. Pace. Conditional heteroscedasticity as a leading indicator of ecological regime shifts. *The American Naturalist*, 178:442–451, 10 2011.

[94] Yuanhang Zhu, Vikrant Gupta, and Larry K. B. Li. Coherence resonance in low-density jets. *Journal of Fluid Mechanics*, 881:R1, 12 2019.

[95] Aditya Saurabh, Lipika Kabiraj, Richard Steinert, and Christian Oliver Paschereit. Noise-induced dynamics in the subthreshold region in thermoacoustic systems. *Journal of Engineering for Gas Turbines and Power*, 139, 3 2017.

[96] Vineeth Nair and R.I. Sujith. Multifractality in combustion noise: predicting an impending combustion instability. *Journal of Fluid Mechanics*, 747:635–655, 5 2014.

[97] Aditya Saurabh, Hassan Imran, Holger Nawroth, Christian Oliver Paschereit, and Lipika Kabiraj. Fractal characteristics of combustion noise. *Journal of Engineering for Gas Turbines and Power*, 140, 12 2018.

[98] Günther Waxenegger-Wilfing, Ushnish Sengupta, Jan Martin, Wolfgang Armbruster, Justin Hardi, Matthew Juniper, and Michael Oschwald. Early detection of thermoacoustic instabilities in a cryogenic rocket thrust chamber using combustion noise features and machine learning. *Chaos: An Interdisciplinary Journal of Nonlinear Science*, 31, 6 2021.

[99] Yanni Fu, Yuming Zhang, Peng Zang, Yongfeng Sui, Yao Zheng, and Yifan Xia. An early detection indicator of combustion instability for an industrial gas turbine combustor. *Physics of Fluids*, 36, 1 2024.

[100] Vineeth Nair and R. I. Sujith. Identifying homoclinic orbits in the dynamics of intermittent signals through recurrence quantification. *Chaos: An Interdisciplinary Journal of Nonlinear Science*, 23:033136, 9 2013.

[101] Vineeth Nair, Gireeshkumaran Thampi, and R. I. Sujith. Intermittency route to thermoacoustic instability in turbulent combustors. *Journal of Fluid Mechanics*, 756:470–487, 10 2014.

[102] Eustaquio A. Ruiz, Vishnu R. Unni, Induja Pavithran, R. I. Sujith, and Abhishek Saha. Convolutional neural networks to predict the onset of oscillatory instabilities in turbulent systems. *Chaos: An Interdisciplinary Journal of Nonlinear Science*, 31, 9 2021.

[103] Tim Lieuwen. Online combustor stability margin assessment using dynamic pressure data. *Journal of Engineering for Gas Turbines and Power*, 127:478–482, 7 2005.

[104] Yajie Li, Zhiqiang Wu, Guoqi Zhang, Feng Wang, and Yuancen Wang. Stochastic p-bifurcation in a bistable van der pol oscillator with fractional time-delay feedback under gaussian white noise excitation. *Advances in Difference Equations*, 2019:448, 12 2019.

[105] Xinyan Li, Yuanhao Wang, Ningfei Wang, and Dan Zhao. Stochastic properties of thermoacoustic oscillations in an annular gas turbine combustion chamber driven by colored noise. *Journal of Sound and Vibration*, 480:115423, 8 2020.

[106] O A Rosso, H A Larrondo, M T Martin, A Plastino, and M A Fuentes. Distinguishing noise from chaos. *Physical Review Letters*, 99:154102, 10 2007.

[107] Takayoshi Hachijo, Shinga Masuda, Takuya Kurosaka, and Hiroshi Gotoda. Early detection of thermoacoustic combustion oscillations using a methodology combining statistical complexity and machine learning. *Chaos: An Interdisciplinary Journal of Nonlinear Science*, 29, 10 2019.

[108] Minwoo Lee. Early warning detection of thermoacoustic instability using three-dimensional complexity-entropy causality space. *Experimental Thermal and Fluid Science*, 130:110517, 1 2022.

[109] Hiroshi Gotoda, Masahito Amano, Takaya Miyano, Takuya Ikawa, Koshiro Maki, and Shigeru Tachibana. Characterization of complexities in combustion instability in a lean premixed gas-turbine model combustor. *Chaos: An Interdisciplinary Journal of Nonlinear Science*, 22, 12 2012.

[110] Hiroshi Gotoda, Hikaru Kinugawa, Ryosuke Tsujimoto, Shohei Domen, and Yuta Okuno. Characterization of combustion dynamics, detection, and prevention of an unstable combustion state based on a complex-network theory. *Physical Review Applied*, 7:44027, 4 2017.

[111] Minwoo Lee, Yuanhang Zhu, Larry K. B. Li, and Vikrant Gupta. System identification of a low-density jet via its noise-induced dynamics. *Journal of Fluid Mechanics*, 862:200–215, 3 2019.

[112] Minwoo Lee, Yu Guan, Vikrant Gupta, and Larry K B Li. Input-output system identification of a thermoacoustic oscillator near a hopf bifurcation using only fixed-point data. *Physical Review E*, 101:13102, 1 2020.

[113] Minwoo Lee, Kyu Tae Kim, Vikrant Gupta, and Larry K.B. Li. System identification and early warning detection of thermoacoustic oscillations in a turbulent combustor using its noise-induced dynamics. *Proceedings of the Combustion Institute*, 38:6025–6033, 1 2021.

[114] Christoph Bandt and Bernd Pompe. Permutation entropy: a natural complexity measure for time series. *Physical Review Letters*, 88:174102, 4 2002.

[115] Shogo Murayama, Hikaru Kinugawa, Isao T Tokuda, and Hiroshi Gotoda. Characterization and detection of thermoacoustic combustion oscillations based on statistical complexity and complex-network theory. *Physical Review E*, 97:22223, 2 2018.

[116] Matthew P. Juniper. Triggering in the horizontal rijke tube: non-normality, transient growth and bypass transition. *Journal of Fluid Mechanics*, 667:272–308, 2011.

[117] Nicolas Noiray. Linear growth rate estimation from dynamics and statistics of acoustic signal envelope in turbulent combustors. *Journal of Engineering for Gas Turbines and Power*, 139, 4 2017.

[118] Giacomo Bonciolini, Dominik Ebi, Edouard Boujo, and Nicolas Noiray. Experiments and modelling of rate-dependent transition delay in a stochastic subcritical bifurcation. *Royal Society Open Science*, 5:172078, 3 2018.

[119] Juan Ma, Tiejun Xiao, Zhonghuai Hou, and Houwen Xin. Coherence resonance induced by colored noise near hopf bifurcation. *Chaos: An Interdisciplinary Journal of Nonlinear Science*, 18:043116, 12 2008.

[120] Valentina Beato, Irene Sendiña-Nadal, Ingeborg Gerdes, and Harald Engel. Coherence resonance in a chemical excitable system driven by coloured noise. *Philosophical Transactions of the Royal Society A: Mathematical, Physical and Engineering Sciences*, 366:381–395, 2 2008.

[121] Dongxi Li, Bing Hu, Jia Wang, Yingchuan Jing, and Fangmei Hou. Coherence resonance in the two-dimensional neural map driven by non-gaussian colored noise. *International Journal of Modern Physics B*, 30:1650012, 2 2016.

[122] S. Brugioni, D.-U. Hwang, R. Meucci, and S. Boccaletti. Coherence resonance in excitable electronic circuits in the presence of colored noise. *Physical Review E*, 71:062101, 6 2005.

[123] XiaoYu Zhang, Yong Xu, Qi Liu, and Jürgen Kurths. Rate-dependent tipping-delay phenomenon in a thermoacoustic system with colored noise. *Science China Technological Sciences*, 63:2315–2327, 11 2020.

[124] Xiaoyu Zhang, Yong Xu, Qi Liu, Jürgen Kurths, and Celso Grebogi. Rate-dependent bifurcation dodging in a thermoacoustic system driven by colored noise. *Nonlinear Dynamics*, 104:2733–2743, 5 2021.

[125] Xiaoyu Zhang, Yong Xu, Qi Liu, Jürgen Kurths, and Celso Grebogi. Rate-dependent tipping and early warning in a thermoacoustic system under extreme operating environment. *Chaos: An Interdisciplinary Journal of Nonlinear Science*, 31, 11 2021.

[126] Xinyan Li, Dan Zhao, and Xuan Li. Effects of background noises on nonlinear dynamics of a modelled thermoacoustic combustor. *Journal of the Acoustical Society of America*, 143:60–70, 1 2018.

[127] Xinyan Li, Bo Xu, Xiaosi Li, Kai Pang, Xuan Li, and Hao Zhang. Effects of multiplicative and additive colored noises on the stability of a simplified thermoacoustic combustor. *Combustion and Flame*, 249:112413, 3 2023.

[128] J Panda and DK McLaughlin. Experiments on the instabilities of a swirling jet. *Physics of Fluids*, 6(1):263–276, 1994.

[129] A Lacarelle, T Faustmann, D Greenblatt, CO Paschereit, O Lehmann, DM Luchtenburg, and BR Noack. Spatiotemporal characterization of a conical swirler flow field under strong forcing. 2009.

[130] Kilian Oberleithner, Moritz Sieber, Christian Navid Nayeri, Christian Oliver Paschereit, Christoph Petz, H-C Hege, Bernd R Noack, and I Wygnanski. Three-dimensional coherent structures in a swirling jet undergoing vortex breakdown: stability analysis and empirical mode construction. *Journal of fluid mechanics*, 679:383–414, 2011.

[131] Moritz Sieber, Christian Oliver Paschereit, and Kilian Oberleithner. Advanced identification of coherent structures in swirl-stabilized combustors. *Journal of Engineering for Gas Turbines and Power*, 139(2):021503, 2017.

[132] Piero Iudiciani and Christophe Duwig. Large eddy simulation of the sensitivity of vortex breakdown and flame stabilisation to axial forcing. *Flow, turbulence and combustion*, 86:639–666, 2011.

[133] Sammy Khalil, Kerry Hourigan, and Mark C Thompson. Response of unconfined vortex breakdown to axial pulsing. *Physics of Fluids*, 18(3), 2006.

[134] Jonas P Moeck, Jean-François Bourgouin, Daniel Durox, Thierry Schuller, and Sébastien Candel. Nonlinear interaction between a precessing vortex core and acoustic oscillations in a turbulent swirling flame. *Combustion and Flame*, 159(8):2650–2668, 2012.

[135] Sergey V Alekseenko, Vladimir M Dulin, Yuriy S Kozorezov, and Dmitriy M Markovich. Effect of axisymmetric forcing on the structure of a swirling turbulent jet. *International Journal of Heat and Fluid Flow*, 29(6):1699–1715, 2008.

[136] Shanwu Wang and Vigor Yang. Unsteady flow evolution in swirl injectors with radial entry. ii. external excitations. *Physics of Fluids*, 17(4), 2005.

[137] K. T. Feldman. Review of the literature on rijke thermoacoustic phenomena. *Journal of Sound and Vibration*, 7:83–89, 1 1968.

[138] Maria A. Heckl. Non-linear acoustic effects in the rijke tube. *Acta Acustica*, 72:63–71, 1990.

[139] R.L. Raun, M.W. Beckstead, J.C. Finlinson, and K.P. Brooks. A review of rijke tubes, rijke burners and related devices. *Progress in Energy and Combustion Science*, 19:313–364, 1 1993.

[140] F. Nicoud and K. Wieczorek. About the zero mach number assumption in the calculation of thermoacoustic instabilities. *International Journal of Spray and Combustion Dynamics*, 1:67–111, 3 2009.

[141] Koushik Balasubramanian and R. I. Sujith. Thermoacoustic instability in a rijke tube: non-normality and nonlinearity. *Physics of Fluids*, 20, 4 2008.

[142] Priya Subramanian, Sathesh Mariappan, R. I. Sujith, and Pankaj Wahi. Bifurcation analysis of thermoacoustic instability in a horizontal rijke tube. *International Journal of Spray and Combustion Dynamics*, 2:325–355, 12 2010.

[143] Vishnu R. Unni, E. A. Gopalakrishnan, K. S. Syamkumar, R. I. Sujith, Elena Surovyatkina, and Jürgen Kurths. Interplay between random fluctuations and rate dependent phenomena at slow passage to limit-cycle oscillations in a bistable thermoacoustic system. *Chaos: An Interdisciplinary Journal of Nonlinear Science*, 29, 3 2019.

[144] JR Mahan. A critical review of noise production models for turbulent, gas-fueled burners. Technical report, Mahan, J. R. (Virginia Polytechnic Inst. and State Univ. Blacksburg, 6 1984.

[145] Kurt Wiesenfeld. Noisy precursors of nonlinear instabilities. *Journal of Statistical Physics*, 38:1071–1097, 3 1985.

[146] Marten Scheffer, Jordi Bascompte, William A. Brock, Victor Brovkin, Stephen R. Carpenter, Vasilis Dakos, Hermann Held, Egbert H. van Nes, Max Rietkerk, and George Sugihara. Early-warning signals for critical transitions. *Nature*, 461:53–59, 9 2009.

[147] Espen A. F. Ihlen. Introduction to multifractal detrended fluctuation analysis in matlab. *Frontiers in Physiology*, 3, 2012.

[148] Bruce J West and Ary L Goldberger. Physiology in fractal dimensions. *American Scientist*, 75:354–365, 1987.

[149] Lipika Kabiraj, Aditya Saurabh, Pankaj Wahi, and R. I. Sujith. Route to chaos for combustion instability in ducted laminar premixed flames. *Chaos: An Interdisciplinary Journal of Nonlinear Science*, 22, 6 2012.

[150] B. Van der Pol. A theory of the amplitude of free and forced triode vibrations. *Radio Review*, 1:701–710, 1920.

[151] Roman Belousov, Florian Berger, and A. J. Hudspeth. Volterra-series approach to stochastic nonlinear dynamics: Linear response of the van der pol oscillator driven by white noise. *Physical Review E*, 102:032209, Sep 2020.

[152] Richard FitzHugh. Impulses and physiological states in theoretical models of nerve membrane. *Biophysical Journal*, 1:445–466, 7 1961.

[153] Balth. Van der Pol and J. Van der Mark. The heartbeat considered as a relaxation oscillation, and an electrical model of the heart. *The London, Edinburgh and Dublin philosophical magazine and journal of science*, 6:763–775, 11 1928.

[154] Julyan H. E. Cartwright, Victor M. Eguiluz, Emilio Hernandez-Garcia, and Oreste Piro. Dynamics of elastic excitable media. *International Journal of Bifurcation and Chaos*, 5 1999.

[155] Stéphane Barland, Oreste Piro, Massimo Giudici, Jorge R. Tredicce, and Salvador Balle. Experimental evidence of van der pol–fitzhugh–nagumo dynamics in semiconductor optical amplifiers. *Physical Review E*, 68:036209, 9 2003.

[156] F. S. Mousavinejad, M. FatehiNia, and A. Ebrahimi. P-bifurcation of stochastic van der pol model as a dynamical system in neuroscience. *Communications in Applied Mathematics and Computational Science*, 4:1293–1312, 12 2022.

[157] René Yamapi, André Chéagé Chamgoué, Giovanni Filatrella, and Paul Woafo. Coherence and stochastic resonance in a birhythmic van der pol system. *European Physical Journal B*, 90:153, 8 2017.

[158] Giacomo Bonciolini, Dominik Ebi, Edouard Boujo, and Nicolas Noiray. Experiments and modelling of rate-dependent transition delay in a stochastic subcritical bifurcation. *Royal Society Open Science*, 5:172078, 3 2018.

[159] Steven H. Strogatz. *Nonlinear dynamics and chaos.* CRC Press, 5 2018.

[160] Yong Xu, Rencai Gu, Huiqing Zhang, Wei Xu, and Jinqiao Duan. Stochastic bifurcations in a bistable duffing–van der pol oscillator with colored noise. *Physical Review E*, 83:056215, 5 2011.

[161] Neha Vishnoi, Vikrant Gupta, Aditya Saurabh, and Lipika Kabiraj. System parameter identification of a colored-noise-driven rijke tube simulator. *Journal of Engineering for Gas Turbines and Power*, 144, 9 2022.

[162] Neha Vishnoi, Vikrant Gupta, Aditya Saurabh, and Lipika Kabiraj. Effect of correlation time of combustion noise on early warning indicators of thermoacoustic instability. *Chaos: An Interdisciplinary Journal of Nonlinear Science*, 34, 3 2024.

[163] Peter J. Brockwell and Richard A. Davis. *Introduction to Time Series and Forecasting.* Springer International Publishing, 2016.

[164] George E. P. Box, Gwilym M. Jenkins, Gregory C. Reinsel, and Greta M. Ljung. *Time series analysis: forecasting and control.* Wiley, 5th edition, 6 2015.

[165] Jan W. Kantelhardt, Stephan A. Zschiegner, Eva Koscielny-Bunde, Shlomo Havlin, Armin Bunde, and H. Eugene Stanley. Multifractal detrended fluctuation analysis of nonstationary time series. *Physica A: Statistical Mechanics and its Applications*, 316:87–114, 12 2002.

[166] Yinhe Cao, Wen wen Tung, J. B. Gao, V. A. Protopopescu, and L. M. Hively. Detecting dynamical changes in time series using the permutation entropy. *Physical Review E*, 70:046217, 10 2004.

[167] Matthaus Staniek and Klaus Lehnertz. Parameter selection for permutation entropy measurements. *International Journal of Bifurcation and Chaos*, 17:3729–3733, 10 2007.

[168] M. Riedl, A. Müller, and N. Wessel. Practical considerations of permutation entropy. *European Physical Journal Special Topics*, 222:249–262, 6 2013.

[169] T Miyano, T Moriya, H Nagaike, N Ikeuchi, and T Matsumoto. Dynamical properties of acoustic emission by anomalous discharge in plasma processing system. *Journal of Physics D: Applied Physics*, 41(3):035209, 2008.

[170] Hiroshi Gotoda, Keisuke Michigami, Kota Ikeda, and Takaya Miyano. Chaotic oscillation in diffusion flame induced by radiative heat loss. *Combustion Theory and Modelling*, 14(4):479–493, 2010.

[171] Yao Li, Chunyan Hu, Youhao Shen, Bo Han, Jinhu Yang, and Gang Xu. A new methodology for early detection of thermoacoustic combustion oscillations based on permutation entropy. *Journal of Thermal Science*, 7 2023.

[172] P.W Lamberti, M.T Martin, A Plastino, and O.A Rosso. Intensive entropic non-triviality measure. *Physica A: Statistical Mechanics and its Applications*, 334:119–131, 3 2004.

[173] Vineeth Nair and RI Sujith. Precursors to self-sustained oscillations in aeroacoustic systems. *International Journal of Aeroacoustics*, 15(3):312–323, 2016.

[174] Vishnu R Unni and RI Sujith. Multifractal characteristics of combustor dynamics close to lean blowout. *Journal of Fluid Mechanics*, 784:30–50, 2015.

[175] D Durox, T Schuller, and S Gandel. Self-induced instability of a premixed jet flame impinging on a plate. *Proceedings of the Combustion Institute*, 29(1):69–75, 2002.

[176] Giulio Ghirardo, Matthew P Juniper, and Mirko R Bothien. The effect of the flame phase on thermoacoustic instabilities. *Combustion and Flame*, 187:165–184, 2018.

[177] Giacomo Bonciolini, Abel Faure-Beaulieu, Claire Bourquard, and Nicolas Noiray. Low order modelling of thermoacoustic instabilities and intermittency: flame response delay and nonlinearity. *Combustion and Flame*, 226:396–411, 2021.

[178] Vasilis Dakos, Stephen R Carpenter, Egbert H van Nes, and Marten Scheffer. Resilience indicators: prospects and limitations for early warnings of regime shifts. *Philosophical Transactions of the Royal Society B*, 370(1659):20130263, 2015.

[179] Marina Hirota, Milena Holmgren, Egbert H Van Nes, and Marten Scheffer. Global resilience of tropical forest and savanna to critical transitions. *Science*, 334(6053):232–235, 2011.

[180] Vishwesha Guttal, C. Jayaprakash, and Omar P. Tabbaa. Robustness of early warning signals of regime shifts in time-delayed ecological models. *Theoretical Ecology*, 6:271–283, 8 2013.

[181] Partha Sharathi Dutta, Yogita Sharma, and Karen C. Abbott. Robustness of early warning signals for catastrophic and non-catastrophic transitions. *Oikos*, 127:1251–1263, 9 2018.

[182] T. M. Bury, C. T. Bauch, and M. Anand. Detecting and distinguishing tipping points using spectral early warning signals. *Journal of the Royal Society Interface*, 17:20200482, 9 2020.

[183] Krishnendu Pal, Smita Deb, and Partha Sharathi Dutta. Tipping points in spatial ecosystems driven by short-range correlated noise. *Physical Review E*, 106:054412, 11 2022.

[184] Taranjot Kaur and Partha Sharathi Dutta. Effects of noise correlation and imperfect data sampling on indicators of critical slowing down. *Theoretical Ecology*, 15:129–142, 6 2022.

[185] Ville Laitinen, Vasilis Dakos, and Leo Lahti. Probabilistic early warning signals. *Ecology and Evolution*, 11:14101–14114, 10 2021.

[186] Neha Vishnoi, Vikrant Gupta, Aditya Saurabh, and Lipika Kabiraj. Effect of correlation time of combustion noise on early warning indicators of thermoacoustic instability. *Chaos: An Interdisciplinary Journal of Nonlinear Science*, 34, 3 2024.

[187] Tim C. Lieuwen. Experimental investigation of limit-cycle oscillations in an unstable gas turbine combustor. *Journal of Propulsion and Power*, 18:61–67, 1 2002.

[188] Jonas Moeck, Mirko Bothien, Sebastian Schimek, Arnaud Lacarelle, and Christian Paschereit. Subcritical thermoacoustic instabilities in a premixed combustor. American Institute of Aeronautics and Astronautics, 5 2008.

[189] Xiaoqin Luo and Shiqun Zhu. Stochastic resonance driven by two different kinds of colored noise in a bistable system. *Physical Review E*, 67:021104, 2 2003.

[190] Neha Vishnoi, Pankaj Wahi, Aditya Saurabh, and Lipika Kabiraj. On the effect of noise induced dynamics on linear growth rates of oscillations in an electroacoustic rijke tube simulator. In *Volume 3A: Combustion, Fuels, and Emissions*, page V03AT04A013. American Society of Mechanical Engineers, 6 2021.

[191] Ho CH Townend. A method of air flow cinematography capable of quantitative analysis. *Journal of the Aeronautical Sciences*, 3(10):343–352, 1936.

[192] Sayan Biswas and Li Qiao. A comprehensive statistical investigation of schlieren image velocimetry (siv) using high-velocity helium jet. *Experiments in Fluids*, 58:1–20, 2017.

[193] John E Pellessier, Heather E Dillon, and Wyatt Stoltzfus. Schlieren flow visualization and analysis of synthetic jets. *Fluids*, 6(11):413, 2021.

[194] Shan Fu and Yajue Wu. Detection of velocity distribution of a flow field using sequences of schlieren images. *Optical Engineering*, 40(8):1661–1666, 2001.

[195] Dimitri Papamoschou. Structure of the compressible turbulent shear layer. *AIAA journal*, 29(5):680–681, 1991.

[196] Dennis R Jonassen, Gary S Settles, and Michael D Tronosky. Schlieren "piv" for turbulent flows. *Optics and Lasers in Engineering*, 44(3-4):190–207, 2006.

[197] Michael J Hargather, Michael J Lawson, Gary S Settles, and Leonard M Weinstein. Seedless velocimetry measurements by schlieren image velocimetry. *AIAA journal*, 49(3):611–620, 2011.

[198] Yuta Ozawa, Takuma Ibuki, Taku Nonomura, Kento Suzuki, Atsushi Komuro, Akira Ando, and Keisuke Asai. Single-pixel resolution velocity/convection velocity field of a supersonic jet measured by particle/schlieren image velocimetry. *Experiments in Fluids*, 61:1–18, 2020.

[199] Xin Wen, Kaiwen Zhou, Peicong Liu, Haijun Zhu, Qian Wang, and Yingzheng Liu. Schlieren visualization of coflow fluidic thrust vectoring using sweeping jets. *AIAA Journal*, 60(1):435–444, 2022.

[200] Danilo Almeida Machado, Fernando de Souza Costa, José Carlos de Andrade, Gabriel Silva Dias, and Gustavo Alexandre Achilles Fischer. Schlieren image velocimetry of swirl sprays. *Flow, Turbulence and Combustion*, 110(2):489–513, 2023.

[201] Gary S Settles. *Schlieren and shadowgraph techniques: visualizing phenomena in transparent media*. Springer Science & Business Media, 2001.

[202] Kai-Erik Peiponen, Risto Myllylä, and Alexander V Priezzhev. *Optical measurement techniques: Innovations for industry and the life sciences*. Springer, 2009.

[203] Viktor Józsa, Milan Malỳ, Dániel Füzesi, Erika Rácz, Réka Anna Kardos, and Jan Jedelskỳ. Schlieren analysis of non-mild distributed combustion in a mixture temperature-controlled burner. *Energy*, 273:127230, 2023.

[204] MA Kegerise and GS Settles. Schlieren image-correlation velocimetry and its application to free-convection flows. In *International Symposium on Flow Visualization*, 2000.

[205] Mathew G Berry, AS Magstadt, and Mark N Glauser. Application of pod on time-resolved schlieren in supersonic multi-stream rectangular jets. *Physics of Fluids*, 29(2), 2017.

[206] Byron Andrew Pritchard Jr, Allen Michael Danis, Michael Jerome Foust, Mark David Durbin, and Hukam Chand Mongia. Multiple annular combustion chamber swirler having atomizing pilot, May 7 2002. US Patent 6,381,964.

[207] Guoqiang Li and Ephraim J Gutmark. Effect of exhaust nozzle geometry on combustor flow field and combustion characteristics. *Proceedings of the combustion institute*, 30(2):2893–2901, 2005.

[208] Guoqiang Li and Ephraim J Gutmark. Boundary conditions effects on nonreacting and reacting flows in a multiswirl combustor. *AIAA journal*, 44(3):444–456, 2006.

[209] Guoqiang Li and Ephraim J Gutmark. Effects of swirler configurations on flow structures and combustion characteristics. In *Turbo Expo: Power for Land, Sea, and Air*, volume 41669, pages 423–433, 2004.

[210] Saad Akhtar, Stefano Piffaretti, and Tariq Shamim. Numerical investigation of flame structure and blowout limit for lean premixed turbulent methane-air flames under high pressure conditions. *Applied Energy*, 228:21–32, 2018.

[211] Elizaveta Ivanova, Berthold Noll, and Manfred Aigner. Rans and les of turbulent mixing in confined swirling and non-swirling jets. In *6th AIAA Theoretical Fluid Mechanics Conference*, page 3934, 2011.

[212] HW Coleman, BK Hodge, and RP Taylor. A re-evaluation of schlichting's surface roughness experiment. *Journal of Fluids Engineering*, 1984.

[213] Vladimir Zimont, Wolfgang Polifke, Marco Bettelini, and Wolfgang Weisenstein. *An efficient computational model for premixed turbulent combustion at high Reynolds numbers based on a turbulent flame speed closure*, volume 78699. American Society of Mechanical Engineers, 1997.

[214] GP Smith, DM Golden, M Frenklach, NW Moriarty, B Eiteneer, M Goldenberg, CT Bowman, RK Hanson, S Song, WC Gardiner Jr, et al. Gri-mech 3.0, 2000. *URL http://www. me. berkeley. edu/gri_mech*, 2021.

[215] Gabriel J DeSalvo and John A Swanson. *ANSYS Engineering Analysis System: User's Manual*. Swanson Analysis Systems, 1979.

[216] User Manual. Ansys fluent 12.0. *Theory Guide*, 67, 2009.

[217] Stephen R Turns et al. *Introduction to combustion*, volume 287. McGraw-Hill Companies New York, NY, USA, 1996.

[218] Ludovic Durand. *Development, implementation and validation of LES models for inhomogeneously premixed turbulent combustion.* PhD thesis, Technische Universität München, 2008.

[219] R Mercier, TF Guiberti, A Chatelier, D Durox, O Gicquel, N Darabiha, Thierry Schuller, and Benoit Fiorina. Experimental and numerical investigation of the influence of thermal boundary conditions on premixed swirling flame stabilization. *Combustion and flame*, 171:42–58, 2016.

[220] Chih-Ming Ho and Lein-Saing Huang. Subharmonics and vortex merging in mixing layers. *Journal of Fluid Mechanics*, 119:443–473, 1982.

[221] Ying Huang and Vigor Yang. Effect of swirl on combustion dynamics in a lean-premixed swirl-stabilized combustor. *Proceedings of the combustion institute*, 30(2):1775–1782, 2005.

[222] Shanwu Wang, Vigor Yang, George Hsiao, Shih-Yang Hsieh, and Hukam C Mongia. Large-eddy simulations of gas-turbine swirl injector flow dynamics. *Journal of Fluid Mechanics*, 583:99–122, 2007.

[223] Christoph M Arndt, Michael Stöhr, Michael J Severin, Claudiu Dem, and Wolfgang Meier. Influence of air staging on the dynamics of a precessing vortex core in a dual swirl gas turbine model combustor. In *53rd AIAA/SAE/ASEE Joint Propulsion Conference*, page 4683, 2017.

[224] Amir Mardani, Benyamin Asadi, and Amir A Beige. Investigation of flame structure and precessing vortex core instability of a gas turbine model combustor with different swirler configurations. *Physics of Fluids*, 34(8):085129, 2022.

[225] Mao Li, Yiheng Tong, Marcus Thern, and Jens Klingmann. Influence of the steam addition on premixed methane air combustion at atmospheric pressure. *Energies*, 10(7):1070, 2017.

[226] Steffen Terhaar, Katharina Goeckeler, Sebastian Schimek, Sebastian Göke, and Christian Paschereit. Non-reacting and reacting flow in a swirl-stabilized burner for ultra-wet combustion. In *41st AIAA Fluid Dynamics Conference and Exhibit*, page 3584, 2011.

[227] Wolfgang Polifke. Fundamental and practical limitations of nox reduction in lean-premixed combustion. In *Euroconference 'Premixed Turbulent Combustion: Introduction to the State of the Art'*, page 1, 1995.

[228] RW Schefer. Hydrogen enrichment for improved lean flame stability. *International Journal of Hydrogen Energy*, 28(10):1131–1141, 2003.

[229] Jeong Park, Dong Jin Hwang, June Sung Park, Jeong Soo Kim, Sang In Keel, Han Chang Cho, Dong Soon Noh, and Tae Kwon Kim. Hydrogen utilization as a fuel: hydrogen-blending effects in flame structure and no emission behaviour of ch4–air flame. *International journal of energy research*, 31(5):472–485, 2007.

[230] Uri Shavit, Ryan J Lowe, and Jonah V Steinbuck. Intensity capping: a simple method to improve cross-correlation piv results. *Experiments in Fluids*, 42:225–240, 2007.

[231] Azriel Rosenfeld. *Digital picture processing*. Academic press, 1976.

[232] William Thielicke and René Sonntag. Particle image velocimetry for matlab: Accuracy and enhanced algorithms in pivlab. *Journal of Open Research Software*, 9(1), 2021.

[233] Philip Holmes. *Turbulence, coherent structures, dynamical systems and symmetry*. Cambridge university press, 2012.

[234] Zhi X Chen, Ivan Langella, Nedunchezhian Swaminathan, Michael Stöhr, Wolfgang Meier, and Hemanth Kolla. Large eddy simulation of a dual swirl gas turbine combustor:

Flame/flow structures and stabilisation under thermoacoustically stable and unstable conditions. *Combustion and Flame*, 203:279–300, 2019.

[235] S Terhaar, B Ćosić, CO Paschereit, and K Oberleithner. Suppression and excitation of the precessing vortex core by acoustic velocity fluctuations: An experimental and analytical study. *Combustion and Flame*, 172:234–251, 2016.

[236] Mustafa Percin, Maarten Vanierschot, and BW van Oudheusden. Analysis of the pressure fields in a swirling annular jet flow. *Experiments in fluids*, 58:1–13, 2017.

[237] Maarten Vanierschot, Mustafa Percin, and BW Van Oudheusden. Double helix vortex breakdown in a turbulent swirling annular jet flow. *Physical Review Fluids*, 3(3):034703, 2018.

[238] Maarten Vanierschot, Jens S Müller, Moritz Sieber, Mustafa Percin, Bas W Van Oudheusden, and Kilian Oberleithner. Single-and double-helix vortex breakdown as two dominant global modes in turbulent swirling jet flow. *Journal of Fluid Mechanics*, 883:A31, 2020.

[239] Guillaume Vignat, Daniel Durox, Antoine Renaud, Théa Lancien, Ronan Vicquelin, and Sébastien Candel. Investigation of transient pvc dynamics in a strongly swirled spray flame using high speed planar laser imaging of sno2 microparticles. *Combustion and Flame*, 225:305–319, 2021.

[240] Moritz Sieber, C Oliver Paschereit, and Kilian Oberleithner. Spectral proper orthogonal decomposition. *Journal of Fluid Mechanics*, 792:798–828, 2016.

[241] Dan Wu and Shiqun Zhu. Effects of cross-correlated noises on the transport of active brownian particles. *Physical Review E*, 90:012131, Jul 2014.

[242] Zhiqin Ma, Yuhui Luo, Chunhua Zeng, and Bo Zheng. Spatiotemporal diffusion as early warning signal for critical transitions in spatial tumor-immune system with stochasticity. *Physical Review Research*, 4:023039, Apr 2022.

[243] Luca Giuggioli and Zohar Neu. Fokker–planck representations of non-markov langevin equations: application to delayed systems. *Philosophical Transactions of the Royal Society A*, 377(2153):20180131, 2019.

Appendices

Appendix A: Effect of f^2 part of combustion noise on EWIs

While OU noise has a flat spectrum till the cutoff frequency, combustion noise features a power law increase (approximately following f^2) until the peak frequency. The f^2 increase at lower frequencies does not change the conclusions drawn on the basis of OU noise. To understand the effects of f^2 part of the combustion noise spectra on the results, we perform additional numerical simulations which are discussed as follows:

For capturing the increasing part in the combustion noise spectrum, we obtain the modified colored noise ($\widehat{\xi}(s)$) by filtering $\widehat{\epsilon}(s)$ in the frequency domain, using the following transfer function ($H(s)$) [61],

$$\frac{\widehat{\xi}(s)}{\widehat{\epsilon}(s)} = H(s) = \Gamma \frac{\sqrt{\mathrm{D}}\tau_c^2 s}{(1+\tau_c s)^2} \tag{A1}$$

where, $s = i\omega$ is the Laplace variable. ϵ is Gaussian white noise (a vector of size $n \times 1$, where n is the number of samples based on sampling frequency). Γ is the measure of white noise intensity. D is a constant used to adjust the power of ξ, and τ_c is the noise correlation time. The resulting power spectrum is given by,

$$S_{\xi\xi}(\omega) = |H|^2 S_{\epsilon\epsilon} = \frac{\Gamma}{2\pi} \frac{\mathrm{D}\omega^2\tau_c^4}{\left(1+\omega^2\tau_c^2\right)^2} \tag{A2}$$

which features f_{peak} at,

$$f_{peak} = \frac{1}{2\pi\tau_c} \tag{A3}$$

Similar to the OU noise, the modified colored noise power is equated to that of a white noise in the band $[\omega_1; \omega_2]$, which yields

$$\mathrm{D} = \frac{2\left(\omega_2 - \omega_1\right)}{\tau_c} \left(\mathrm{atan}\left(\omega_2\tau_c\right) - \mathrm{atan}\left(\omega_1\tau_c\right) - \frac{\omega_2\tau_c}{1+\omega_2^2\tau_c^2} + \frac{\omega_1\tau_c}{1+\omega_1^2\tau_c^2} \right)^{-1} \tag{A4}$$

Figure A.1 shows the comparison of the power spectrum between white noise, OU noise and corresponding modified colored noise (given by Eqn.(A1)) generated by keeping the power within $\frac{\Delta\omega}{\omega_0} = 0.7$ constant. We generate the modified colored noise in such a way that the decay part of the spectrum (controlled by f^{-r}) for both OU and modified colored noise are nearly identical as shown in Fig. A.1(a).

From Fig. A.1(b), we can observe that increasing noise correlation times shift the f_{peak} to lower frequencies (in accordance with Eqn. (A3)). We also observe that the thermoacoustic frequency of the system (f_0) will equal to f_{peak} at $\tau_c/T_0 = 0.16$. This implies that f_0 sees the f^2 growth in the spectrum amplitude for all $\tau_c/T_0 \leq 0.16$. We find that noise-induced response of the system would be nearly identical to that of white noise up to the τ_c at which $f_0 = f_{peak}$. This is because, within the bandwidth, the curves in the power spectrum corresponding to $\tau_c/T_0 \leq 0.16$

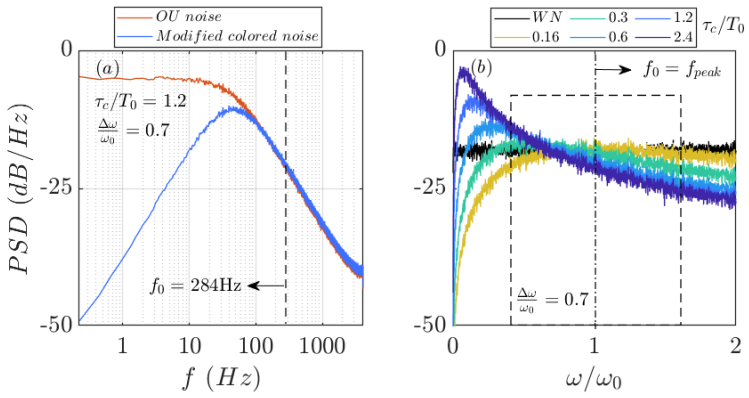

Figure A.1: Comparison of the power spectrum of (a) OU noise and modified colored noise at $\tau_c/T_0 = 1.2$ and (b) white noise and modified colored noise. The OU noise and modified colored noise are generated such that the powers provided by ξ and by the white noise of intensity Γ within $\frac{\Delta\omega}{\omega_0} = 0.7$ are equal. The correlation time, τ_c, is normalized by the duct acoustic time period, T_0 $(= 1/f_0)$.

are nearly similar to the white noise (for example, yellow and black curves in plot (b)). For all $\tau_c/T_0 > 0.16$, noise-induced response of a system would be similar to OU noise.

To elucidate the effect of f^2 increase on the coherence factor, we present the results by subjecting the system to the modified colored noise for $\Delta\omega/\omega_0 = 0.7$. Figure A.2 shows the variation of coherence factor (β) as a function of τ_c and σ_b at $K = 0.40$ (lines + markers correspond to the system when subjected to OU noise and lines (solid, dashed and dotted) correspond to the system subjected to modified colored noise). We can observe that at $\tau_c/T_0 = 0.16$ (where $f_0 = f_{peak}$), β has a peak at $\sigma_b/\sigma_W \simeq 1$ for modified colored noise forcing. We find that when $\tau_c/T_0 \leq 0.16$, the β trends would be nearly identical to that of white noise with optimal noise intensity (σ_b/σ_w) varying between 0.9 to 1. For all $\tau_c/T_0 > 0.16$, the qualitative trends for β are similar for both the types of noise forcing: (i) increase in τ_c, shifts the optimum noise intensity

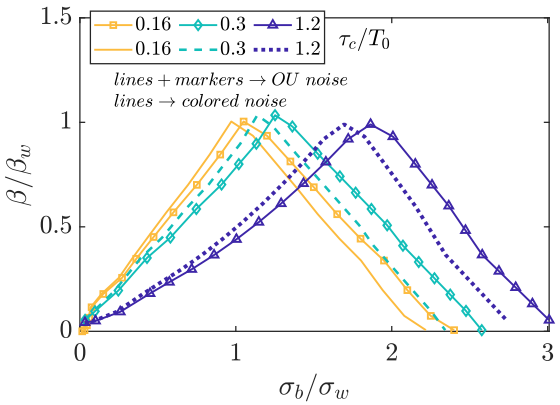

Figure A.2: Comparison between OU noise and modified colored noise forcing: variation of coherence factor (β) as a function of noise intensity within a given band (σ_b) and noise correlation time (τ_c) for $\Delta\omega/\omega_0 = 0.7$ at $K = 0.40$. Lines + markers correspond to the system when subjected to OU noise and lines (solid, dashed and dotted) correspond to the system subjected to modified colored noise. σ_w and β_w correspond to the *optimum* white noise intensity and corresponding maximum coherence resonance at specified control parameter values.

to higher levels; (ii) β increases as the system is brought closer to the saddle-node point; (iii) for $\sigma_b/\sigma_w < 1$, β decreases monotonously with increase in τ_c; whereas for $\sigma_b/\sigma_w \geq 2$, β increases monotonously with increase in τ_c.

The Hurst exponent (H_q) also exhibits the similar variation as β with modified colored noise forcing: for $\tau_c/T_0 \leq 0.16$, the H_q curves overlap the white noise curve shown in Fig. 2.18(d); thereafter, H_q increases with increase in τ_c. The dependence of H_q on τ_c may lead to inaccurate predictions of impending instability.

Thus, the difference between the flat OU noise spectrum and the f^2 increase in combustion noise spectrum at low frequencies leads to small quantitative differences in terms of the coherence factor, but the trends in the coherence factor – therefore the primary conclusions of the study concerning early warning indicators – are preserved.

Appendix B: Algorithm for numerical integration

Eqn. (3.4)-(3.5) can be re-written as,

$$\ddot{x} + f(x, \dot{x}, t) = \xi(t) \tag{B1}$$

where, $f(x, \dot{x}, t)$ is the deterministic part of the system and $\xi(t)$ is the OU noise, given as,

$$\dot{\xi}(t) = -\frac{1}{\tau_c}\xi(t) + \frac{\sqrt{D}}{\tau_c}\epsilon(t) \tag{B2}$$

The algorithm for numerical integration can be written as [54, 241, 242]:

1. Initialize the time step size (Δt), state vector (x_0) and its first derivative ($u = \dot{x}_0$), stochastic term (ξ_0), and time (t_0).

2. For each time step (n) from 1 to N:

   (a) Compute the deterministic increments:

$$\begin{aligned}
k_{1x} =& \dot{x}_n \Delta t \\
k_{1u} =& f(x_n, \dot{x}_n, t_n)\Delta t \\
k_{2x} =& (\dot{x}_n + 0.5k_{1u})\Delta t \\
k_{2u} =& f(x_n + 0.5k_{1x}, \dot{x}_n + 0.5k_{1u} \\
& t_n + 0.5\Delta t)\Delta t \\
k_{3x} =& (\dot{x}_n + 0.5k_{2u})\Delta t \\
k_{3u} =& f(x_n + 0.5k_{2x}, \dot{x}_n + 0.5k_{2u} \\
& t_n + 0.5\Delta t)\Delta t \\
k_{4x} =& (\dot{x}_n + k_{3u})\Delta t \\
k_{4u} =& f(x_n + k_{3x}, \dot{x}_n + k_{3u}, t_n + \Delta t)\Delta t
\end{aligned} \tag{B3}$$

   (b) Calculate the stochastic increment through Euler-Maruyama approach:

$$\xi_{n+1} = \xi_n - \frac{\Delta t}{\tau_c}\xi_n + \frac{\sqrt{D}}{\tau_c}\epsilon_n\sqrt{\Delta t} \tag{B4}$$

   (c) Update the state vector:

$$\begin{aligned}
x_{n+1} =& x_n + \frac{1}{6}(k_{1x} + 2k_{2x} + 2k_{3x} + k_{4x}) \\
\dot{x}_{n+1} =& \dot{x}_n + \frac{1}{6}(k_{1v} + 2k_{2v} + 2k_{3v} + k_{4v})
\end{aligned} \tag{B5}$$

3. Increment the time by the time step size, Δt.

4. Repeat the steps until the desired number of time steps is completed.

This general formulation combines the deterministic part (using the classic 4th order Runge-Kutta method) and the stochastic part (using the Euler-Maruyama method) to solve the second-order ODE with a stochastic term.

Appendix C: Effect of κ variation on skewness and kurtosis

Figure C.1 shows the variation of skewness as a function of v, τ_c/T_0, σ_b and κ for subcritical Van der Pol system. We can observe that at $\kappa = 4$ (Figs. C.1(a-b)), skewness decreases with increase in noise color for all v and σ_b; while it increases with increase in noise intensity for all v and τ_c/T_0. Skewness also decreases as the system approaches the saddle-node point. However, at $\kappa = 12$ (Figs. C.1(c-d)), although skewness increases with increase in both noise color and intensity but it remains relatively constant as the system approach the saddle-node point.
Similarly, Fig. C.2 shows the variation of kurtosis as a function of v, τ_c/T_0, σ_b and κ for the subcritical system. We can observe that at $\kappa = 4$ (Figs. C.2(a-b)), kurtosis increases with increase in noise color for all v and σ_b; while it decreases with increase in noise intensity and control parameter for all τ_c/T_0. Whereas, at $\kappa = 12$ (Figs. C.2(c-d)), at low noise level, kurtosis decreases with increase in noise color, while it exhibit increasing-decreasing trend with noise color at high noise levels. Further, at low noise levels, the trends in kurtosis becomes indistinguishable for all $\tau_c/T_0 > 1$. Kurtosis also shows different trends with respect to control parameter at different noise levels: kurtosis increases as the system approaches the saddle-node point at low noise level; while at high noise level, it decrease for $\tau_c/T_0 < 0.1$ and increases for all $\tau_c/T_0 > 0.1$ as the system approach the Hopf bifurcation.
Figs. 3.7-3.8 and C.1-C.2 shows that both skewness and kurtosis not only depends on noise characteristics and control parameter but also depends on constant equation parameters, hence they can not serve as reliable EWIs.

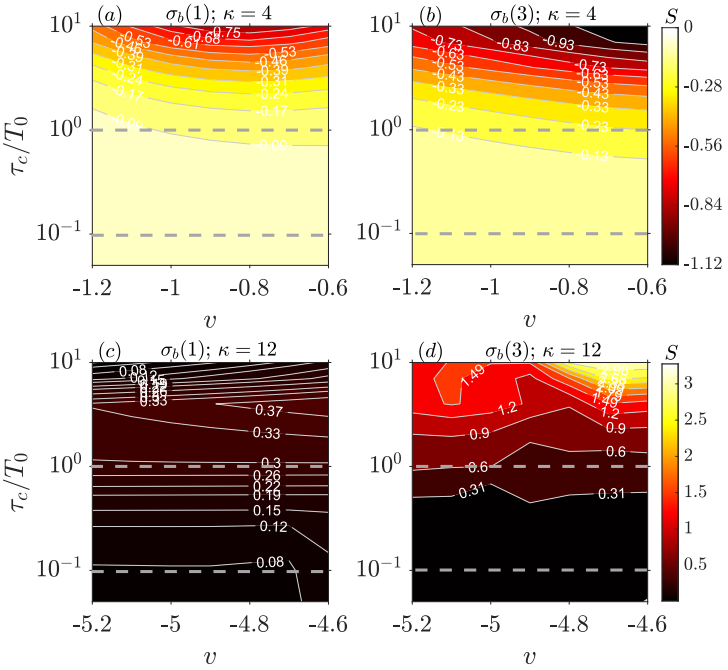

Figure C.1: 2D contour map of skewness (S) as the control parameter (v) and noise correlation time (τ_c/T_0) are varied at two noise intensities ($\sigma_b(1)$ (a, c) and $\sigma_b(3)$ (b, d)) for subcritical Van der Pol systems at $\kappa = 4$ (a-b) and $\kappa = 12$ (c-d). The dashed grey line separate the plots into categories of low and moderate to high noise correlation times.

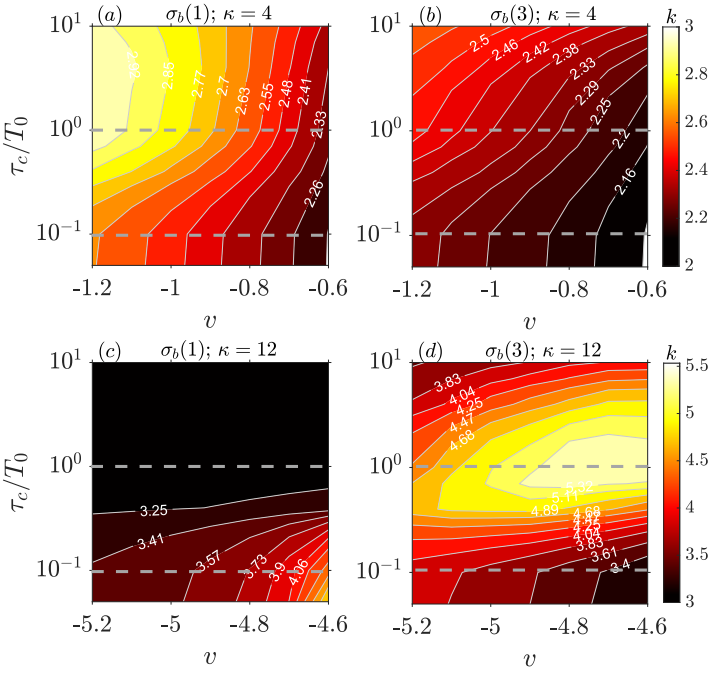

Figure C.2: 2D contour map of kurtosis (k) as the control parameter (v) and noise correlation time (τ_c/T_0) are varied at two noise intensities ($\sigma_b(1)$ (a, c) and $\sigma_b(3)$ (b, d)) for subcritical Van der Pol systems at $\kappa = 4$ (a-b) and $\kappa = 12$ (c-d). The dashed grey line separate the plots into categories of low and moderate to high noise correlation times.

The variation in κ value do not affect the qualitative trends of other EWIs discussed above.

Appendix D: Time delayed stochastic Van der Pol oscillators

While fundamental aspects of thermoacoustic instability can be understood through the classical Van der Pol oscillator, the instability in combustors employing flames is essentially a time delay feedback phenomenon; the time delay being a characteristic feature of the response of flames to acoustic fluctuations [175–177]. Recently Bonciolini et al. [177] have proposed modification of Van der Pol oscillators (Eqn. (3.4)-(3.5)) to include time delay as,

$$\ddot{x} + \kappa \dot{x}_\tau x_\tau^2 - \beta^* \dot{x}_\tau + \alpha \dot{x} + \omega_0^2 x = \xi(t) \tag{D1}$$

and

$$\ddot{x} + \mu \dot{x}_\tau x_\tau^4 - \kappa \dot{x}_\tau x_\tau^2 - \beta^* \dot{x}_\tau + \alpha \dot{x} + \omega_0^2 x = \xi(t) \tag{D2}$$

where, τ is the flame response time delay. The control parameter, v, is modified from $v = (\beta^* - \alpha)/2$ to $v = (\beta^* cos(\omega_0 \tau) - \alpha)/2$. The time delay becomes an additional parameter whose effect on system dynamics must be studied. Moreover, noise may be present in the time delay. Noise in time delay will be a parametric noise source to the oscillator system with a mean $\bar{\tau}$ and standard deviation σ. In such a case, the time delay model is given as [177],

$$\tau = \bar{\tau}(1 + \zeta(t)) \tag{D3}$$

where, $\zeta(t)$ is the random process generating the distribution of time delay which can be modelled as both white and colored noise. Eqn. (D1)-(D2) are also simulated using the fourth-order Runge-Kutta method for ODE and Euler-Maruyama method for $\xi(t)$ in Matlab. Figure D.1 shows the effect of time delay on the bifurcation of both supercritical and subcritical Van der Pol systems in the absence of noise. We find that when the time delay is an integer multiple of acoustic time period (T_0), such as, $\tau/T_0 = 1, 2, 3, \ldots$, then the system's response is similar to

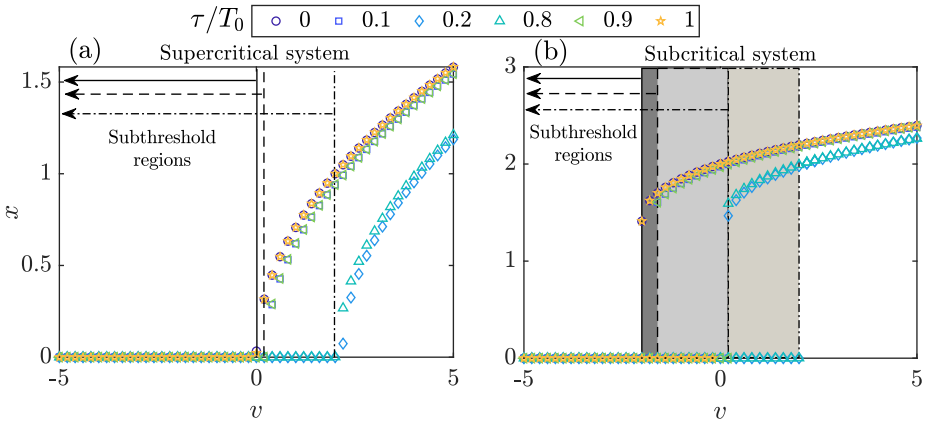

Figure D.1: Effect of time delay (τ/T_0) of flame response on bifurcation diagram in the absence of noise for (a) supercritical Hopf bifurcation and (b) subcritical Hopf bifurcation. The Hopf and saddle-node points changes with time delay. The grey regions in plot (b) shows the bistable region at varied τ/T_0. The subthreshold regions for corresponding time delay are marked with solid, dashed and dash-dot arrows.

Table D.1: Stability margins of time delayed Van der Pol oscillator systems in the absence of noise

	τ/T_0					
	0	**0.1**	**0.2**	**0.8**	**0.9**	**1**
Hopf point (v_H)	0	0.2	2	2	0.2	0
Saddle-node point (v_{SN})	-2	-1.6	0.2	0.2	-1.6	-2

shown in Fig. 3.2 with Hopf and saddle-node points observed at $v = 0$ and $v = -2$ respectively. However, when the time delay is a non-integer number, such as $\tau/T_0 = 0.1, 0.2, 0.8, 0.9$, then the system's response varies such that the Hopf and saddle-node points are observed at higher v values compared to $\tau/T_0 = 0$, as shown in Fig. D.1. The corresponding values of Hopf and saddle-node points are tabulated in Table D.1. It is important to note here that the Van der Pol systems displays a discontinuous (or alternating) behaviour with variation in the time delay: the system becomes unconditionally stable when the values of time delay are $0.3 \leq \tau/T_0 \leq 0.7$ or $1.3 \leq \tau/T_0 \leq 1.7$. In such cases, the bifurcation cannot be tracked to identify subthreshold or limit cycle regions. There are, therefore, limitations on the values of time delay that can be assumed. This behaviour of the Van der Pol systems with time delay is also reported by Ghirardo et al. [176] and Bonciolini et al. [177]. Also, the systems become unconditionally unstable for large enough delays. Therefore, the dynamics of the deterministic, delayed-feedback oscillators deviates substantially from that of classical Van der Pol systems.

Figure D.2 shows the effect of time delay on coherence factor and Hurst exponent. Results are presented for three different additive noise correlation times as columns (column 1 corresponds to white noise) at a fixed intensity, $\sigma_b(3)$. The top two rows are for coherence factor, β, while the bottom rows are for the Hurst exponent, H. Since the Hopf point changes with time delay, the x-axis is modified to $v^* = v - v_H$, where v_H denotes the Hopf point. The effect of parameter variation on β and H is evaluated at six different time delays. For fixed time delay, noise color, and noise intensity, the coherence factor increases as the system approaches the instability except at $\tau/T_0 = 0.8$ for supercritical system and $\tau/T_0 = 0.2$ for subcritical system, where the increase in β is not significant. The variation of coherence factor with noise color is same as those shown in Fig. 5. When time delay is close to an integer multiple of T_0 ($\tau/T_0 = 0.1$ and 0.9), the coherence factor values are close to the those obtained from the oscillator without time delay. On the other hand, when time delay is close to the unconditionally stable regions [177] ($\tau/T_0 = 0.8$ and 0.2 for supercritical and subcritical cases respectively), coherence factor values show a substantial deviation from those obtained without time delay in the oscillator. We can also conclude that the sensitivity of coherent factor to small changes in time delay (which may be expected for small changes in combustor operating conditions) is a non-monotonous function of the time delay: close to τ/T_0 of 0.2 or 0.8, small changes in time delay will lead to changes in β much larger than changes in response to parameter variation; close to 0.1, small time delay changes will lead to small β variation.

The Hurst exponent (Fig. D.2g–l) also responds to changes in τ/T_0; the response is dependent

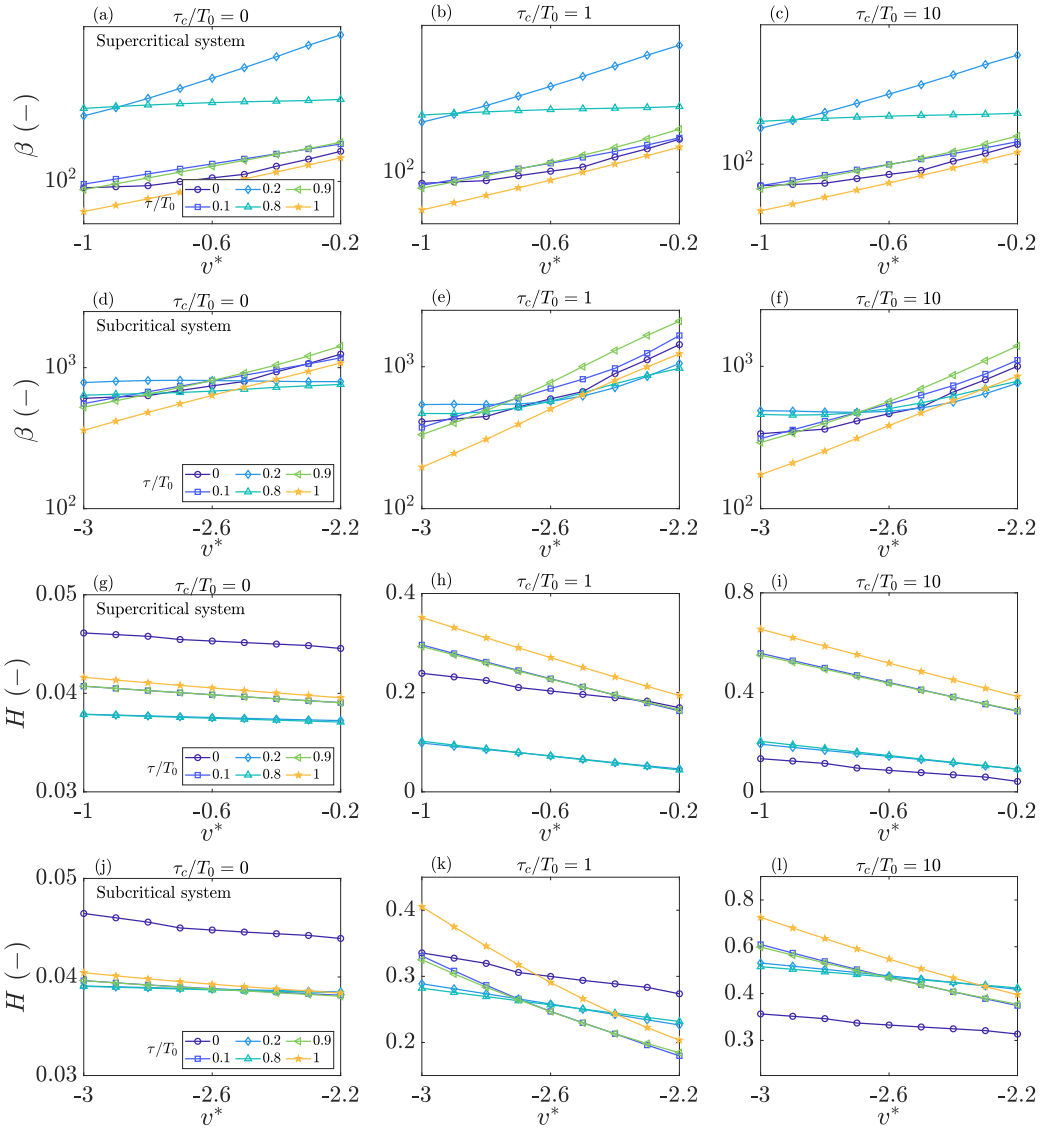

Figure D.2: Effect of time delay of flame response on coherence factor (plots (a)-(f)) and Hurst exponent (plots (g)-(l)) for supercritical and subcritical Van der Pol systems for varied noise color (τ_c/T_0) of additive noise at $\sigma_b(3)$.

on noise color. For white additive noise (Fig. D.2g, j) and for any given v^*, the Hurst exponent decreases with increase in time delay up to $\tau/T_0 = 0.8$ and increases thereafter. For colored noise, (Fig. D.2h, i, k, l), the Hurst exponent exhibits a non-monotonic trend with time delay. For a given time delay, the Hurst exponent decreases as the system approaches the instability, however, the decrease is evident only when noise color of additive noise is greater than the system's time scale, i.e. $\tau_c/T_0 \geq 1$. Additionally, Hurst exponent increases with increase in noise color. These trends of H with τ_c and v^* for a fixed time delay are similar to those presented in Fig. 3.11.

Differences in the effects of time delay variation on coherence factor and Hurst exponent could be explained on the basis of the occurrence of intermittent oscillations on the introduction of a time delay [177]. In the power spectrum such oscillations are expected to exhibit minimal impact close to dominant peak and thus result in relatively minor variation in the coherence factor

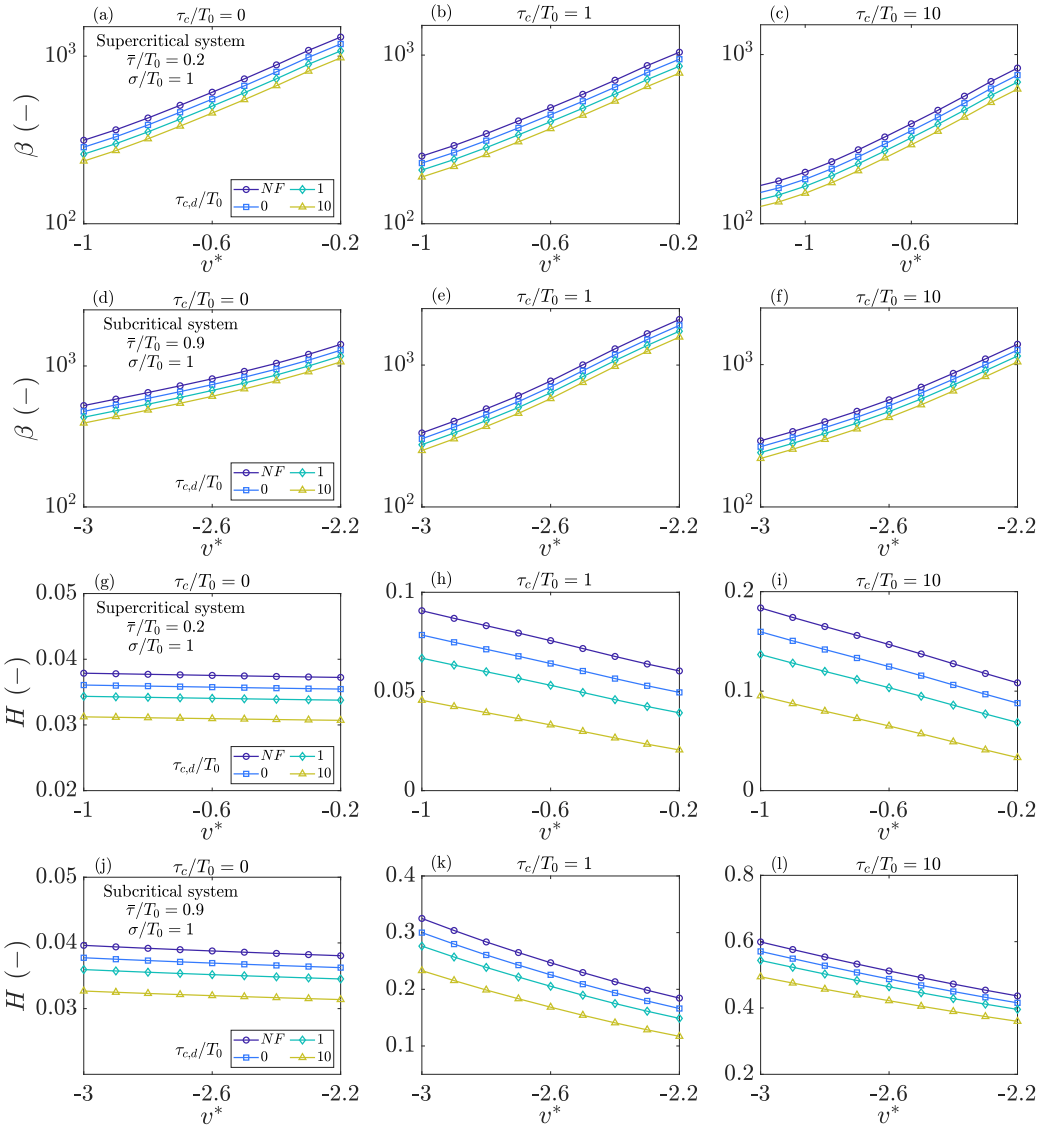

Figure D.3: Effect of time delay fluctuations ($\tau_{c,d}/T_0$) on coherence factor (a–f) and Hurst exponent (g–l) for supercritical ($\bar{\tau}/T_0 = 0.2$) and subcritical ($\bar{\tau}/T_0 = 0.9$) Van der Pol systems for varied noise color (τ_c/T_0) of additive noise at $\sigma_b(2)$. The variance of time delay fluctuations is kept constant as $\sigma/T_0 = 1$. NF represents the case without noise, shown in Fig. D.2.

(except for $\tau/T_0 = 0.2$ and 0.8). In contrast, Hurst exponent estimation relies on analyzing fluctuations in the time series, making them more susceptible to the presence of intermittent oscillations introduced by time delays. Finally, we note that time delay adds non-Markovian effects to system dynamics. A method to identify the non-Markovian effect is presented by Giugioli et al. [243]. However, such analysis is out of the scope of the present study.

Figure D.3 shows the variation of coherence factor (a–f) and Hurst exponent (g–l) as a function of time delay fluctuations ($\tau_{c,d}/T_0$) at $\sigma/T_0 = 1$ in response to variation in the control parameter, v^*, for white and colored additive noise with a fixed intensity, $\sigma_b(3)$ for supercritical and subcritical time delay Van der Pol systems. We find that when $\sigma/T_0 < 1$, the estimated coherence factor and Hurst exponent remains close to those shown in Fig. D.2. But when $\sigma/T_0 \geq 1$, the values of the precursors deviate from that of constant time delay. We can observe that for a given

mean time delay ($\bar{\tau}/T_0$), both coherence factor and Hurst exponent decrease with increase in color of time delay noise. The variation in Hurst exponent with $\tau_{c,d}/T_0$ is more pronounced than the coherence factor. Further, for a fixed $\tau_{c,d}/T_0$ and τ_c/T_0, coherence factor increases while the Hurst exponent decreases as the systems approach the instability. The decrease in Hurst exponent is prominent only when $\tau_c/T_0 \geq 1$. We note that adding fluctuations in the time delay corresponds to multiplicative noise.

Appendix E: Iteration of bifurcation experiments (noise-free system)

Multiple realizations (a total of 11) of the bifurcation experiments are performed, as shown in Fig. E.1, to ensure accuracy in the experimental results and to ensure that all the tests are performed in the subthreshold region (prior to the bistable region). In the last two measurement iterations, ϕ was varied in smaller steps (0.0035). However, on the grounds of being too close to the error in ϕ measurements (0.002), experiments with noise were conducted with a step size of 0.007. Fig. E.1 shows that in all the experiments, the system was stable in all experiments for $\phi \leq 0.714$ (closest point to the Hopf bifurcation).

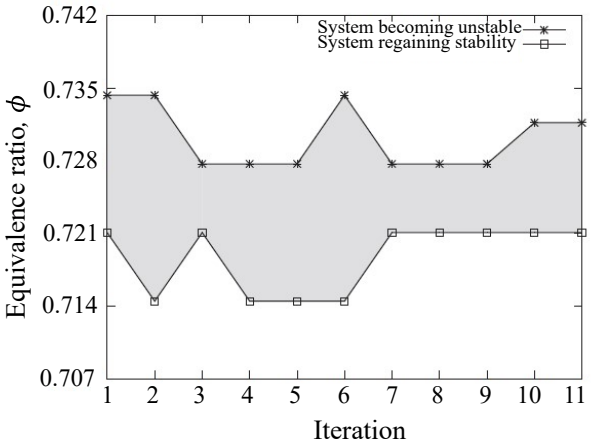

Figure E.1: Iterations of the bifurcation experiments and the obtained critical parameter values. The shaded region marks the hysteresis zone for each iteration (reproduced from Kabiraj et al. [6]).

Appendix F: Effect of time series length on estimation of EWIs (lean premixed combustion system)

We have also examined how sensitive the estimated early warning indicators (EWIs) are to the length of the time series of acoustic pressure fluctuations. Figure F.1 illustrates the variation of different EWIs as a function of time series length and the control parameter (ϕ) at three different noise intensities: $\sigma = 5.66$ Pa, 11.33 Pa, and 16.99 Pa. Our findings reveal that the skewness (S), kurtosis (k), and Hurst exponent (H) are significantly influenced by the length of the time series, particularly at low and intermediate noise intensities. These metrics show considerable variation with changes in the time series length, which can affect their reliability in real-time applications. Conversely, other EWIs like the coherence factor (β), variance (V), exhibit relatively stable trends regardless of the time series length, making them more dependable for accurate prediction.

In practical combustor configurations, the onset of instability can occur rapidly, often within a few seconds. Given this time constraint, we recommend using β and V as they provide reliable predictions even with shorter time series lengths. Their estimation process is also faster and less sensitive to variations in noise characteristics, making them suitable for real-time monitoring. On the other hand, EWIs such as the Hurst exponent and entropy/complexity measures require

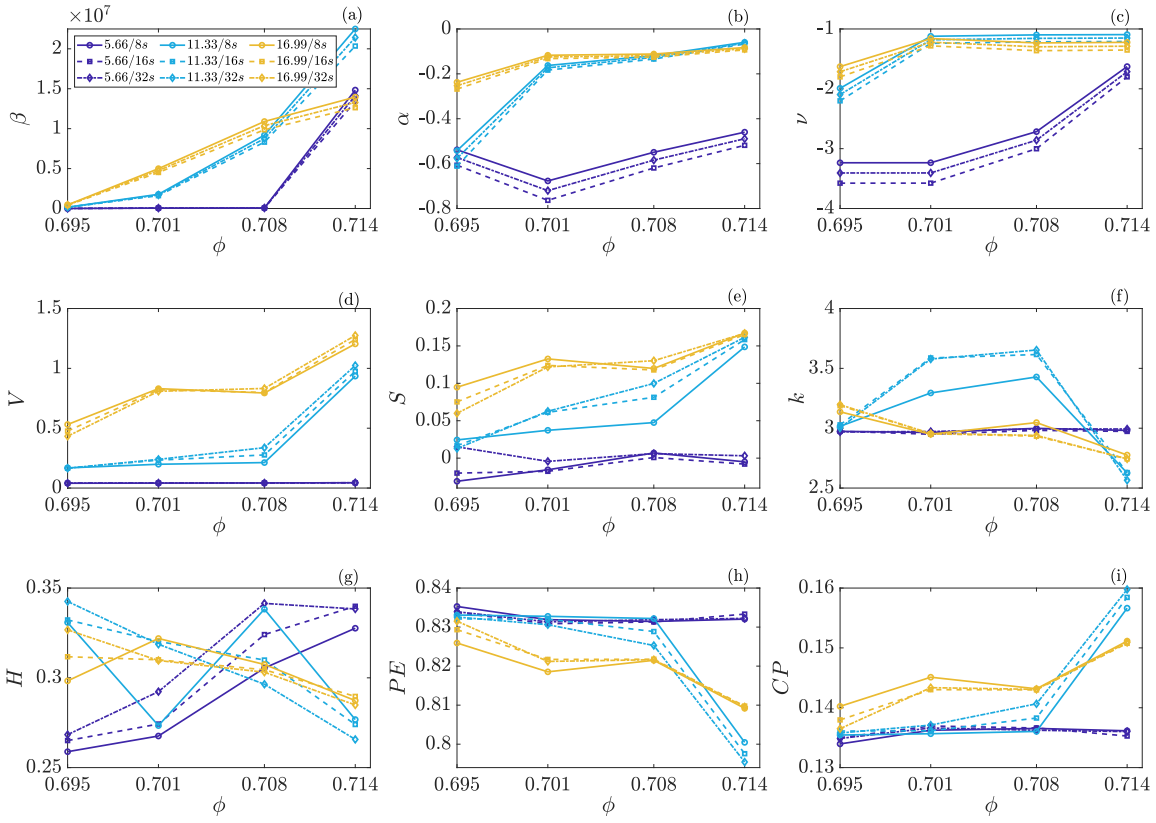

Figure F.1: Sensitivity of the various EWIs (estimated using p' data) on the length of the time series at three noise intensities, $\sigma = 5.66$ Pa, 11.33 Pa and 16.99 Pa, as ϕ is increased towards the Hopf bifurcation.

longer time series for accurate estimation and are more reliable at higher noise levels. This limitation hinders their effectiveness in real-time scenarios where quick decision-making is critical. Additionally, the decay rates of the autocorrelation function (ACF) and p' can be estimated with any time series length but require more computational time, which might not be feasible in fast-paced operational environments.

Overall, while various EWIs offer different insights, our study highlights the importance of selecting appropriate indicators like the coherence factor (β) and variance (V) for real-time applications due to their robustness, quick estimation, and minimal sensitivity to time series length and noise intensity. This approach ensures timely and accurate detection of thermoacoustic instability.

Appendix G: SPOD analysis: temporal coefficients and Lissajous curves (phase portraits) for dominant mode pairs

In addition to the general POD analysis, we also conducted the SPOD (spectral proper orthogonal decomposition) analysis on the instantaneous velocity snapshots obtained from SIV. SPOD [240], derived from space-time POD, performs the modal decomposition in the frequency domain and helps in obtaining the energetic coherent structures under all characteristic frequencies. For, a detailed derivation and discussion on SPOD, the reader is referred to Sieber et al. [240]. Figure G.1 shows the obtained results from SPOD analysis for two cases: (i) natural flow (plots (a)-(c)) and (ii) white noise forced flow (plots (d)-(f)). We can observe from Fig. G.1(a) and (d) that the single helical PVC (modes 2 and 4) is observed at $St = 0.53$, similar to the POD results (Fig. 7.8 and 7.11). A phase difference of $\pi/2$ is observed between the two time coefficient for each case (Fig. G.1(b) and (e)), which is further confirmed by the circular shape of corresponding Lissajous curves (Fig. G.1(c) and (f)). We can further observe that the single helical PVC is not always present in the flow in both cases: the amplitude grows and decays more often in case of natural flow suggesting its dynamic nature compared to the forced flow (Fig. G.1(b) and (e)). The evolution of amplitude indicates that the mode is marginally stable and gets excited by turbulent fluctuations or stochastic changes of the mean flow. These observations for the growth/decay of a amplitudes is also reported by Vanierschot et al. [238]. The time coefficient plots also indicates that white noise forcing stabilizes the single helical PVC mode. We find a good qualitative agreement between the results from POD and SPOD analysis

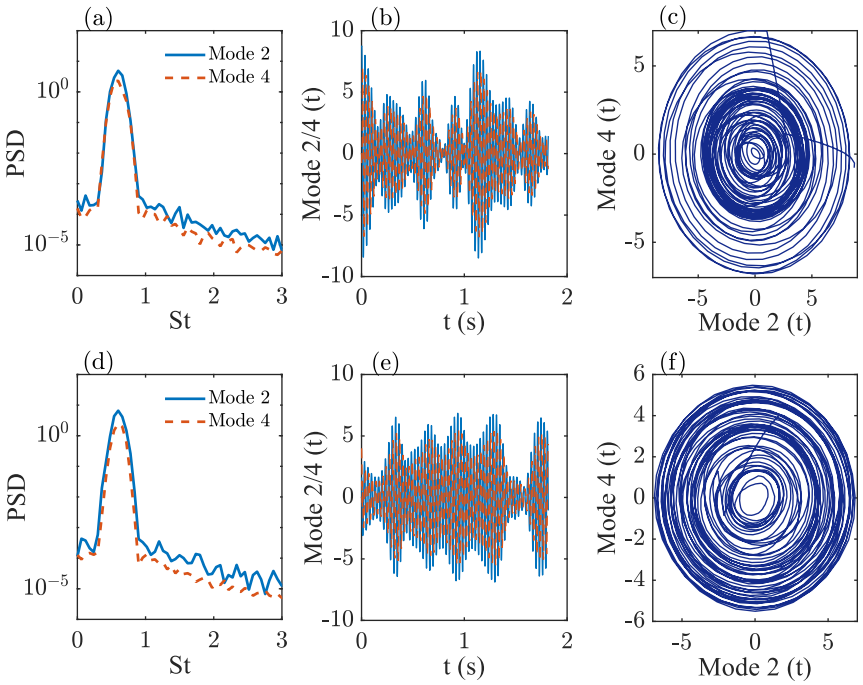

Figure G.1: SPOD analysis of (a)-(c) natural flow and (d)-(f) white noise forced flow. Plots (a), (d) shows the power spectral density of the dominant mode pair (2-4). The temporal characteristics of the mode pair are shown in plots (b), (e) –temporal coefficients– and (c), (f) –phase portraits– respectively.

of the SIV snapshots. Hence, SIV and the corresponding modal decomposition study can help in capturing the typical flow features and provides reliable results for burner design.

INDIAN INSTITUTE OF TECHNOLOGY ROPAR
RUPNAGAR 140001 PUNJAB, INDIA

PhD Thesis Evaluation Report

(Form No. I)

Name of the PhD Scholar : Neha Vishnoi

Department : Mechanical Engg.

Title of the thesis : Study of noise-induced dynamics in model gas turbine combustors

RECOMMENDATIONS

Tick one of the following:

1. The thesis in its present form is recommended for the award of the PhD degree. ☑

2. The thesis is recommended for the award of the PhD degree. However, my suggestions for improving the thesis may be considered at the time of the viva voce examination and if the viva voce board deems it appropriate, the same may be incorporated in the thesis based on the discussions during the viva voce examination. The revised thesis need not be sent to me. ☐

3. The thesis should be revised as per the suggestions enclosed. I would like to see the revised thesis incorporating my suggestions before I give further recommendations. ☐

4. The thesis is not acceptable for the award of the **PhD** degree ☐

M. Sathesh

Name of Examiner : Sathesh Mariappan

Signature and Date : M. Sathesh 5-9-24

Please give your detailed report in the attached sheet.
Please use additional sheets, if required.

INDIAN INSTITUTE OF TECHNOLOGY ROPAR
RUPNAGAR 140001 PUNJAB, INDIA

PhD Thesis Evaluation Report

(Form No. II)

Name of the PhD Scholar : Neha Vishnoi

Department : Mechanical Engg.

Title of the thesis : Study of noise induced dynamics in model gas turbine combustor.

DETAILED REPORT

(Attach additional sheets if necessary)

The thesis is one of the best one that I have read in the recent past. The student has performed a complete spectrum of analysis: theory & experiment. Even more important that the implementation of early warning indicators in practical combustor. Needless to say the thesis is well written & the figures are nicely illustrated & discussed. Many publications indicate the dedication of the student. I appreciate and wish her a great career ahead. I should also put my congradulations on the thesis supervisor, who provided the necessary motivation & infrastructure to bring out an excellent thesis.

Name of Examiner : Sathesh Mariappan.

Signature and Date : M. Sathesh. 5-9-24

INDIAN INSTITUTE OF TECHNOLOGY ROPAR
RUPNAGAR 140001 PUNJAB, INDIA

PhD Thesis Evaluation Report

(Form No. I)

Name of the PhD Scholar : **Neha Vishnoi**

Department : **Mechanical Engineering**

Title of the thesis : **Study of Noise-Induced Dynamics in Model Gas Turbine Combustors**

RECOMMENDATIONS

Tick one of the following:

1. The thesis in its present form is recommended for the award of the PhD degree. [*]

2. The thesis is recommended for the award of the PhD degree. However, my suggestions for improving the thesis may be considered at the time of the viva voce examination and if the viva voce board deems it appropriate, the same may be incorporated in the thesis based on the discussions during the viva voce examination. The revised thesis need not be sent to me. [ ]

3. The thesis should be revised as per the suggestions enclosed. I would like to see the revised thesis incorporating my suggestions before I give further recommendations. [ ]

4. The thesis is not acceptable for the award of the **PhD** degree [ ]

Name of Examiner : **Hiroshi Gotoda**

Signature and Date : Hiroshi Gotoda September 30, 2024

Please give your detailed report in the attached sheet.
Please use additional sheets, if required.

INDIAN INSTITUTE OF TECHNOLOGY ROPAR
RUPNAGAR 140001 PUNJAB, INDIA

PhD Thesis Evaluation Report

(Form No. II)

Name of the PhD Scholar : **Neha Vishnoi**

Department : **Department of Mechanical Engineering**

Title of the thesis : **Study of Noise-induced Dynamics in Model Gas Turbine Combustors**

DETAILED REPORT

(Attach additional sheets if necessary)

A self-excited thermoacoustic instability with large amplitudes is govern by the strong coupling among acoustic pressure fluctuations, heat release rate fluctuations, and hydrodynamics in various combustion systems. The onset of thermoacoustic instability induces the mechanical vibrations of the combustor, leading to the serious structural damage of combustors. The construction of detection methodologies to capture a warning of thermoacoustic instability is a challenging and significant topic is current combustion engineering and physics. Nonlinear dynamical systems have opened up a new pathway to treat a rich variety of thermoacoustic instabilities.

In this thesis, Neha Vishnoi conducts a systematic study on the noise effects on the prediction of thermoacoustic instability, focusing on electroacoustic modeling and stochastic Van der Pol oscillators of thermoacoustic instability. Neha Vishnoi estimates many metrics: statistical measures, spectral measures, multi-fractal measures, and entropy/complexity measures to investigate reliable indicators for stochastic Van der Pol oscillators exhibiting both supercritical and subcritical systems. Neha Vishnoi experimentally explores the potential utility using a laminar premixed combustion system. As shown in the list of prestigious journal publications, all the results obtained in this thesis deserve praise in the fields of combustion engineering and physics. Neha Vishnoi shows scientific accomplishment worthy of Ph. D thesis in the Indian Institute of Technology Ropar. I would like to highly evaluate the novelty of this thesis.

Name of Examiner : **Hiroshi Gotoda**

Signature and Date : Hiroshi Gotoda September 30, 2024